

**The University of Sheffield**



**NOVEL SENSORLESS CONTROL OF SURFACE-  
MOUNTED PERMANENT MAGNET  
SYNCHRONOUS MACHINES**

**Ximeng Wu**

**A thesis submitted for the degree of Doctor of Philosophy**

**Department of Electronic and Electrical Engineering**

**University of Sheffield**

**Mappin Street, Sheffield, S1 3JD, UK**

**04 July 2020**

# ABSTRACT

This thesis is focused on the sensorless control of surface-mounted permanent magnet synchronous machines (SPMSM) at zero and low speed, with due account for rotor eccentricity.

Based on magnetic saturation effect, short pulse injection based initial position estimation methods are systematically investigated. To obtain a reliable estimation, a voltage pulse selection strategy is presented by considering the measurement noise, torque production and rotor movement. A reliable selection area (RSA) is obtained which defines a selecting area for reliable estimation result. Two novel initial position estimation methods are proposed. The first one utilizes three-phase current responses so that only 3 pulses are required while maintaining 30 degrees resolution as conventional methods which requires 4-6 pulses. Moreover, a boundary detection strategy (BDS) is presented which enhances the estimation against the measurement noise and further improves the resolution to 15 degrees. The second method utilizes the DC-link voltage response instead of the current response, which shows a better performance. Furthermore, initial position estimation under parameter asymmetry is considered. The influences of resistance and inductance asymmetries are illustrated and compensation strategies are proposed.

A sensorless control method is proposed for start-up operation of SPMSMs which is always a challenge. By using a simplified fundamental model, only stator current information is required for position estimation without the need of parameters and voltage information. With rotor initial position information, a stable start-up performance is achieved even under load. When the initial position is unavailable, a reverse rotation compensation method is developed which guarantees the correct rotation direction during starting.

Finally, conventional sensorless control methods are based on a healthy and ideal condition of PMSMs. However, PMSMs are often non-ideal and the rotor eccentricity which is a common issue is considered in this thesis. The rotor eccentricity effect on PMSM characteristics is illustrated and its influence on fundamental model based sensorless position estimation is investigated. A modified back-EMF observer is proposed by adopting an adaptive notch filter which eliminates the harmonics in the position error caused by the rotor eccentricity.

# ACKNOWLEDGEMENTS

First of all, I would like to express my sincere gratitude to my supervisor Prof. Z. Q. Zhu. During my PhD study, not only his professional technical guidance and constructive help are valuable, but also his logical thinking and methodologies are very precious for the rest of my life. I am really glad that I had the opportunity to become his PhD student.

I am also very grateful to Dr. Zhan-yuan Wu for his great help in my PhD study. Many thanks to Dr. Yanxin Li, Dr. Hanlin Zhan and Dr. Peilin Xu who gave me great support at the beginning of my PhD study. I would also thank Dr. Jiaming Liu for his great help during my internship at Keele. Discussions with Mr. Tianyi Liu and Mr. Jin Xu were helpful. I would like to give my further thanks to all the group members in the Electrical Machines and Drives Group, as well as the staff of SiemensGamesa Renewable Energy in Sheffield.

I warmly thank my parents for their financial supports and encouragements, which make me dedicate great efforts on my PhD study. Finally, I am very grateful to my fiancé Murong Yang's endless love and unconditional faith to me.

# CONTENTS

ABSTRACT .....	II
ACKNOWLEDGEMENTS.....	III
CONTENTS.....	IV
LIST OF SYMBOLS.....	XI
LIST OF ABBREVIATIONS.....	XXI

## **CHAPTER 1 ..... 1**

### **GENERAL INTRODUCTION**

1.1 Introduction .....	1
1.1.1 PMSM Topologies.....	2
1.1.2 Control Strategy of PMSMs .....	4
1.1.3 Sensorless Control Techniques.....	7
1.2 Fundamental Model Based Sensorless Control Methods .....	7
1.2.1 Machine Model Coordinate .....	9
1.2.2 Back-EMF Based Methods.....	14
1.2.3 Flux-linkage Based Methods .....	17
1.2.4 Modern Control Theory Based Methods .....	21
1.2.5 Speed and Position Observer .....	25
1.3 Saliency Based Sensorless Control Methods.....	29
1.3.2 HF Machine Model.....	31
1.3.3 HF Signal Injection Methods.....	34
1.3.4 Polarity Detection .....	45
1.3.5 Cross-coupling Effect and Compensation .....	46
1.4 Sensorless Control of Surface-mounted PMSMs .....	47
1.4.1 Fundamental Model Based Method.....	48
1.4.2 Magnetic Saliency Based Method .....	49

1.4.3 Resistive Saliency Based Method.....	49
1.5 Sensorless Control Considering Rotor Eccentricity .....	51
1.6 Outline and Contributions of the Thesis .....	51
<b>CHAPTER 2 .....</b>	<b>55</b>
<b>VOLTAGE PULSE SELECTION STRATEGY FOR ROTOR INITIAL POSITION ESTIMATION</b>	
2.1 Introduction .....	55
2.2 Magnetic Saturation Effect .....	56
2.3 Rotor Initial Position Estimation .....	57
2.4 Conventional Rotor Initial Position Estimation.....	60
2.4.1 Three-phase Current Based Method .....	60
2.4.2 DQ Reference Frame Current Based Method.....	61
2.4.3 DC-link Current Based Method.....	62
2.4.4 Three-Phase Terminal Voltage Based Method.....	62
2.4.5 Simulation Validation.....	64
2.4.6 Experimental Validation.....	66
2.4.7 Overall Comparison.....	68
2.5 Proposed Simple Voltage Pulse Selection Strategy .....	70
2.5.1 Magnitude and Duration Selection .....	70
2.5.2 Reliable Selection Area .....	75
2.5.3 Experimental Validation.....	75
2.5.4 Summary.....	80
2.6 Overall Voltage Pulse Selection Investigation .....	80
2.6.1 Constraints .....	80
2.6.2 Extended Reliable Selection Area .....	81
2.6.3 Application of ERSA in Siemens Wind Power PM Generators.....	83
2.7 Conclusion .....	87

## **CHAPTER 3 ..... 88**

### **ROTOR INITIAL POSITION ESTIMATION METHOD BASED ON THREE PHASE CURRENT**

3.1 Introduction .....	88
3.2 Utilization of Three Phase Currents .....	89
3.3 Voltage Pulse Injection Process .....	92
3.3.1 First Voltage Pulse Injection .....	93
3.3.2 Second Voltage Pulse Injection .....	94
3.3.3 Polarity Determination .....	97
3.3.4 Improving Estimation Resolution.....	97
3.4 Boundary Detection Strategy.....	98
3.4.1 Noise Impact Reduction .....	98
3.4.2 Estimation Performance Improvement.....	99
3.5 Experimental Validation.....	103
3.5.1 An Example of Proposed Rotor Initial Position Estimation.....	104
3.5.2 Overall Rotor Initial Position Estimation Performance.....	106
3.5.3 Boundary Detection Performance .....	107
3.6 Conclusion .....	109

## **CHAPTER 4 ..... 110**

### **ROTOR INITIAL POSITION ESTIMATION METHOD BASED ON DC-LINK VOLTAGE**

4.1 Introduction .....	110
4.2 Utilization of DC-link Voltage .....	111
4.3 Excitation Configuration Investigation .....	112
4.3.1 Three-phase Based Excitation Configuration.....	112
4.3.2 Two-phase Based Excitation Configuration.....	113
4.3.3 Comparison Between Three-phase and Two-phase Excitation .....	113

4.3.4 Equivalent Injection Position.....	114
4.4 Voltage Pulse Injection Process .....	116
4.5 Consideration of Practical Issues.....	117
4.5.1 DC-link Measurement Errors .....	118
4.5.2 DC-link Capacitance.....	118
4.5.3 DC-link Resistance .....	121
4.5.4 DC-link Voltage Ripple.....	122
4.5.5 Duration and Magnitude Selection of Voltage Pulse .....	124
4.6 Experimental Validation.....	125
4.6.1 Voltage Pulse Selection .....	126
4.6.2 An Estimation Example.....	126
4.6.3 Overall Rotor Initial Position Estimation Performance.....	127
4.6.4 Comparison with Estimation Using Current Responses.....	128
4.7 Conclusion .....	128

## **CHAPTER 5 ..... 130**

### **ROTOR INITIAL POSITION ESTIMATION CONSIDERING PARAMETER ASYMMETRY**

5.1 Introduction .....	130
5.2 Current Response Model .....	130
5.2.1 Parameter Symmetry .....	131
5.2.2 Resistance Asymmetry .....	132
5.2.3 Inductance Asymmetry.....	137
5.2.4 Summary.....	142
5.3 Position Estimation under Parameter Asymmetries .....	143
5.3.1 Resistance Asymmetry .....	144
5.3.2 Inductance Asymmetry.....	149
5.3.3 Feasible Estimation Area Ratio .....	152

5.3.4 Summary.....	154
5.4 Compensation Methods for Parameter Asymmetries.....	154
5.4.1 Adjustment of Voltage Pulse Duration.....	154
5.4.2 Current Response Compensation Method.....	158
5.5 Conclusion.....	161
<b>CHAPTER 6 .....</b>	<b>163</b>
<b>A NEW SIMPLIFIED FUNDAMENTAL MODEL BASED SENSORLESS CONTROL FOR SURFACE-MOUNTED PERMANENT MAGNET SYNCHRONOUS MACHINES</b>	
6.1 Introduction .....	163
6.2 Conventional Fundamental Model Based Sensorless Control Methods .....	165
6.2.1 Back-EMF Based Sensorless Control Methods.....	165
6.2.2 Flux-linkage Based Sensorless Control Methods.....	168
6.2.3 Summary.....	169
6.3 Proposed Simplified Fundamental Model Based Method for Starting and Low Speed Operation.....	170
6.3.1 Simplified Model.....	170
6.3.2 Phase-locked Loop .....	174
6.3.3 Speed Estimator.....	175
6.3.4 Inverter Nonlinearity Effect.....	176
6.3.5 Starting Procedure .....	178
6.3.6 Experimental Validation.....	179
6.4 Application of Proposed Simplified Fundamental Model Based Method in Wind Power System.....	190
6.4.1 Starting Performance .....	190
6.4.2 Reverse Rotation Compensation Strategy .....	199
6.5 Conclusion.....	204

## **CHAPTER 7 ..... 205**

### **SENSORLESS CONTROL OF PERMANENT MAGNET SYNCHRONOUS MACHINES CONSIDERING ROTOR ECCENTRICITY**

7.1 Introduction .....	205
7.2 Rotor Eccentricity.....	207
7.2.1 Definition.....	207
7.2.2 Experimental Setup.....	208
7.3 Rotor Eccentricity Effects on PMSMs .....	209
7.3.1 Back-EMF and Flux-linkages.....	209
7.3.2 Inductance.....	212
7.3.3 Mechanical Frequency Torque Ripple .....	214
7.3.4 Summary.....	216
7.4 Rotor Eccentricity Effects on Fundamental Model Based Sensorless Control .....	217
7.4.1 Conventional Back-EMF Sensorless Control.....	217
7.4.2 Rotor Eccentricity Effects on Position Estimation .....	218
7.4.3 Suppression of Rotor Eccentricity Effects on Rotor Position Estimation .....	219
7.5 Experimental Validation.....	220
7.5.1 Machine Parameter Variation under Rotor Eccentricity .....	221
7.5.2 Position Estimation under Rotor Eccentricity .....	223
7.6 Conclusion .....	226

## **CHAPTER 8 ..... 227**

### **GENERAL CONCLUSIONS AND FUTURE WORK**

8.1 Introduction .....	227
8.2 Rotor Initial Position Estimation .....	228
8.3 Sensorless Start-up Operation of SPMSM .....	230
8.4 Sensorless Control under Rotor Eccentricity.....	232
8.5 Future Work.....	233

<b>REFERENCES.....</b>	<b>236</b>
<b>APPENDIX A DESCRIPTION OF EXPERIMENTAL PLATFORMS .....</b>	<b>261</b>
<b>APPENDIX B PUBLICATIONS .....</b>	<b>264</b>

# LIST OF SYMBOLS

Symbol	Explanation of Symbol	Units
$A_{Est\_wrong}$	Incorrect estimation area	Degree
$AE$	Average error	Degree
$\alpha_E$	Feasible estimation area ratio	%
$C_{abc-dq0}$	Transform matrix from ABC reference to synchronous reference frame	
$C_{abc-\alpha\beta0}$	Transform matrix from ABC reference to stationary reference frame	
$C_{dc}$	DC-link capacitance	F
$C_{dq0-abc}$	Transform matrix from synchronous reference frame to ABC reference	
$C_{\alpha\beta0-abc}$	Transform matrix from stationary reference frame to ABC reference	
$\hat{E}_d, \hat{E}_q$	Back-EMF in estimated synchronous reference frame	V
$\hat{E}_d^u, \hat{E}_q^u$	Unbalanced back-EMFs in estimated synchronous reference frame	V
$\hat{e}_c$	Estimated back-EMF of current model	V
$\Delta E_d, \Delta E_q$	Errors in back-EMFs of estimated synchronous reference frame	V
$E_d^u, E_q^u$	Unbalanced back-EMFs in synchronous reference frame	V
$E_{ex}$	Extended back-EMF	V
$\Delta e_{d2}$	Amplitude of 2 <sup>nd</sup> order harmonic in d-axis back-EMF	V
$\Delta e_m$	Equivalent mechanical frequency order harmonic component in back-EMF	V
$e_\alpha, e_\beta$	Back-EMF in stationary reference frame	V
$e_{\alpha\beta}$	Back-EMF vector in stationary reference frame	V
$f_c$	Cut-off frequency of RC LPF	Hz
$f(\Delta\theta_r)$	Position error signal	

$g$	Air gap with mixed rotor eccentricity	mm
$g_0$	Length of air gap	mm
$g_{DE}$	Magnitude of dynamic eccentricity	mm
$g_{SE}$	Magnitude of static eccentricity	mm
$ \hat{i}_{qh} $	Amplitude of q-axis high frequency carrier current in estimated reference frame	A
$\hat{i}_{d,CM}, \hat{i}_{q,CM}$	Stator current in current model	A
$\hat{i}_d, \hat{i}_q$	Stator current in estimated synchronous reference frame	A
$\hat{i}_{dh}, \hat{i}_{qh}$	High frequency current in estimated synchronous reference frame	A
$\Delta I_{th}$	Current response difference threshold considering boundary width	A
$\Delta I_{th0}$	Current response difference threshold considering noise impact	A
$\Delta I_{th1}$	Current response difference threshold considering optimal boundary width	A
$I_0$	DC-offset of current response	A
$I_1$	Current change caused by armature reaction	A
$I_2$	Current change due to PM	A
$I_{hf}$	High frequency carrier current vector	A
$I_A, I_B, I_C$	Three-phase current responses	A
$I_{A0}^u, I_{B0}^u, I_{C0}^u$	DC offsets in three-phase current responses under parameter asymmetries	A
$I_{A2}^u, I_{B2}^u, I_{C2}^u$	Amplitudes of 2 <sup>nd</sup> order harmonic in three-phase current responses under parameter asymmetries	A
$I_A^c, I_B^c, I_C^c$	Compensated three-phase current responses	A
$I_{MAX}$	Maximum value of recorded current	A
$I_{MEAN}$	Average value of recorded current	A
$I_{dc}$	DC-link current	A

$I_{error}$	Current error	A
$I_n$	Amplitude of negative high frequency carrier current	A
$I_p$	Amplitude of positive high frequency carrier current	A
$I_{q\_MAX}$	Maximum q-axis current	A
$I_{real}$	Actual current	A
$I_{record}$	Recorded current response	A
$I_s$	Stator current	A
$I_{\alpha\beta}$	Stator current vector in stationary reference frame	A
$i_A^P, i_B^P, i_C^P$	Primary three-phase current responses	A
$i_A^S, i_B^S, i_C^S$	Secondary three-phase current responses	A
$i_a, i_b, i_c$	3 phase stator currents	A
$i_d, i_q$	Stator current in synchronous reference frame	A
$i_{dh}, i_{qh}$	High frequency current in synchronous reference frame	A
$i_f$	Fundamental component of stator current	A
$i_n$	Negative sequence component of stator current	A
$i_{nd}, i_{nq}$	Negative sequence current in estimated reference frame	A
$i_p$	Positive sequence component of stator current	A
$i_x$	Arbitrary phase current	A
$i_\alpha, i_\beta,$	Stator current in stationary reference frame	A
$i_{\alpha h}, i_{\beta h}$	High frequency current in stationary reference frame	A
$\Delta\hat{i}_{dh}, \Delta\hat{i}_{qh}$	Differential current response in estimated reference frame	A
$\Delta\hat{i}'_{dh}, \Delta\hat{i}'_{qh}$	Polarity normalized differential current response in estimated reference frame	A
$\Delta I_{LA}, \Delta I_{LB}, \Delta I_{LC}$	DC offsets in current responses due to inductance asymmetry	A

$\Delta I_{RA}, \Delta I_{RB}, \Delta I_{RC}$	DC offsets in current responses due to resistance asymmetry	A
$I(t)$	Current response of pulse injection	A
$K_{\Delta L_A}, K_{\Delta L_B}, K_{\Delta L_C}$	Gains of current responses due to inductance asymmetry	
$K_{\Delta R_A}, K_{\Delta R_B}, K_{\Delta R_C}$	Gains of current responses due to resistance asymmetry	
$K_{LPF}$	Decay ratio of LPF	
$K_c$	Cross-coupling compensation coefficient	Rad/A
$K_i$	Integral gain	
$K_p$	Proportional gain	
$k_{L0}$	Equivalent gain of DC offset in current response due to inductance asymmetry	
$k_{L2}$	Equivalent gain of 2 <sup>nd</sup> order harmonic in current response due to inductance asymmetry	
$k_{R0}$	Equivalent gain of DC offset in current response due to resistance asymmetry	
$k_{R2}$	Equivalent gain of 2 <sup>nd</sup> order harmonic in current response due to resistance asymmetry	
$\Delta L_A, \Delta L_B, \Delta L_C$	Unbalanced terms in three-phase self-inductances	mH
$L_{MAX}$	Maximum inductance	mH
$L_{MIN}$	Minimum inductance	mH
$L_{aa}, L_{bb}, L_{cc}$	Three-phase self- inductances	mH
$L_d, L_q$	Dq-axis inductance	mH
$L_{dh}, L_{qh}$	Dq-axis incremental dq-axis inductances	mH
$L_d^{RE}, L_q^{RE}$	Dq-axis inductances under rotor eccentricity	mH
$L_{dqh}, L_{qdh}$	Incremental cross-couple inductance	mH
$L_d^u, L_q^u$	Unbalanced dq-axis inductances in estimated synchronous reference	mH
$L_{eq}$	Equivalent inductance	mH

$L_n$	Negative sequence inductance	mH
$L_p$	Positive sequence inductance	mH
$L_s$	Synchronous inductance	mH
$L_{s0}$	Amplitude of dc component of self-inductance	mH
$L_{s2}$	Amplitude of 2 <sup>nd</sup> order harmonic component of self-inductance	mH
$L_{sa}$	Average value of dq-axis inductances	mH
$L_{sd}$	Differential value of dq-axis inductances	mH
$L_{\alpha\alpha}, L_{\beta\beta}$	Self-inductances in stationary reference frame	mH
$\Delta L_{q2h}$	Amplitude of 2 <sup>nd</sup> order harmonic in q-axis inductance	mH
$\Delta L_{2h}$	Amplitude of 2 <sup>nd</sup> order harmonic due to unbalanced inductance	mH
$\Delta L_{d\_DC}, \Delta L_{q\_DC}$	DC offset inductances caused by unbalance	mH
$ME$	Maximum error	Degree
$M_{ab}, M_{ac}, M_{ba},$ $M_{bc}, M_{ca}, M_{cb}$	3-phase mutual- inductances	mH
$M_{s0}$	Amplitudes of dc component of mutual-inductance	mH
$M_{s2}$	Amplitudes of 2 <sup>nd</sup> order harmonic component of mutual-inductance	mH
$M_{\alpha\beta}, M_{\beta\alpha}$	Mutual-inductances in stationary reference frame	mH
$N_p$	Required pulse number	
$N_s$	Required sensor number	
$P$	Number of pole pairs	
$P_1$	Instantaneous real power	W
$P_{eddy}$	Eddy current loss	W
$P_m$	Mechanical frequency order component of instantaneous real power	W

$p$	Derivative operator	
$R_{dc}$	DC-link resistance	$\Omega$
$R_{eq}$	Equivalent resistance	$\Omega$
$R_s$	Stator phase resistance	$\Omega$
$R_{\alpha\beta}$	Resistances in stationary reference frame	$\Omega$
$\Delta R_A, \Delta R_B, \Delta R_C$	Unbalance terms in three-phase resistances	$\Omega$
$\Delta R$	Differential value of asymmetric resistance	$\Omega$
$\Sigma R$	Average value of asymmetric resistance	$\Omega$
$S$	Cost-effective index	
$T^{-1}(\Delta\theta_r)$	Transform matrix from estimated synchronous reference frame to actual synchronous reference frame	
$T(\theta_r)$	Transform matrix from stationary reference frame to synchronous reference frame	
$T(\Delta\theta_r)$	Transform matrix from actual synchronous reference frame to estimated synchronous reference frame	
$T_p$	Duration of voltage pulse	s
$T_{P\_MAX}$	Duration of voltage pulse for maximum current response difference	s
$T'_{P\_MAX}$	Approximate duration of voltage pulse for maximum current response difference	s
$T_e$	Electromagnetic torque	Nm
$T_s$	Sampling period	s
$t$	Time	s
$\Delta T$	Half period of injected square wave voltage signal	s
$U_{hf}$	Amplitude of injected high frequency voltage	V
$\hat{v}_{d,VM}, \hat{v}_{q,VM}$	Stator voltage in voltage model	V
$\hat{v}_d, \hat{v}_q$	Stator voltage in estimated synchronous reference frame	V

$\hat{v}_{dh}, \hat{v}_{qh}$	High frequency voltage in estimated synchronous reference frame	V
$V_p$	Magnitude of voltage pulse	V
$V_c$	Amplitude of controlled voltage source	V
$V_{comp}$	Compensation voltage	V
$V_{dc}$	DC-link voltage	V
$V_m$	Amplitude of stator voltage	V
$V_{p\_MAX}$	Minimum magnitude of voltage pulse	V
$V_{p\_MIN}$	Maximum magnitude of voltage pulse	V
$V_{\alpha\beta}$	Stator voltage vector in stationary reference frame	V
$v^{**}$	Voltage command with inverter nonlinearity compensation	V
$v_a, v_b, v_c$	3 phase stator voltages	V
$v_d, v_q$	Stator voltage in synchronous reference frame	V
$v_d^*$	D-axis voltage reference	V
$v_{dh}, v_{qh}$	High frequency voltage in synchronous reference frame	V
$v_\alpha, v_\beta,$	Stator voltage in stationary reference frame	V
$v_{\alpha h}, v_{\beta h}$	High frequency voltage in stationary reference frame	V
$\Delta V_{dc}$	DC-link voltage variation	V
$\Delta v_d$	D-axis voltage error	V
$\Delta v_{error-x}$	Arbitrary phase distortion voltage due to inverter nonlinearity	V
$z_{eq,\alpha}, z_{eq,\beta}$	Equivalent back-EMF of sliding mode observer	V
$z$	Sliding mode control function	
$\varepsilon_{V_{dc}}$	Error due to DC-link voltage variation	A
$\varepsilon_0$	Measurement DC offset error	A

$\varepsilon_{ADC}$	Error due to ADC quantization	A
$\varepsilon_{DE}$	Relative magnitudes of dynamic eccentricity	%
$\varepsilon_{PLL}$	Input error of PLL	
$\varepsilon_{SE}$	Relative magnitudes of static eccentricity	%
$\varepsilon_d$	Error due to disturbance	A
$\varepsilon_k$	Measurement scaling error	A
$\varepsilon_n$	Error due to noise	A
$\varepsilon_{ripple}$	Error due to DC-link voltage ripple	V
$\Delta\hat{\theta}_r$	Estimated position error	Degree
$\hat{\theta}_r$	Estimated rotor position	Degree
$\theta_M$	Rotating angle of rotor	Degree
$\theta_R$	Spatial information in asymmetric resistance	Degree
$\theta_{comp}$	Compensation angle	Degree
$\theta_m$	Position error caused by cross-coupling	Degree
$\theta_{max}$	Maximum rotor movement	Degree
$\theta_p$	Reactance angle	Degree
$\theta_r$	Electrical rotor position	Degree
$\theta_v$	Voltage angle	Degree
$\theta_w$	Boundary width	Degree
$\theta_x$	Geometric angle from x-axis	Degree
$\Delta\theta_r$	Rotor position error	Degree
$\tau_e$	Electrical time constant	s
$\tau_{e\_MAX}$	Maximum electrical time constant	s
$\tau_{e\_MIN}$	Minimum electrical time constant	s

$\tau_{eN}$	Nominal electrical time constant	s
$\varphi_{DE}$	Phase shift of dynamic rotor eccentricity	Degree
$\varphi_{SE}$	Phase shift of static rotor eccentricity	Degree
$\psi_{AF}$	Active flux	Wb
$\psi_a, \psi_b, \psi_c$	3 phase stator flux-linkages	Wb
$\psi_d, \psi_q$	Stator flux-linkage in synchronous reference frame	Wb
$\psi_m$	PM flux-linkage	Wb
$\psi_{m\alpha}, \psi_{m\beta}$	PM flux-linkage in stationary reference frame	Wb
$\psi_\alpha, \psi_\beta$	Stator flux-linkage in stationary reference frame	Wb
$\hat{\psi}_{AFd}, \hat{\psi}_{AFq}$	Active flux in estimated synchronous reference frame	Wb
$\vec{\psi}_{PM}$	PM flux on stator iron core	Wb
$\vec{\psi}_{coil}$	Coil excitation flux on stator iron core	Wb
$\hat{\psi}_d, \hat{\psi}_q$	Flux-linkage in estimated synchronous reference frame	Wb
$\hat{\psi}_{md}, \hat{\psi}_{mq}$	Original PM flux-linkages in estimated synchronous reference	Wb
$\hat{\psi}_{md}^u, \hat{\psi}_{mq}^u$	Unbalanced PM flux-linkages in estimated synchronous reference	Wb
$\vec{\psi}_{total}$	Total flux on stator iron core	Wb
$\Delta\psi_A, \Delta\psi_B, \Delta\psi_C$	Unbalanced three-phase flux-linkages	Wb
$\omega_h$	Center frequency of adaptive notch filter	Rad/s
$\omega_{hf}$	Frequency of injected high frequency voltage	Rad/s
$\omega_c$	Cut-off frequency of LPF	Rad/s
$\omega_n$	Natural frequency	Rad/s
$\omega_r$	Electrical rotor angular speed	Rad/s
$\hat{\omega}_{r,ff}$	Estimated feedforward rotor speed	Rad/s

$\hat{\omega}_r$	Estimated rotor speed	Rad/s
$\Delta\omega_r$	Rotor angular speed error	Rad/s
$\lambda$	Coupling factor	
$\mu$	Bandwidth of adaptive notch filter	Rad/s
$\xi$	Damping ratio	

# LIST OF ABBREVIATIONS

AC	Alternating current
ADC	Analog to digital converter
AF	Active flux
ANF	Adaptive notch filter
BDS	Boundary selection strategy
BLAC	Brushless AC
BLDC	Brushless DC
BPF	Band pass filter
DC	Direct current
DE	Dynamic eccentricity
DSP	Digital signal processor
DTC	Direct torque control
EEMF	Extended electromotive force
EKF	Extended Kalman Filter
EM	Extended modulation
EMF	Electromotive force
ERSA	Extended reliable selection area
FOC	Field oriented control
HF	High frequency
HIL	Hardware in loop
HPF	High pass filter
IM	Induction machine
INFORM	Indirect flux detection by online reactance measurement

IPMSM	Interior permanent magnet synchronous machine
LFP	Low pass filter
LUT	Look-up table
MMP	Magnetic motive force
MRAS	Model reference adaptive system
PI	Proportional integral
PID	Proportional integral derivative
PLL	Phase-locked loop
PM	Permanent magnet
PMSM	Permanent magnet synchronous machine
PWM	Pulse width modulation
RE	Rotor eccentricity
RPM	Revolutions per minute
RSA	Reliable selection area
SE	Static eccentricity
SMC	Sliding mode controller
SMO	Sliding mode observer
SNR	Signal to noise ratio
SPMSM	Surface-mounted permanent magnet synchronous machine
SPWM	Sinusoidal pulse width modulation
SRFF	Synchronous reference frame filter
SVPWM	Space vector pulse width modulation
VC	Vector control
VSI	Voltage source inverter
VVVF	Variable voltage variable frequency

ZVC	Zero vector current
ZVCD	Zero vector current derivative

# CHAPTER 1

## GENERAL INTRODUCTION

### 1.1 Introduction

In the last decades, permanent magnet (PM) synchronous machine (PMSM) drives have become increasingly attractive in both industrial and domestic applications. Especially accompanied by the development of PM materials, power electronics devices and microcontroller, PM synchronous machine drives nowadays have many advantages including high efficiency, high torque and power density, and good control performance. A general PMSM drive system is shown in Fig. 1.1.

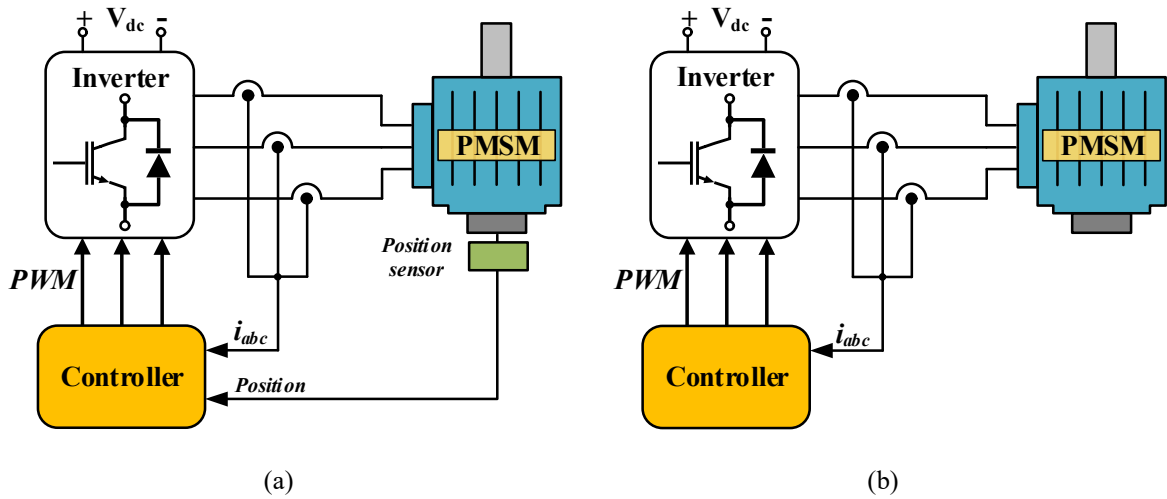


Fig. 1.1. Schematic of PM synchronous machine drive system. (a) Sensored. (b) Sensorless.

As shown in Fig. 1.1, the drive system consists of a controller, a voltage source inverter (VSI) and a PMSM. In order to achieve a desirable torque and speed control performance of PMSM, accurate rotor position information is necessary. In general, physical position sensors, such as encoder and resolver, are often mounted on the shaft of the machine to measure the rotor position as shown in Fig. 1.1(a). However, the utilization of position sensors will increase the cost and system complexity and decrease the system reliability. Hence, sensorless control techniques are developed so that the physical position sensors can be eliminated as shown in Fig. 1.1(b). For the sensorless control techniques, the rotor position is estimated based on the current and voltage information of PMSM.

This chapter firstly introduces the main PMSM topologies as well as basic control strategies of PMSM, i.e. field-oriented control (FOC) and direct torque control (DTC). Then, sensorless control techniques are introduced. At the end of this chapter, the research scope and the contributions of this thesis are highlighted.

### 1.1.1 PMSM Topologies

PMSMs are characterized by using PMs to produce magnetic field. According to [CHU13], there are various topologies of PMSMs and they can be briefly classified as Fig. 1.2.

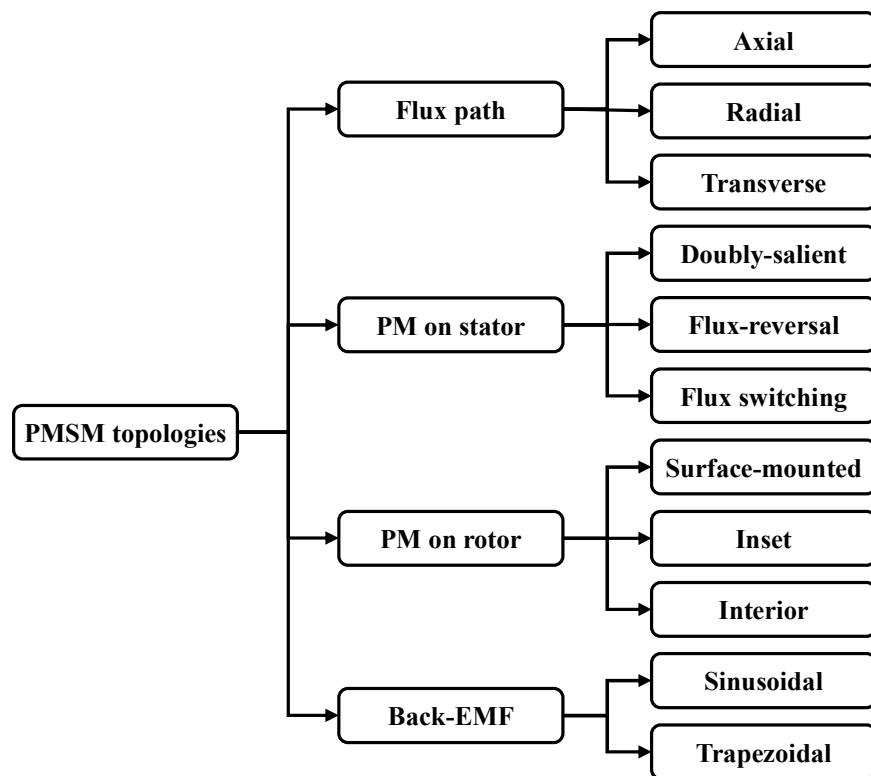


Fig. 1.2. Classification of PMSM topologies [CHU13].

Three different flux-path PM machines are shown in Fig. 1.3 as radial-field, axial-field [AYD06] [RAH06] [AYD07] [DON12] and transverse-flux PM machines [WEH86], [ZHA05]. Among them, the most popular one is the radial-field PM machines since they are simple, low cost and robust [CHU13].

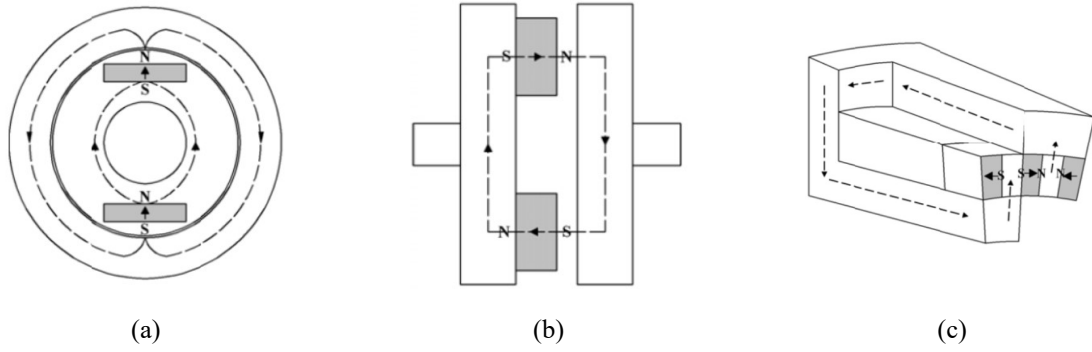


Fig. 1.3. Flux path types of PM Machines. (a) Radial-field. (b) Axial-field. (c) Transverse-flux [CHU13].

In case of the locations of PMs, there are mainly two groups: PMs on the stator and PMs on the rotor. Considering PMs on the stator, doubly-salient PM machines, flux-reversal PM machines and flux switching PM machines are mainly investigated, as depicted in Fig. 1.4.

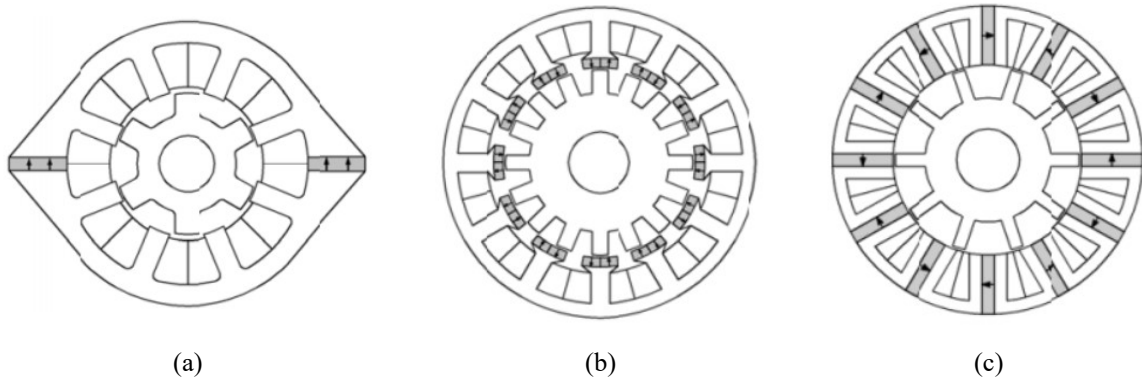


Fig. 1.4. PM Machine topologies with PMs on the stator. (a) Doubly-salient. (b) Flux-reversal. (c) Flux switching [CHU13].

For PMs on the rotor, in general there are three types, namely surface-mounted, inset and interior PM machines, as shown in Fig. 1.5.

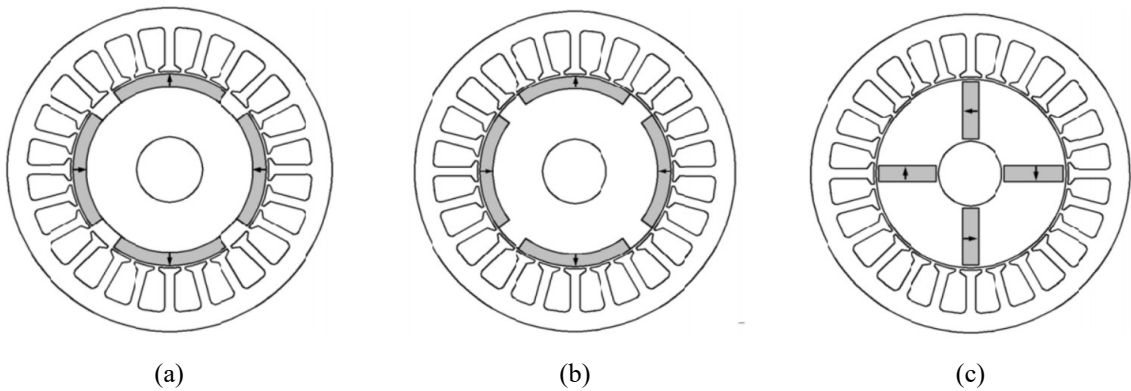


Fig. 1.5. PM Machine topologies with PMs on the rotor. (a) Surface-mounted. (b) Inset. (c) Interior [CHU13].

Compared with stator PM type, the rotor PM type is simpler and more robust. For the same torque density, the rotor PM type requires less volumes of PM which reduces the cost. Therefore, rotor PM type machines are more popular in majority of various applications. Moreover, since the PM materials have the permeability close to that of the air. Consequently, among the rotor PM type machines, the surface-mounted PM machines have negligible geometric saliency while the other two have significant saliency effect due to the geometric anisotropy [LIU13].

According to the back-EMF waveforms, PMSMs can be categorized as brushless DC (BLDC) machines and brushless AC (BLAC) machines, as shown in Fig. 1.6(a). Moreover, in case of the current excitation, it can be divided into square wave current excitation and sinusoidal current excitation, as shown in Fig. 1.6(b). Normally, in order to obtain a better torque performance, BLAC machine is driven by sinusoidal wave current and BLDC is driven by square wave current.

For this thesis, the main focus is on the surface-mounted BLAC machines with sinusoidal current excitation.

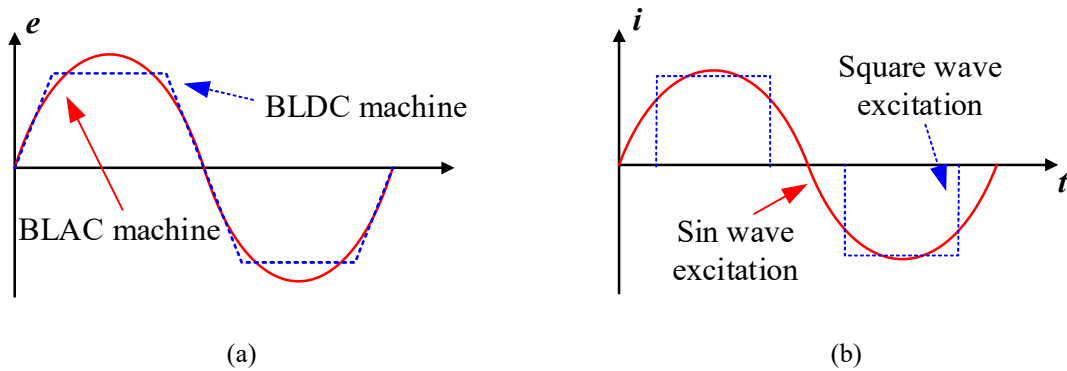


Fig. 1.6. BLDC and BLAC machines. (a) Back-EMF. (b) Current excitation.

### 1.1.2 Control Strategy of PMSMs

Field-oriented control (FOC), or vector control, was initially developed in early 1970s. By adopting the FOC, the three-phase alternative current (AC) motor can be controlled as a separately excited direct current (DC) motor. Based on the reference frame transformation, the three-phase sinusoidal stator currents are transformed into two orthogonal DC components: one defines the magnetic flux and the other defines the torque. With FOC, an excellent performance of PMSM drive is achieved. The PMSMs can operate over the full speed range and provide desirable torque at even zero speed. Besides, FOC shows a good dynamic performance and more control accuracy. The block diagram of a typical FOC used for PMSM speed control is

shown in Fig. 1.7. The stator q-axis current is related to the torque and d-axis current is related to the flux, and they can be regulated separately.

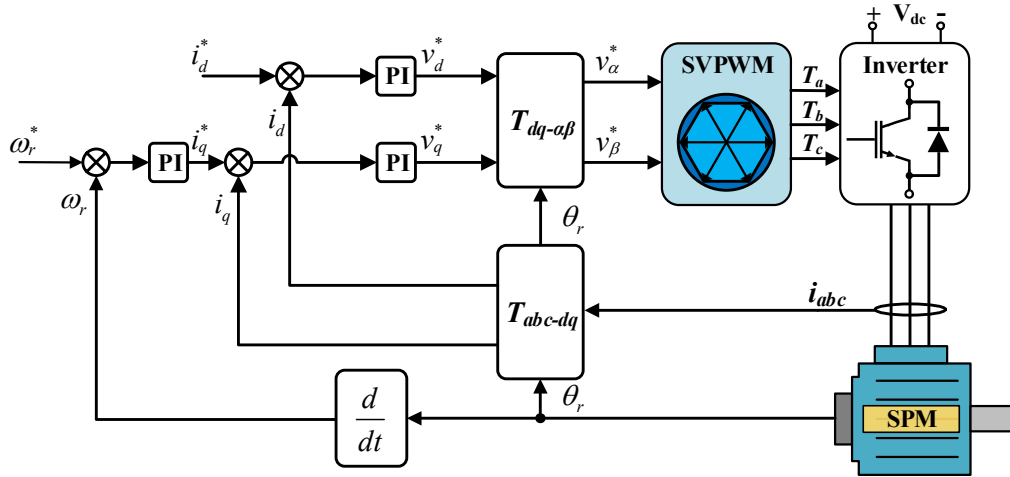


Fig. 1.7. Block diagram of field-oriented control (FOC).

Another well-known control strategy for PMSMs is called “Direct Torque Control (DTC)”. DTC control scheme is initially proposed for induction machines (IM) [TAK86] and is further extended to PMSMs [ZHO97] [PAC05] [FOO09] [ZHA11]. Different from FOC control scheme, DTC control scheme controls the flux directly. DTC offers a simple control structure, fast response and robust operation against machine parameters. The block diagram of a conventional switching table based DTC control scheme is given in Fig. 1.8.

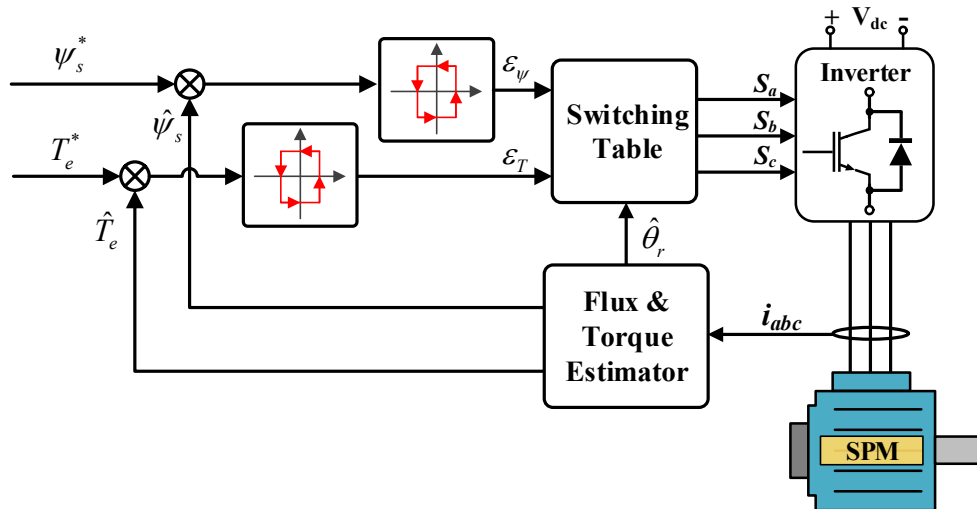


Fig. 1.8. Block of direct torque control (DTC).

For a conventional DTC, the electromagnetic torque and stator flux are regulated using hysteresis controllers. A switching table is used to select the optimal voltage vector of VSI. Different from FOC, coordinate transformation and specific modulation techniques are

eliminated. Hence, the dynamic performance is significantly improved. However, inherent torque and flux ripples will lead to acoustic noise and deteriorate the control performance, especially in the low speed range.

The overall comparison between FOC and DTC control schemes is summarized in TABLE 1.1.

TABLE 1.1  
OVERALL COMPARISON BETWEEN FOC AND DTC

Method	FOC	DTC
Parameter dependency	Dependent	Independent
Switching frequency	Constant	Variable
Sampling frequency	Low	High
Switching loss	Low	High
Computation burden	High	Low
Modulation	Yes	No
Implementation complexity	Complex	Easy
Requirement of Rotor position	Yes	No
Torque response	Slower	Faster

### 1.1.3 Sensorless Control Techniques

There are various sensorless control methods proposed in the past. They can be categorized into fundamental model based methods and saliency based methods. A brief classification of sensorless control techniques for BLAC machines is shown in Fig. 1.9.

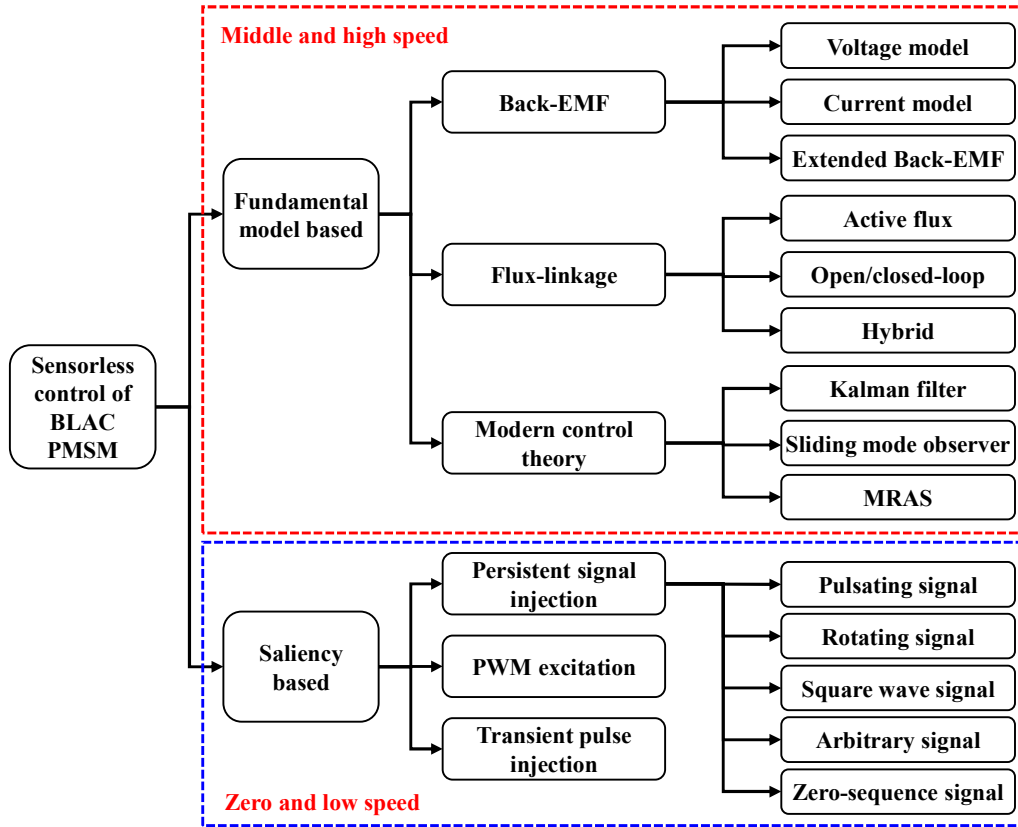


Fig. 1.9. Classification of sensorless control techniques for BLAC machines.

For fundamental model based methods, since they are based on the back-EMF or flux-linkage, accurate parameters and observable machine model are necessary. Therefore, they are more preferred in middle and high speed ranges. For saliency based methods, the PM machine saliency is independent of the rotor speed. This type of method can be used in zero and low speed range. However, as speed increases, the injected signal frequency will approach the fundamental current frequency, which will reduce the signal to noise ratio (SNR) of position dependent current responses. The detailed introduction of these two types of methods is illustrated in the following sections.

## 1.2 Fundamental Model Based Sensorless Control Methods

For fundamental model based sensorless control methods, the basic idea of is to estimate the back-EMF or flux-linkage based on the fundamental model of PM machines. Most of them

can fit into the frame as shown in Fig. 1.10. For each part of the frame, different types of method are shown in Fig. 1.11.

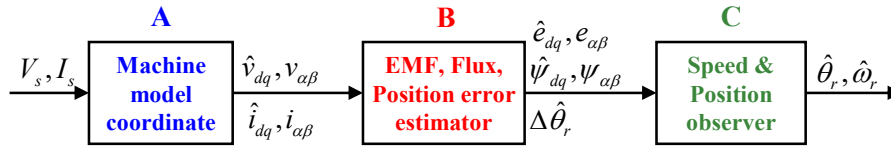


Fig. 1.10. General frame of fundamental model based sensorless control techniques.

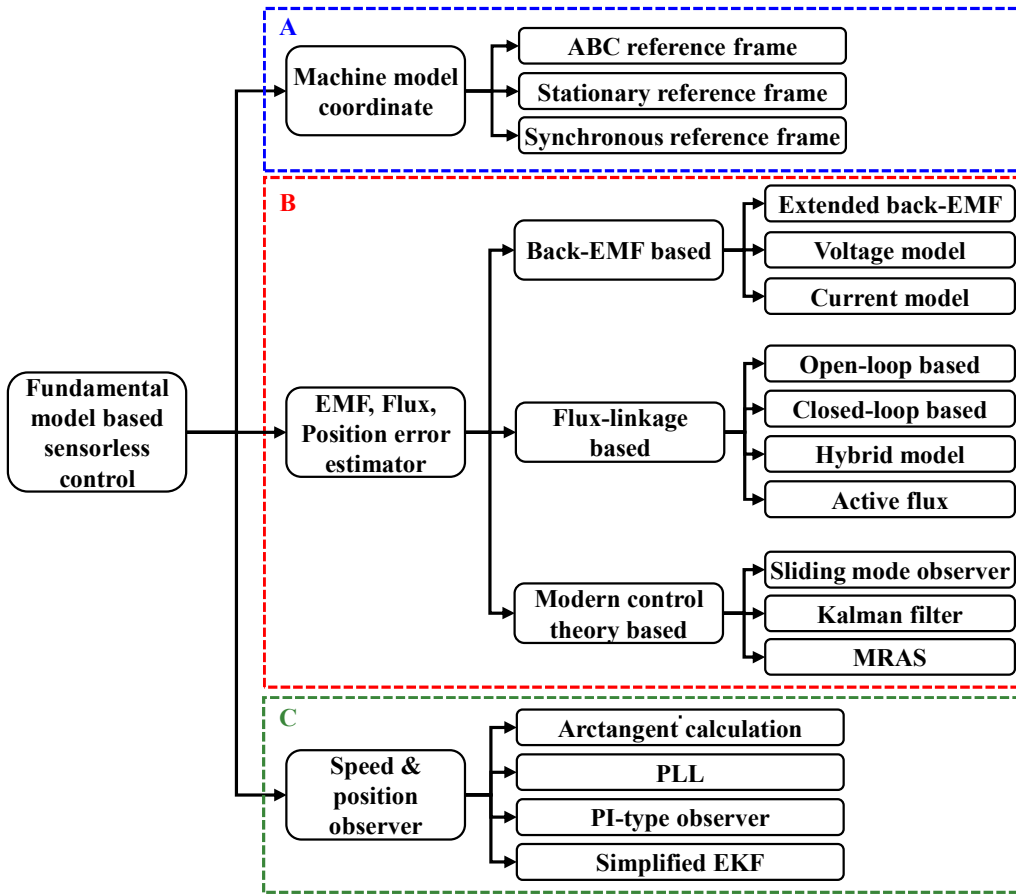


Fig. 1.11. Classification of fundamental model based sensorless control techniques.

For different methods, they can be characterised in terms of parts A, B and C in Fig. 1.11. In part A, the machine model coordinate based on which the sensorless control techniques is established is classified. Then, majority of the research focuses on part B. Different techniques are developed to estimate the back-EMF, flux-linkage or position error as shown in Fig. 1.11. For part C, after back-EMF, flux-linkage or position error is estimated, a position and speed observer is applied to generate the speed and position information. All three parts will be introduced in detail in this section.

### 1.2.1 Machine Model Coordinate

For the 3-phase PMSM, it can be modelled in different reference frames including ABC reference frame [ERT94], stationary reference frame ( $\alpha\beta 0$ ) [HU98] and synchronous reference frame (dq0) [CHE03]. Most of sensorless control methods are established based on stationary and synchronous reference frames which are transformed from ABC reference frame.

#### A. Model in ABC reference frame

In the ABC reference frame, the voltage equation is given by:

$$\begin{bmatrix} v_a \\ v_b \\ v_c \end{bmatrix} = \begin{bmatrix} R_s & 0 & 0 \\ 0 & R_s & 0 \\ 0 & 0 & R_s \end{bmatrix} \cdot \begin{bmatrix} i_a \\ i_b \\ i_c \end{bmatrix} + p \begin{bmatrix} \psi_a \\ \psi_b \\ \psi_c \end{bmatrix} \quad (1.1)$$

where  $v_a, v_b, v_c, i_a, i_b, i_c, \psi_a, \psi_b$  and  $\psi_c$  are the 3 phase voltages, currents and flux-linkages, respectively.  $R_s$  is the phase resistance, and  $p$  is the derivative operator, i.e.  $p = d/dt$ .

The 3-phase flux-linkages can be written as:

$$\begin{bmatrix} \psi_a \\ \psi_b \\ \psi_c \end{bmatrix} = \begin{bmatrix} L_{aa} & M_{ab} & M_{ac} \\ M_{ba} & L_{bb} & M_{bc} \\ M_{ca} & M_{cb} & L_{cc} \end{bmatrix} \cdot \begin{bmatrix} i_a \\ i_b \\ i_c \end{bmatrix} + \psi_m \begin{bmatrix} \cos \theta_r \\ \cos \left( \theta_r - \frac{2\pi}{3} \right) \\ \cos \left( \theta_r + \frac{2\pi}{3} \right) \end{bmatrix} \quad (1.2)$$

where  $L_{aa}, L_{bb}, L_{cc}, M_{ab}, M_{ac}, M_{ba}, M_{bc}, M_{ca}$  and  $M_{cb}$  are the 3-phase self- and mutual-inductances, respectively.  $\psi_m$  is the PM flux-linkage. For the inductance matrix, it is given by:

$$\begin{cases} L_{aa} = L_{s0} - L_{s2} \cos 2\theta \\ L_{bb} = L_{s0} - L_{s2} \cos 2(\theta - 120^\circ) \\ L_{cc} = L_{s0} - L_{s2} \cos 2(\theta + 120^\circ) \end{cases} \quad (1.3)$$

where  $L_{s0}$  and  $L_{s2}$  are the amplitudes of dc and the 2<sup>nd</sup> order harmonic component of self-inductances, respectively.

$$\begin{cases} M_{ab} = M_{ba} = M_{s0} - M_{s2} \cos 2(\theta + 120^\circ) \\ M_{bc} = M_{cb} = M_{s0} - M_{s2} \cos 2\theta \\ M_{ca} = M_{ac} = M_{s0} - M_{s2} \cos 2(\theta - 120^\circ) \end{cases} \quad (1.4)$$

where  $M_{s0}$  and  $M_{s2}$  are the amplitudes of dc and the 2<sup>nd</sup> order harmonic component of mutual-inductances, respectively. Furthermore, there is no 2<sup>nd</sup> order harmonic component in the non-salient machines, i.e.  $L_{s2} = M_{s2} = 0$ .

From (1.1) to (1.4), it can be seen that the PMSM machine model in ABC reference frame is very complicated from the control aspect. Therefore, the machine model is normally transformed into the stationary reference frame and the synchronous reference frame.

### ***B. Model in stationary reference frame***

The machine model can be transformed from ABC reference frame to stationary reference frame by using the transformation matrix in equation (1.5) and (1.6).

$$C_{abc-\alpha} = \frac{2}{3} \begin{bmatrix} 1 & -\frac{1}{2} & -\frac{1}{2} \\ 0 & \frac{\sqrt{3}}{2} & -\frac{\sqrt{3}}{2} \\ \frac{1}{2} & \frac{1}{2} & \frac{1}{2} \end{bmatrix} \quad (1.5)$$

$$C_{\alpha\beta 0-abc} = \begin{bmatrix} 1 & 0 & 1 \\ -\frac{1}{2} & \frac{\sqrt{3}}{2} & 1 \\ -\frac{1}{2} & -\frac{\sqrt{3}}{2} & 1 \end{bmatrix} \quad (1.6)$$

Besides, the relationship between ABC reference frame and stationary reference frame is shown in Fig. 1.12.

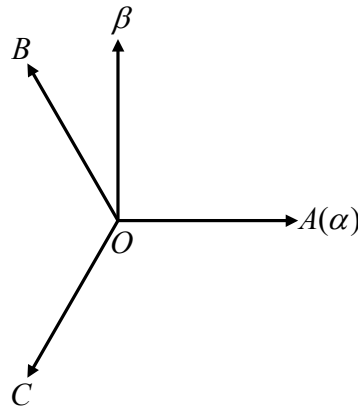


Fig. 1.12. Relationship between ABC reference frame and stationary reference frame.

After transformation, by neglecting the zero sequence component, the voltage and flux-linkage equations in the stationary reference frame are given by:

$$\begin{bmatrix} v_\alpha \\ v_\beta \end{bmatrix} = \begin{bmatrix} R_s & 0 \\ 0 & R_s \end{bmatrix} \begin{bmatrix} i_\alpha \\ i_\beta \end{bmatrix} + p \begin{bmatrix} \psi_\alpha \\ \psi_\beta \end{bmatrix} \quad (1.7)$$

$$\begin{bmatrix} \psi_\alpha \\ \psi_\beta \end{bmatrix} = \begin{bmatrix} L_{\alpha\alpha} & M_{\alpha\beta} \\ M_{\beta\alpha} & L_{\beta\beta} \end{bmatrix} \begin{bmatrix} i_\alpha \\ i_\beta \end{bmatrix} + \psi_m \begin{bmatrix} \cos \theta_r \\ \sin \theta_r \end{bmatrix} \quad (1.8)$$

where  $v_\alpha$ ,  $v_\beta$ ,  $i_\alpha$ ,  $i_\beta$ ,  $\psi_\alpha$  and  $\psi_\beta$  are the stator voltages, currents and flux-linkages in the stationary reference frame, respectively,  $\omega_r$ ,  $\theta_r$  are the electrical rotor speed and the electrical rotor position.  $L_{\alpha\alpha}$ ,  $L_{\beta\beta}$ ,  $M_{\alpha\beta}$  and  $M_{\beta\alpha}$  are the self- and mutual- inductances in the stationary reference frame, respectively. Furthermore, the inductances can be represented as:

$$L_{\alpha\alpha} = \frac{L_d + L_q}{2} + \frac{L_d - L_q}{2} \cos 2\theta_r \quad (1.9)$$

$$L_{\beta\beta} = \frac{L_d + L_q}{2} - \frac{L_d - L_q}{2} \cos 2\theta_r \quad (1.10)$$

$$M_{\alpha\beta} = M_{\beta\alpha} = \frac{L_d - L_q}{2} \sin 2\theta_r \quad (1.11)$$

where  $L_d$  and  $L_q$  are the d- and q-axis inductances. If the machine is non-salient, i.e. SPMSM, the relationship of the inductances is then given by:

$$L_d = L_q = L_s \quad (1.12)$$

$$M_{\alpha\beta} = M_{\beta\alpha} = 0 \quad (1.13)$$

$$L_{\alpha\alpha} = L_{\beta\beta} \quad (1.14)$$

Hence, the voltage and flux-linkage equations for SPMSM are given by:

$$\begin{bmatrix} v_\alpha \\ v_\beta \end{bmatrix} = \begin{bmatrix} R_s + pL_s & 0 \\ 0 & R_s + pL_s \end{bmatrix} \begin{bmatrix} i_\alpha \\ i_\beta \end{bmatrix} + \omega_r \psi_m \begin{bmatrix} -\sin \theta_r \\ \cos \theta_r \end{bmatrix} \quad (1.15)$$

$$\begin{bmatrix} \psi_\alpha \\ \psi_\beta \end{bmatrix} = \begin{bmatrix} L_s & 0 \\ 0 & L_s \end{bmatrix} \begin{bmatrix} i_\alpha \\ i_\beta \end{bmatrix} + \omega_r \psi_m \begin{bmatrix} \cos \theta_r \\ \sin \theta_r \end{bmatrix} \quad (1.16)$$

### ***C. Model in synchronous reference frame***

The machine model can be transformed from the ABC reference frame to the synchronous reference frame by using the transformation matrix as given by:

$$C_{abc-dq0} = \frac{2}{3} \begin{bmatrix} \cos \theta_r & \cos(\theta - 120^\circ) & \cos(\theta + 120^\circ) \\ -\sin \theta_r & -\sin(\theta - 120^\circ) & -\sin(\theta + 120^\circ) \\ \frac{1}{2} & \frac{1}{2} & \frac{1}{2} \end{bmatrix} \quad (1.17)$$

$$C_{dq0-a} = \begin{bmatrix} \cos \theta_r & -\sin \theta_r & 1 \\ \cos(\theta - 120^\circ) & -\sin(\theta - 120^\circ) & 1 \\ \cos(\theta + 120^\circ) & -\sin(\theta + 120^\circ) & 1 \end{bmatrix} \quad (1.18)$$

Besides, the relationship between ABC reference frame and synchronous reference frame is shown in Fig. 1.13.

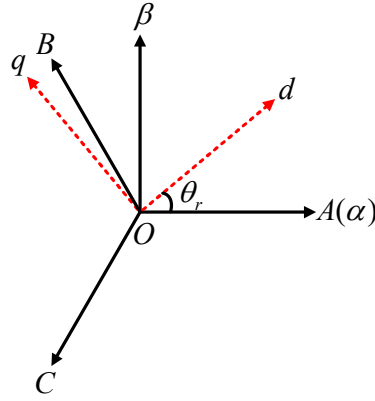


Fig. 1.13. Relationship between ABC reference frame and synchronous reference frame.

After transformation, by neglecting zero sequence component, the voltage and flux-linkage equations in the synchronous reference frame are given by:

$$\begin{bmatrix} v_d \\ v_q \end{bmatrix} = \begin{bmatrix} R_s & 0 \\ 0 & R_s \end{bmatrix} \begin{bmatrix} i_d \\ i_q \end{bmatrix} + p \begin{bmatrix} \psi_d \\ \psi_q \end{bmatrix} + \omega_r \begin{bmatrix} -\psi_q \\ \psi_d \end{bmatrix} \quad (1.19)$$

$$\begin{bmatrix} \psi_d \\ \psi_q \end{bmatrix} = \begin{bmatrix} L_d & 0 \\ 0 & L_q \end{bmatrix} \begin{bmatrix} i_d \\ i_q \end{bmatrix} + \psi_m \begin{bmatrix} 1 \\ 0 \end{bmatrix} \quad (1.20)$$

where  $v_d$ ,  $v_q$ ,  $i_d$ ,  $i_q$ ,  $\psi_d$  and  $\psi_q$  are the stator voltages, currents and flux-linkages in the synchronous reference frame, respectively. If the machine is non-salient, i.e. SPMSM, then,  $L_d = L_q = L_s$ . Hence, the voltage and flux-linkage equations for SPMSM are given by:

$$\begin{bmatrix} v_d \\ v_q \end{bmatrix} = \begin{bmatrix} R_s + pL_s & -\omega_r L_s \\ \omega_r L_s & R_s + pL_s \end{bmatrix} \begin{bmatrix} i_d \\ i_q \end{bmatrix} + \omega_r \psi_m \begin{bmatrix} 0 \\ 1 \end{bmatrix} \quad (1.21)$$

$$\begin{bmatrix} \psi_d \\ \psi_q \end{bmatrix} = \begin{bmatrix} L_s & 0 \\ 0 & L_s \end{bmatrix} \begin{bmatrix} i_d \\ i_q \end{bmatrix} + \psi_m \begin{bmatrix} 1 \\ 0 \end{bmatrix} \quad (1.22)$$

Moreover, for a sensorless control system, the actual rotor position is unknown. Therefore, the voltage equation should be transformed into the estimated synchronous reference frame with the transformation matrix given by:

$$T(\Delta\theta_r) = \begin{bmatrix} \cos(\Delta\theta_r) & \sin(\Delta\theta_r) \\ -\sin(\Delta\theta_r) & \cos(\Delta\theta_r) \end{bmatrix} \quad (1.23)$$

$$T^{-1}(\Delta\theta_r) = \begin{bmatrix} \cos(\Delta\theta_r) & -\sin(\Delta\theta_r) \\ \sin(\Delta\theta_r) & \cos(\Delta\theta_r) \end{bmatrix} \quad (1.24)$$

where  $\Delta\theta_r$  is the rotor position error between the estimation and actual values. Besides, the relationship between the synchronous reference frame and the estimated synchronous reference frame is shown in Fig. 1.14.

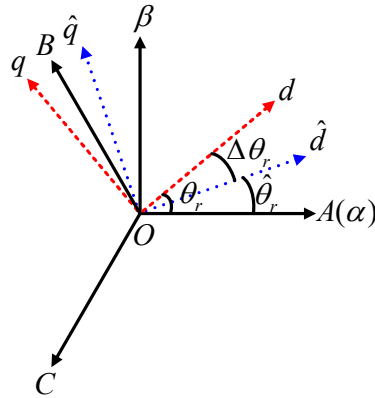


Fig. 1.14. Relationship between ABC reference frame and synchronous reference frame.

Then, the voltage equation in the estimated synchronous reference frame is given by:

$$\begin{bmatrix} \hat{v}_d \\ \hat{v}_q \end{bmatrix} = \begin{bmatrix} R_s + pL_d & -\omega_r L_q \\ \omega_r L_d & R_s + pL_q \end{bmatrix} \begin{bmatrix} \hat{i}_d \\ \hat{i}_q \end{bmatrix} + \omega_r \psi_m \begin{bmatrix} -\sin\Delta\theta_r \\ \cos\Delta\theta_r \end{bmatrix} \quad (1.25)$$

The superscript sign ‘^’ indicates the variables are in the estimated synchronous reference frame.  $\Delta\omega_r$  is the rotor speed error between estimation and actual values, respectively.

Overall, it can be seen that the machine models in stationary reference frame and synchronous reference frame are simpler than in the ABC reference frame. Therefore, conventional back-EMF and flux-linkage sensorless control methods are mainly proposed based on these two reference frames.

### 1.2.2 Back-EMF Based Methods

When there is a relative motion between the PMSM winding and PM magnetic field in the airgap, a voltage occurs in electrical machines, viz. back-EMF, and hence, back-EMF is directly proportional to the rotor speed. However, back-EMF is difficult to directly measure during machine operation. Instead, based on the fundamental model, back-EMF can be estimated from the stator voltage and current. Then, the back-EMF in the stationary reference frame can be calculated by:

$$e_{\alpha\beta} = V_{\alpha\beta} - R_s I_{\alpha\beta} - L_{\alpha\beta} \frac{dI_{\alpha\beta}}{dt} \quad (1.26)$$

$$\begin{bmatrix} e_\alpha \\ e_\beta \end{bmatrix} = \omega_r \psi_m \begin{bmatrix} -\sin \theta_r \\ \cos \theta_r \end{bmatrix} \quad (1.27)$$

Different methods are developed to estimate the back-EMF, [MAT96] proposed two methods, the rotor position and speed are estimated from a voltage model and a current model, respectively. [MOR02] and [CHE03] developed a concept of extended EMF (EEMF). Using EEMF, salient motors such as interior PMSM (IPMSM) can be considered as a non-salient machine. Three classical methods are introduced in this section.

#### A. Voltage model based method

[MAT96] proposed a position estimation algorithm based on the voltage model. The rotor position is estimated by minimizing the reference voltage and the estimated voltage.

Assuming the estimated voltage model is identical with the real one, the estimated voltage and speed of voltage model are given by:

$$\begin{bmatrix} \hat{v}_{d,VM} \\ \hat{v}_{q,VM} \end{bmatrix} = \begin{bmatrix} R_s + pL_d & -\omega_r L_q \\ \omega_r L_d & R_s + pL_q \end{bmatrix} \begin{bmatrix} \hat{i}_d \\ \hat{i}_q \end{bmatrix} + \begin{bmatrix} 0 \\ \hat{\omega}_r \hat{\psi}_m \end{bmatrix} \quad (1.28)$$

$$\hat{\omega}_{r,ff} = \frac{\hat{v}_q - (R_s \hat{i}_q + L_q p \hat{i}_q)}{L_d \hat{i}_d + \psi_m} \quad (1.29)$$

Then, the back-EMF can be estimated from the voltage difference by:

$$\Delta \hat{v}_d = \hat{v}_d - \hat{v}_{d,VM} = -\omega \psi_m \sin \Delta \theta_r \quad (1.30)$$

The overall sensorless control scheme is demonstrated in Fig. 1.15.

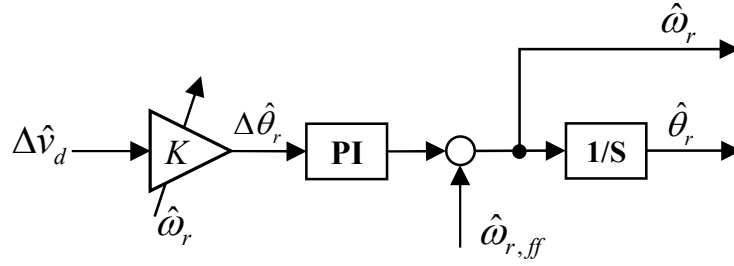


Fig. 1.15. Position and speed observer of voltage model based method. [MAT96]

### B. Current model based method

In [MAT96], a current model based method is introduced. Similar to voltage model one, the difference between the actual current and the calculated current from current model is regarded as the position error.

The calculated current and back-EMF in the current model are expressed as:

$$\frac{d\hat{i}_{d,CM}}{dt} = \frac{1}{L_d} (\hat{v}_d - R_s \hat{i}_d + \hat{\omega}_r L_q \hat{i}_q) \quad (1.31)$$

$$\frac{d\hat{i}_{q,CM}}{dt} = \frac{1}{L_q} (\hat{v}_q - R_s \hat{i}_q - \hat{\omega}_r L_d \hat{i}_d - \hat{\omega}_r \psi_m)$$

$$\hat{e}_c = \hat{\omega}_r \psi_m$$

The actual motor currents in the estimated reference frame are given by:

$$\frac{d\hat{i}_d}{dt} = \frac{1}{L_d} (\hat{v}_d - R_s \hat{i}_d + \omega_r L_q \hat{i}_q + \omega_r \psi_m \sin \Delta\theta_r) \quad (1.32)$$

$$\frac{d\hat{i}_q}{dt} = \frac{1}{L_q} (\hat{v}_q - R_s \hat{i}_q - \omega_r L_d \hat{i}_d - \omega_r \psi_m \cos \Delta\theta_r)$$

The difference between (1.31) and (1.32) is used to produce the estimated rotor position and speed as given by:

$$\begin{bmatrix} \Delta\hat{i}_d \\ \Delta\hat{i}_q \end{bmatrix} = \begin{bmatrix} \hat{i}_d \\ \hat{i}_q \end{bmatrix} - \begin{bmatrix} \hat{i}_{d,CM} \\ \hat{i}_{q,CM} \end{bmatrix} = \psi_m T_s \begin{bmatrix} \omega_r \sin \Delta\theta_r / L_d \\ -\omega_r \cos \Delta\theta_r + \frac{\hat{\omega}_r}{L_q} \end{bmatrix} \approx \psi_m T_s \begin{bmatrix} \frac{\omega_r \Delta\theta_r}{L_d} \\ -\frac{\Delta\omega_r}{L_q} \end{bmatrix} \quad (1.33)$$

The control scheme of the current model based method is illustrated in Fig. 1.16.

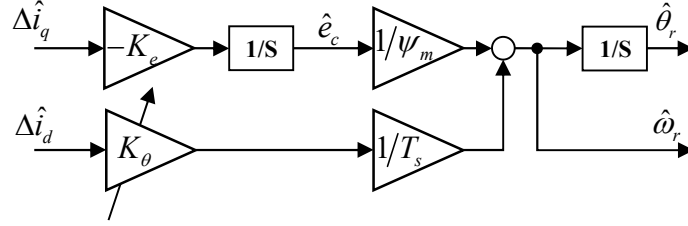


Fig. 1.16. Position and speed observer of current model based method. [MAT96]

### C. Extended back-EMF method

[MOR02] and [CHE03] introduced the Extended back-EMF based method. By using EEMF, salient machines (IPMSM) can be treated as a non-salient machine which simplifies the control algorithm in the implementation. The voltage equation is given as:

$$\begin{bmatrix} v_d \\ v_q \end{bmatrix} = \begin{bmatrix} R_s + pL_d & -\omega_r L_q \\ \omega_r L_q & R_s + pL_d \end{bmatrix} \begin{bmatrix} i_d \\ i_q \end{bmatrix} + \begin{bmatrix} 0 \\ E_{ex} \end{bmatrix} \quad (1.34)$$

where  $v_d$  and  $v_q$  are the d- and q-axis stator voltages,  $i_d$  and  $i_q$  are the d- and q-axis stator currents,  $L_d$  and  $L_q$  are the d- and q-axis inductances respectively. The EEMF, i.e.  $E_{ex} = \omega_r \psi_m + (L_d - L_q)(\omega_r i_d - p i_q)$ . It is worth noting that for SPMSM,  $L_s = L_d = L_q$ . Then, (1.34) is modified as:

$$\begin{bmatrix} v_d \\ v_q \end{bmatrix} = \begin{bmatrix} R_s + pL_s & -\omega_r L_s \\ \omega_r L_s & R_s + pL_s \end{bmatrix} \begin{bmatrix} i_d \\ i_q \end{bmatrix} + \begin{bmatrix} 0 \\ \omega_r \psi_m \end{bmatrix} \quad (1.35)$$

For a sensorless control system, the actual rotor position is unknown. Therefore, the above equations should be transformed into the estimated synchronous reference frame. Then, the voltage equation in the estimated synchronous reference frame is given by:

$$\begin{bmatrix} \hat{v}_d \\ \hat{v}_q \end{bmatrix} = \begin{bmatrix} R_s + pL_d & -\omega_r L_q \\ \omega_r L_q & R_s + pL_d \end{bmatrix} \begin{bmatrix} \hat{i}_d \\ \hat{i}_q \end{bmatrix} + \begin{bmatrix} \hat{E}_d \\ \hat{E}_q \end{bmatrix} \quad (1.36)$$

$$\begin{bmatrix} \hat{E}_d \\ \hat{E}_q \end{bmatrix} = E_{ex} \begin{bmatrix} -\sin \Delta \theta_r \\ \cos \Delta \theta_r \end{bmatrix} + \Delta \omega_r L_d \begin{bmatrix} \hat{i}_q \\ -\hat{i}_d \end{bmatrix} \quad (1.37)$$

The superscript sign ‘^’ indicates the variables are in the estimated synchronous reference frame.  $\Delta \omega_r$  is the rotor speed error between estimation and actual values, respectively. For SPMSM, (1.36) and (1.37) are modified as:

$$\begin{bmatrix} \hat{v}_d \\ \hat{v}_q \end{bmatrix} = \begin{bmatrix} R_s + pL_s & -\omega_r L_s \\ \omega_r L_s & R_s + pL_s \end{bmatrix} \begin{bmatrix} \hat{i}_d \\ \hat{i}_q \end{bmatrix} + \begin{bmatrix} \hat{E}_d \\ \hat{E}_q \end{bmatrix} \quad (1.38)$$

$$\begin{bmatrix} \hat{E}_d \\ \hat{E}_q \end{bmatrix} = \omega_r \psi_m \begin{bmatrix} -\sin \Delta \theta_r \\ \cos \Delta \theta_r \end{bmatrix} + \Delta \omega_r L_d \begin{bmatrix} \hat{i}_q \\ -\hat{i}_d \end{bmatrix} \quad (1.39)$$

Then, the position error can be expressed in the following equations:

$$\Delta \theta_r = \tan^{-1} \left( -\frac{\hat{E}_d}{\hat{E}_q} \right) \quad (1.40)$$

Subsequently, as shown in Fig. 1.17, a position observer is applied to adjust the estimation position to minimize the position estimation error  $\Delta \theta_r$  to make the estimated reference frame align with actual one. It is worth noting that in the implementation, since voltage information is not available, the reference voltage value  $v_d^*$  and  $v_q^*$  are used instead.

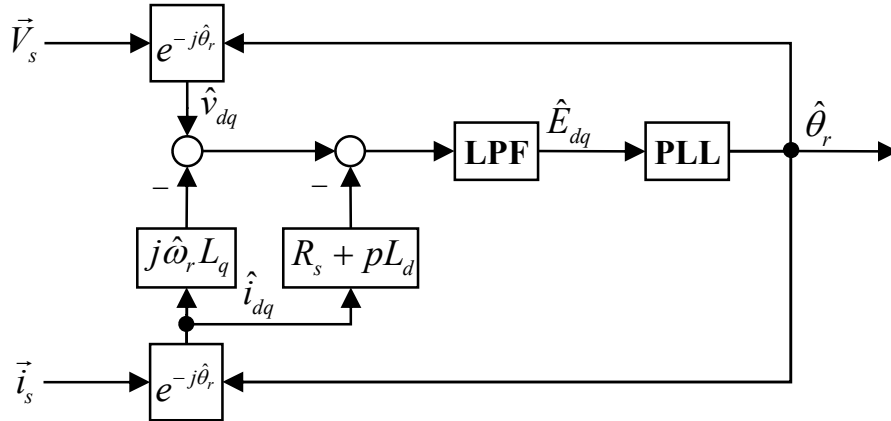


Fig. 1.17. Extended back-EMF based position observer. [CHE03]

### 1.2.3 Flux-linkage Based Methods

Flux-linkage estimation based sensorless control is also widely used and its basic idea is simple. Flux-linkage based method can be realized in both stationary reference frame [WU91] [HU98] [YOO09a] and the estimated synchronous reference [BOL08].

#### A. Open-loop estimation

In the stationary reference frame, the stator flux-linkage can be calculated by integration of stator voltage as expressed by:

$$\psi_{\alpha\beta} = \int (V_{\alpha\beta} - R_s I_{\alpha\beta}) dt \quad (1.41)$$

$$\begin{bmatrix} \psi_{m\alpha} \\ \psi_{m\beta} \end{bmatrix} = \begin{bmatrix} \psi_\alpha \\ \psi_\beta \end{bmatrix} - \begin{bmatrix} L_\alpha i_\alpha \\ L_\beta i_\beta \end{bmatrix} = \psi_m \begin{bmatrix} \cos \theta_r \\ \sin \theta_r \end{bmatrix} \quad (1.42)$$

The flux-linkage is illustrated by the phasor diagram as shown in Fig. 1.18 which corresponds to (1.41) and (1.42).

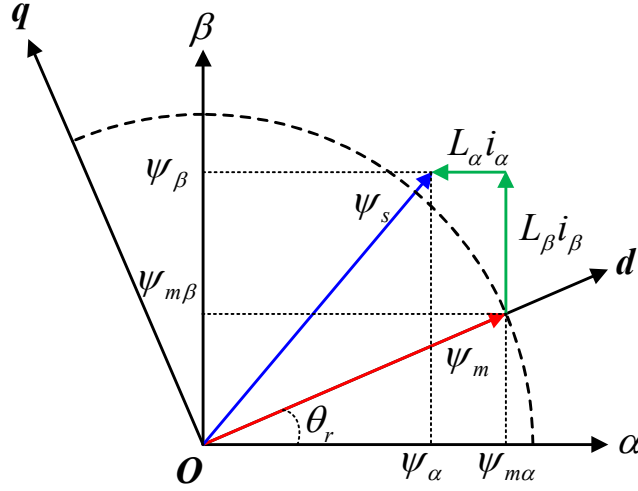


Fig. 1.18. Phasor diagram of flux-linkage of a PMSM.

For the conventional flux-linkage calculation, it is worth noting that as expressed in (1.41), the pure integration process will cause drift and offset issues [CHE19]. For the offset issue, it can be solved by giving a known initial flux value  $\psi_{\alpha\beta}(0)$  as expressed by:

$$\psi_{\alpha\beta} = \int (V_{\alpha\beta} - R_s I_{\alpha\beta}) dt + \psi_{\alpha\beta}(0) \quad (1.43)$$

For the drift issue, since there are a small amount of DC offset and errors exist during the current measurement, these dc offsets will be continuously accumulated by the integration and the drift on flux estimation will cause a divergence of integration process [HOL03] [CHE19]. In [TAJ93], a high-pass filter (HPF) is applied after the integration. Hence, after applying an HPF, the pure integration is equivalently replaced by a Low-pass filter (HPF) with cut-off frequency  $\omega_c$ , of which the transfer function is  $1/(s + \omega_c)$ .

### B. Closed-loop estimation

Introduction of LPF will cause inevitable phase delay during position estimation. In [HU98] [WIP09], a closed-loop flux-linkage estimator with a saturable feedback is presented as shown in Fig. 1.19.

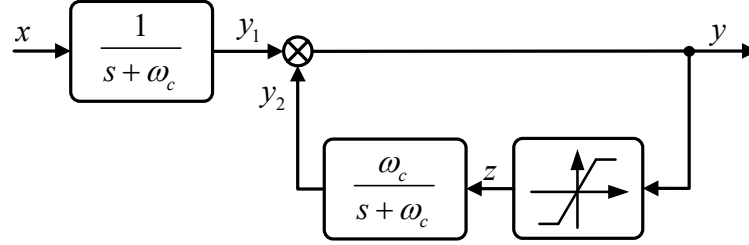


Fig. 1.19. Phasor diagram of flux-linkage of a PMSM.

The output of the integrator is modified and can be expressed as:

$$y = \frac{1}{s + \omega_c} x + \frac{\omega_c}{s + \omega_c} z \quad (1.44)$$

With the compensation, the modified integrator can achieve a better performance than LPF while the issues associated with the pure integrator can also be avoided.

### C. Hybrid model method

In [YOO09a], a hybrid model based flux estimator is proposed. Different from conventional methods which only use the voltage model in (1.41) to estimate the flux, the current model is also involved. The voltage model dominates at higher speed and the current model dominates at lower speed so that speed range can be extended. The block diagram of the hybrid flux observer is shown in Fig. 1.20.

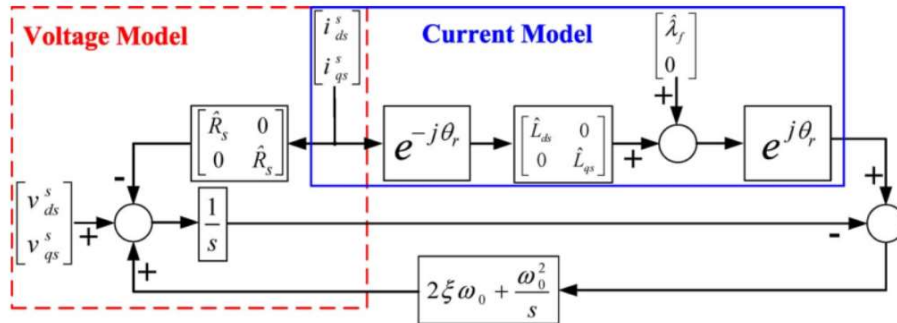


Fig. 1.20. Block diagram of the hybrid flux observer. [YOO09a]

By involving current model, this method is equivalently utilizing the nominal PM flux-linkage value to compare with the estimated flux value by voltage model and the difference is used to correct the integration drift issue [YOO09a] and voltage error due to inverter nonlinearity [BOL08] by the closed-loop feedback. Hence, it can have a better performance at lower speed than the individual voltage model based flux-linkage estimation method.

#### ***D. Active flux method***

Moreover, [BOL08] proposed a so-called ‘Active Flux’ concept. Similar to extended back-EMF based method, the proposed method in [BOL08] unifies all the salient machines into fictitious non-salient machines and hence simplified the position estimation. The active flux (AF) is defined as:

$$\psi_{AF} = \psi_m + (L_d - L_q)i_d \quad (1.45)$$

For SPMSM, since  $L_d = L_q$ , the active flux is modified to:

$$\psi_{AF} = \psi_m \quad (1.46)$$

With the active flux, the flux equation can be generalized as:

$$\begin{bmatrix} \psi_d \\ \psi_q \end{bmatrix} = \begin{bmatrix} L_q & 0 \\ 0 & L_q \end{bmatrix} \begin{bmatrix} i_d \\ i_q \end{bmatrix} + \begin{bmatrix} \psi_{AF} \\ 0 \end{bmatrix} \quad (1.47)$$

Since the rotor position is unknown in the practical sensorless control system, the flux-linkage should be transformed into the estimated reference frame:

$$\begin{bmatrix} \hat{\psi}_d \\ \hat{\psi}_q \end{bmatrix} = \begin{bmatrix} L_q & 0 \\ 0 & L_q \end{bmatrix} \begin{bmatrix} \hat{i}_d \\ \hat{i}_q \end{bmatrix} + \begin{bmatrix} \hat{\psi}_{AFd} \\ \hat{\psi}_{AFq} \end{bmatrix} \quad (1.48)$$

where  $\begin{bmatrix} \hat{\psi}_{AFd} & \hat{\psi}_{AFq} \end{bmatrix}^T$  is the projected AF defined as  $\begin{bmatrix} \hat{\psi}_{AFd} & \hat{\psi}_{AFq} \end{bmatrix}^T = \psi_{AF} [\cos\Delta\theta_r \quad \sin\Delta\theta_r]^T$ . Based on (1.48), the rotor speed and position can be estimated by an observer. The overall control scheme is shown in Fig. 1.21.

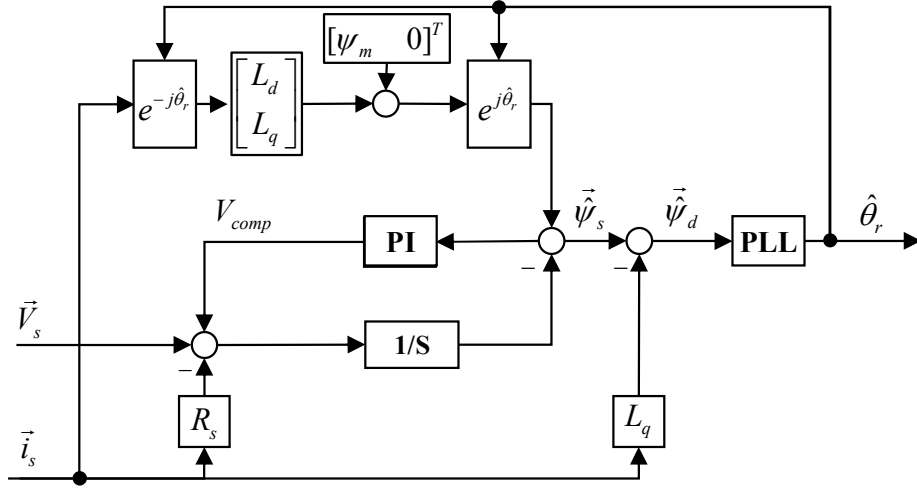


Fig. 1.21. Active flux based position observer. [BOL08]

The estimated d-axis flux-linkage is expressed by:

$$\hat{\psi}_d = \int (\vec{V}_s - R_s \vec{i}_s + V_{comp}) dt - L_q \vec{i}_s \quad (1.49)$$

As illustrated in Fig. 1.21, the same as method in [YOO09a], this algorithm [BOL08] also involves the nominal value of PM flux-linkage  $\psi_m$  and compare it with the estimated flux by voltage model, the difference is regarded as an input of a PI controller. The output  $V_{comp}$  compensates the error caused by inverter non-linearity and integration issues.

## 1.2.4 Modern Control Theory Based Methods

Many position estimation methods are proposed based on modern control theories, including sliding mode observer (SMO), Kalman filter (EKF) and model reference adaptive system (MRAS). This type of methods becomes increasingly popular due to their robustness, good dynamic performance and insensitivity to parameter variations.

### A. Sliding mode observer

For the sliding mode observer [BEN99] [TUR00] [ZHA02], the error between the measured currents and the estimated current is used to re-construct the back-EMF [ZHA02]. For the sliding mode control system, the state variables are restricted on the sliding surface by changing the system structure dynamically [WAN13] [WAN14a]. As demonstrated in Fig. 1.22, a typical sliding mode control system includes two stages. The first stage is the path “**AB**” where the

state starts to converge and arrives at the sliding surface. Then, the second stage is the path “**BC**” where the state arrives at sliding surface and moves around it.

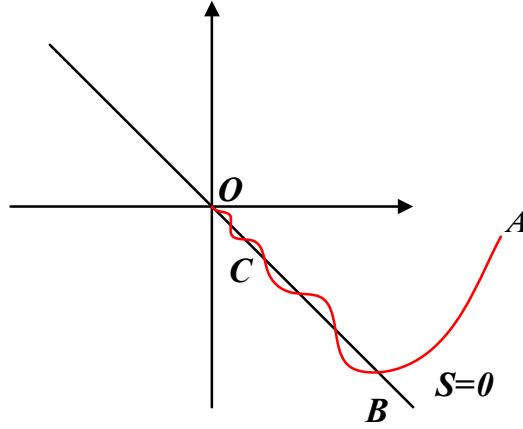


Fig. 1.22. Demonstration of the sliding mode control system.

Sliding mode observer (SMO) is well-known for its robustness, simplicity and good dynamic performance. Thus, SMO is widely adopted in sensorless control in middle and high speed ranges.

The SMO is designed using the extended EMF model of PMSMs as expressed by:

$$\begin{bmatrix} v_\alpha \\ v_\beta \end{bmatrix} = \begin{bmatrix} R_s + pL_d & (L_d - L_q)\omega_r \\ (L_q - L_d)\omega_r & R_s + pL_d \end{bmatrix} \begin{bmatrix} i_\alpha \\ i_\beta \end{bmatrix} + E_{ex} \begin{bmatrix} -\sin\theta_r \\ \cos\theta_r \end{bmatrix} \quad (1.50)$$

where  $E_{ex} = \omega_r \psi_m + (L_d - L_q)(\omega_r i_d - p i_q)$ . It is worth noting that for a SPMSM, EMF model in (1.50) can be simplified by applying  $(L_d - L_q) = 0$ . The state equation of a conventional SMO can be expressed as follows:

$$\dot{\hat{\mathbf{i}}}_s = \mathbf{A}\hat{\mathbf{i}}_s + \mathbf{B}(\mathbf{u}_s + \mathbf{l}\mathbf{z}_{eq} + \mathbf{z}) \quad (1.51)$$

where

$$\mathbf{A} = \begin{bmatrix} -R_s/L_d & -(L_d - L_q)\hat{\omega}_r/L_d \\ (L_q - L_d)\hat{\omega}_r/L_d & -R_s/L_d \end{bmatrix} \quad (1.52)$$

$$\mathbf{B} = \begin{bmatrix} 1/L_d & 0 \\ 0 & 1/L_d \end{bmatrix} \quad (1.53)$$

$$\hat{\mathbf{i}}_s = \begin{bmatrix} \hat{i}_\alpha \\ \hat{i}_\beta \end{bmatrix}, \mathbf{u}_s = \begin{bmatrix} u_\alpha \\ u_\beta \end{bmatrix} \quad (1.54)$$

The symbol “^” denotes the estimated value,  $\mathbf{l}$  is the feedback gain,  $\mathbf{z}_{eq}$  is the equivalent control function, and  $\mathbf{z}$  is the sliding-mode control function defined as follows:

$$\mathbf{z} = \begin{cases} \frac{k}{\delta} \cdot (\hat{\mathbf{i}}_s - \mathbf{i}_s) & |\hat{\mathbf{i}}_s - \mathbf{i}_s| < \delta \\ k \cdot \text{sign}(\hat{\mathbf{i}}_s - \mathbf{i}_s) & |\hat{\mathbf{i}}_s - \mathbf{i}_s| > \delta \end{cases} \quad (1.55)$$

where  $k$  is the sliding mode gain, and  $\delta$  is the boundary layer. From (1.51), the difference between the estimated stator current and the actual one is used to construct the sliding mode control function  $\mathbf{z}$ . The sliding mode surface is defined as  $\mathbf{S} = \hat{\mathbf{i}}_s - \mathbf{i}_s$ . During the operation of SMO controller, the current difference will be controlled to zero and then the estimated position error is reduced to zero too. Hence, the state of SMO is then converged to  $\mathbf{S} = 0$  and the back-EMF is equivalently expressed as:

$$\mathbf{e}_s = -(1 + \mathbf{l})\mathbf{z}_{eq} \quad (1.56)$$

Therefore, the rotor position can be calculated from (1.56) by:

$$\theta_r = \tan^{-1}\left(-\frac{z_{eq,\alpha}}{z_{eq,\beta}}\right) \quad (1.57)$$

Due to the existence of noisy signal, the arc-tangent function will have a large estimation error when EMF crossing zero. Normally, (1.57) can be replaced by a phase-locked loop (PLL) [WAN13] [WAN14a]. Then, the overall block diagram of SMO is shown in Fig. 1.23.

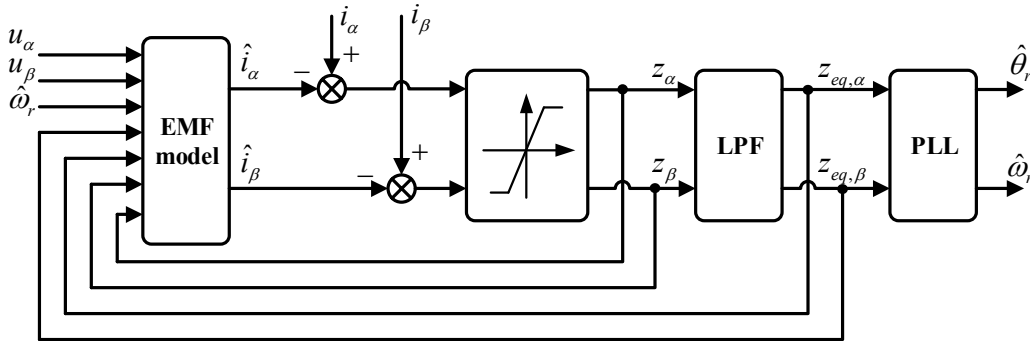


Fig. 1.23. Position and speed observer of SMO sensorless control method. [WAN13]

Sliding mode observer has the advantages of robustness and simplicity. However, the conventional SMO methods has inherent chattering problems [JIN05] [FAN15] [LU18]. Hence,

a low-pass filter is applied as shown in Fig. 1.23. The LPF will bring calculation delay causing position errors [GON20]. Many papers [ZHA13a] [SAG15] [LU18][GON20] have been done by modifying the switching function so that the chattering effect is reduced and the influence of LPF is decreased correspondingly.

### ***B. Kalman filter***

Kalman filter is an optimal estimation algorithm based on the least-square variance estimation for linear systems. It can estimate some unknown variables by given the measurements observed over time, containing noises and other inaccuracies. Extended Kalman filter (EKF) is a nonlinear version for the Kalman filter [BOL99]. EKF based sensorless algorithm is less influenced by measurement noises and shows less affected by parameter inaccuracy than conventional fundamental model based methods [BOL99] [TER01] [RIV13]. However, EKF requires a heavy online calculation, and hence, it may be difficult to implement EKF based sensorless algorithms in some machine drive applications. In order to reduce the computation resources, the reduced order EKF is proposed providing some of the states are immune to noises [FUE11] [QUA14]. By using the reduced order EKF, the system order is reduced and the iteration process can be significantly simplified leading to savings of resource utility while high estimation performance is still maintained [QUA14].

However, the determination of noise covariance matrix and robustness of model uncertainties are still open issues in practice [YIN19]. In real applications, the random disturbance and measurement noise are unknown. Hence, the determinations of system noise and measurement noise are realized by experience or simulation. The convergence and estimation performance of EKF can be greatly influenced by tuning the covariance matrices.

### ***C. Model reference adaptive system***

Model reference adaptive system (MRAS) technique is another option for adaptive rotor position and speed estimation [FAN94] [PII08] [ORL10] [ZHA14a] [ZHA20]. MRAS has advantages of simple concept and lower computation requirement. The basic structure of a MRAS observer is shown in Fig. 1.24.

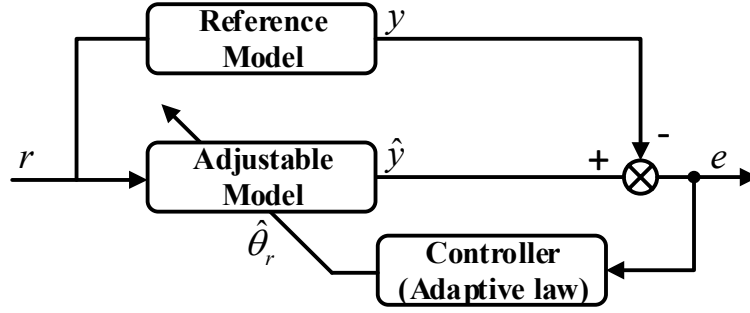


Fig. 1.24. MRAS block diagram. [ZHA13b]

A MRAS consists of a reference model, an adjustable model and a correction controller based on adaption laws. The reference model represents the real plant model of which the parameters are all known. The adjustable model is established based on a fictitious mathematical model which contains uncertain parameters. Both two models have the same physical outputs. The error  $e$  is the difference between the outputs of two models and is the input to the correction controller. Based on Adaption laws, the correction controller can adjust the adaptive model to minimize the error  $e$  so that the adaptive model behaves the same as the reference model. For the correction controller of MRAS, it can be realized by conventional PI-type controller, sliding mode controller (SMC) or fuzzy logic controller. Moreover, in order to achieve a satisfied performance of MRAS, determination of adaptive law is a key issue. The adaptive law can be determined in two mains ways, one is based on a gradient method and another is using the stability theories [COM13].

### 1.2.5 Speed and Position Observer

Since the back-EMF, flux-linkage or position estimation are obtained, a position and speed observer is required to estimate the rotor position from them.

#### A. Direct calculation

The simplest way is the direct calculation using arc-tangent function [MOR02] as expressed by:

$$\theta_r = \tan^{-1}\left(-\frac{e_\alpha}{e_\beta}\right) \quad \& \quad \theta_r = \tan^{-1}\left(\frac{\psi_{m\beta}}{\psi_{m\alpha}}\right) \quad (1.58)$$

However, due to the existence of noisy signal, the arc-tangent function will have a large estimation error when back-EMF or flux-linkage crossing zero. An LPF should be applied which however adds phase lag to the estimate [KIM03].

### B. Phase-locked Loop

Normally, (1.57) can be replaced by a phase-locked loop (PLL) [WAN13] [WAN14b] as shown in Fig. 1.25. The back-EMF and flux-linkage in stationary reference frame are the input of the PLL.

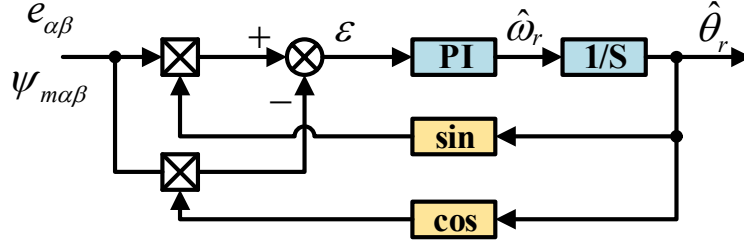


Fig. 1.25. PLL block diagram.

Take the back-EMF based sensorless control as an example, the error input of PLL  $\varepsilon$  can be expressed as:

$$\varepsilon = -e_\alpha \cos \hat{\theta}_r - e_\beta \sin \hat{\theta}_r \approx k(\theta_r - \hat{\theta}_r) \quad (1.59)$$

According to (1.59), the equivalent block diagram of PLL is shown in Fig.1.26.

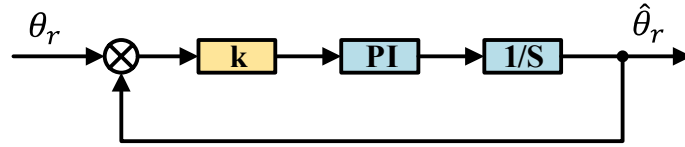


Fig. 1.26. Equivalent PLL block diagram.

Therefore, the closed loop transfer function of the PLL can be given by:

$$H(s) = \frac{2\xi\omega_n s + \omega_n^2}{s^2 + 2\xi\omega_n s + \omega_n^2} \quad (1.60)$$

where  $\xi = \sqrt{kK_i}$ ,  $\omega_n = \frac{K_p}{2} \sqrt{\frac{k}{K_i}}$ ,  $\omega_n$  is the natural frequency and can be used as the bandwidth of PLL.  $\xi$  is the damping factor [GAR05]. A higher damping factor can reduce the overshoot but also sacrifice the dynamic performance. Then, the parameters of PLL can be initially designed based on classical control theory.

### C. PI-type position observer

For sensorless control in the estimated synchronous reference frame, the estimated position error as expressed by

$$\Delta\hat{\theta}_r \approx \begin{pmatrix} -\hat{E}_d \\ \hat{E}_q \end{pmatrix} \quad \& \quad \Delta\hat{\theta}_r \approx \begin{pmatrix} \hat{\psi}_q \\ \hat{\psi}_d \end{pmatrix} \quad (1.61)$$

Then, a PI-type position observer can be used to estimate the rotor speed and position [LEE10] as shown in Fig. 1.27.

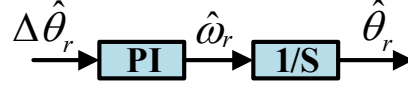


Fig. 1.27. PI-type observer block diagram.

#### D. Simplified EKF position observer

In [HAR96], a simplified EKF algorithm is proposed to extract the position information from the noisy output of a resolver. It is further extended to sensorless control to estimate the rotor position [LIU04] [LIU06] [ALM14] [LIU15]. For the simplified EKF, the Kalman filter gain matrix of the conventional EKF is greatly simplified as follows:

$$K = \begin{bmatrix} 0 & K_1 \\ 0 & K_2 \\ 0 & K_3 \end{bmatrix} \cdot \begin{bmatrix} \cos \hat{\theta}_r & \sin \hat{\theta}_r \\ -\sin \hat{\theta}_r & \cos \hat{\theta}_r \end{bmatrix} \quad (1.62)$$

where  $K_1, K_2, K_3$  are tuning parameters. The basic block diagram of the simplified EKF is shown in Fig. 1.28.

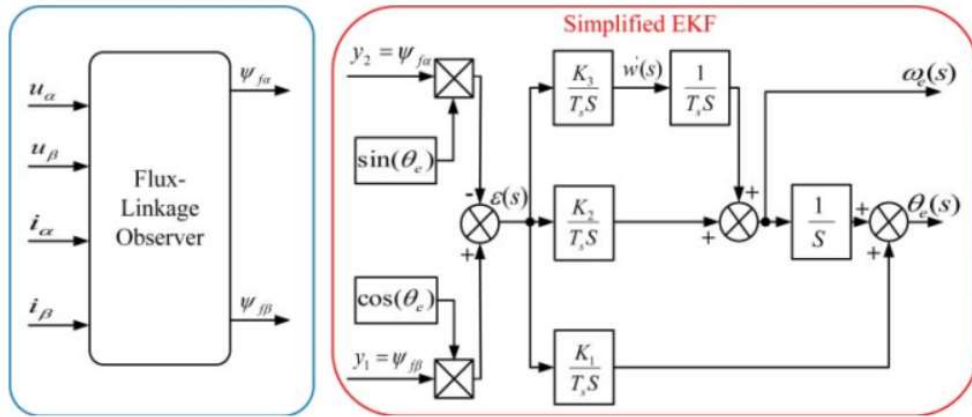


Fig. 1.28. Simplified EKF block diagram. [ALM14]

Compared to conventional arc-tangent method, the simplified EKF shows a smaller position error and its estimation accuracy is less affected by the back-EMF harmonics since it is less sensitive to such noises [ALM14].

### E. Mechanical model based position observer

In [KIM03], a position observer is realized by involving mechanical model with zero-phase lag under the assumption of precise mechanical parameters by feed-forwarding the torque command  $T_e^*$  to the observer. The block diagram is shown in Fig. 1.29.

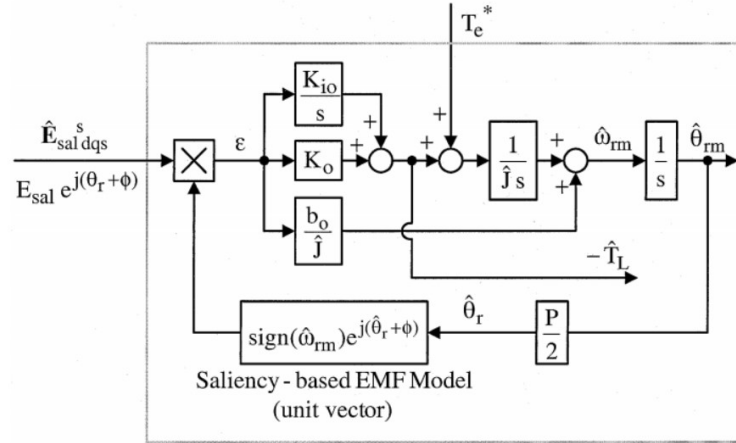


Fig. 1.29. Block diagram of position observer with zero phase lag. [KIM03]

Compared with conventional methods, such as direct arc-tangent calculation and PLL, the position observer in [KIM03] has zero-phase lag and also enhances the dynamic performance of sensorless control.

### 1.3 Saliency Based Sensorless Control Methods

Due to the anisotropy property of PMSMs, there is geometric or magnetic saliency, which is a function of rotor position. Since the machine saliency is independent of the rotor speed, it can be exploited for sensorless position estimation at zero and low speed. Considering a salient machine (IPMSM), the inductance variation against rotor position is illustrated in Fig. 1.30.

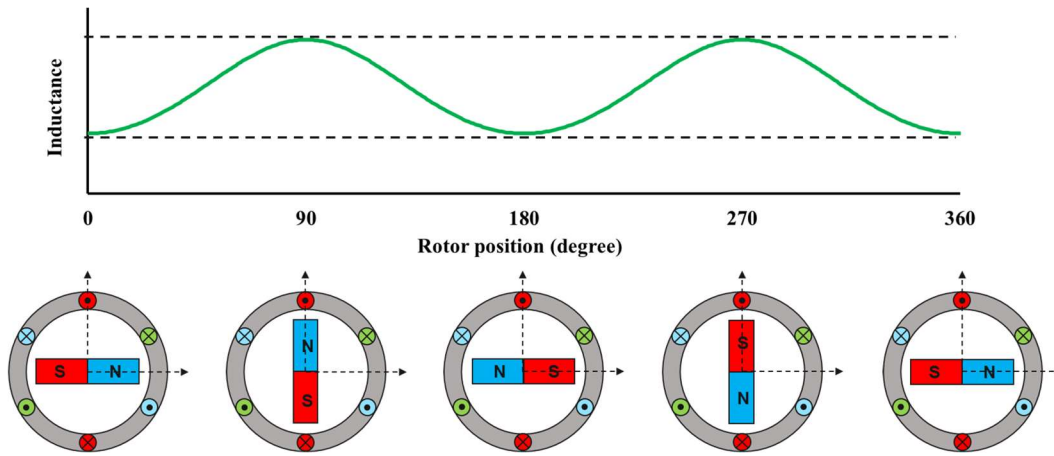


Fig. 1.30. Inductance variation against rotor position without considering armature reaction [KAN10].

In order to explicit the saliency to estimate the rotor position, various methods have been developed and the majority of saliency based methods can fit into the frame in Fig. 1.31.

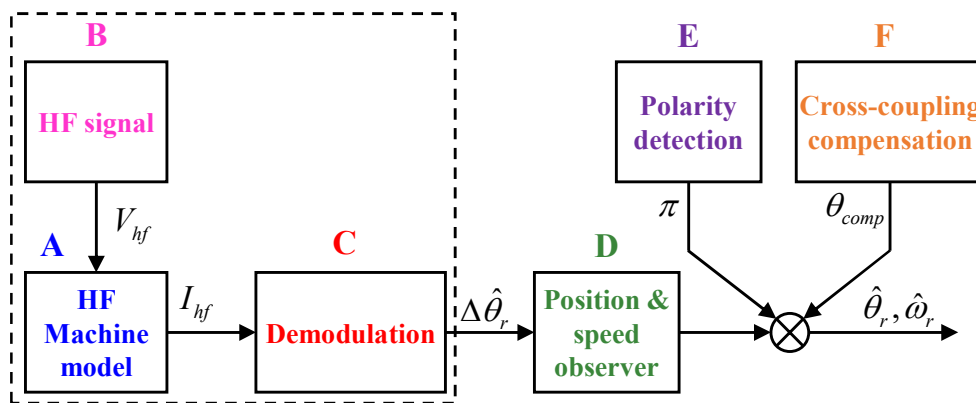


Fig. 1.31. General frame of saliency based sensorless control techniques.

As shown in Fig. 1.31, there are 5 main parts of a saliency based method. For each part, the relevant main methods are also demonstrated in Fig. 1.32.

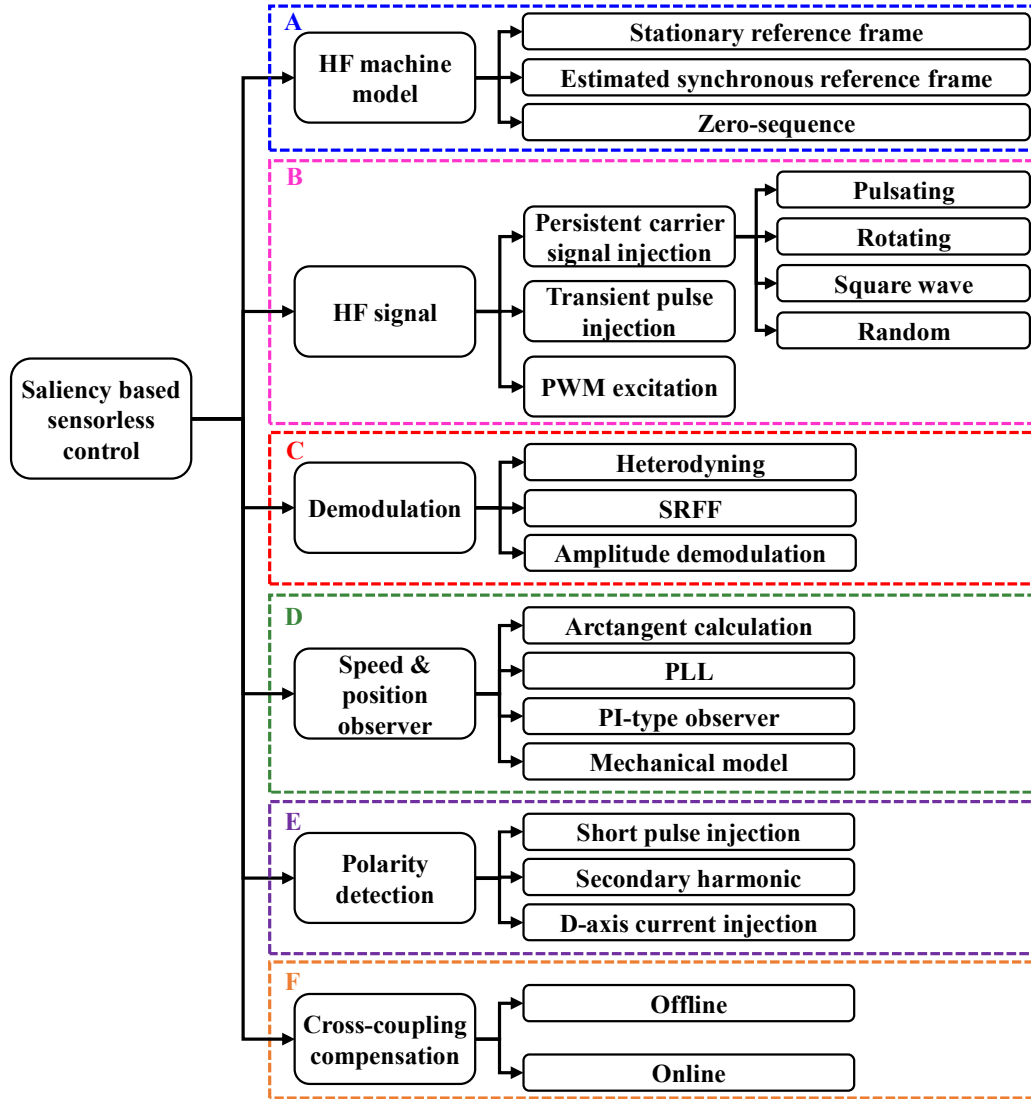


Fig. 1.32. Classification of saliency based sensorless control techniques.

Part A represents the high-frequency (HF) machine model when a high frequency signal is injected. HF signals can be injected in the stationary reference frame and the estimated synchronous reference frame. For the injected high frequency signal in Part B, persistent carrier signal injection, transient pulse injection or PWM excitation are mainly utilized. For Part C, after injecting HF signals, the current response should be demodulated to remove the high frequency component and obtain the position dependent signal. In the following sections, the demodulation process is illustrated combining with corresponding injection methods. In Part D, the demodulated position dependent signal is used as an input of a speed and position observer to generate the rotor speed and position information. For saliency based method, the position observer is basically the same as introduced in Section 1.2.5 and hence not illustrated in this section. Next, for Part E, as indicated in Fig. 1.30, the inductance varies twice in one electrical

period and hence an extra polarity detection is necessary. At last, Part F compensates the position estimation error caused by cross-coupling inductance which will be illustrated afterwards.

### 1.3.2 HF Machine Model

In the synchronous reference frame, the voltage equation of PMSM is given by:

$$\begin{bmatrix} v_d \\ v_q \end{bmatrix} = \begin{bmatrix} R_s & 0 \\ 0 & R_s \end{bmatrix} \begin{bmatrix} i_d \\ i_q \end{bmatrix} + p \begin{bmatrix} \psi_d \\ \psi_q \end{bmatrix} + \omega_r \begin{bmatrix} -\psi_q \\ \psi_d \end{bmatrix} \quad (1.63)$$

$$\begin{bmatrix} \psi_d \\ \psi_q \end{bmatrix} = \begin{bmatrix} L_d & 0 \\ 0 & L_q \end{bmatrix} \begin{bmatrix} i_d \\ i_q \end{bmatrix} + \psi_m \begin{bmatrix} 1 \\ 0 \end{bmatrix} \quad (1.64)$$

When a high frequency signal is injected at zero or low speed, if the injection frequency is sufficiently higher than the fundamental excitation frequency, then a high frequency voltage model can be expressed by:

$$\begin{bmatrix} v_{dh} \\ v_{qh} \end{bmatrix} = \begin{bmatrix} L_{dh} & 0 \\ 0 & L_{qh} \end{bmatrix} p \begin{bmatrix} i_{dh} \\ i_{qh} \end{bmatrix} \quad (1.65)$$

where  $L_{dh}$  and  $L_{qh}$  are the high frequency incremental dq-axis inductances.  $v_{dh}$ ,  $v_{qh}$ ,  $i_{dh}$  and  $i_{qh}$  are the high frequency voltage and current terms in d-q axes. It is worth noting that in (1.65), the back-EMF and the resistance voltage drop are neglectable and the PMSM can be regarded as a pure inductive load [RAC08]. When considering the cross-saturation effect [LI09], (1.65) is modified as expressed by:

$$\begin{bmatrix} v_{dh} \\ v_{qh} \end{bmatrix} = \begin{bmatrix} L_{dh} & L_{dqh} \\ L_{qdh} & L_{qh} \end{bmatrix} p \begin{bmatrix} i_{dh} \\ i_{qh} \end{bmatrix} \quad (1.66)$$

where  $L_{dqh}$  and  $L_{qdh}$  are the high frequency incremental mutual inductances due to cross-saturation effect.

Generally, saliency tracking based method can be realized in either stationary reference frame or estimated synchronous reference frame. The relationship between different reference frames is shown in Fig. 1.33.

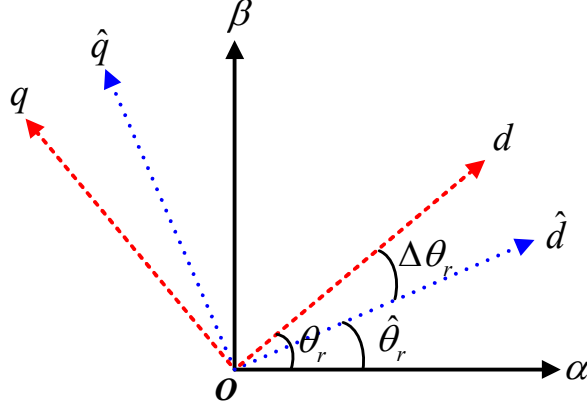


Fig. 1.33. Relationship between three reference frames.

### A. Stationary reference frame

The voltage model in (1.66) can be transformed into the stationary reference frame by the transformation matrix given as:

$$T(\theta_r) = \begin{bmatrix} \cos \theta_r & -\sin \theta_r \\ \sin \theta_r & \cos \theta_r \end{bmatrix} \quad (1.67)$$

Then, the high frequency voltage model of PMSMs in the stationary reference frame is expressed by:

$$\begin{bmatrix} v_{\alpha h} \\ v_{\beta h} \end{bmatrix} = T(\theta_r) \begin{bmatrix} L_{dh} & L_{dqh} \\ L_{qdh} & L_{qh} \end{bmatrix} T^{-1}(\theta_r) \cdot p \begin{bmatrix} i_{\alpha h} \\ i_{\beta h} \end{bmatrix} \quad (1.68)$$

$$= \begin{bmatrix} L_{sa} - L_{sd} \cos 2\theta_r - L_{dqh} \sin 2\theta_r & -L_{sd} \sin 2\theta_r + L_{dqh} \cos 2\theta_r \\ -L_{sd} \sin 2\theta_r - L_{dqh} \cos 2\theta_r & L_{sa} + L_{sd} \cos 2\theta_r + L_{dqh} \sin 2\theta_r \end{bmatrix} \cdot p \begin{bmatrix} i_{\alpha h} \\ i_{\beta h} \end{bmatrix}$$

$$L_{sa} = \frac{L_{dh} + L_{qh}}{2} \quad (1.69)$$

$$L_{sd} = -\frac{L_{dh} - L_{qh}}{2} \quad (1.70)$$

Then, by solving the voltage equation (1.68), the differential terms of high frequency current response in the stationary reference frame can be given by:

$$p \begin{bmatrix} i_{\alpha h} \\ i_{\beta h} \end{bmatrix} = \begin{bmatrix} \frac{1}{L_p} + \frac{1}{L_n} \cos(2\theta_r + \theta_m) & \frac{1}{L_n} \sin(2\theta_r + \theta_m) \\ \frac{1}{L_n} \sin(2\theta_r + \theta_m) & \frac{1}{L_p} - \frac{1}{L_n} \cos(2\theta_r + \theta_m) \end{bmatrix} \cdot \begin{bmatrix} v_{\alpha h} \\ v_{\beta h} \end{bmatrix} \quad (1.71)$$

$$\theta_m = \tan^{-1} \left( \frac{-L_{dqh}}{L_{sd}} \right) \quad (1.72)$$

$$L_p = \frac{L_{dh}L_{qh} - L_{dqh}^2}{L_{sa}}, L_n = \frac{L_{dh}L_{qh} - L_{dqh}^2}{\sqrt{L_{sd}^2 + L_{dqh}^2} L_{sa}} \quad (1.73)$$

From (1.71), it can be seen that the current response contains the rotor position information. Moreover, it is worth noting that there is a constant position error  $\theta_m$  in (1.71) which is caused by cross-saturation effect.

### ***B. Estimated synchronous reference frame***

In a sensorless control system, the real position is unknown. Hence, the voltage model in (1.66) can be transformed into the estimated synchronous reference frame by the transformation matrix given as:

$$T(\Delta\theta_r) = \begin{bmatrix} \cos \Delta\theta_r & -\sin \Delta\theta_r \\ \sin \Delta\theta_r & \cos \Delta\theta_r \end{bmatrix} \quad (1.74)$$

where  $\Delta\theta_r$  is the position error between real and estimated positions. Then, the high frequency voltage model of PMSMs in the stationary reference frame can be derived as:

$$\begin{aligned} \begin{bmatrix} \hat{v}_{dh} \\ \hat{v}_{qh} \end{bmatrix} &= T(\Delta\theta_r) \begin{bmatrix} L_{dh} & L_{dqh} \\ L_{qdh} & L_{qh} \end{bmatrix} T^{-1}(\Delta\theta_r) \cdot p \begin{bmatrix} \hat{i}_{dh} \\ \hat{i}_{qh} \end{bmatrix} \\ &= \begin{bmatrix} L_{sa} - L_{sd} \cos 2\Delta\theta_r - L_{dqh} \sin 2\Delta\theta_r & -L_{sd} \sin 2\Delta\theta_r + L_{dqh} \cos 2\Delta\theta_r \\ -L_{sd} \sin 2\Delta\theta_r - L_{dqh} \cos 2\Delta\theta_r & L_{sa} + L_{sd} \cos 2\Delta\theta_r + L_{dqh} \sin 2\Delta\theta_r \end{bmatrix} \cdot p \begin{bmatrix} \hat{i}_{dh} \\ \hat{i}_{qh} \end{bmatrix} \end{aligned} \quad (1.75)$$

Further, the differential terms of high frequency current response in the estimated synchronous reference frame can be given by:

$$p \begin{bmatrix} \hat{i}_{dh} \\ \hat{i}_{qh} \end{bmatrix} = \begin{bmatrix} \frac{1}{L_p} + \frac{1}{L_n} \cos(2\Delta\theta_r + \theta_m) & \frac{1}{L_n} \sin(2\Delta\theta_r + \theta_m) \\ \frac{1}{L_n} \sin(2\Delta\theta_r + \theta_m) & \frac{1}{L_p} - \frac{1}{L_n} \cos(2\Delta\theta_r + \theta_m) \end{bmatrix} \cdot \begin{bmatrix} \hat{v}_{dh} \\ \hat{v}_{qh} \end{bmatrix} \quad (1.76)$$

Similar to the stationary model, the carrier current responses in the estimated synchronous reference frame also have rotor position information and a position error  $\theta_m$  caused by cross-saturation effect.

### C. Zero-sequence based method

Apart from the aforementioned two models, the zero-sequence response can also be used for position estimation [CON00] [BRI05] [CON05] [XU16a]. Zero-sequence carrier voltage can be measured as shown in Fig. 1.34 [BRI05] [XU16a].

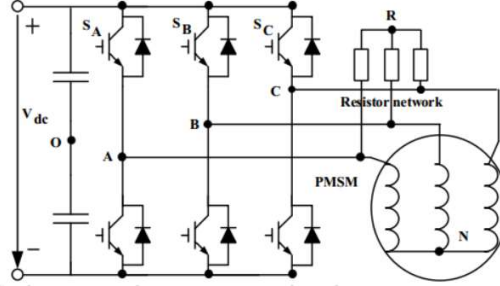


Fig. 1.34. Zero-sequence carrier voltage measurement [XU16a].

According to [XU15], the zero-sequence carrier voltage can be derived as:

$$U_{RN} \approx \frac{L_0 L_2 U_{hf}}{2L_0^2 - \frac{1}{2}L_2^2} \cos(\omega_{hf}t + \hat{\theta}_r) \quad (1.77)$$

where  $\omega_{hf}$  and  $U_{hf}$  are the frequency and amplitude of the injected high-frequency voltage.

Compared with conventional current response based methods, the zero-sequence model based method requires extra voltage measurement which makes it less attractive than utilizing present current sensors based methods [BRI05]. Nevertheless, zero-sequence based method has two main benefits [BRI05][XU16a]. Firstly, the magnitude of the zero-sequence carrier-signal voltage is independent on the frequency of the injected carrier-signal [BRI04]. Hence a larger frequency signal can be injected leading to an increased system bandwidths and stability of the system [GAR07]. Moreover, the associated torque ripple and acoustic noise can be reduced [BRI05]. Secondly, it is easier to decouple the harmonics introduced in the carrier-signal voltage due to inverter nonlinearity [TES03][GUE05][GON11] from the zero-sequence carrier-signal voltage and hence, improving the position estimation performance.

### 1.3.3 HF Signal Injection Methods

For saliency based methods, in order to obtain the rotor position information from the saliency, an extra excitation signal is normally required to inject to the stator winding to modulate the saliency information. Then, a rotor position dependent response is demodulated to estimate the rotor speed and position. In the past, various methods have been proposed depending on different types of injection signals.

According to the injected signals, saliency based method can be divided into persistent carrier signal injection, transient pulse injection [SCH96] and PWM excitation [HOL05] [GAO07] [RAU08] [BOL11] [HUA11]. Moreover, the persistent carrier signal injection method includes pulsating signal injection [COR98] [LIN02] [JAN03a] [LIU14] [XU16a], rotating signal injection [JAN95] [DEG98] [RAC10], square wave injection [HAM10] [YOO11] and random injection [WAN16] [WAN17a].

### A. Pulsating signal injection

For the pulsating signal injection based method [COR98] [LIN02] [JAN03a] [LIU14] [XU16], an additional high frequency sinusoidal voltage signal is injected to the stator windings as expressed by:

$$\begin{bmatrix} v_{dh} \\ v_{qh} \end{bmatrix} = U_{hf} \begin{bmatrix} \cos(\omega_{hf}t) \\ 0 \end{bmatrix} \quad (1.78)$$

where  $U_{hf}$  and  $\omega_{hf}$  are the amplitude and frequency of the injected pulsating voltage, respectively. The injection is depicted in Fig. 1.35.

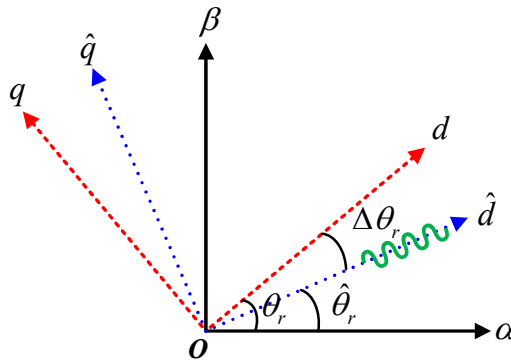


Fig. 1.35. Conventional pulsating signal injection in the estimated d-axis.

It is worth noting that, the pulsating signal can be injected in the estimated d-axis [LIN02] [JAN03a], the estimated q-axis [COR98] [LIN03] [YAN11] and the stationary reference frame [LIU14]. Injection in the estimated d-axis is normally used which however is sensitive to the inverter nonlinearity effect [LIN03] [GON11] and the q-axis injection is less sensitive but generates more torque ripples. Injection in the stationary reference frame [LIU14] offers a medium performance between these two methods, which however requires knowledge of parameters. Take the commonly used d-axis injection as an example and the injection is illustrated in Fig. 1.35.

After injection, the carrier current responses in the estimated synchronous reference frame can be expressed by:

$$\begin{bmatrix} \hat{i}_{dh} \\ \hat{i}_{qh} \end{bmatrix} = \begin{bmatrix} \frac{U_{hf}}{\omega_{hf} L_p} + \frac{U_{hf}}{\omega_{hf} L_n} \cos(2\Delta\theta_r + \theta_m) \\ \frac{U_{hf}}{\omega_{hf} L_n} \sin(2\Delta\theta_r + \theta_m) \end{bmatrix} \cdot \sin(\omega_{hf} t) \quad (1.79)$$

$$\begin{bmatrix} \hat{i}_{dh} \\ \hat{i}_{qh} \end{bmatrix} = \begin{bmatrix} I_p + I_n \cos(2\Delta\theta_r + \theta_m) \\ I_n \sin(2\Delta\theta_r + \theta_m) \end{bmatrix} \cdot \sin(\omega_{hf} t) \quad (1.80)$$

$$I_p = \frac{U_{hf}}{\omega_{hf} L_p}, I_n = \frac{U_{hf}}{\omega_{hf} L_n} \quad (1.81)$$

Clearly, as shown in (1.80), the carrier current response, i.e.  $\hat{i}_{qh}$  has the rotor position information. In order to extract the rotor position information, a demodulation process is required, as shown in Fig. 1.36, so that the high frequency component is filtered and the rotor position information is extracted.

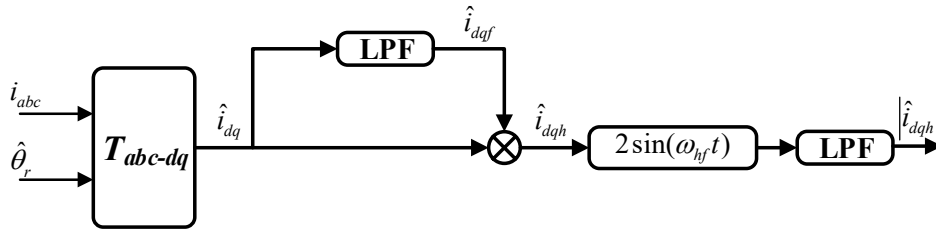


Fig. 1.36. Demodulation of pulsating signal injection based method.

The demodulation process can be expressed by:

$$\begin{bmatrix} |\hat{i}_{dh}| \\ |\hat{i}_{qh}| \end{bmatrix} = LPF \left( \begin{bmatrix} \hat{i}_{dh} \\ \hat{i}_{qh} \end{bmatrix} \cdot 2 \sin(\omega_{hf} t) \right) = \begin{bmatrix} I_p + I_n \cos(2\Delta\theta_r + \theta_m) \\ I_n \sin(2\Delta\theta_r + \theta_m) \end{bmatrix} \quad (1.82)$$

Next, the magnitude of the q-axis carrier current is the input of a position observer.

$$f(\Delta\theta_r) = |\hat{i}_{qh}| = I_n \sin(2\Delta\theta_r + \theta_m) \quad (1.83)$$

After the estimated q-axis current is minimized, the estimated position aligns with the actual position.

$$f(\Delta\theta_r) = |\hat{i}_{qh}| = I_n \sin(2\Delta\theta_r + \theta_m) = 0 \quad (1.84)$$

In (1.84), an error angle  $\theta_m$  is introduced by cross-coupling effect, the amplitude of this error mainly depends on the load, i.e. q-axis current. Several methods have been proposed to compensate for it and they will be introduced in Section 1.3.5.

### B. Rotating signal injection based method

For the rotating signal injection based method [JAN95] [DEG98] [RAC10], a balanced high frequency sinusoidal voltage vector is injected into the stationary reference as expressed by:

$$\begin{bmatrix} v_{\alpha h} \\ v_{\beta h} \end{bmatrix} = U_{hf} \begin{bmatrix} \cos(\omega_{hf} t) \\ \sin(\omega_{hf} t) \end{bmatrix} \quad (1.85)$$

where  $U_{hf}$  and  $\omega_{hf}$  are the amplitude and frequency of the injected rotating voltage, respectively. The injection is depicted in Fig. 1.37.

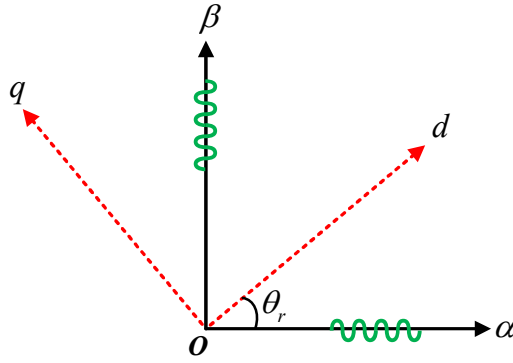


Fig. 1.37. Conventional rotating signal injection in stationary reference frame.

After injection, the carrier current responses in the stationary reference frame can be expressed by:

$$p \begin{bmatrix} i_{\alpha h} \\ i_{\beta h} \end{bmatrix} = \begin{bmatrix} \frac{1}{L_p} + \frac{1}{L_n} \cos(2\theta_r + \theta_m) & \frac{1}{L_n} \sin(2\theta_r + \theta_m) \\ \frac{1}{L_n} \sin(2\theta_r + \theta_m) & \frac{1}{L_p} - \frac{1}{L_n} \cos(2\theta_r + \theta_m) \end{bmatrix} \cdot \begin{bmatrix} v_{\alpha h} \\ v_{\beta h} \end{bmatrix} \quad (1.86)$$

$$\begin{bmatrix} i_{\alpha h} \\ i_{\beta h} \end{bmatrix} = \begin{bmatrix} \frac{1}{L_p} + \frac{1}{L_n} \cos(2\theta_r + \theta_m) & \frac{1}{L_n} \sin(2\theta_r + \theta_m) \\ \frac{1}{L_n} \sin(2\theta_r + \theta_m) & \frac{1}{L_p} - \frac{1}{L_n} \cos(2\theta_r + \theta_m) \end{bmatrix} \cdot \int \begin{bmatrix} v_{\alpha h} \\ v_{\beta h} \end{bmatrix} \quad (1.87)$$

$$\begin{bmatrix} i_{\alpha h} \\ i_{\beta h} \end{bmatrix} = \begin{bmatrix} I_p \cos(\omega_{hf} t - \frac{\pi}{2}) \\ I_p \sin(\omega_{hf} t - \frac{\pi}{2}) \end{bmatrix} + \begin{bmatrix} I_n \cos(-\omega_{hf} t + 2\theta_r + \theta_m + \frac{\pi}{2}) \\ I_n \sin(\omega_{hf} t + 2\theta_r + \theta_m + \frac{\pi}{2}) \end{bmatrix} \quad (1.88)$$

The carrier current responses in stationary reference frame can be expressed by using complex vector as:

$$I_{hf} = I_p e^{j(\omega_{hf}t - \frac{\pi}{2})} + I_n e^{j(\omega_{hf}t + 2\theta_r + \theta_m + \frac{\pi}{2})} \quad (1.89)$$

Clearly, as shown in (1.89), there are two main components in the carrier current response. The first component is a positive sequence which has the same frequency as the injected voltage signal. The second component is a negative sequence which has the rotor position information. Therefore, rotor position can be estimated by the negative sequence current.

In order to estimate the rotor position from the negative sequence carrier current response, a demodulation process is required. There are two typical demodulation methods, one is so-called ‘‘Heterodyning method’’ shown in Fig. 1.38(a), the positive sequence component in the carrier current is shifted to the high frequency domain and easily filtered by an LPF and the negative sequence is obtained for position estimation [JAN95]. Another demodulation method is called ‘‘SRFF (synchronous reference frame filter) [DEG98] [GAR07] [RAC10] shown in Fig. 1.38(b). The basic idea of the SRFF is to transform the fundamental current component to a dc value and an LPF is applied to filter out the high frequency components, and thus, the fundamental current can be easily obtained by transforming inversely finally.

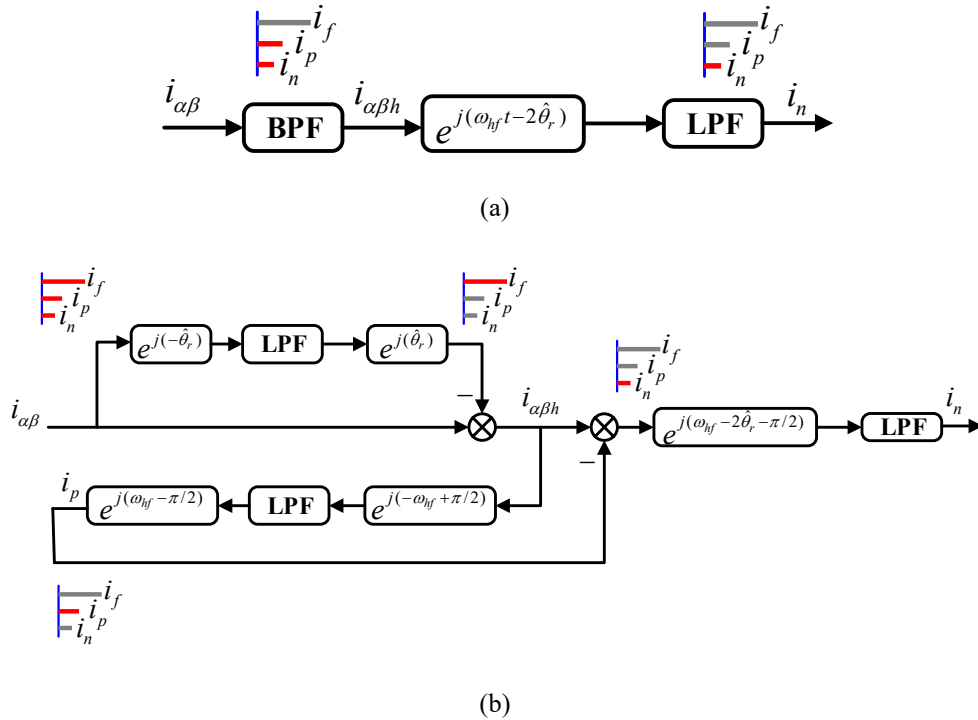


Fig. 1.38. Demodulation of rotating signal injection based method. (a) Heterodyning method [JAN95]. (b) SRFF method [GON12].

After demodulation process, the negative sequence current  $i_n$  can be expressed in the estimated reference frame by:

$$i_n = I_n e^{j(2\Delta\theta_r + \theta_m)} \quad (1.90)$$

$$i_n = \begin{bmatrix} i_{nd} \\ i_{nq} \end{bmatrix} = \begin{bmatrix} I_n \cos(2\Delta\theta_r + \theta_m) \\ I_n \sin(2\Delta\theta_r + \theta_m) \end{bmatrix} \quad (1.91)$$

Then, the magnitude of q-axis carrier current is the input of a position observer.

$$f(\Delta\theta_r) = i_{nq} = I_n \sin(2\Delta\theta_r + \theta_m) \quad (1.92)$$

After the estimated q-axis current is minimized, the estimated position aligns with the actual position.

$$f(\Delta\theta_r) = i_{nq} = I_n \sin(2\Delta\theta_r + \theta_m) = 0 \quad (1.93)$$

In (1.84), the same as the pulsating signal injection method, an error angle  $\theta_m$  exists in the estimated rotor position.

### C. Square wave signal injection based method

Similar to conventional pulsating signal injection scheme, in [YOO11], a pulsating square wave signal is injected into the stator windings [HAM10] [YOO11] [KIM12] [KIM16] [WAN20a]. The injected frequency can be much higher than rotating and pulsating injection schemes [WAN20a], and hence, the LPFs during demodulation process are eliminated, the bandwidth of position estimation is improved and the dynamic performance is greatly enhanced [HAM10]. Square wave signal can be injected into the estimated synchronous reference frame [KIM12][WAN20a] and the stationary reference frame [YOO11]. Take the estimated synchronous injection as an example, the square wave signal injected into the estimated d-axis is shown in Fig. 1.39.

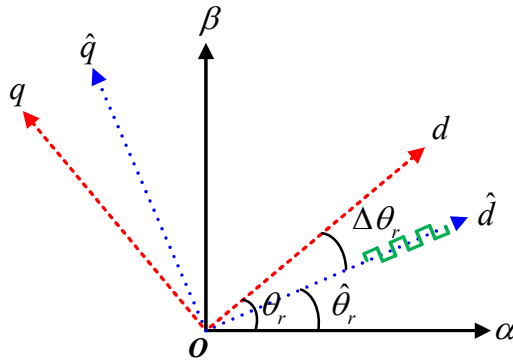


Fig. 1.39. Conventional square signal injection in estimated d-axis.

The injected square wave signal is expressed by:

$$\hat{v}_{dh} = \begin{cases} U_{hf} & \text{half duty} \\ -U_{hf} & \text{otherwise} \end{cases} \quad (1.94)$$

where  $U_{hf} > 0$  and  $\hat{v}_{qh=0}$ . After injection, the differential carrier current responses in the estimated reference frame can be expressed by:

$$\begin{bmatrix} \Delta \hat{i}_{dh} \\ \Delta \hat{i}_{qh} \end{bmatrix} = \begin{cases} U_{hf} \Delta T \begin{bmatrix} \frac{1}{L_p} + \frac{1}{L_n} \cos(2\Delta\theta_r + \theta_m) \\ \frac{1}{L_n} \sin(2\Delta\theta_r + \theta_m) \end{bmatrix} & \hat{v}_{dh} > 0 \\ -U_{hf} \Delta T \begin{bmatrix} \frac{1}{L_p} + \frac{1}{L_n} \cos(2\Delta\theta_r + \theta_m) \\ \frac{1}{L_n} \sin(2\Delta\theta_r + \theta_m) \end{bmatrix} & \hat{v}_{dh} < 0 \end{cases} \quad (1.95)$$

where  $\Delta T$  is half period of the injected square wave voltage signal. The current response by normalizing the polarity is expressed by:

$$\begin{bmatrix} \Delta \hat{i}'_{dh} \\ \Delta \hat{i}'_{qh} \end{bmatrix} = \begin{cases} U_{hf} \Delta T \begin{bmatrix} \frac{1}{L_p} + \frac{1}{L_n} \cos(2\Delta\theta_r + \theta_m) \\ \frac{1}{L_n} \sin(2\Delta\theta_r + \theta_m) \end{bmatrix} \end{cases} \quad (1.96)$$

where  $\Delta \hat{i}'_{dh}$  and  $\Delta \hat{i}'_{qh}$  are the polarity normalized current responses. The signal process is described Fig. 1.40.

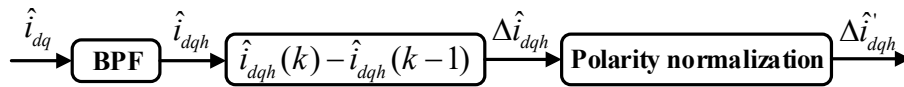


Fig. 1.40. Signal processing of square wave signal injection based method.

Similar to conventional methods, the current response  $\Delta \hat{i}'_{qh}$  is regarded as the input of position observer as:

$$f(\Delta\theta_r) = \Delta \hat{i}'_{qh} = \frac{U_{hf} \Delta T}{L_n} \sin(2\Delta\theta_r + \theta_m) \quad (1.97)$$

In (1.97), the same as the pulsating signal injection method, an error angle  $\theta_m$  exists in the estimated rotor position.

#### D. Random signal injection based method

For conventional high frequency signal injection methods, the injected high frequency voltage signal has fixed frequency and amplitude. However, these methods with fixed signals suffer from acoustic noise [WAN16] and EMI issues [WAN17a]. Hence, methods by injecting non-fixed frequency or amplitude high frequency signals are proposed [JIA11] [TAN14] [WAN16] [WAN17a]. By injecting random voltage signals, the spectra of the induced currents can be extended, which will reduce the noises. In [JIA11], [TAN14], a high frequency pulsating voltage signal is injected but the frequency of the signal is changed randomly, the acoustic noise is reduced in sensorless control at low speed [JIA11]. Moreover, in [WAN16], a pseudo-random high frequency square wave voltage injection method is proposed. The high frequency signal is injected into the estimated synchronous reference frame as shown in Fig. 1.41.

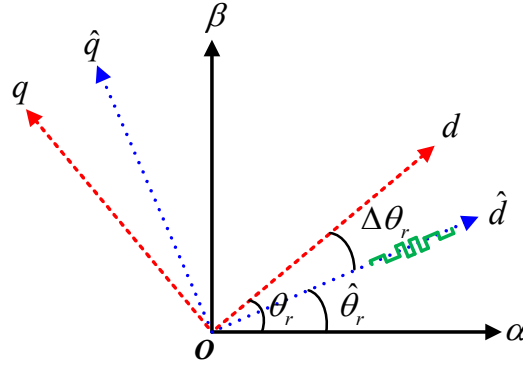


Fig. 1.41. Random injection in the estimated synchronous reference frame.

The generating mechanism of the pseudo-random signal in [WAN16] is shown in Fig. 1.42.

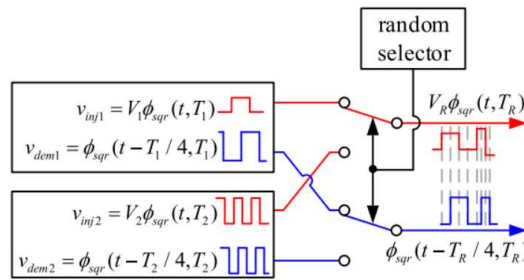
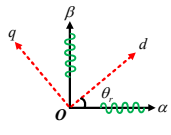
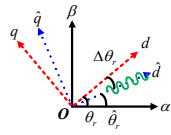
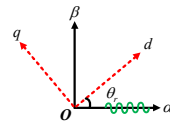
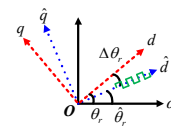
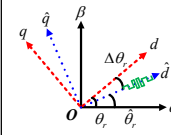


Fig. 1.42. Random signal generating mechanism [WAN16].

As shown in Fig. 1.42, two different voltage signals are selected randomly and hence outputs pseudo-random voltage signal. By injecting the pseudo-random signal, the distribution of injected high frequency and the induced current response in frequency domain is extended. As a consequence, the audible noise is reduced.

The comparison between different persistent signal injection methods are shown in TABLE 1.2.

TABLE 1.2  
COMPARISON OF PERSISTENT SIGNAL INJECTION BASED METHODS

	Rotating	Pulsating		Square wave	Random
Coordinate	Stationary	Estimated synchronous	Stationary	Estimated synchronous	Estimated synchronous
Signal injection					
Injected signal	Rotating	Pulsating	Pulsating	Square wave	Square wave
Current response	Phase-modulated	Amplitude-modulated	Amplitude-modulated	Amplitude-modulated	Amplitude-modulated
Cross-saturation position error	$-\theta_m/2$	$-\theta_m/2$	$-\theta_m/2$	$-\theta_m/2$	$-\theta_m/2$
Demodulation	Complex	Medium	Medium	Simple	Medium
Bandwidth	Low	Medium	Medium	High	High
Torque ripple	Large	Medium	Medium	Small	Small
Audible noise	Large	Large	Medium	Medium	Small
Requirement of Parameter	No	No	Yes	No	No

### ***E. Transient pulse injection based method***

The rotor position can also be obtained from the current responses by injecting short period voltage vectors. A typical method is the so-called “INFORM (Indirect flux detection by online reactance measurement)” method [SCH96].

The main principle is to measure the current responses induced by the voltage vectors applied in different directions. During the null part of one PWM cycle, two opposite voltage vectors are injected. Three successive PWM cycles with one current response measurement per cycle are required to estimate the position. However, a major issue of INFORM method is the induced current disturbance due to extra injected voltage vectors.

### ***F. PWM excitation based method***

It is known that the voltage vectors used in transient voltage vector injection methods also exist in normal operations with standard PWM [LIU13]. Hence, it is possible to extract the rotor position information by measuring the current response introduced by the inherent PWM operations. Based on this, several methods without additional injection signals are proposed [HOL05] [GAO07] [RAU08] [BOL11] [HUA11]. By eliminating the requirement of additional voltage signal injection, the current or torque ripple and switching loss can be reduced. [HOL05] presented an extended modulation (EM) scheme to obtain the rotor position information by modifying the PWM excitation. Besides, [GAO07] [RAU08] [BOL11] [HUA11] estimate the position with the standard PWM. A typical and simple method called “ZVCD (zero vector current derivative)” is proposed in [RAU08], the current during zero voltage vector dwelling time is used to estimate the rotor position as expressed by:

$$\frac{d\hat{i}_d}{dt} = \frac{R}{2} \left( \frac{1}{L_d} - \frac{1}{L_q} \right) \hat{i}_q \sin 2\Delta\theta_r - \frac{\omega_r \psi_m}{L_q} \sin \Delta\theta_r \quad (1.98)$$

In (1.98),  $\hat{i}_d$  is assuming to be zero. If the  $\Delta\theta_r$  is zero then  $\frac{d\hat{i}_d}{dt}$  goes to zero as well and hence  $\frac{d\hat{i}_d}{dt}$  can be regarded as the input of position observer. However, the method has to be applied when  $\hat{i}_d = 0$ . Besides, a long duration of zero voltage vector is necessary for measuring the d-axis current derivative response.

Overall, the comparison between persistent signal injection, transient pulse injection, and PWM excitation is given in TABLE 1.3.

TABLE 1.3  
COMPARISON OF PERSISTENT INJECTION BASED METHODS

	Persistent signal	Transient pulse	PWM excitation
Additional signal	Yes	Yes	No
Current measurement cost	Low	Medium	High
Torque ripple	Large	Medium	Low
Noise	Large	Medium	Low
Speed operation range	Narrow	Medium	Wide
Bandwidth of position estimation	Low	Medium	High

### 1.3.4 Polarity Detection

For saliency based sensorless control methods, the polarity of magnet should be identified since the inductance varies twice in one electrical period causing an angle ambiguity of 180 degrees. Otherwise, the starting torque cannot be guaranteed [JAN06]. The basic principle of detecting polarity is based on the magnetic saturation effect [SCH97][NAK00]. A positive d-axis current will increase the saturation of stator iron core and therefore decrease the d-axis inductance, whereas a negative d-axis current decreases the saturation and increases the d-axis inductance. Basically, the magnetic polarity can be identified by short pulse injection [NOG98] [AIH99] [HAQ03] [HOL08] [WAN12a], secondary harmonics of carrier current response due to magnetic saturation [KIM04] [JEO05] [RAC10] [XU16b], or d-axis current injection [GON13].

For short pulse injection based method, two opposite pulses are injected and the difference indicates the magnetic polarity. Short pulse injection based method is simple, robust and reliable. However, it is executed as a separate process, the position estimation should be stopped when identifying the polarity [HOL08]. The secondary harmonics based methods is integrated with the position estimation [KIM04], but the SNR is limited due to small value of the secondary harmonics of carrier currents [XU16b]. In [GON13], a polarity detection method is proposed which can be seamlessly integrated with conventional carrier signal injection based method. A constant current is injected at the estimated d-axis, and then, the changes of high frequency current in the estimated d-axis is used to obtain the polarity information. The overall comparison between three types of method is shown Fig. 1.43

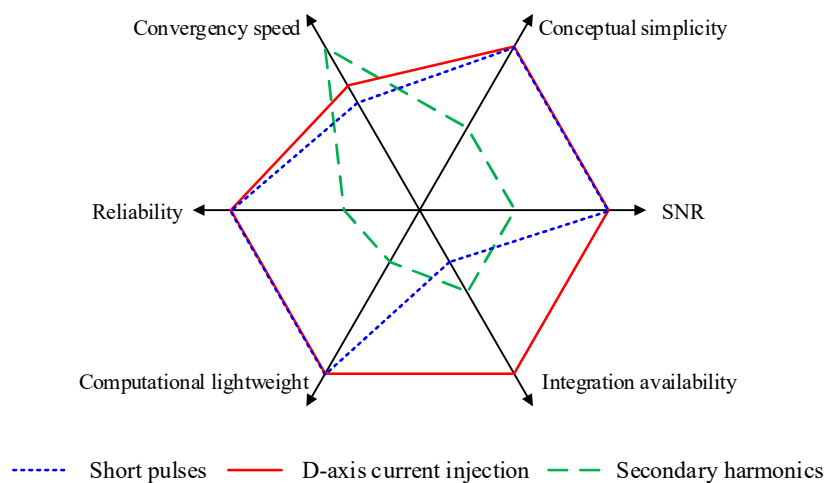


Fig. 1.43. Comparison between different types of polarity detection methods [GON13].

### 1.3.5 Cross-coupling Effect and Compensation

In [COR98], it was found experimentally that the position estimation error increases with load current. [BIA05] and [GUG06] states that it is the cross-coupling saturation between the d and q axes that caused the position error in carrier signal injection based methods. By considering the cross-saturation effect [LI09], the high frequency voltage model is expressed by:

$$\begin{bmatrix} v_{dh} \\ v_{qh} \end{bmatrix} = \begin{bmatrix} L_{dh} & L_{dqh} \\ L_{qdh} & L_{qh} \end{bmatrix} p \begin{bmatrix} i_{dh} \\ i_{qh} \end{bmatrix} \quad (1.99)$$

where  $L_{dqh}$  and  $L_{qdh}$  are the high frequency incremental mutual inductances due to cross-saturation effect and they are normally regarded as the same [LIN02] [LI07] [REI08], i.e.  $L_{dqh} \approx L_{qdh}$ . As illustrated in Section 1.3.3, for conventional carrier signal injection based methods, due to the cross-coupling effect, a position estimation error appears and can be expressed by:

$$\Delta\theta_r = \theta_m/2, \theta_m = \tan^{-1} \left( \frac{-L_{dqh}}{L_{sd}} \right) \quad (1.100)$$

This position error can be a critical issue which reduces the torque capability and reliability of the sensorless control. Hence, several methods are proposed to compensate for the cross-coupling effect including offline based compensation method [ZHU07] [LI09] [GON11] and online based compensation method [WAN20b].

For the offline based compensation methods, the compensation coefficient or factors are measured or simulated offline. In [ZHU07], a straightforward method is proposed by simply compensating the position error refers to the load current. The compensation angle is expressed by:

$$\theta_{comp} \approx K_c i_q \quad (1.101)$$

where  $K_c$  is the compensation factor. The parameter  $K_c$  should be measured in the offline test.

Another offline compensation method for pulsating signal injection method is proposed in [LI09] by introducing a coupling factor between d- and q-axis currents as expressed by:

$$\lambda = \frac{L_{dqh}}{L_{qh}} = -\frac{i_{qh}}{i_{dh}} \quad (1.102)$$

By introducing the coupling factor  $\lambda$ , the signal input of the position observer is modified as:

$$f(\Delta\theta_r) = |\hat{i}_{qh}| + \lambda|\hat{i}_{dh}| \approx 2I_n \cos \theta_m \Delta\theta_r \quad (1.103)$$

In the steady state,  $f(\Delta\theta_r)$  will be controlled to zero and hence the error introduced by cross-coupling is eliminated.

[GON11] proposed a compensation method for rotating signal injection method. Without compensation, the negative sequence current is expressed by:

$$i_n = I_n e^{j(\omega_{hf}t + 2\theta_r + \theta_m + \frac{\pi}{2})} \quad (1.104)$$

In [GON11], the injected carrier voltage is phase shifted by  $\theta_m$ . Consequently, in the negative sequence the phase shift of  $\theta_m$  is eliminated, as expressed by:

$$i_n = I_n e^{j(\omega_{hf}t + 2\theta_r + \frac{\pi}{2})} \quad (1.105)$$

Although offline measurement or FE simulation is required, both offline methods work effectively and show a satisfied compensation performance.

Instead of offline based compensation method, an online compensation method is proposed in [WAN20b]. The load-dependent position error can be identified by simply varying the direction of the current vector based on the torque equation. However, this method has some limitations, it requires the knowledge of machine parameters, i.e.  $L_d$ ,  $L_q$  and  $\psi_m$ . Besides, the online identification requires steady state operation with a constant load torque.

## 1.4 Sensorless Control of Surface-mounted PMSMs

As introduced in previous sections, the sensorless control techniques can be divided into fundamental model based method and saliency based method. Specifically, considering the zero and low speed sensorless control of SPMSMs, it is still a challenge. For fundamental model based methods, they normally cannot be used in zero and low speed due to unobservable machine model. Besides, the lack of saliency of SPMSM increases the difficulty of using saliency based sensorless control methods.

In order to realize sensorless control of SPMSM in zero and low speed, several potential methods are proposed based on fundamental model, magnetic saliency and resistive saliency.

### 1.4.1 Fundamental Model Based Method

For fundamental model based method, mainly back-EMF or flux-linkage is used for position estimation. It is known that back-EMF is proportional to speed, the SNR of EMF voltage decreases as the speed decreases [HAN00]. Apparently, back-EMF estimation cannot be used in zero speed. At the low speed, the back-EMF estimation is affected by resistance variation [FOO10] and voltage errors due to inverter nonlinearity [PEL10] [RAU10]. Different from back-EMF, flux-linkage is not related with rotor speed ideally. Potentially, it can provide a better estimation performance at low speed [WAN14b]. However, since the flux cannot be directly measured and has to be calculated from stator voltage and current, which is equivalently integration of back-EMF. Therefore, at low speed, it is still difficult to estimate the position using flux-linkage based methods. For the integration of back-EMF, dc-offset will be produced and normally an LPF is necessary to eliminate the dc-offset. However, introducing LPF will degrade the dynamic performance [CHE20]. Moreover, the same as back-EMF estimation, resistance deviation and inverter related voltage errors also induce errors in estimation of flux-linkage.

As stated in [PEL10] and [RAU10], the voltage errors due to inverter nonlinearity primarily affect the low speed estimation. Therefore, some work have been done to compensate the voltage errors due to inverter nonlinearity [HEJ11] [PAR12] [WAN14a]. After compensation, the low speed estimation performance can be improved. However, it is not easy to realize an accurate compensation due to strong nonlinearities and junction temperature variation [WAN18]. Moreover, using measured voltage [CHE15] [WAN17b] [SCH18] [CHE20] [WU20] can provide a better performance at lower speed rather than reference voltage. In [CHE20], an instantaneous voltage sensing method is proposed, after applying the measured voltage instead of command value, a lowest speed at 30rpm of sensorless operation is achieved. Besides, it is reported in [CHE20] that a closed-loop start-up and speed reverse under full load are realized by EMF estimation using measured voltage. However, the test is done only with a small position error before start. Furthermore, extra voltage sensing signal processing circuit is required which increases the cost and complexity and reduces the system reliability.

As stated in [CHE20], although the fundamental model based sensorless control cannot estimate the rotor position at zero speed, it is still possible to converge the estimated position to the real one quickly once the rotor starts to rotate. Hence, fundamental model based sensorless control methods can be assumed as a possible solution to realize the startup and low speed sensorless control of SPMSM.

### 1.4.2 Magnetic Saliency Based Method

Due to the symmetrical structure of rotor, there is not enough geometric saliency in SPMSMs. Nevertheless, zero and low speed sensorless control of SPMSMs can be realized by the magnetic saliency due to the magnetic saturation effect [JAN03a] [SIL06] [HA08]. Magnetic saturation is introduced by two parts, one is PM flux and the other is coil flux. The PM flux creates an inductance variation against rotor position at twice frequency of electrical frequency of rotor. The coil flux produces an inductance variation against rotor position at same frequency as electrical frequency of rotor [LAI03]. The total flux depends on the directions between the PM flux and the coil flux.

Based on magnetic saturation effect, initial position estimation of SPMSMs can be realized by short pulse injection based methods [MAT96] [SCH97] [NAK00] [LAI03] [TUR03] [LEE06] [CHA09]. Although estimation resolution may be lower than carrier signal injection based methods, short pulse injection based methods can still provide a reliable estimation with a satisfying signal-to-noise ratio (SNR) [GON13]. Since filters and signal demodulation processes are not necessary, short pulse injection based methods are more robust and simpler for implementation. Besides, there is no issue of audible noise. Moreover, compared with carrier signal injection based methods, injection of voltage pulses can enhance the saturation effect which can be beneficial to utilization of magnetic saliency. Therefore, they can be a desirable option for some applications using SPMSM.

It is worth noting that a combination of an initial position estimation using short pulse injection and a proper fundamental model based method, the zero and low speed sensorless of SPMSMs can be possibly realized.

### 1.4.3 Resistive Saliency Based Method

An alternative position estimation method for SPMSM at low speed by injecting high frequency voltage signals is proposed by [YAN12]. The method tracks the high frequency eddy current loss reflected resistive saliency to estimate the rotor position.

In [YAN12], it is approved that the eddy current loss  $P_{eddy}$  varies against the rotor position and its spatial variation can be enhanced by superimposing a high frequency voltage as shown in Fig. 1.44.

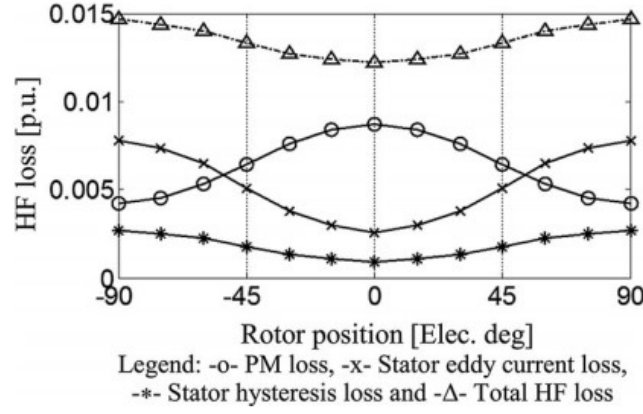


Fig. 1.44. HF losses versus position in the SPM machine [YAN12].

Hence, if there is some differences between d- and q-axis eddy current losses, the resistance in the stationary reference frame can be expressed by:

$$R_{\alpha\beta} = \Sigma R \begin{bmatrix} 1 & 0 \\ 0 & 1 \end{bmatrix} + \Delta R \begin{bmatrix} \pm \cos(2\theta_R) & \mp \sin(2\theta_R) \\ \mp \sin(2\theta_R) & \pm \cos(2\theta_R) \end{bmatrix} \quad (1.106)$$

where  $\Sigma R$  and  $\Delta R$  are the average and differential values of the asymmetric resistance and  $\theta_R$  is the spatial information in the asymmetric resistance which is related to rotor position. The variation of asymmetric resistance against rotor position is shown in Fig. 1.45.

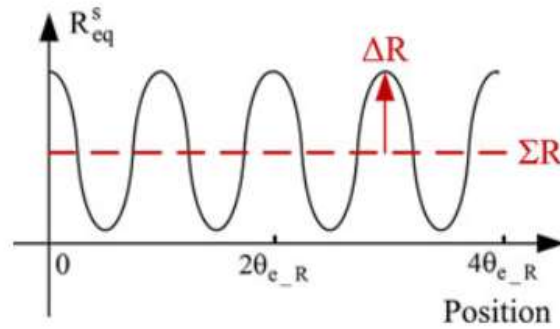


Fig. 1.45. Spatial variation of asymmetric resistance  $R_\alpha$  [YAN12].

Although this method provides an alternative for SPM to estimate the position at low speed, several limitations exist. In [YAN12], the switching frequency is 25kHz and the injected voltage frequency is 2.5kHz, which are much higher compared to conventional carrier based methods, and hence increases the requirement of system cost. The feasibility of resistive saliency method also highly depends on the machine topology, especially eddy-current loss is often greatly minimized by laminations.

## 1.5 Sensorless Control Considering Rotor Eccentricity

For most of the sensorless control techniques, they are normally developed under a healthy condition of PMSMs. However, in practice, the PMSMs are normally unideal due to manufacture imperfection. Rotor eccentricity is a common issue that exists in PMSMs. The effect of rotor eccentricity on the PMSM characteristics has been widely investigated in the past [HWA01] [EBR09] [DOR10] [WU10] [HON12] [ZHU13] [FIS17]. However, its relationship between sensorless control is discussed by only a few research.

[FAI06] and [YAG14] discussed the rotor eccentricity effect on SRM sensorless control by FE simulation. However, only a few simple FE simulation results of flux-linkage or inductance change under rotor eccentricity are given, the relationship between sensorless control and rotor eccentricity is not explained mathematically or systematically. [HUR94] and [SON15] utilize the eccentricity induced current harmonics for speed estimation of an induction motor. However, the signal process and control strategy are very complex and the SNR of utilized harmonics may not be guaranteed. In [KWO15] and [KWO16], an IPMSM with eccentric rotor is designed for absolute position sensorless drive. The eccentric rotor creates a mechanical frequency component in the inductance so that can be utilized for absolute position estimation.

## 1.6 Outline and Contributions of the Thesis

Sensorless control methods for PM machines are extensively reviewed in this chapter. The major objective of the thesis includes:

- Sensorless control of SPMSMs at zero speed and startup operation.
- Investigation of conventional sensorless control under rotor eccentricity.

The research structure is illustrated in Fig. 1.46.

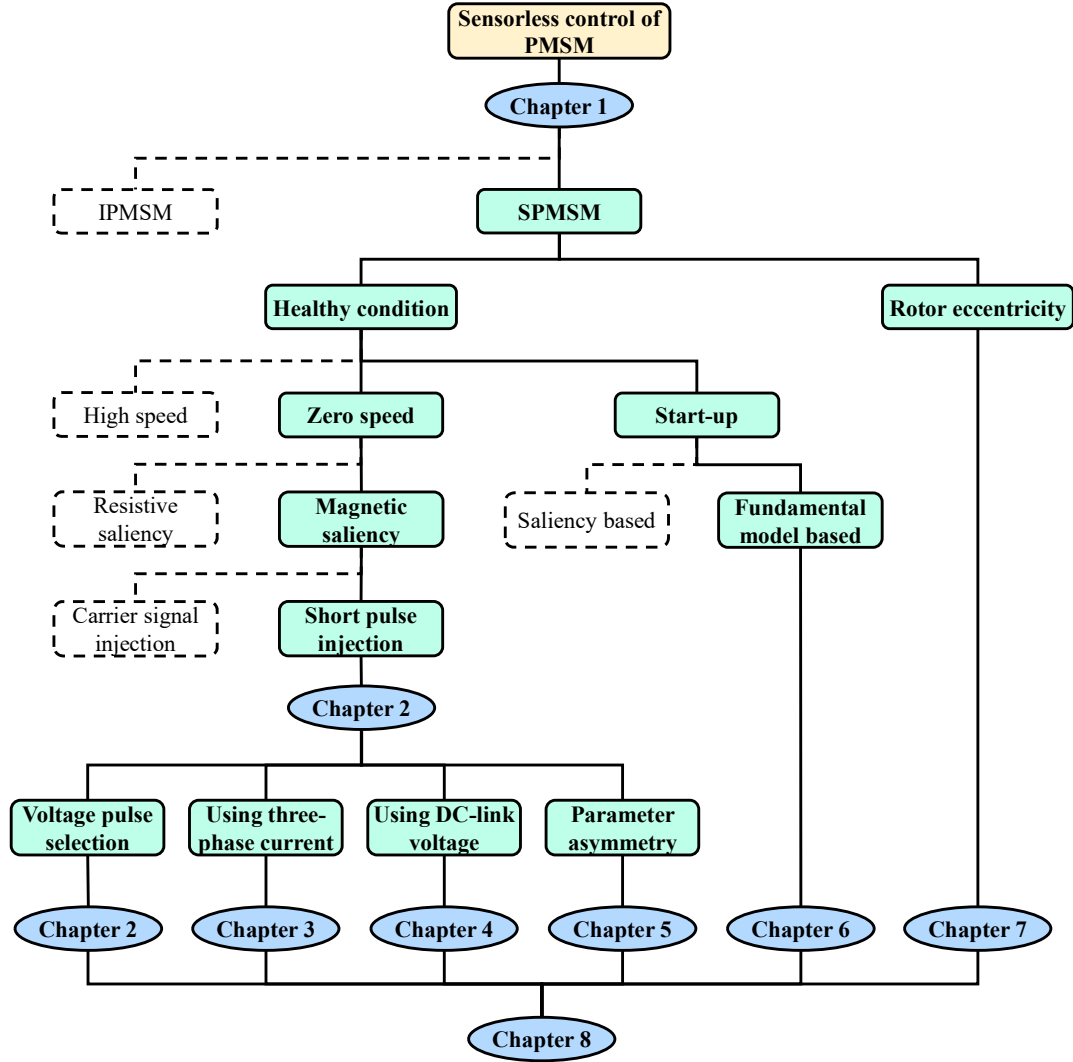


Fig. 1.46. Research structure.

The thesis is organized as follows:

**Chapter 2** introduces conventional short-pulse-injection based rotor initial position estimation techniques in details, and a comparative study is given. Besides, a voltage selection strategy is developed for a reliable rotor initial position estimation.

**Chapter 3** proposes a short-pulse-injection-based rotor initial position estimation technique using three-phase current for SPMSMs. Novel strategies are applied, and therefore, the efficiency of the method is improved in terms of reducing the pulse injection number and increasing the estimation resolution.

**Chapter 4** proposes a novel short-pulse-injection-based rotor initial position estimation method utilizing DC-link voltage. By using the DC-link voltage variation as a rotor position dependent response, the estimation performance can be enhanced compared to conventional current response based methods.

**Chapter 5** investigates the influence of parameter asymmetry, including resistance and inductance asymmetries, on rotor initial position estimation by using short-pulse-injection-based techniques, and proposes two compensation strategies for parameter asymmetry.

**Chapter 6** proposes a simplified fundamental model based sensorless control method for SPMSM. By simplifying the model, only stator current is required for sensorless control without any knowledge of parameters. By applying the proposed method, a satisfied low speed sensorless control performance is obtained and the machine is able to start up even under load. Moreover, the proposed method is extended to Siemens Wind Power Turbine for sensorless starting by hardware-in-loop (HIL) simulation.

**Chapter 7** investigates the conventional fundamental model based sensorless control under rotor eccentricity. The rotor eccentricity effect on PM machine is discussed. It is approved that mainly harmonics are introduced in position estimation errors. A modified back-EMF based position estimator incorporating with an adaptive notch filter is developed to eliminate the undesired harmonics.

**Chapter 8** summarizes the research work and discusses about some future work

The major contributions of this thesis are:

- Based on the magnetic saturation effect, conventional short-pulse-injection-based methods are comparatively studied, which has not been done in the past.
- A voltage pulse selection strategy for short-pulse-injection-based rotor initial position estimation techniques is developed. Based on the proposed selection rules, a Reliable Selection Area (RSA) is introduced so that the reliable estimation performance is guaranteed.
- A new short-pulse-injection-based rotor initial position estimation method using three-phase current is proposed. Compared with conventional methods which normally require 4-6

pulses for injection, the proposed method simplifies the injection procedure so that the total number of pulses is reduced to only 3 while achieving the same estimation resolution of 30 degrees at least. Moreover, a “boundary detection strategy (BDS)” is introduced and the estimation performance can be enhanced against measurement noises. Furthermore, with BDS, the estimation resolution can be further improved to 15 degrees.

- A novel short-pulse-injection-based rotor initial position estimation method using DC-link voltage is proposed. Different from conventional methods using current response. The proposed method uses the DC-link voltage response which is also rotor position dependent. By using the DC-link voltage response, the estimation performance can be improved compared with initial position estimation using current response.
- Short-pulse-injection-based rotor initial position estimation under parameter asymmetries including both resistance and inductance asymmetries is investigated which has not been done in literature. Two compensation strategies are developed which effectively eliminate the influence from parameter asymmetry.
- Sensorless control of PMSMs under rotor eccentricity is investigated which has not been done in the past. The rotor eccentricity effect on PMSM characteristics and sensorless control are discussed. It is shown that mainly the mechanical frequency and the 2<sup>nd</sup> order frequency harmonics are introduced in the position estimation error. An adaptive notch filter is introduced to eliminate the harmonics effectively.

The publications originating from this PhD research work are listed in Appendix B.

# CHAPTER 2

## VOLTAGE PULSE SELECTION STRATEGY FOR ROTOR INITIAL POSITION ESTIMATION

### 2.1 Introduction

For a SPM machine or an IPM machine, knowledge of rotor initial position at standstill is required, otherwise the starting performance is un-reliable. The rotor initial position may be obtained from magnetic saturation effect since the stator iron core will be saturated by the permanent magnet and the armature reaction together. Due to non-linear characteristics, the stator iron core under saturation will have smaller inductance than that of the linear case. One of the common approaches is to inject voltage pulses for estimating the rotor initial position from the current responses, which is called “Short-pulse-injection-based” method.

Short-pulse-injection-based methods are a type of simple, robust and low cost approach to obtain rotor initial position information by utilizing magnetic saturation effect. For short-pulse-injection-based methods, several short voltage pulses are injected into stator windings and rotor initial position can be obtained from the rotor position dependant current responses. Alternatively, it is possible to inject voltage pulses and extract rotor position from voltage responses. Although many techniques have been presented in the past [MAT96][SCH97][NAK00][LAI03][LEE06], few of them discuss the selection of voltage pulses including duration and magnitude when they are used for both brushless ac (BLAC) and dc (BLDC) drives. Therefore, it is worth investigating and developing a selection strategy of voltage pulses so that the estimation performance could be improved considering reliability and effectiveness.

This chapter firstly explains the magnetic saturation effect and demonstrate the basic procedure of rotor initial position estimation based on the magnetic saturation effect. Introduction and validation of conventional methods are provided afterwards. Then, based on these conventional methods, a simple voltage pulse selection strategy is presented and a reliable selection area (RSA) is derived. Selecting voltage pulse within this RSA, reliable and effective rotor initial position estimation is guaranteed. Moreover, it is found out that outside the RSA, reliable results may also be obtained. In order to fully utilize the selection area, an extended reliable selection area (ERSA) is developed. Both RSA and ESRA are examined by experiments.

Furthermore, the selection strategy is extended to Siemens 3MW Wind Power PM generators and validated by FE based co-simulation.

This chapter is based on the papers:

[WU20a] X. M. Wu, and Z.Q. Zhu, “A simple voltage pulse selection strategy for rotor initial position estimation,” *10th IET International Conference on Power Electronics, Machines and Drives (PEMD2020)*, Nottingham, 2020, Accepted.

[WU20b] X. M. Wu, and Z.Q. Zhu, “Comparative study of rotor initial position estimation,” *10th IET International Conference on Power Electronics, Machines and Drives (PEMD2020)*, Nottingham, 2020, Accepted.

## 2.2 Magnetic Saturation Effect

The stator iron core is a non-ideal magnetic material, as the magnetic flux which carries increases, it begins to saturate resulting in the decrease of inductance as shown in Fig. 2.1.

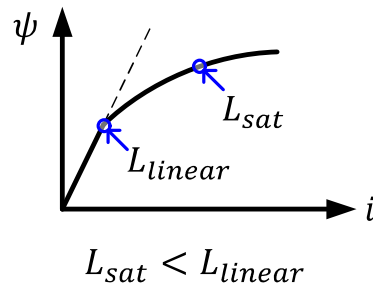


Fig. 2.1. Nonlinear magnetization characteristic and variation of inductance with saturation.

[WU20a]

In Fig. 2.2, a simplified schematic of a surface mounted permanent magnet synchronous machine is shown.

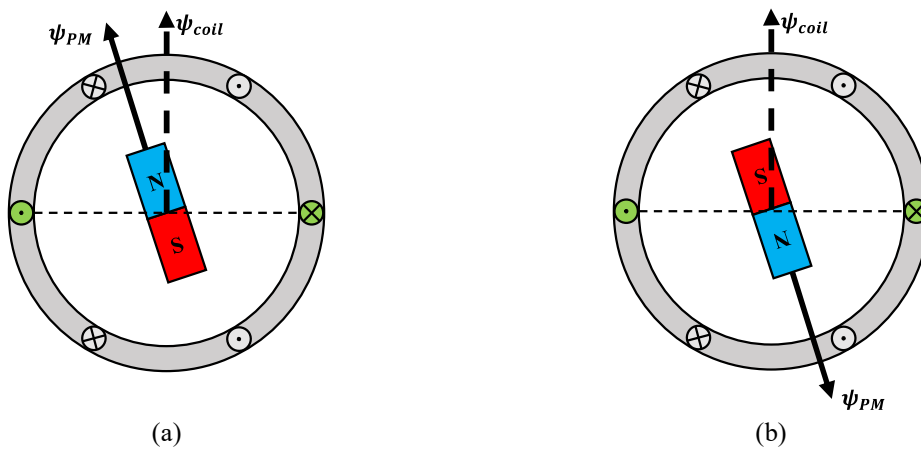


Fig. 2.2. Simplified SPM schematic for polarity identification. (a) Alignment with north pole. (b)

Alignment with south pole. [WU20a]

From Fig. 2.2, it can be seen that the magnetic flux that saturates stator iron core consists of two sources: PM and coil current. The total flux  $\vec{\psi}_{total}$  is given by:

$$\vec{\psi}_{total} = \vec{\psi}_{PM} + \vec{\psi}_{coil} \quad (2.1)$$

where  $\vec{\psi}_{PM}$  is the flux produced by PM and  $\vec{\psi}_{coil}$  is the flux produced by coil current, i.e. armature reaction. Firstly, for the PM part, the stator iron core becomes strongly magnetized when it is close to rotor magnetic poles of PM causing inductance to decrease. As the rotor magnetic poles move away, the inductance will increase. Therefore, inductance will vary against rotor position as shown in Fig. 2.3.

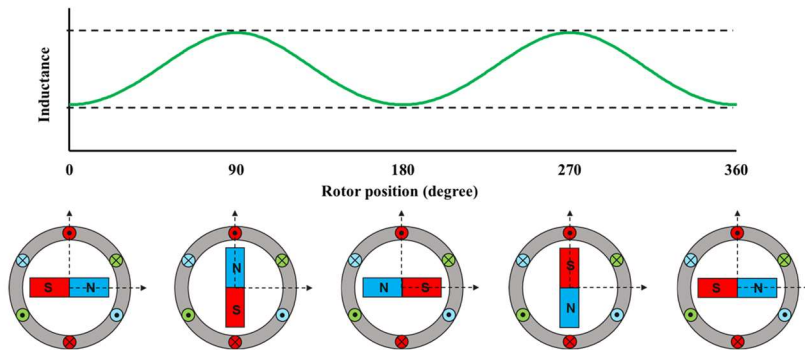


Fig. 2.3. Inductance variation against rotor position without considering armature reaction.

However, PM has north pole and south pole which introduce same saturation level, and inductance will vary twice over one electrical period which can cause an ambiguity of  $\pi$  in the rotor initial position estimation. As illustrated in Figs. 1(a) and 1(b), depending on the polarity of magnet, the flux in the coil can increase or decrease the total saturation level, resulting in different inductances as shown in Fig. 2.4.

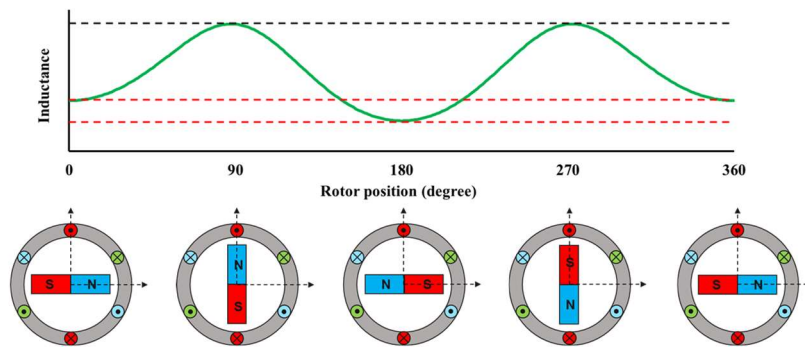


Fig. 2.4. Inductance variation against rotor position with armature reaction.

## 2.3 Rotor Initial Position Estimation

As described in the previous section, inductance varies against rotor position due to magnetic saturation effect. From this phenomenon, several voltage pulses are injected and the

current responses can be used for rotor initial position estimation. The basic estimation approach based on [SCH97] is introduced in this section to demonstrate the rotor initial position estimation procedure.

Firstly, voltage pulses can be injected into 6 positions, with the same duration and magnitude, at selected 6 voltage vectors of a 3-phase inverter (V1~V6), as shown in Fig. 2.5.

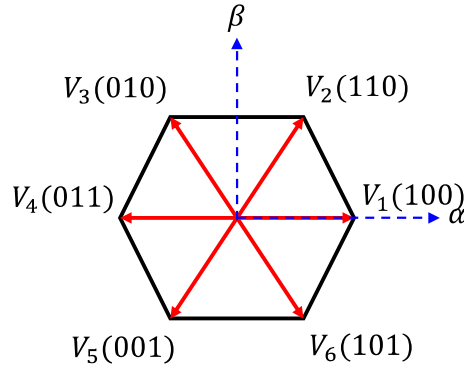


Fig. 2.5. Voltage vectors. [WU20a]

In this case, these 6 injection positions are 0, 60, 120, 180, 240, 300 degrees, respectively.

For different voltage vectors, the excitation configuration is shown below:

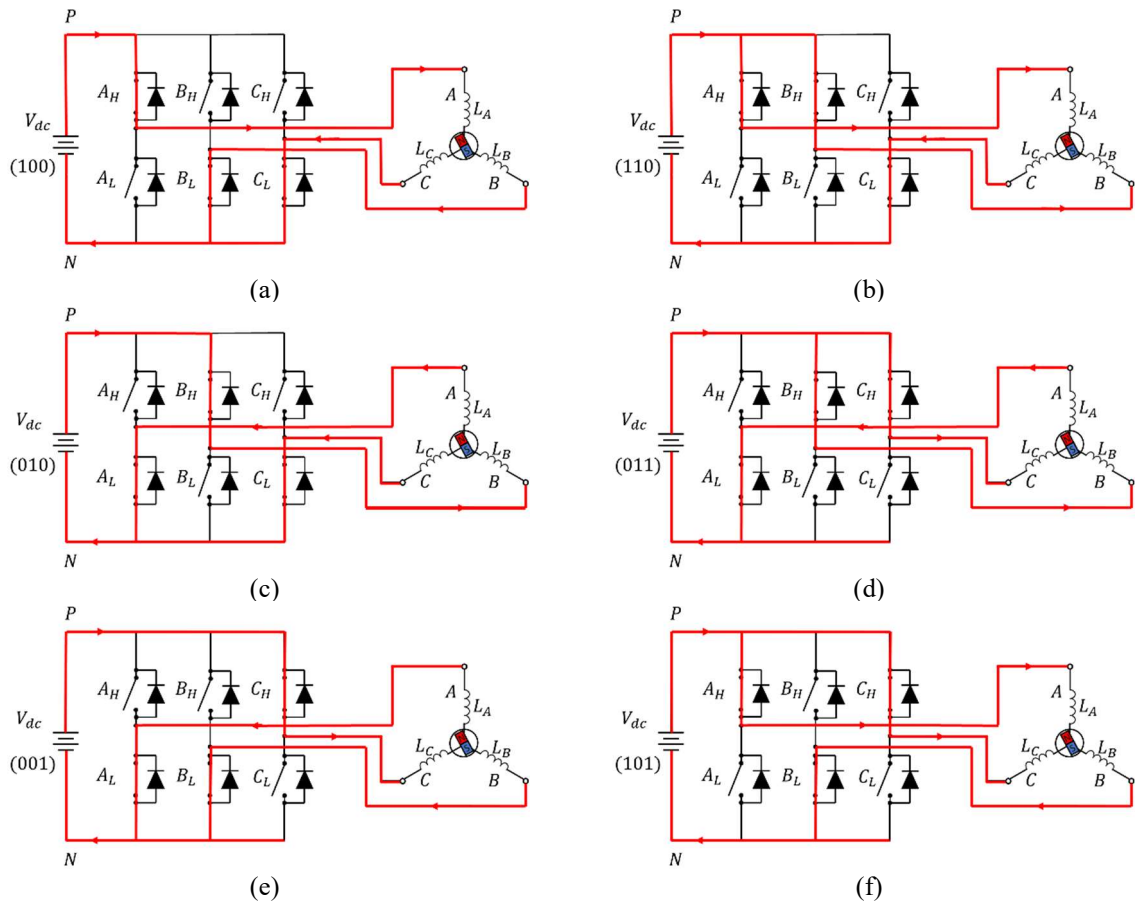


Fig. 2.6. Excitation configuration associated with voltage vectors. (a) V1. (b) V2. (c) V3. (d) V4. (e) V5. (f) V6.

Then, after excitation, the current response can be regarded as a step response:

$$I(t) = \frac{V_P}{R_{eq}} (1 - e^{-\frac{t}{L_{eq}/R_{eq}}}) \quad (2.2)$$

where  $I$  is the current response,  $t$  is the time,  $V_P$  is the voltage magnitude,  $R_{eq}$  and  $L_{eq}$  are the equivalent resistance and inductance in the excitation circuit. Since inductance varies against rotor position, current responses are rotor position dependent. A larger peak value of the current response indicates the voltage pulse injection position is closer to the rotor magnetic poles. Therefore, after injecting several voltage pulses at different positions, rotor initial position can be determined by comparing the peak values of current responses. Besides, as illustrated in Fig. 2.2(a) and (b), depending on the polarity of magnet, the flux in the coil can increase or decrease the total saturation level, resulting in different inductances. Thus, a current difference associated with the south pole and the north pole will be introduced. Based on this, the polarity can be identified.

It is known that the current response is related with inductance and thereby rotor position dependent. Hence, by injecting voltage pulses at different rotor positions, the three-phase current responses can be modelled as a function of rotor position:

$$\begin{aligned} I_A &= I_0 + I_1 \cos(\theta_r) + I_2 \cos(2\theta_r) \\ I_B &= I_0 + I_1 \cos\left(\theta_r - \frac{2\pi}{3}\right) + I_2 \cos\left(2\left(\theta_r - \frac{2\pi}{3}\right)\right) \\ I_C &= I_0 + I_1 \cos\left(\theta_r + \frac{2\pi}{3}\right) + I_2 \cos\left(2\left(\theta_r + \frac{2\pi}{3}\right)\right) \end{aligned} \quad (2.3)$$

where  $I_0$  is the DC-offset of current response,  $I_1$  is current change caused by armature reaction,  $I_2$  is the current change due to PM and  $\theta_r$  is the rotor position. Normally,  $I_1$  is much smaller than  $I_2$ . Therefore, according to [MAT96] and [SCH97], the model can be simplified as:

$$\begin{aligned} I_A &= I_0 + I_2 \cos(2\theta_r) \\ I_B &= I_0 + I_2 \cos\left(2\left(\theta_r - \frac{2\pi}{3}\right)\right) \\ I_C &= I_0 + I_2 \cos\left(2\left(\theta_r + \frac{2\pi}{3}\right)\right) \end{aligned} \quad (2.4)$$

Then, the measured three-phase current responses against rotor position are shown in Fig. 2.7. The measurement is taken from the prototype 3kW SPM motor, whose parameters are listed in the Appendix, by injecting three positive voltage pulses into three-phase windings. It can be seen from Fig. 2.7(a) that the measured current responses vary with rotor positions. Besides, in

Fig. 2.7(b), it is clear that there is a 0.5A difference between the north and the south poles of the rotor, which is large enough for polarity identification.

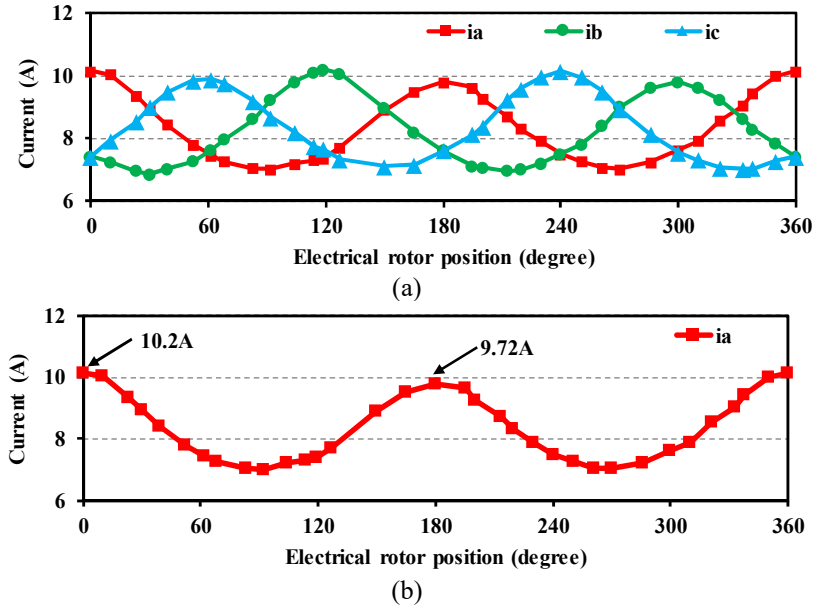


Fig. 2.7. Measured current responses against rotor position. (a) Three-phase current responses. (b) Phase A current responses.

## 2.4 Conventional Rotor Initial Position Estimation [WU20b]

Based on the magnetic saturation effect, several rotor initial position estimation techniques have been proposed in the past [SCH97][NAK00][LEE06][LAI03]. Based on different measurement or component that are used for rotor initial position estimation, 4 classical conventional methods are introduced in this part.

### 2.4.1 Three-phase Current Based Method

In [SCH97] [MAT96], the peak values of three-phase current responses are used to calculate the rotor initial position. At first, three negative voltage pulses and three positive voltage pulses are applied to the stator windings, i.e. a positive and a negative pulse are applied to each phase. After injection, the three-phase currents are modelled as:

$$\begin{aligned} I_A &= I_0 + \Delta I_0 \cos(2\theta_r) \\ I_B &= I_0 + \Delta I_0 \cos(2\theta_r - 2\pi/3) \\ I_C &= I_0 + \Delta I_0 \cos(2\theta_r + 2\pi/3) \end{aligned} \quad (2.5)$$

$$\begin{aligned} \Delta I_A &= I_A - I_0 \\ \Delta I_B &= I_B - I_0 \\ \Delta I_C &= I_C - I_0 \end{aligned} \quad (2.6)$$

$$I_0 = (I_A + I_B + I_C)/3 \quad (2.7)$$

where  $I_0$  is the average value,  $\Delta I_0$  is the offset and the actual rotor position is  $\theta$ .  $\Delta I_A$ ,  $\Delta I_B$  and  $\Delta I_C$  are the differences between the three-phase currents and their average value. The phase current with the largest difference determines which region the rotor north pole is the closest to. The remaining two phase current differences are used to calculate the estimated rotor initial position. For example, if phase A current has the maximum difference, currents of phase B and phase C are used for rotor initial position estimation. The estimated rotor initial position  $\hat{\theta}$  is given by:

$$\hat{\theta} = \kappa \frac{\Delta I_C - \Delta I_B}{\Delta I_C + \Delta I_B} \quad (2.8)$$

where  $\kappa = \cos(2\pi/3) / \sin(2\pi/3)$ . In all, according to the method in [SCH97], after injection of 6 voltage pulses into three-phase windings, a 24 degree resolution is obtained with  $\pm 12$  degrees error.

## 2.4.2 DQ Reference Frame Current Based Method

Method in [NAK00] uses the current in the estimated D-Q reference frame. The basic idea is that the estimated d-axis current increases as the injection position approaches the north pole of the rotor. The estimation method is divided into two steps. In the first step, 12 voltage vectors are applied to stator windings as shown in Fig. 2.8(a). The maximum d-axis current is recorded. In this step, a 30-degree resolution is obtained with  $\pm 15$  degrees error.

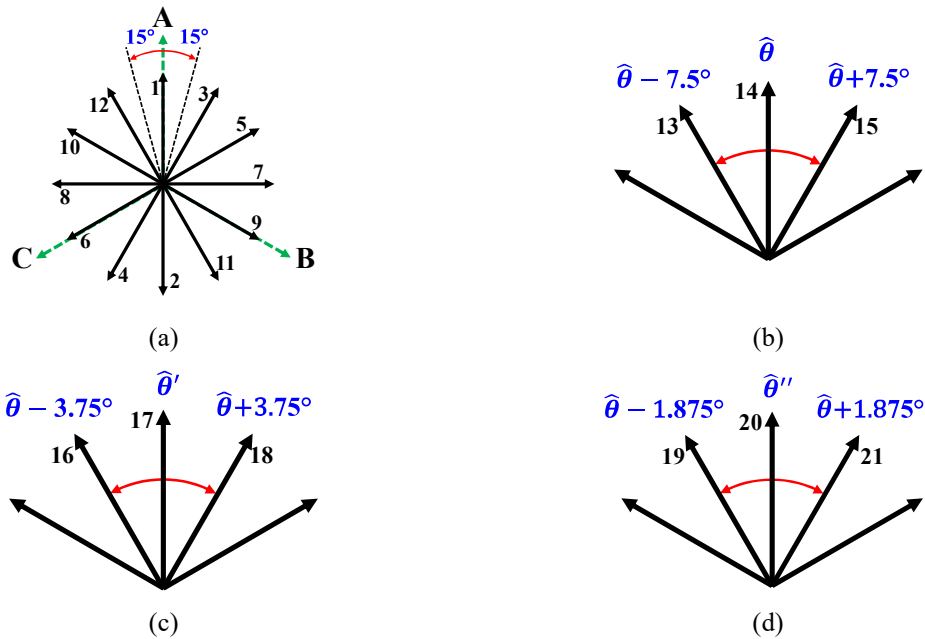


Fig. 2.8. Estimation process. (a) Step I with 30-degree resolution, (b) Step II with 15-degree resolution, (c) Step II with 7.5-degree resolution, (b) Step II with 3.85-degree resolution. [WU20b]

In the second step, more vectors which are adjacent to the selected vector in step I are applied as shown in Fig. 2.8(b)-(d). At last, a 3.85-degree resolution is obtained. Overall, referring to [NAK00], this method estimates rotor initial position with  $\pm 3.8$  degrees average estimation error and 18.75 degrees maximum estimation error.

### 2.4.3 DC-link Current Based Method

Method in [LEE06] proposed a low cost method using only dc-link current to estimate the rotor initial position. The total estimation process has three steps shown below.

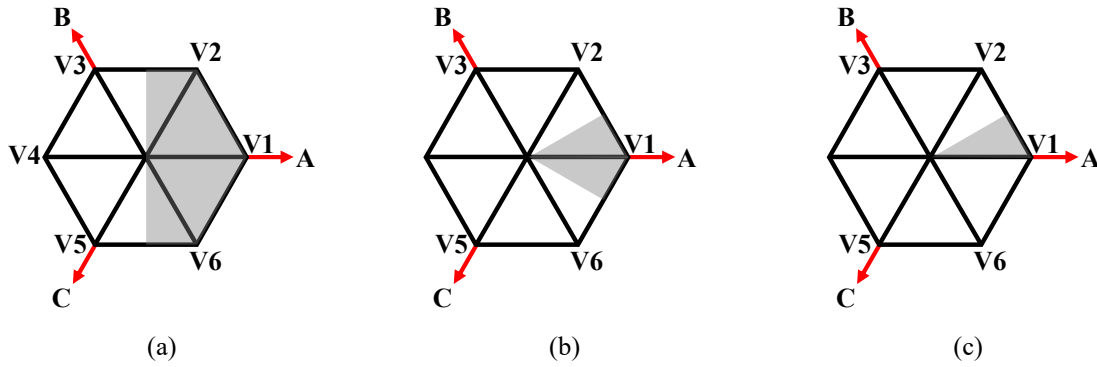


Fig. 2.9. Estimation process (a) Step I, (b) Step II, (c) Step III. [WU20b]

In step I, two opposite voltage vectors (V1 and V4) are applied to gain a 180-degree estimation resolution at first as shown in Fig. 2.9(a). In step II, the two adjacent voltage vectors (V2 and V6) are applied and the current responses are utilized to obtain a 60-degree estimation resolution as shown in Fig. 2.9(b). Step III is shown in Fig. 2.9(c), after locating the north pole of rotor in a 60-degree sector, comparing the current responses of two adjacent voltage vectors (V2 and V6) can further improve the estimation resolution to 30 degrees. Ideally, only 4 voltage pulses are required. However, due to existing of sample noises, the results of first step can be distorted, another set of voltage pulses (V2 and V5) should be applied in step I as well. Hence, at least one more pulse is required in practical drive systems. In all, with 5 pulses injected, this method has a 30-degree estimation resolution with  $\pm 15$  degrees estimation error.

### 2.4.4 Three-Phase Terminal Voltage Based Method

Apart from utilizing current information, voltage information can also be measured and utilized for rotor initial position estimation. In [LAI03], a technique is proposed by measuring terminal three-phase voltages. This technique is based on freewheeling time. It is introduced in Section 2.2 that inductance varies against rotor position due to magnetic saturation. As indicated in Fig. 2.10, the greater inductance stores more electric energy and therefore increases the falling time of discharge after the voltage pulse is removed.

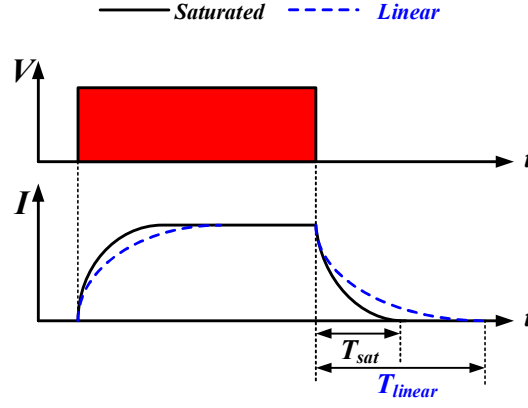


Fig. 2.10. Falling time comparison. [WU20b]

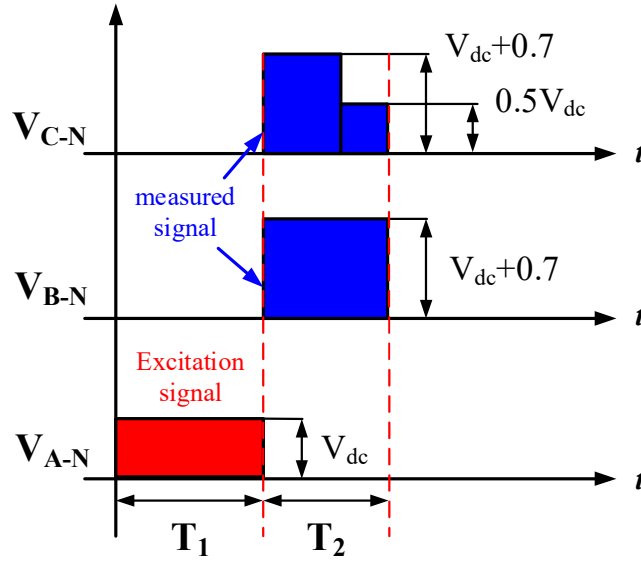


Fig. 2.11. Illustration of terminal voltage detection. [WU20b]

As indicated in Fig. 2.11, the terminal voltage across one phase during freewheeling stage is equal to  $(V_{dc} + 0.7)V$ . After the freewheeling stage, the terminal voltage goes down and is approximately equal to  $0.5V_{dc}$ . The terminal voltage level is used for the detection of rotor initial position. In this chapter, three voltage pulses are applied to three-phase windings and the freewheeling times are measured to offer a 60-degree estimation resolution. It is worth mentioning that the method in [LAI03] only considered the saturation caused by armature reaction and there is no need of polarity identification. However, as discussed in Section 2.2, in this thesis, the magnetic saturation caused by PM flux is considered as the main source. Therefore, the method in [LAI03] should be modified with one more pulse injection in order to identify the polarity. In total, at least 4 pulses are required.

### 2.4.5 Simulation Validation

In this section, both 4 conventional methods are validated by simulations based on Matlab/Simulink. The specifications of the prototype SPM-I are given in Appendix A. The real electrical rotor position is 120 degrees. Magnitude and duration of voltage pulses are 60V and 5ms, respectively.

#### A. Three-phase currents based method

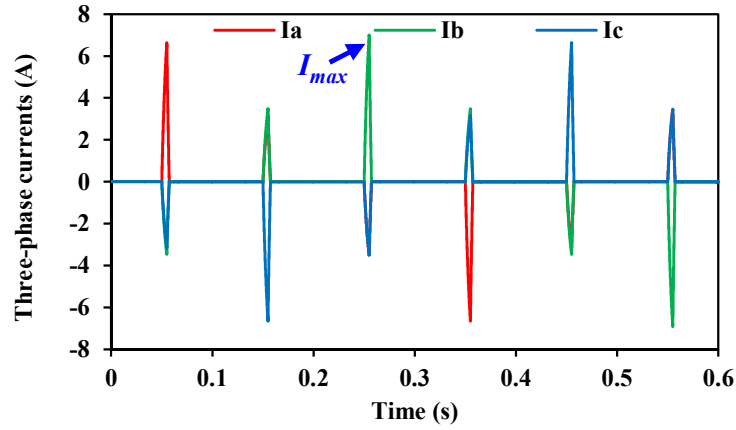


Fig. 2.12. Simulation results of three-phase current responses based on the method in [SCH97].

The method in [SCH97] is simulated and the results of three-phase currents are shown in Fig. 2.12. It is found that current response of phase B has the largest magnitude. Then the estimated rotor initial position  $\hat{\theta}_r$  is calculated as 119.2 degrees and the estimation error is 0.8 degrees.

#### B. DQ reference frame current based method

Simulation results of [NAK00] are given in Fig. 2.13, 18 voltage vectors are injected in total and the largest current response is found as the 13<sup>th</sup> one, and therefore,  $\hat{\theta}_r$  is estimated as 127.5 degrees and the estimation error is 7.5 degrees.

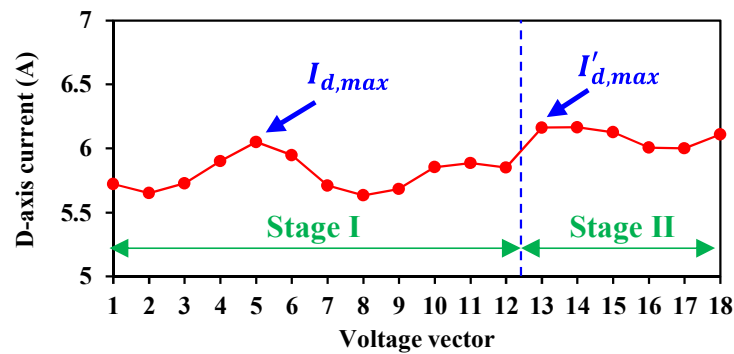


Fig. 2.13. Simulation results of recorded d-axis current based on the method in [NAK00].

### C. DC-link current based method

Simulation results of the method in [LEE06] are given in Fig. 2.14. In total, 4 voltage vectors are injected. It is found that the fourth dc-link current response is the largest and thus  $\hat{\theta}_r$  is estimated at 120 degrees and the estimation error is 0 degree.

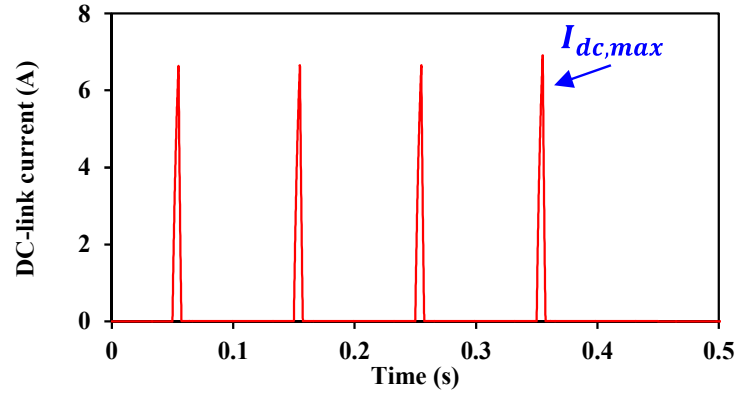


Fig. 2.14. Simulation results of dc-link current responses based on the method in [LEE06].

### D. Three-phase terminal voltage based method

Fourthly, the method of [LAI03] is simulated and the results are shown in Fig. 2.15. In total, 4 pulses are injected and the corresponding voltage levels during freewheeling stage are recorded and compared. After comparison,  $\hat{\theta}_r$  is estimated at 90 degrees and the estimation error is 30 degrees.

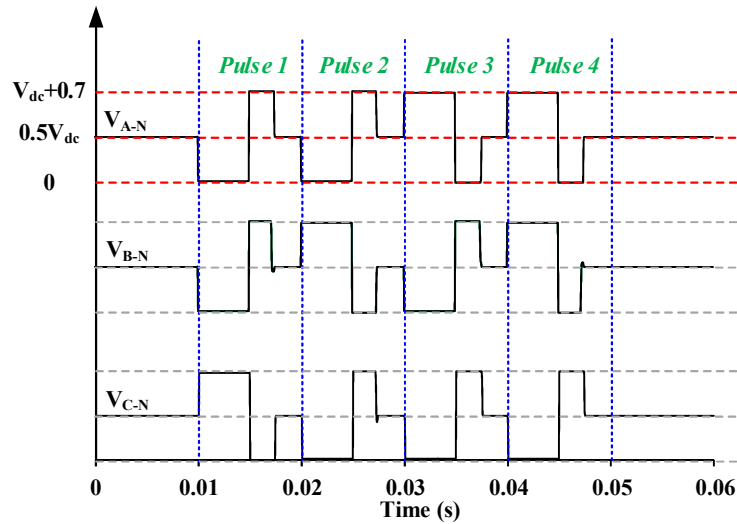


Fig. 2.15. Simulation results of terminal three-phase voltages based on the method in [LAI03].

## 2.4.6 Experimental Validation

In this section, 4 methods are tested by experiments. Same as simulation, each method is tested by one example with real rotor position at 120 degrees and the corresponding current and voltage responses are given.

### A. Three-phase currents based method

Firstly, the method in [SCH97] is tested by injecting 6 voltage pulses and the current responses are shown in Fig. 2.16. The peak values of the current responses are recorded and for position estimation. According to Section 2.4.1, the estimated rotor initial position  $\hat{\theta}_r$  is calculated as 123.23 degrees, the estimation error is 3.23 degrees. The experimental estimation performance is not as good as simulation. This is because the method [SCH97] is based on an ideal sinusoidal current response model. However, in the real drive system, the current response waveform against rotor position is not ideally sinusoidal containing harmonics and noises. Therefore, the experimental results could be affected.

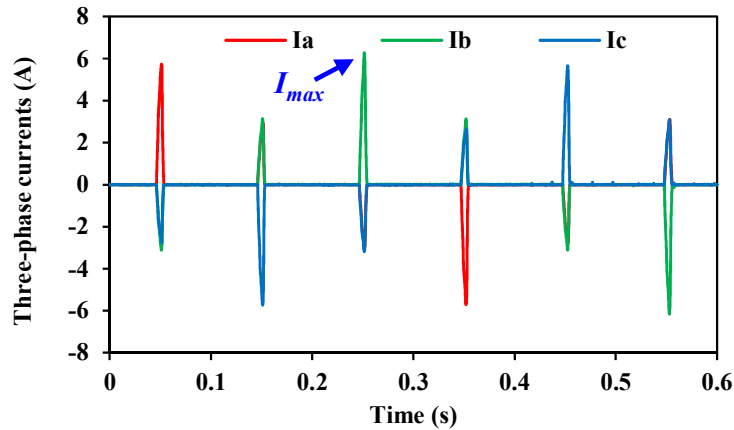


Fig. 2.16. Experiment results of three-phase current responses based on the method in [SCH97].

### B. DQ reference frame current based method

The method in [NAK00] is tested. 18 voltage pulses are injected and the peak values of each current response are recorded and shown in Fig. 2.17. The estimated position is 112.5 degrees with 7.5 degrees error. In practical system, due to existence of noise, although many voltage pulses are injected, the estimated position may not be as accurate as expected. Besides, pulse width modulation (PWM) strategies such as sinusoidal PWM (SPWM) and space vector PWM (SVPWM) are necessary for this method to generate the required voltage vectors as depicted in Fig. 2.8, which adds the control and implementation complexity in low cost applications.

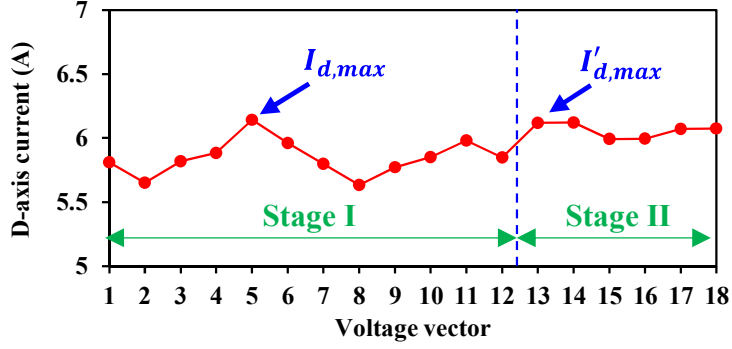


Fig. 2.17. Experiment results of recorded d-axis current based on the method in [NAK00].

### C. DC-link current based method

The method in [LEE06] is tested and the measured dc-link currents are shown in Fig. 2.18. In total, only 4 voltage pulses are injected and the dc-link current responses are recorded. Their peak values are compared and the rotor initial position is estimated at 120 degrees. [LEE06] selects voltage vectors based on results of former step so that only 4 pulses are required ideally.

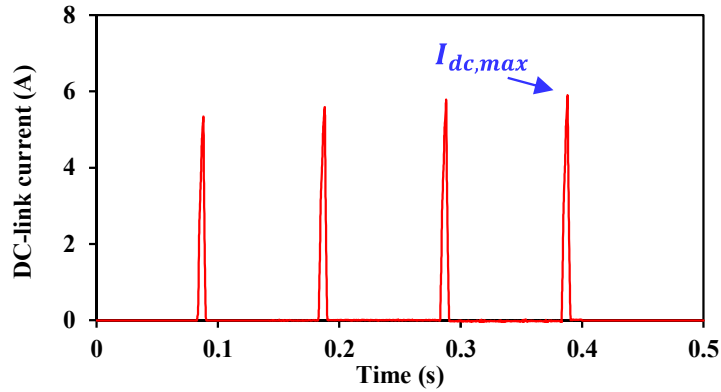


Fig. 2.18. Experiment results of recorded d-axis current based on the method in [LEE06].

### D. Three-phase terminal voltage based method

The method in [LAI03] is tested by measuring terminal three-phase voltages. The measured terminal three-phase voltages are shown in Fig. 2.19. After excitations, the terminal three-phase voltages are measured and the freewheeling times are compared. The estimated rotor initial position is 150 degrees with an estimation error of 30 degrees. After injecting in one phase, the responses of other two phases are used for position estimation, and therefore, more information can be obtained based on one injection so that only 4 pulses are required.

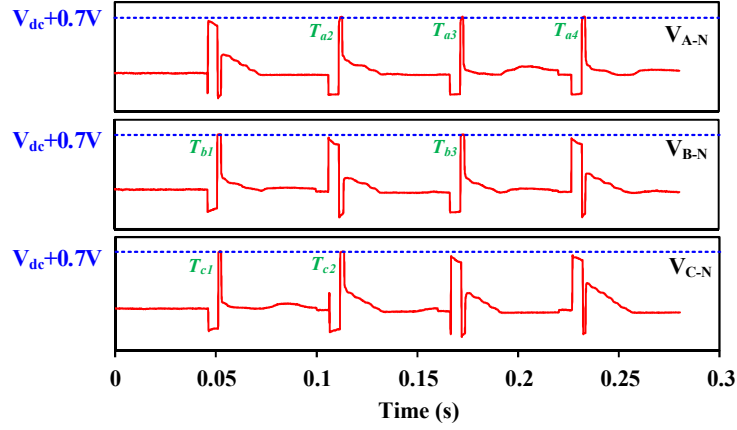


Fig. 2.19. Experiment results of terminal three-phase voltages based on the method in [LAI03].

## 2.4.7 Overall Comparison

In all, 4 conventional methods are implemented and validated through both simulation and experiment. The simulation and experiment estimation results are summarized in Table 2.1. In the tested case, both methods estimate rotor initial position correctly and are align with their claimed estimation performance.

TABLE 2.1  
ESTIMATION RESULTS

Method	Simulation		Experiment	
	$\hat{\theta}_r(^{\circ})$	Error( $^{\circ}$ )	$\hat{\theta}_r(^{\circ})$	Error( $^{\circ}$ )
[SCH97]	119.2074	0.8	123.23	2.23
[NAK00]	127.5	7.5	112.5	7.5
[LEE06]	120	0	120	0
[LAI03]	90	30	150	30

Furthermore, the overall estimation against rotor position is provided in Table 2.2. In Table 2.2, the overall estimation results at different rotor positions are given. Both estimation resolutions and maximum estimation errors are shown. First of all, all 4 methods have achieved their claimed estimation performance. Then, according to Table 2.2, it can be summarized that [SCH97] has the best estimation performance with the least estimation error, so that the starting torque can be maximized. [LEE06] requires the smallest number of pulses which minimize the time consumption and losses. [LEE06] only need one sensor which can be a better option in low cost applications. Only [NAK00] requires PWM strategy to generate vectors adding control

and implementation complexity. At last, in order to find out the most cost-effective method considering the estimation performance and cost together, a cost-effective index  $S$  is defined as:

$$S = (AE + ME) * N_p * N_s \quad (2.9)$$

where  $AE$  and  $ME$  are the average error and the maximum error, respectively.  $N_p$  is the required pulse number and  $N_s$  is the required sensor number. Apparently, a smallest number of  $S$  indicates the most cost-effective method. It is shown in Table 2.2 that the method in [LEE06] is the most cost-effective selection, since only one dc-link current sensor is used and an estimation resolution of 30 degrees can be achieved with 5 pulses. Moreover, this summarized comparison could provide a comprehensive guideline in the selection of rotor initial position estimation methods.

TABLE 2.2  
OVERALL COMPARISON

Method	[SCH97]	[NAK00]	[LEE06]	[LAI03]
Estimation resolution (degree)	<b><u>24</u></b>	30	30	60
Maximum estimation error (degree)	<b><u>15</u></b>	18	<b><u>15</u></b>	30
Required pulses	6	18	5	<b><u>4</u></b>
Current sensor	3	3	<b><u>1</u></b>	0
Voltage sensor	<b><u>0</u></b>	<b><u>0</u></b>	<b><u>0</u></b>	3
Requirement of PWM	<b><u>No</u></b>	Yes	<b><u>No</u></b>	<b><u>No</u></b>
Cost-effective index	392.4	1377	<b><u>112.5</u></b>	540

## 2.5 Proposed Simple Voltage Pulse Selection Strategy [WU20a]

As introduced in Section 2.3, the current response after injecting voltage pulse is given as:

$$I(t) = \frac{V_P}{R_{eq}} (1 - e^{-\frac{T_P}{L_{eq}/R_{eq}}}) \quad (2.10)$$

It is obvious that the magnitude and duration of the voltage pulse can affect the value of current response and therefore the estimation performance. It is worth noting that in this chapter, the DC-link voltage is assumed to be adjustable. Thus, in order to obtain a reliable estimation performance, it is necessary to develop a strategy to effectively select the magnitude and duration of voltage pulses, which has not been discussed in literature. In this part, the magnitude and duration of the voltage pulse are defined as  $V_P$  and  $T_P$ . Besides, for some applications with fixed DC-link voltage, only duration of voltage pulse is to be adjusted by following the proposed method.

### 2.5.1 Magnitude and Duration Selection

#### *A. Selection rules*

In this section, a simple voltage pulse selection strategy including duration and magnitude is presented. Initially, there are two design rules for selection:

The first rule is to limit the produced torque which may induce rotor movement and other undesired results including damage to rotor shaft and noise issues. Hence, a limitation of q-axis current, i.e.  $I_{q\_MAX}$ , should be given, depending on different applications. The first rule is associated with upper limitation during selection of  $V_P$  and  $T_P$ .

The second one is to make sure the current responses against rotor position are observable. The observable current responses guarantees a reliable estimation results and therefore a better start-up capability. The second rule is associated with lower limitation during selection of  $V_P$  and  $T_P$ .

#### *B. Selection of duration $T_P$*

For the same voltage pulse magnitude, the current response will vary with duration. The desirable duration of voltage pulses can be selected by considering the large differences between the current responses associated with 6 vector positions (and also 6 rotor positions). It is obvious that a larger difference can improve the performance and guarantee a reliable start-up of the motor. Therefore, selection of duration is to find out  $T_{P\_MAX}$  which generates the maximum difference between current responses.

First, considering two voltage pulses injected at two different positions, the corresponding current responses  $I_1$  and  $I_2$  are given in (2.11) and the difference  $\Delta I$  between two current responses is calculated by (2.12).

$$\begin{aligned} I_1(t) &= \frac{V_P}{R_{eq}} (1 - e^{-\frac{T_P}{\tau_{e1}}}) \\ I_2(t) &= \frac{V_P}{R_{eq}} (1 - e^{-\frac{T_P}{\tau_{e2}}}) \end{aligned} \quad (2.11)$$

$$\Delta I(t) = \frac{V_P}{R_{eq}} (e^{-\frac{T_P}{\tau_{e2}}} - e^{-\frac{T_P}{\tau_{e1}}}) \quad (2.12)$$

where  $\tau_{e1}$  and  $\tau_{e2}$  are the electrical time constants of two injection cases.  $R_{eq}$  is the equivalent resistance in the excitation circuit. The excitation configuration is referred to Fig. 2.6. The injection positions are different so that the saturation levels are different leading to different inductances and therefore electrical time constants. Then, by differential  $\Delta I(t)$  by time  $T_P$ , the theoretical duration that produces the maximum difference can be obtained by:

$$T_{P\_MAX} = \frac{\tau_{e1}\tau_{e2} \log \frac{\tau_{e2}}{\tau_{e1}}}{\tau_{e2} - \tau_{e1}} \quad (2.13)$$

By way of example, Fig. 2.20 illustrates that the maximum difference of two current responses occurs at  $T_{P\_MAX}$  according to (2.13).

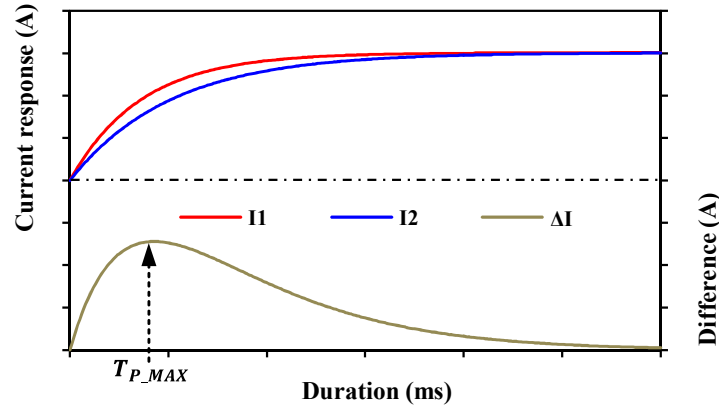


Fig. 2.20. Current responses and variation of current difference with duration. [WU20a]

However,  $T_{P\_MAX}$  in (2.13) is too complicated for practical use. Therefore, an approximation is used instead. Define  $\tau_{e2} = \tau_{e1} + \Delta\tau$ , for a small  $\Delta\tau$ ,  $T_{P\_MAX}$  can be approximated as  $T'_{P\_MAX}$  which is given by:

$$T'_{P\_MAX} = \frac{\tau_{e1} + \tau_{e2}}{2} \approx \tau_{eN} \quad (2.14)$$

Fig. 2.21 demonstrates the relationship between  $\Delta\tau$  and the difference between the theoretical duration  $T_{P\_MAX}$  and the approximated duration  $T'_{P\_MAX}$ . It is obvious that the difference between  $T_{P\_MAX}$  and  $T'_{P\_MAX}$  is relatively small. Hence, the approximated duration  $T'_{P\_MAX}$  can be used for easier implementation. Based on the above analyses, the duration  $T_p$  can be selected around the nominal electrical time constant  $\tau_{eN}$  in order to achieve the maximum current difference.

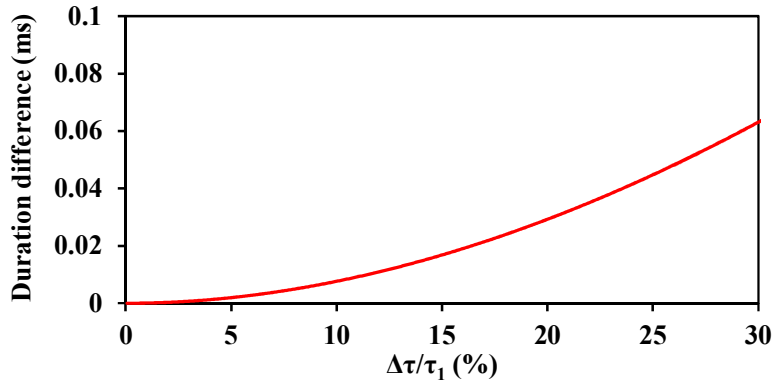


Fig. 2.21. Duration difference against  $\Delta\tau$ . [WU20a]

### C. Selection of magnitude $V_p$

For the magnitude of voltage pulses, there are two limitations,  $V_{p\_MAX}$  and  $V_{p\_MIN}$ , which should be determined for magnitude selection.

First, the upper limitation  $V_{p\_MAX}$  limits the torque produced by voltage injection. Since there will be a q-axis current induced, which generates the impulse torque during injection and may cause rotor rotating or shaft damage. Hence, the upper limitation of voltage pulse can be calculated based on the torque/q-axis current limitation and the rotor movement limitation.

#### (1) Torque/q-axis current limitation

As some applications are restricted with the q-axis current or torque, it is necessary to limit the maximum voltage pulse by:

$$\begin{aligned} \frac{V_p}{R_{eq}} = I &< I_{q\_MAX} \\ \downarrow \\ V_{P\_MAX\_1} &< R_{eq} I_{q\_MAX} \end{aligned} \quad (2.15)$$

In (2.15), a maximum q-axis current  $I_{q\_MAX}$  can be determined according to the requirement of real application. Furthermore, based on the selection of duration  $T_P$ , which is chosen around electrical time constant, a coefficient of 0.63 is applied to (2.16):

$$\frac{V_P}{R_{eq}}(1 - e^{-1}) = I \leq I_{q\_MAX} \quad (2.16)$$

$$V_{P\_MAX\_1} \leq \frac{R_{eq}I_{q\_MAX}}{(1-e^{-1})} \quad \text{i.e.} \quad V_{P\_MAX\_1} \leq \frac{R_{eq}I_{q\_MAX}}{0.63}$$

## (2) Rotor movement limitation

Apart from induced torque limitation, the rotor movement should also be limited. By neglecting load torque and friction, the rotor movement can be calculated as:

$$\theta_r = \frac{3P^2}{2J} \psi_m \frac{V_P}{R_{eq}} \left( \frac{T_P^2}{2} - \left( \frac{L_{eq}}{R_{eq}} \right)^2 e^{-\frac{T_P}{L_{eq}/R_{eq}}} \right) \quad (2.17)$$

where  $J$  is the inertia,  $P$  is the number of pole pairs,  $\theta_r$  is the electrical rotor position,  $\psi_m$  is the permanent magnet flux-linkage. Furthermore, based on the selection of duration  $T_P$ , which is chosen around electrical time constant, (2.17) can be updated as:

$$\theta_r \approx \frac{1}{5} \frac{p^2}{J} \psi_m \frac{V_P}{R_{eq}} \left( \frac{L_{eq}}{R_{eq}} \right)^2 \quad (2.18)$$

The induced rotor movement is limited as:

$$\theta_r \approx \frac{1}{5} \frac{p^2}{J} \psi_m \frac{V_P}{R_{eq}} \left( \frac{L_{eq}}{R_{eq}} \right)^2 \leq \theta_{max} \quad (2.19)$$

Therefore, the maximum voltage pulse is:

$$V_{P\_MAX\_2} \leq 5 \frac{JR_{eq}}{p^2 \psi_m} \left( \frac{R_{eq}}{J_{eq}} \right)^2 \theta_{max} \quad (2.20)$$

It is worth mentioning that in the derivation of rotor movement, the load torque and friction are neglected, the induced rotor movement could be actually larger than calculated value.

At last, the upper limitation of voltage pulse magnitude is given as:

$$V_{P\_MAX} = \min (V_{P\_MAX\_1}, V_{P\_MAX\_2}) \quad (2.21)$$

Next, the lower limitation  $V_{P\_MIN}$  is defined to guarantee the rotor initial position estimation reliable. According to the magnetic saturation effect, in order to identify the polarity, enough voltage pulse should be given to produce sufficient armature reaction to produce an observable difference between north and south poles during polarity identifications. Otherwise, a reverse starting can happen with 180 degrees position error. Therefore, it is necessary to determine an appropriate  $V_{P\_MIN}$  during the selection of voltage pulse magnitude. In real application, during estimation, the current responses recorded in the controllers could be different from the actual values as shown by (2.22). This current recording error can affect the estimation performance.

$$I_{record} = I_{real} + I_{error} \quad (2.22)$$

The current recording error  $I_{error}$  consists of several components and can be represented as:

$$I_{error} = \varepsilon_k + \varepsilon_0 + \varepsilon_{ADC} + \varepsilon_n + \varepsilon_d + \varepsilon_{V_{dc}} \quad (2.23)$$

where  $\varepsilon_k$  is the measurement scaling error,  $\varepsilon_0$  is the measurement DC offset error and  $\varepsilon_{ADC}$  is the error due to ADC quantization.  $\varepsilon_n$  and  $\varepsilon_d$  are errors caused by noise and disturbance, respectively.  $\varepsilon_{V_{dc}}$  is the error caused by DC-link voltage variation. The value of  $I_{error}$  should be determined based on the hardware. A simple way to determine the maximum value of  $I_{error}$  is introduced here. Several voltage pulses with same magnitude and duration are injected at the same position, the difference between the maximum and average values of current responses are recorded and  $I_{error}$  can be calculated by

$$I_{error} \geq 2(I_{MAX} - I_{MEAN}) \quad (2.24)$$

Then, as shown in (2.25), two opposite voltage pulses are injected into one position, the difference between two current responses is recorded and compared with  $I_{error}$ .

$$\left| |I(V_{P\_MIN})| - |I(-V_{P\_MIN})| \right| = \Delta I > I_{error} \quad (2.25)$$

According to (2.24) and (2.25), the minimum limitation of voltage pulse magnitude  $V_{P\_MIN}$  should be selected by ensuring  $\Delta I > I_{error}$ .

### 2.5.2 Reliable Selection Area (RSA)

From the determined duration and magnitude of the voltage pulse, a reliable selection area (RSA) can be obtained as shown in Fig. 2.22. Selecting voltage pulse within this RSA, a more reliable and effective estimation performance can be guaranteed.

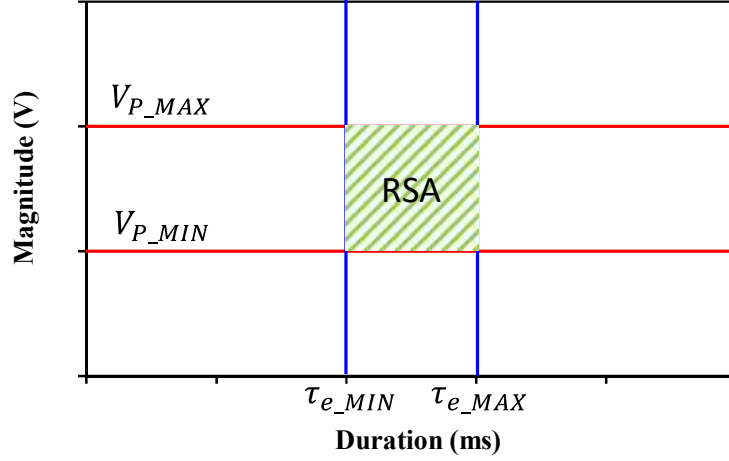


Fig. 2.22. Reliable selection area. [WU20a]

For pulse magnitude, it can be selected between  $V_{p\_MIN}$  and  $V_{p\_MAX}$ . It is suggested to select the pulse duration around  $\tau_{eN}$  first. However, considering the variation of electrical time constant against rotor position, i.e. inductance changes, rather than to select a single duration value it is better to select a duration range between the maximum and minimum electrical time constants given by (2.26):

$$\begin{aligned}\tau_{e\_MAX} &= \frac{L_{MAX}}{R_{eq}} \\ \tau_{e\_MIN} &= \frac{L_{MIN}}{R_{eq}}\end{aligned}\tag{2.26}$$

where  $L_{MAX}$  and  $L_{MIN}$  are the maximum and minimum inductances respectively over all rotor positions. These two time constants can be obtained easily based on FE analyses or experiments according to current limitation.

### 2.5.3 Experimental Validation

Based on a SPM-I test platform, the experiments are carried out to validate the proposed voltage pulse selection strategy and calculate the RSA region.

### A. Selection of magnitude $V_p$

As aforementioned, for the magnitude of voltage pulses, there are two limitations,  $V_{P\_MAX}$  and  $V_{P\_MIN}$ , that need to be determined for selection. Firstly, the upper limitation  $V_{P\_MAX}$  can be defined based on the machine parameters and the current limitation. At first, the current limitation is set as 6A. Then, the calculated upper limitation of voltage pulse magnitude is derived as:

$$V_{P\_MAX\_1} < \frac{R_{eq} I_{q\_MAX}}{0.63} \approx 60V \quad (2.27)$$

The rotor movement limitation  $\theta_{max}$  is set as 1 degree, then the calculated upper limitation of voltage pulse magnitude is derived as:

$$V_{P\_MAX\_2} \leq 5 \frac{J R_{eq}}{P^2 \psi_m} \left( \frac{R_{eq}}{L_{eq}} \right)^2 \theta_{max} \approx 130V \quad (2.28)$$

Therefore, the finalised upper limitation of voltage pulse magnitude is selected as 60V.

For the lower limitation  $V_{P\_MIN}$ , the current error  $I_{error}$  needs to be determined firstly. Several voltage pulses with the same magnitude and duration are injected into the same position as shown in Fig. 2.23. In Fig. 2.23, the blue line indicates the average value of all the peak values. The difference between the mean value and the maximum value gives the measurement error  $I_{error}$ .

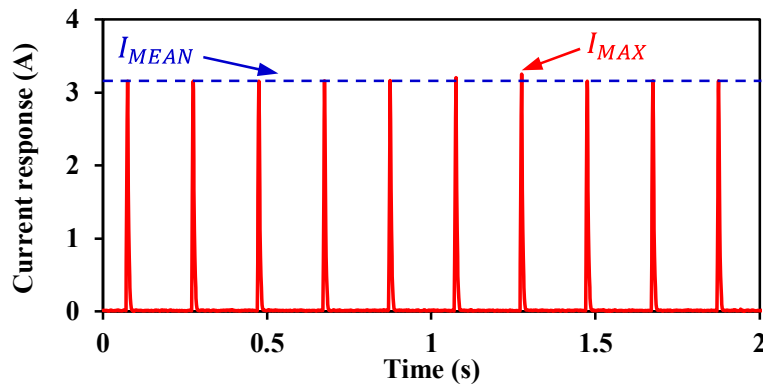


Fig. 2.23. Determination of current error  $I_{error}$ . [WU20a]

The current error can be determined from (2.24), as:

$$I_{error} = 2(I_{MAX} - I_{MEAN}) = 0.1A \quad (2.29)$$

The measured current difference against voltage pulse magnitude is shown in Fig. 2.24. According to  $I_{error}$ , the difference below 0.1A is unreliable. Thus, from (2.25), the lower limitation  $V_{P\_MIN}$  can be determined as 30V.

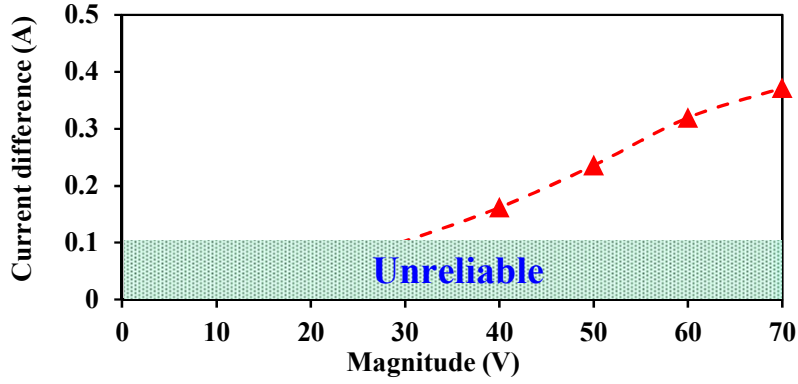


Fig. 2.24. Current difference against voltage pulse magnitude  $V_P$ . [WU20a]

### B. Selection of duration $T_P$

Referring to analyses before, two opposite voltage pulses with the same magnitude are injected at the same position. Fig. 2.25 illustrates the analytically calculated and measured variations of current response difference against voltage pulse duration. The analytical results are based on (2.11) and (2.12). It can be seen that the experimental results match well with analytical results. For both analytical and experimental results, a larger current difference can be obtained within the green dashed circle. Hence, according to experimental results,  $\tau_{e\_MAX}$  and  $\tau_{e\_MIN}$  can be determined as 4ms and 6ms. It is worth noting that although selection of duration outside the green dashed circle is also acceptable as long as the difference could be larger than the current error, better and more reliable performance could be obtained by choosing the duration  $T_P$  within the green dashed circle which has the largest current response difference.

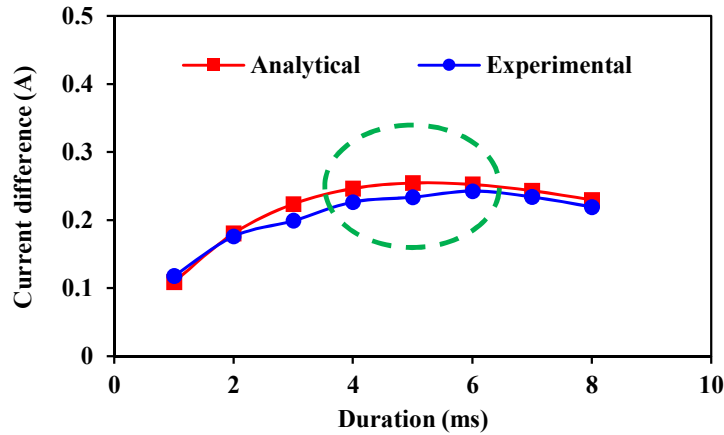


Fig. 2.25. Current difference against voltage pulse duration  $T_P$ . [WU20a]

### C. Reliable selection area

From the results of previous sections,  $V_{P\_MAX}$ ,  $V_{P\_MIN}$ ,  $\tau_{e\_MAX}$  and  $\tau_{e\_MIN}$  are obtained. By utilizing these four parameters, a reliable selection area RSA can be depicted, as presented in Fig. 2.26. Based on the estimation method described before, several tests are carried out to investigate the rotor initial position estimation performance. Different voltage pulse magnitude and duration combinations are considered, both inside and outside RSA. In Fig. 2.26, the blue circles indicate the acceptable estimation performance with correct estimation result and allowable q-axis current produced. Otherwise, the estimation performance is un-acceptable marking with a red cross.

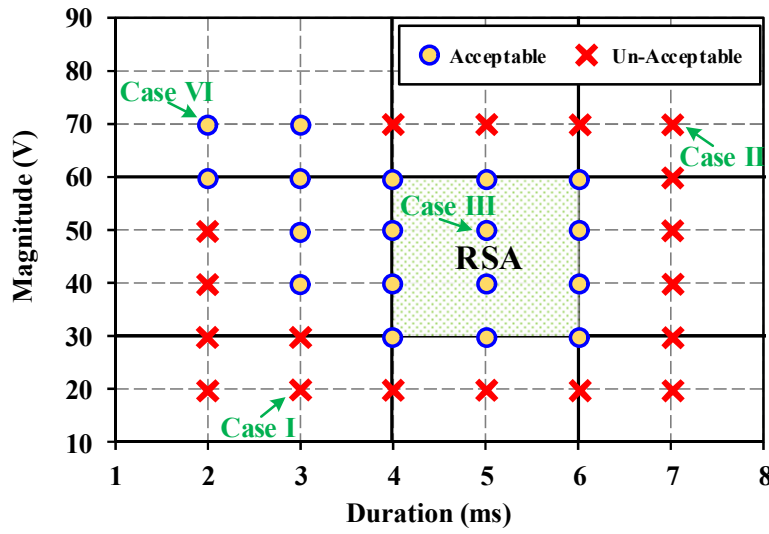


Fig. 2.26. Reliable selection area. [WU20a]

Besides, from Fig. 2.26, four different cases are chosen to illustrate the measured results when selected voltage pulse is inside and outside RSA, Fig. 2.27(a)-(d). In Fig. 2.27, according to the real rotor initial position (117 electrical degrees), phase B current response of the 3<sup>rd</sup> pulse should be the largest, otherwise, the estimation will be incorrect. Besides, the produced q-axis current should not exceed 6A.

Firstly, selected voltage pulses are outside RSA at a lower level which will result in a wrong estimation. An example is given in Fig. 2.27(a), the current response of the 5<sup>th</sup> pulse is the largest which is wrong. Then, selected voltage pulses are outside RSA at a higher level, although the estimation could be correct, the produced q-axis current will exceed the limit. For case II in Fig. 2.27(b), by calculation, the produced q-axis current (6.38A) is over the limit. Next, from case III in Fig. 2.27(c), selected voltage pulses are inside RSA, estimation performances are all acceptable. At last, it is worth mentioning that the proposed RSA is a simple and approximate selection strategy. From case VI in Fig. 2.27(d), although voltage pulse

is selected outside RSA, an acceptable estimation performance can also be obtained. Nevertheless, it can be concluded that by selecting the voltage pulse within RSA, reliable estimation performance is guaranteed.

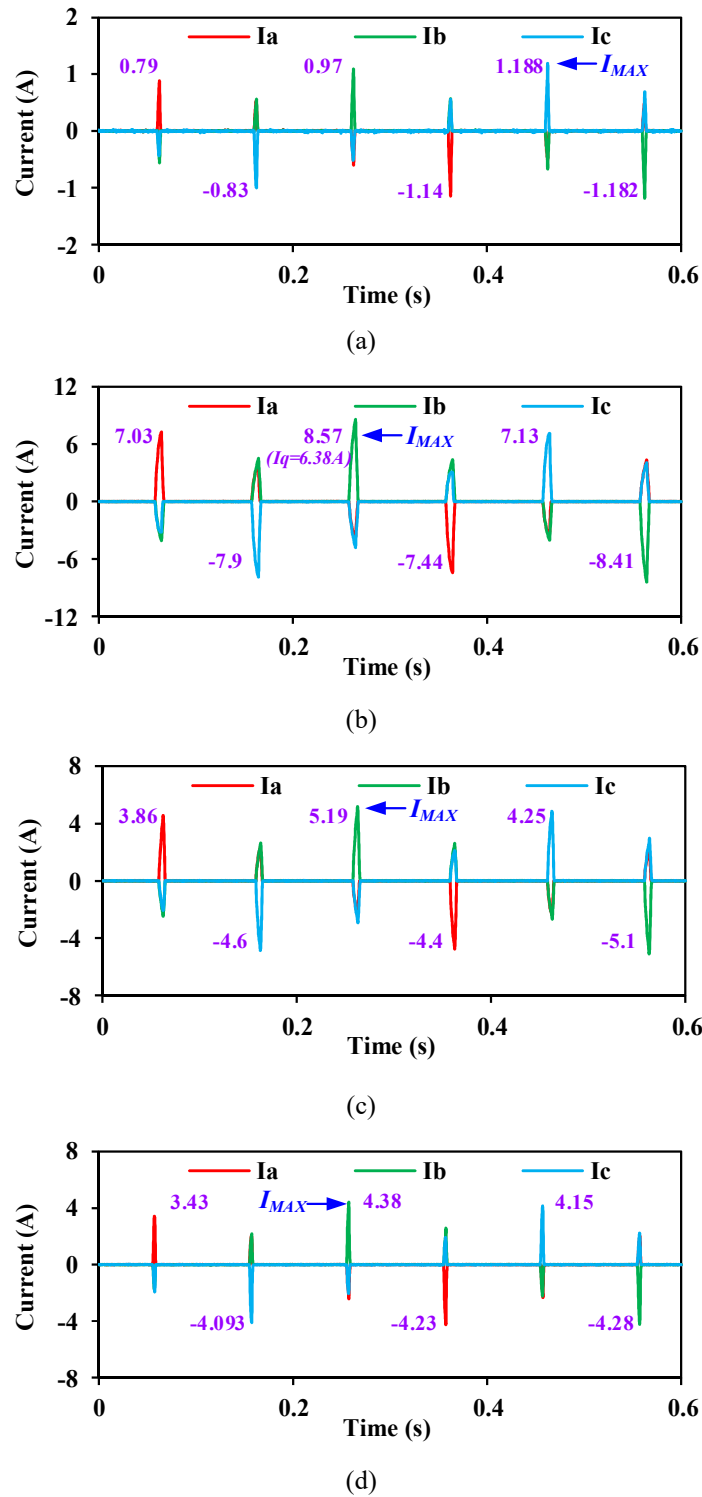


Fig. 2.27. Measured current responses of typical injections. (a) Case I with wrong estimation outside RSA. (b) Case II with q-axis current over limit outside RSA. (c) Case III with acceptable estimation inside RSA (d) Case IV with acceptable estimation outside RSA. [WU20a]

## 2.5.4 Summary

For rotor initial position estimation, voltage pulse injection based methods are a popular option. A simple voltage pulse selection strategy is proposed and introduced, besides a reliable selection area (RSA) is obtained. The proposed RSA provides an effective and simple way to select the duration and magnitude of voltage pulses for rotor initial position estimation. By selecting voltage pulse within RSA, more reliable performance can be achieved, as validated by experiments. It is worth mentioning that based on the experiment results, acceptable estimation can also be obtained if voltage pulse is selected outside the RSA, and hence the selection area may not be fully utilized. Therefore, the overall selection of voltage pulse with all different combinations of magnitude and duration is investigated and a so-called “Extended RSA” is further developed in the next section.

## 2.6 Overall Voltage Pulse Selection Investigation

As discussed in Section 2.5, a simple voltage pulse selection strategy is introduced. However, it is found that reliable estimation results can also be obtained outside of the reliable selection area (RSA). Therefore, in this section, outside the RSA, all the other combinations of magnitude and duration are investigated by ways of simulation and experiment. In the investigation, several constraints are considered and defined initially in order to fulfil the requirement depends on the applications and obtain reliable results. In the investigation, all the parameters are based on the prototype machine and the practical test platform given in Appendix.

### 2.6.1 Constraints

#### *A. Reliable estimation*

A reliable estimation should be defined at first. By testing with different sets of magnitude and duration of voltage pulse, the current differences are calculated and compared with measurement noise. If the current difference is larger than the noise and gives the right result, then it is regarded as correct and reliable.

#### *B. Rotor movement constraints*

In the selection, the maximum rotor movement is considered which happens when voltage pulse is injected at q-axis. The rotor movement can be calculated as follows:

$$\theta_r = \frac{3P}{2J} P \psi_m \frac{V_P}{R_{eq}} \left( \frac{T_P^2}{2} - \left( \frac{L_{eq}}{R_{eq}} \right)^2 e^{-\frac{T_P}{L_{eq}/R_{eq}}} \right) \quad (2.30)$$

### C. Maximum q-axis current

As introduced in Section 2.5, the induced q-axis current should be limited depends on applications. Hence, in the simulation, for each set of magnitude and duration, the induced q-axis current is calculated by (2.31) and a maximum q-axis current limitation curve can be obtained.

$$i_q(t) = \frac{V_P}{R_{eq}} \left( 1 - e^{-\frac{T_P}{L_{eq}/R_{eq}}} \right) \quad (2.31)$$

## 2.6.2 Extended Reliable Selection Area (ESRA)

### A. Simulation results

Based on the constraints introduced in previous section, simulation tests of different combinations of magnitude and duration are carried out and a reliable estimation map against voltage pulse magnitude and duration can be obtained as shown in Fig. 2.28.

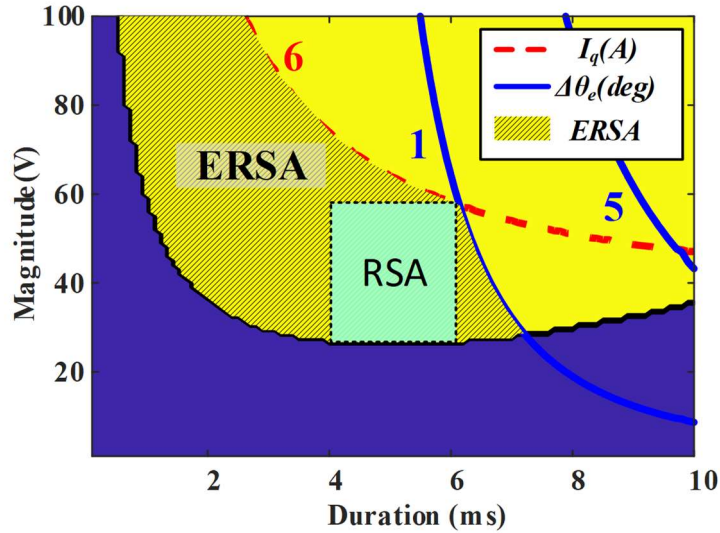


Fig. 2.28. Extended reliable selection area.

In Fig.2.28, the yellow part is the reliable estimation area where the estimation is correct. The induced q-axis current curve is shown in the red dashed line and the rotor movement is shown in the blue solid line which both limit the voltage pulse selection area. Then, an intersection is shown in the shadow area indicating the reliable selection area. It can be seen

that the Reliable Selection Area (RSA) shown in green block is included in this intersected area. Hence, this intersected area is called “Extended Reliable Selection Area (ERSA)”.

### B. Experimental results

Fig. 2.29 shows both the simulation and experiment results of voltage pulse selection results.

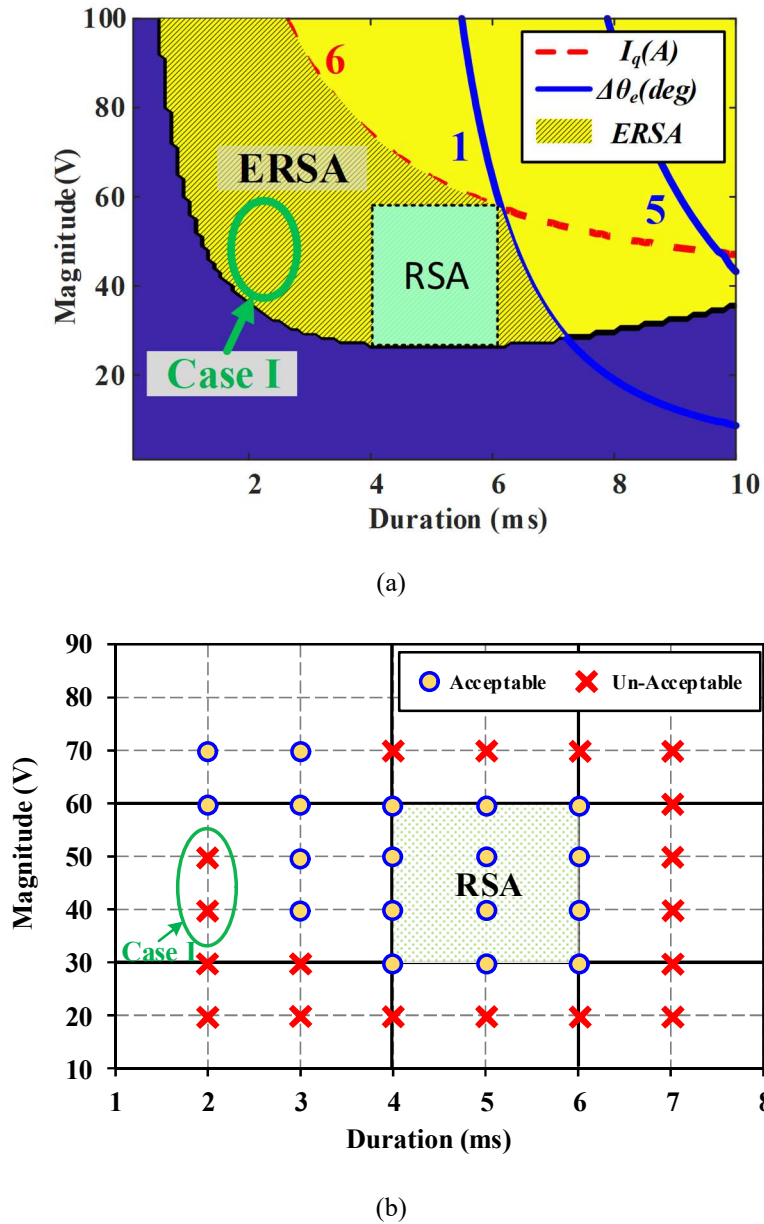


Fig. 2.29. Voltage pulse selection area. (a) Simulation results. (b) Experimental results.

As shown in Fig. 2.29(a) and (b), the simulation and experiment results do not align perfectly with each other. The main different case between the simulation and experiment results is shown within the green circle. It is found out that unreliable results are obtained in the experiment whereas reliable results are obtained in the simulation. This happens when the duration is relatively small. There are two main reasons:

(1) Limited sampling frequency: In the practical system, it is known that as duration decreases, the sampled points become less which affect the estimation performance.

(2) Decayed current response: In the practical system, due to the existing DC-link capacitance, the applied voltage pulse will be decayed and therefore the current response will be influenced as well. Since the DC-link capacitance and resistance forms as low-pass filter, current response with smaller duration will be more decayed.

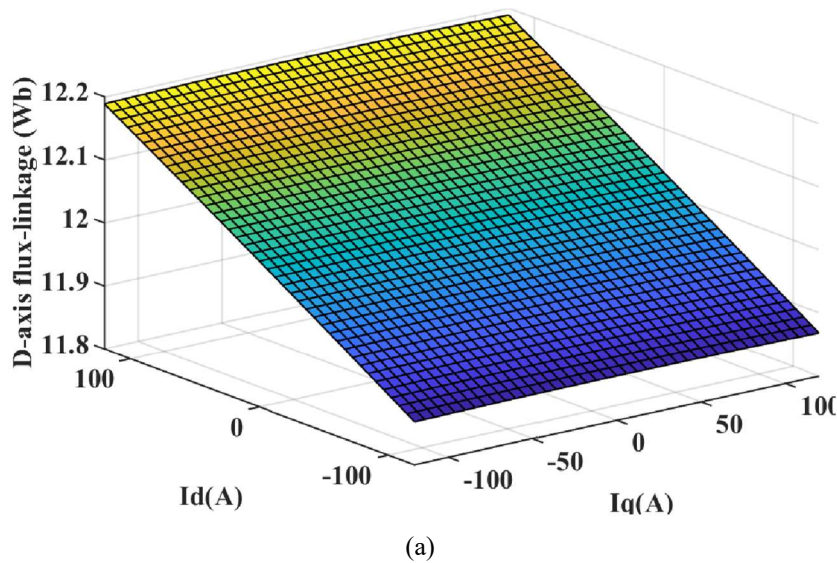
Similar to simulation results, for the experiment results shown in Fig. 2.29(b), it is also found that the proposed reliable selection area (RSA) is included in the extended reliable selection area (ERSA), which aligns with the discussion in the previous section. Although some areas are not utilized, the proposed RSA provides a simple and approximate strategy for voltage pulse selection.

### 2.6.3 Application of ERSa in Siemens Wind Power PM Generators

In order to verify the effectiveness and capability of rotor initial position estimation, the voltage pulse selection investigation is further extended to the Siemens 3MW wind power PM generator. The parameters and FE simulation results of the tested 3MW PM generator are given in Appendix. Due to limitation of practical test, the investigation is mainly focused on the simulation by FEA and Matlab/Simulink software.

#### A. Co-simulation model

Initially, a FE based 3MW PM generator model is built. In order to save the simulation time, flux-linkage and inductance against current information are calculated by FE software at first and are made as look-up table. Fig. 2.30 shows the flux variations against current in dq-axis.



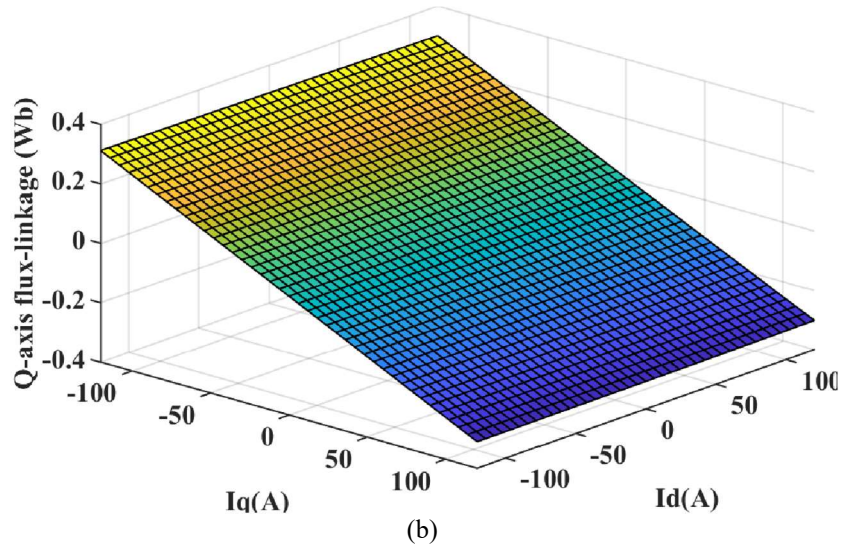


Fig. 2.30. Flux-linkages against current map. (a) D-axis flux-linkage. (b) Q-axis flux-linkage.

Furthermore, based on the relationship between flux and current, the inductances in dq-axis can be calculated as well. The calculated inductances in dq-axis are shown in Fig. 2.31.

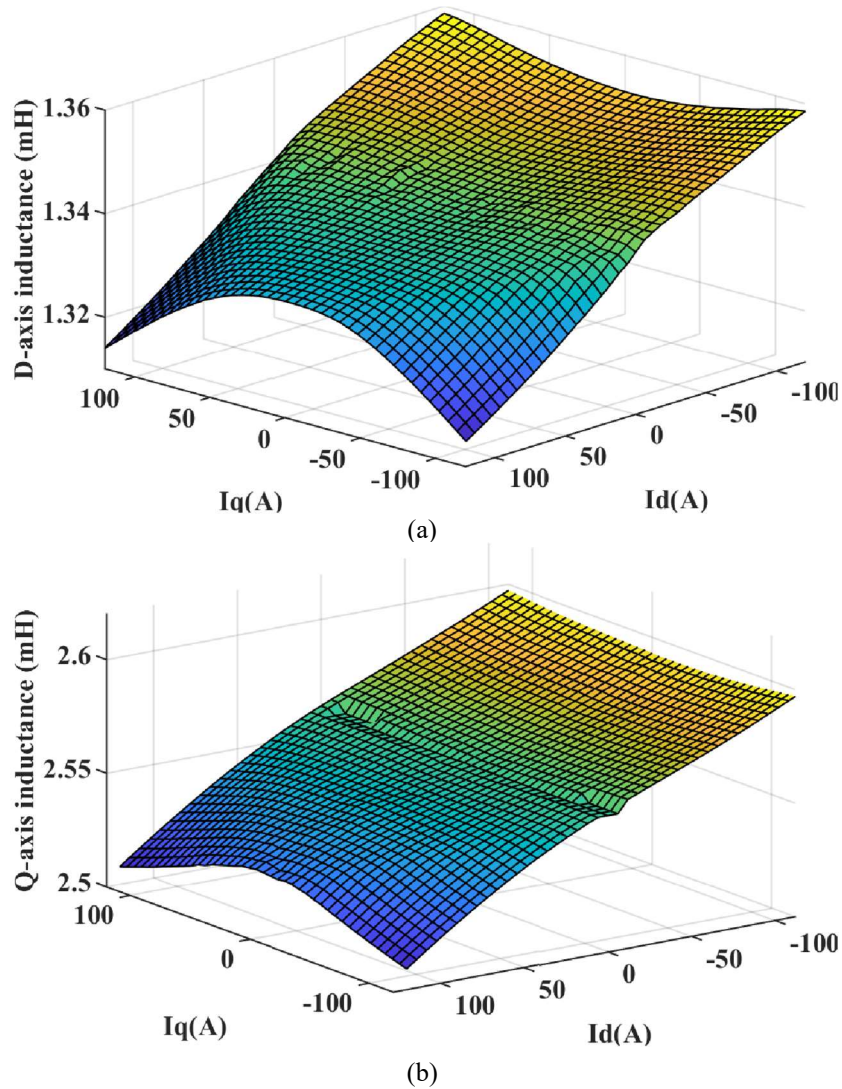


Fig. 2.31. Inductance against current map. (a) D-axis inductance. (b) Q-axis inductance.

Then, based on the FE results, the 3MW PM machine model is built in Matlab/Simulink environment incorporating with the inverter and control circuit parts. The simulation model block diagram is shown in Fig. 2.32.

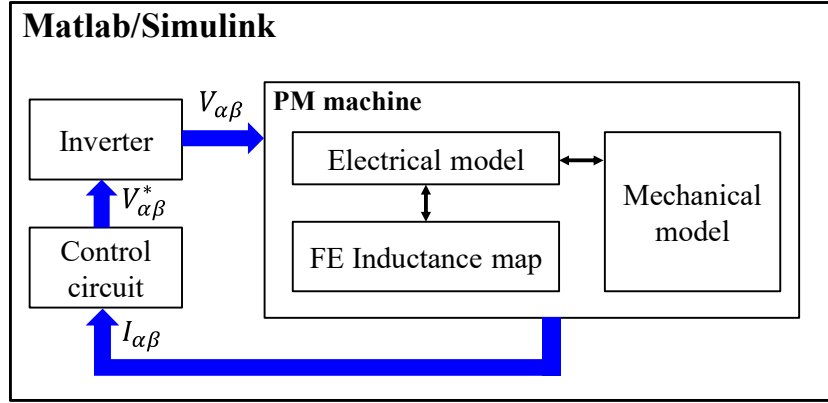
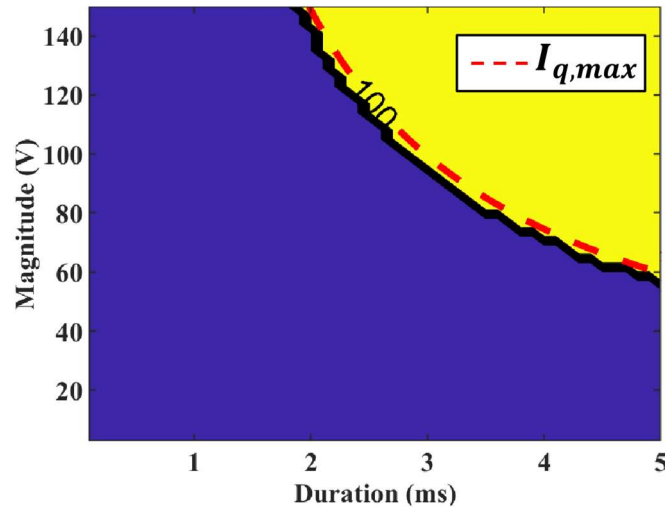


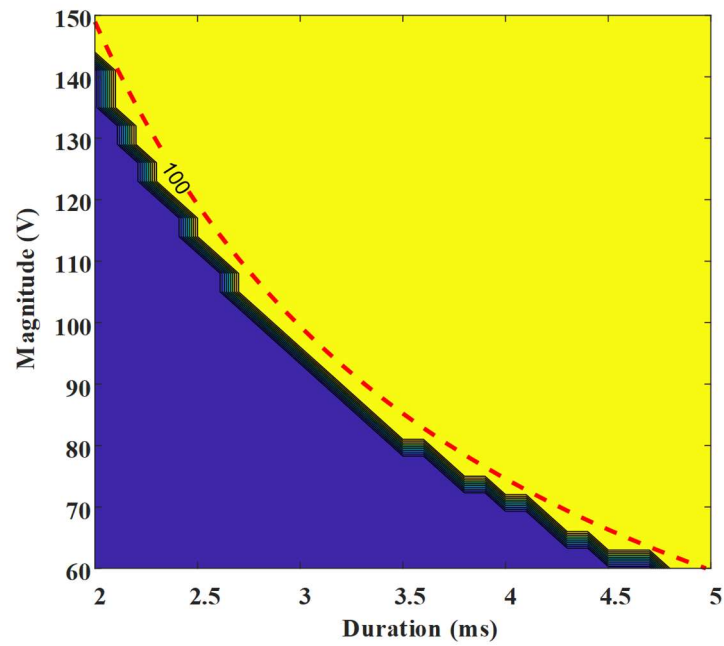
Fig. 2.32. FE based simulation model.

### B. Voltage pulse selection area

Based on the built model of 3MW PM generator, voltage pulse selection area can be investigated. For the 3MW PM generator, the induced q-axis current is limited by 100A and the maximum measurement error of current is 1A. Then, the voltage pulse selection area is calculated and depicted in Fig. 2.33.



(a)



(b)

Fig. 2.33. Voltage pulse selection area for 3MW PM generator. (a) Overall. (b) Zoom in.

For the 3MW PM generators, due to very large inertia, rotor movement will only be induced when duration goes beyond 50ms, and therefore, the rotor movement constraint is not included in Fig. 2.33. It can be seen that the intersection between current limitation and correct estimation results is quite small but still exists. Compared with 3kW PM generator, the much smaller selection area of 3MW PM generator is caused by several reasons:

- a. Large current measurement error (1A)
- b. Small phase resistance ( $6\text{m}\Omega$ )
  - A small resistance will cause large current induced including q-axis current so that to be limited.
- c. Small current limitation (100A)
  - The current limitation is set as 2% of the rated current.
- d. Small inductance variation against rotor position
  - Due to large airgap and open slot, the magnetic saturation effect may be less on the 3MW PM generator than 3kW PM generator.
  - The limited current will restrict the armature reaction.

## 2.7 Conclusion

In this chapter, the short-pulse-injection-based rotor initial position estimation is introduced. Based on the magnetic saturation effect, several conventional methods are illustrated and validated. Since this type of methods relies on injecting voltage pulse to detect the rotor initial position, the selection of voltage pulse should be considered which will influence the estimation performance. Hence, a simple voltage pulse selection strategy is presented in this chapter and a reliable selection area (RSA) is obtained. Selection voltage pulse within this area, reliable estimation performance can be obtained. Furthermore, it is found out that outside the RSA, there are also some areas that provide reliable estimation results. Thus, in order to fully utilize the selection area, voltage pulse selection outside the RSA is also investigated and a so called “extended reliable selection area (ERSA)” is obtained which actually contains the RSA. The effectiveness of both RSA and ERSA is validated by experiment results. Moreover, the voltage pulse selection is further extended to the Siemens 3MW Wind Power PM Generator. For 3MW PM generators, it is found out that the available selection area is relatively small compared with the 3kW PM generator.

# CHAPTER 3

## ROTOR INITIAL POSITION ESTIMATION METHOD BASED ON THREE PHASE CURRENT

### 3.1 Introduction

Based on the magnetic saturation effect, several short-pulse-injection-based methods [SCH97][NAK00][LAI03][LEE06][CHA09] are proposed for SPMs, which can be categorized as current-response-based and voltage-response-based methods. For current-response-based methods, in [SCH97], 6 voltage pulses are injected into stator windings, the current responses in ABC reference frame is used to estimate the rotor initial position. This method offers a 30-degree resolution but consumes longer execution time due to 6 pulses. For [NAK00], the estimated d-axis current is used to estimate the rotor initial position with a 7.5-degree resolution. However, a large number of voltage pulses are necessary and the estimation resolution may not be guaranteed. In [LEE06], the rotor position is determined by utilizing dc-link current with a 30-degree resolution. For voltage-response-based methods, [LAI03] estimates rotor initial position by comparing freewheeling time using three voltage sensors with a 60-degree resolution. [CHA09] utilizes both freewheeling period and dc-link current to determine the rotor initial position. A 30-degree resolution is achieved at the cost of 2 voltage sensors and 1 dc-link current sensor. For these conventional methods, in order to determine rotor initial position with an acceptable estimation resolution, many pulses or extra sensors are necessary, which may increase the cost and complexity to the sensorless drive system.

In this chapter, a new simplified short-pulse-injection-based rotor initial position estimation method for SPMs is proposed. The proposed method shows more effective estimation performance than conventional methods by adopting three novel strategies. The first one is the utilization of three-phase current responses after one pulse while conventional methods only use the injected phase current. For the second aspect, conventional methods inject voltage pulses at some fixed positions, e.g. 0, 60, 120, 180, 240, 300 degrees, some of which are redundant. The proposed method selects injection position based on previous injection results in way of closed-loop selection. Based on first two strategies, the estimation process is simplified with only three pulses while achieving the desired estimation performance with at least 30-degree resolution at no cost of extra sensors.

The third one is the proposed boundary detection strategy (BDS). A so-called ‘boundary case’ is considered when the rotor magnetic pole locates around the boundary of two adjacent sectors resulting in low SNR current responses for estimation. For conventional methods which do not consider the boundary case, the estimation performance could be deteriorated. In order to solve this, either high voltage pulse level or extra pulse injection are required leading to extra complexity and loss to the system. In this chapter, a simple boundary detection strategy is introduced to solve the issue which improves the estimation performance. Furthermore, the concept of ‘boundary width’ is proposed and by selecting a proper boundary width during boundary detection, the estimation resolution can be further improved to 15 degrees.

In this Chapter, firstly, the principle of the proposed method is illustrated in detail including the utilization of three phase current responses and the proposed voltage pulse selection process. Then, the proposed boundary detection strategy is presented. At last, experimental results are given to verify the effectiveness of the proposed method and followed by the conclusion.

This chapter is based on the paper:

[WU20c] X. M. Wu, Z. Q. Zhu, and Z. Y. Wu, “A novel rotor initial position estimation method for surface-mounted permanent magnet synchronous machine,” submitted to *IEEE Transactions on Energy Conversion*.

## 3.2 Utilization of Three Phase Currents

The first major novel strategy of the proposed method is the utilization of three-phase current responses after one voltage pulse is injected. The principle of three-phase current utilization is illustrated in this section.

For a symmetrical three-phase PM machine, assuming one voltage pulse is injected in phase A, the three-phase current responses can be represented as:

$$\begin{aligned} i_A(t) &= \frac{V_A}{R_A} \left( 1 - e^{-\frac{t}{L_A/R_A}} \right) \\ i_B(t) &= \frac{V_B}{R_B} \left( 1 - e^{-\frac{t}{L_B/R_B}} \right) \\ i_C(t) &= \frac{V_C}{R_C} \left( 1 - e^{-\frac{t}{L_C/R_C}} \right) \end{aligned} \quad (3.1)$$

where  $V_A$ ,  $V_B$  and  $V_C$  are the phase voltages across three-phase windings.  $L_A$ ,  $L_B$  and  $L_C$  are the self-inductances of three-phase windings.  $R_A$ ,  $R_B$  and  $R_C$  are the phase resistances of three-phase windings.

For the three-phase current responses, the phase A current is called “Primary current response” since the voltage pulse is injected in phase A with the largest amplitude of current response. The phase B and C currents are called “Secondary current responses”. Then, (3.1) is re-write as:

$$\begin{aligned} i_A^P(t) &= \frac{V_A}{R} \left( 1 - e^{-\frac{t}{L_A/R}} \right) \\ i_B^S(t) &= \frac{V_B}{R} \left( 1 - e^{-\frac{t}{L_B/R}} \right) \\ i_C^S(t) &= \frac{V_C}{R} \left( 1 - e^{-\frac{t}{L_C/R}} \right) \end{aligned} \quad (3.2)$$

where the sign “*P*” indicates the primary current response and “*S*” indicates the secondary current response.

For conventional methods, only the current of the injected phase, i.e. primary current response, is recorded and used for estimation. Therefore, several voltage pulses are necessary to be injected so that three-phase current responses can be obtained. However, as shown in (3.2) currents of the other two phases, i.e. secondary current responses, also contain the rotor initial position information which can be used for position estimation.

An experimental example is given in Fig. 3.1. The rotor initial position is at 41 degrees and one voltage pulse is injected to phase A. The three phase current responses are shown in Fig. 3.1. Apart from phase A current (primary current response), the other two-phase currents (secondary current responses) can be utilized as well. The peak value of the phase C current is larger than that of the phase B current, which indicates the rotor magnetic pole is closer to phase C than phase B which aligns with the real rotor position.

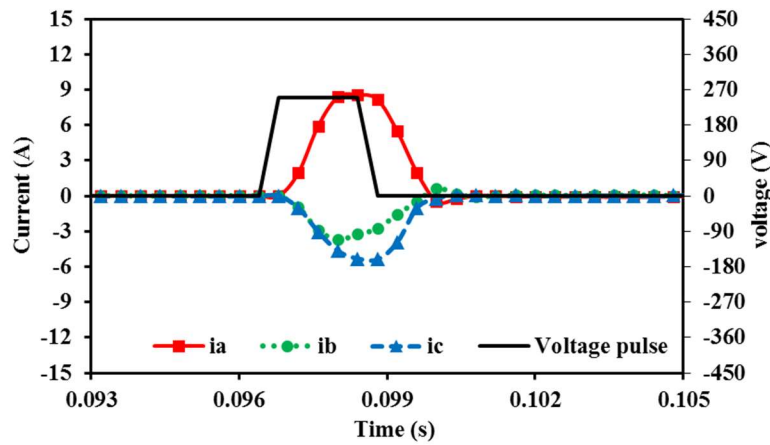


Fig. 3.1. Experimental example of three-phase current utilization. [WU20c]

Furthermore, the mathematic model of the three-phase current responses associated with rotor position can be derived. Assuming one voltage pulse is injected to phase A, since the duration is small, the three-phase current responses can be modelled as:

$$\begin{aligned} i_A^P(t) &= I_m(L_0 + L_2 \cos(2\theta_r)) \\ i_B^S(t) &= -I_m \left( \frac{1}{2}L_0 + L_2 \cos \left( 2 \left( \theta_r + \frac{\pi}{6} \right) \right) \right) \\ i_C^S(t) &= -I_m \left( \frac{1}{2}L_0 + L_2 \cos \left( 2 \left( \theta_r - \frac{\pi}{6} \right) \right) \right) \end{aligned} \quad (3.3)$$

where  $I_m = \frac{4V_{dc}t}{9(L_0^2 - L_2^2)}$ .  $V_{dc}$  is amplitude of the DC-link voltage,  $t$  is the duration time,  $L_0$  and  $L_2$  are the amplitudes of the dc and 2<sup>nd</sup> order harmonic components of three-phase self-inductances.

From (3.3), the amplitude of dc component of primary current response is twice of the secondary current response one. Nevertheless, it is worth noting that the amplitude of the 2<sup>nd</sup> order harmonic component is the same for both primary and secondary current responses.

Fig. 3.2 shows the measured results of three-phase current responses. Voltage pulse is injected at phase A and the three-phase current responses at different rotor position are measured and given in Fig. 3.2. Furthermore, in Fig. 3.3 the harmonic spectra of three-phase current responses is also given. Clearly, the measured results match well with (3.3), and apart from primary current response ( $i_A^P$ ), the two secondary current responses ( $i_B^S$  and  $i_C^S$ ) both vary with rotor position. The 2<sup>nd</sup> order harmonic component is the same for each phase current response.

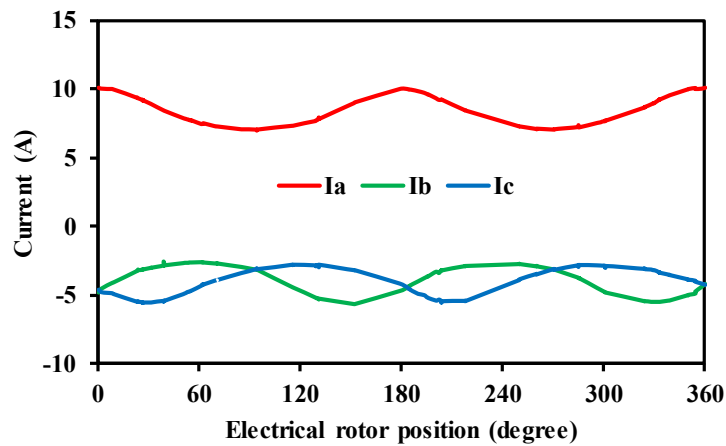


Fig. 3.2. Measured three-phase current responses against rotor position.

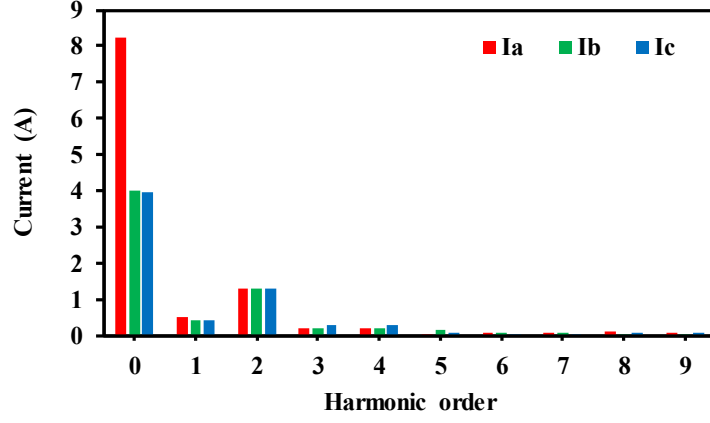


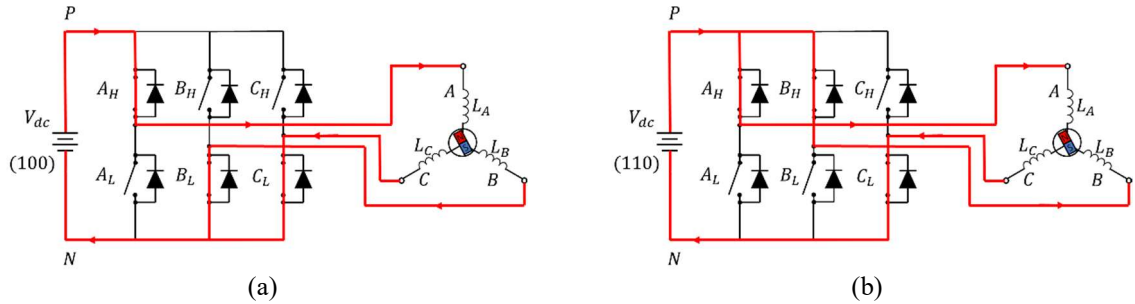
Fig. 3.3. Harmonic spectra of measured three-phase current response waveform.

Therefore, for the proposed method, by utilizing both three-phase current responses, more information can be obtained within one pulse injection, which helps to reduce the number of voltage pulses required.

### 3.3 Voltage Pulse Injection Process

Based on utilization of both primary and secondary current responses, a specific voltage pulse injection process is proposed. During the injection process, the injection position is selected based on the results from the previous pulse. Consequently, only three voltage pulses in total are injected and a 30-degree estimation resolution can be achieved without extra cost of sensors.

After injection of voltage pulses, the current responses are recorded and the peak values of current responses are used for rotor initial position estimation. For simplicity,  $|i_A|$ ,  $|i_B|$ ,  $|i_C|$  represent the absolute peak values of current responses in three phases.  $|i_{A+}|$  and  $|i_{A-}|$  are the absolute peak values of positive and negative current responses in phase A, and they are same for phases B and C. Moreover, for the proposed method, the excitation configurations of all injection positions are shown in Fig.3.4.



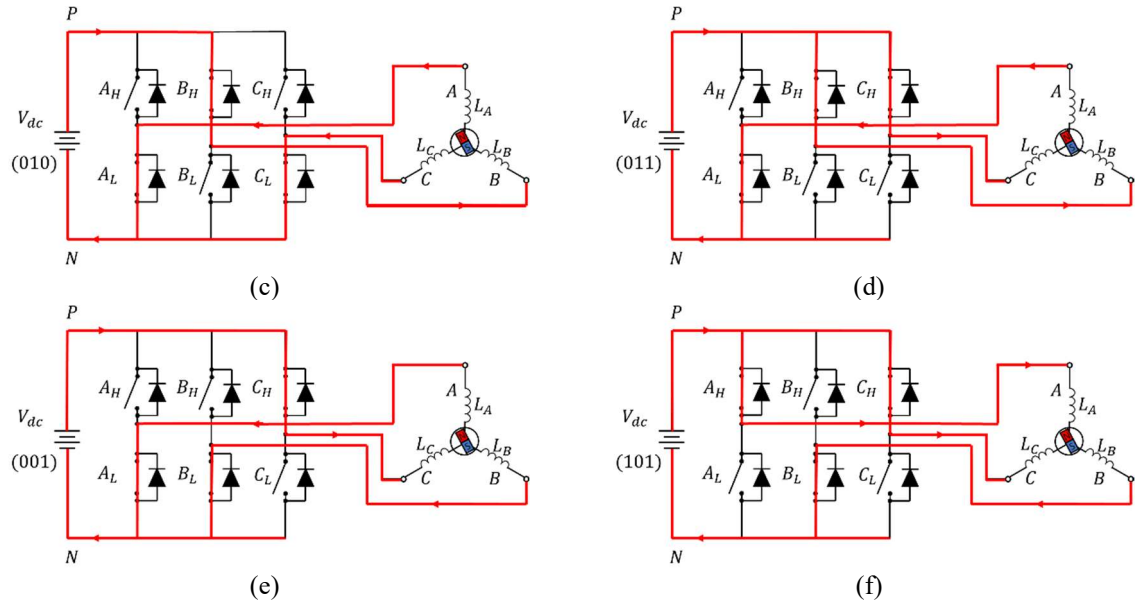


Fig. 3.4. Excitation configurations associated with injection position. (a) A+. (b) C-. (c) B+. (d) A-. (e) C+. (f) B-.

The whole process can be divided into 5 steps. In the first step, a positive voltage pulse is injected at phase A and the current responses in phase B and phase C are used to determine the injection position of the second voltage pulse in the next step. In the second step, based on the results of the first voltage pulse, a second voltage pulse will be injected at phase B or phase C. According to the results of first and second pulses together, the phase where the rotor magnetic pole is the closest to can be determined. Then, the third step is to identify the polarity. At this stage, a 60-degree resolution can be achieved. Next, the fourth step is to improve the estimation resolution from 60 degrees to 30 degrees by utilizing current responses from step 3. Meanwhile, there are some cases that the rotor magnetic pole locates at the boundary between adjacent sectors of which the estimation results are sensitive to noise, thus a boundary detection strategy is introduced to enhance the estimation accuracy. The whole estimation process is demonstrated by the flow chart in Fig. 3.6.

### 3.3.1 First Voltage Pulse Injection

In the first step, a positive voltage pulse is injected at phase A. After injection of the first voltage pulse, three current responses of three phases,  $i_{A1+}$ ,  $i_{B1-}$ ,  $i_{C1-}$ , are recorded. Then,  $i_{B1-}$  and  $i_{C1-}$  are compared to determine whether the rotor magnetic pole is closer to phase B or phase C. This is demonstrated by Fig. 3.5(a), where only the phases with the solid black line are compared and the dashed grey lines are not. If  $|i_{B1-}| > |i_{C1-}|$ , the rotor magnetic pole is closer to phase B, then a positive voltage pulse will be injected at phase B in the next step.

Otherwise,  $|i_{B1-}| < |i_{C1-}|$ , the rotor magnetic pole is closer to phase C, a positive voltage pulse will be injected at phase C in the next step.

### 3.3.2 Second Voltage Pulse Injection

For the second voltage pulse, the injection position is based on the results from step 1. For example, if it is known that  $|i_{B1-}| > |i_{C1-}|$  from the first pulse results, then a positive pulse is injected at phase B. After injection, there are three current responses,  $i_{A2-}$ ,  $i_{B2+}$ ,  $i_{C2-}$ . Then, as shown in Fig. 3.5(b), current responses in phase A and phase C are compared which are represented by solid black lines, i.e.  $i_{A2-}$  and  $i_{C2-}$ . An example is shown in Fig. 3.5(b). If  $|i_{A2-}| < |i_{C2-}|$ , it means that the rotor magnetic pole is closer to phase C than phase A. Combining the results from step 1, i.e.  $|i_{B1-}| > |i_{C1-}|$ , the rotor magnetic pole is closer to phase B than phase C. It can be determined at last that the magnetic pole of rotor is the closest to phase B, as shown in Fig. 3.5(c). Therefore, the phase where the rotor magnetic pole is the closest to can be identified in this step. Then, a corresponding negative voltage pulse will be injected at the selected phase in the next step to identify the polarity of rotor magnetic pole. The total estimation cases and injection phase selections are listed in TABLE 3.1.

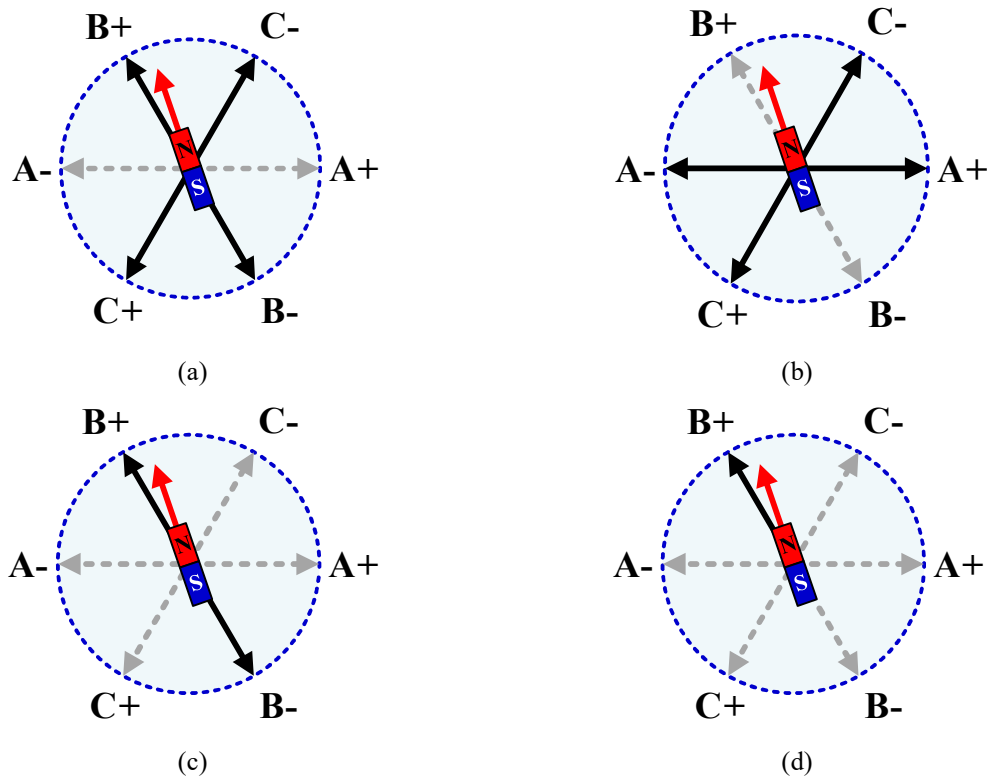


Fig. 3.5. Illustration of current responses between different phases. (a) Comparing phase B and phase C. (b) Comparing phase C and phase A. (c) Polarity determination. (d) North pole determined. [WU20c]

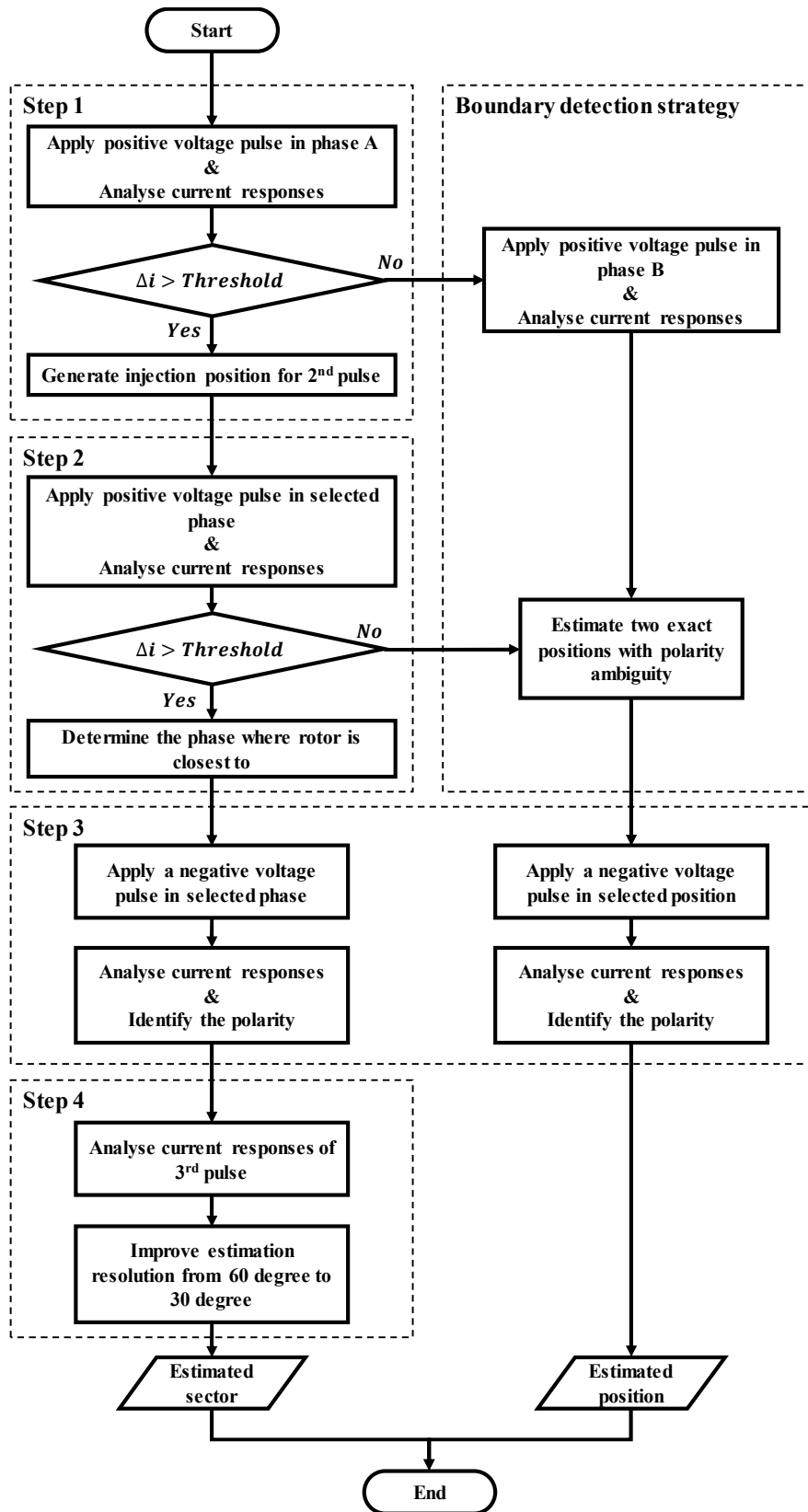


Fig. 3.6. Flow chart of the whole estimation process. [WU20c]

TABLE 3.1  
OVERALL ROTOR INITIAL POSITION DETERMINATION SCHEME

Step 1 Case	Inject Phase	Step 2 Case		Estimated Phase (Position)	Injection Phase	Step 3 Case	Sector: 60 degrees	Step 4 Case	Sector: 30 degrees			
$i_{B1-} > i_{C1-}$	B+	$i_{A2-} > i_{C2-}$	$i_{A1+} > i_{B2+}$	A	A-	$i_{A1+} > i_{A3-}$	1	$i_{B3+} > i_{C3+}$	1a			
								$i_{B3+} < i_{C3+}$	1b			
						$i_{A1+} < i_{A3-}$	4	$i_{B3+} > i_{C3+}$	4a			
								$i_{B3+} < i_{C3+}$	4b			
			$i_{A1+} \approx i_{B2+}$ (*)	150°, 330°	B-	$i_{B2+} > i_{B3-}$	150°					
						$i_{B2+} < i_{B3-}$	330°					
			$i_{A1+} < i_{B2+}$	B	B-	$i_{B2+} > i_{B3-}$	3	$i_{A3+} > i_{C3+}$	3b			
							$i_{A3+} < i_{C3+}$	3a				
						$i_{B2+} < i_{B3-}$	6	$i_{A3+} > i_{C3+}$	6b			
								$i_{A3+} < i_{C3+}$	6a			
			$i_{A2-} < i_{C2-}$	B	B-	$i_{B2+} > i_{B3-}$	3	$i_{A3+} > i_{C3+}$	3b			
							$i_{A3+} < i_{C3+}$	3a				
		$i_{B2+} < i_{B3-}$				6	$i_{A3+} > i_{C3+}$	6b				
							$i_{A3+} < i_{C3+}$	6a				
		$i_{A2-} \approx i_{C2-}$ (*)	B	B-	$i_{B2+} > i_{B3-}$	120°						
					$i_{B2+} < i_{B3-}$	300°						
$i_{A2-} > i_{B2-}$	$i_{A1+} > i_{C2+}$				A	A-	$i_{A1+} > i_{A3-}$	1	$i_{B3+} > i_{C3+}$	1a		
									$i_{B3+} < i_{C3+}$	1b		
		$i_{A1+} < i_{A3-}$	4	$i_{B3+} > i_{C3+}$			4a					
				$i_{B3+} < i_{C3+}$			4b					
	$i_{A1+} \approx i_{C2+}$ (*)	30°, 210°	C-	$i_{C2+} > i_{C3-}$	210°							
				$i_{C2+} < i_{C3-}$	30°							
	$i_{A1+} < i_{C2+}$	C	C-	$i_{C2+} > i_{C3-}$	5	$i_{A3+} > i_{B3+}$	5a					
					$i_{A3+} < i_{B3+}$	5b						
$i_{C2+} < i_{C3-}$				2	$i_{A3+} > i_{B3+}$	2a						
					$i_{A3+} < i_{B3+}$	2b						
$i_{A2-} < i_{B2-}$	C	C-	$i_{C2+} > i_{C3-}$	5	$i_{A3+} > i_{B3+}$	5a						
				$i_{A3+} < i_{B3+}$	5b							
			$i_{C2+} < i_{C3-}$	2	$i_{A3+} > i_{B3+}$	2a						
					$i_{A3+} < i_{B3+}$	2b						
$i_{A2-} \approx i_{B2-}$ (*)	C	C-	$i_{C2+} > i_{C3-}$	240°								
			$i_{C2+} < i_{C3-}$	60°								
			$i_{B1-} \approx i_{C1-}$ (*)	B+	$i_{A2-} > i_{C2-}$		0°, 180°	A-	$i_{A1+} > i_{A3-}$	0°		
									$i_{A1+} < i_{A3-}$	180°		
$i_{A2-} < i_{C2-}$		90°, 270°			B-	$i_{B2+} < i_{B3-}$	270°					
						$i_{B2+} > i_{B3-}$	90°					
All current values are absolute value; (*): boundary cases												

### 3.3.3 Polarity Determination

After the identification of which phase the rotor magnetic pole is closest to in step 2, the polarity will be determined in this step. For the proposed method, the north pole of the magnet is to be identified. Based on the results from step 2, a corresponding negative voltage pulse is injected at the selected phase in this step. If the rotor magnetic pole is the closest to phase B, then a negative voltage pulse is injected at phase B in this step to determine the polarity. By way of example, Fig. 3.5(d) shows that it is determined the rotor north magnetic pole locates at the positive phase B, by only showing phase B with solid black lines. The other situations are similar and summarized in TABLE 3.1. By this step, a 60-degree estimation resolution is achieved, as shown in Fig. 3.7.

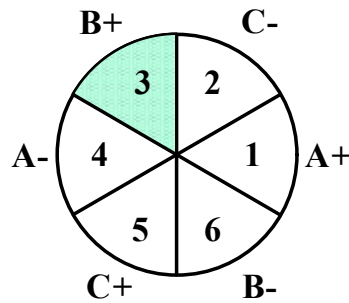


Fig. 3.7. Sector associated with 60 degree resolution estimation result. [WU20c]

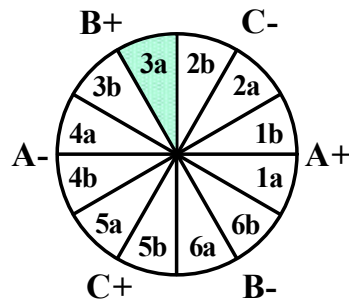


Fig. 3.8. Sector associated with 30 degree resolution estimation result. [WU20c]

### 3.3.4 Improving Estimation Resolution

In this step, the estimation resolution is improved from 60 degrees to 30 degrees as shown in Fig. 3.7 and Fig. 3.8. After injection of the third voltage pulse, there are three phase current responses. One of them is used for polarity determination in the previous step and another two will be subsequently used for improving estimation resolution in this step. By way of example, if the rotor magnetic pole locates at phase B, after injecting a negative voltage pulse at phase B, three current responses are recorded, i.e.  $i_{A3+}$ ,  $i_{B3-}$ ,  $i_{C3+}$ . After determination of polarity in the previous step, the rotor north magnetic pole is in sector 3 as shown in Fig. 3.7. If  $|i_{A3+}| < |i_{C3+}|$ ,

then the rotor north magnetic pole locates at sector 3a as depicted in Fig. 3.8. Hence, a 30-degree resolution estimation is obtained in this step. The overall process of rotor initial position estimation is demonstrated in TABLE 3.1.

### 3.4 Boundary Detection Strategy

In some cases, when the rotor magnetic pole locates at the boundary of two adjacent sectors shown by pink shadow areas in Fig. 3.9. The difference between two current responses may not be easily observed and become more sensitive to noise. Consequently, an estimation error will be introduced and affect the estimation accuracy. In order to solve this problem, higher level of voltage pulse or extra injections should be applied. However, these approaches consume more time and losses. Moreover, a higher level of voltage pulse may lead to rotor movement. Therefore, a simple boundary detection strategy (BDS) is proposed. With BDS, the estimation performance can be enhanced in two aspects, one is the reduction of the impact from current sampling noise to guarantee a reliable estimation. Another aspect is further improving the estimation resolution. In all, there are 12 boundary cases in total shown in Fig. 3.9 and included in TABLE 3.1 marked with a sign of star.

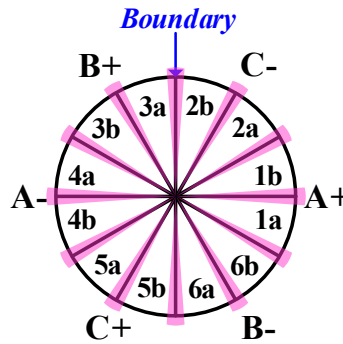


Fig. 3.9. Overall boundary cases associated with estimation sector. [WU20c]

#### 3.4.1 Noise Impact Reduction

The first merit by applying BDS is the reduction of impact from noise during current sampling. In the real drive systems, due to existence of noises, the current recorded in controller may not be the same as the real current. Therefore, the recorded current  $I_{record}$  can be represented as:

$$I_{record} = I_{real} \pm I_{error} \quad (3.4)$$

where  $I_{real}$  is the real current,  $I_{error}$  is the error between real and recorded currents. The error current  $I_{error}$  can come from several sources, such as measurement error, ADC quantization error and noises.

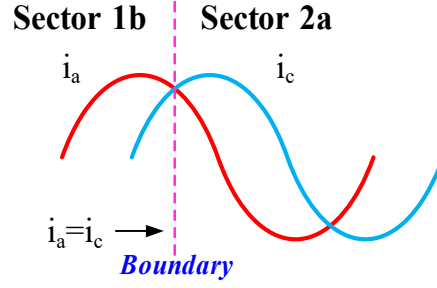


Fig. 3.10. Current responses at boundary. [WU20c]

Fig. 3.10 shows an example, at the boundary between sector 1b and sector 2a, the current responses in phase B and phase C should be ideally equal. However, due to measurement error, these two values may be different. Besides, if the rotor magnetic pole is close to the boundary, the difference between two current responses can be very small and becomes more sensitive to noise, the sign of the difference may be opposite from actual value, which affects the estimation performance.

In order to solve this issue, a threshold value of the current response difference  $\Delta I_{th0}$  is set, if the difference between two current responses is lower than the threshold value, the rotor magnetic pole is judged to be located at the boundary and an exact initial position can be estimated.

The threshold  $\Delta I_{th0}$  considering only noise impact is determined through pre-test. The error  $I_{error}$  is measured initially. A simple way of obtaining this value is introduced in Section 2.5. After  $I_{error}$  is obtained, the threshold considering noise impact is defined as:

$$\Delta I_{th0} = I_{error} \quad (3.5)$$

### 3.4.2 Estimation Performance Improvement

The second merit by applying BDS is the improvement of estimation performance. A definition called “boundary width” is introduced in this section. Furthermore, it is found out by selecting a proper boundary width, the estimation performance can be improved from 30 degrees estimation resolution to 15 degrees estimation.

#### A. Primary and secondary three-phase current responses

Firstly, according to the proposed estimation method introduced before, there will be primary current response in three-phase and secondary current response in three-phase as well. Hence, the primary responses of three-phase currents against rotor position are shown in Fig. 3.11. Then, the absolute values of the difference between two secondary responses against the rotor position are also shown in Fig. 3.11.

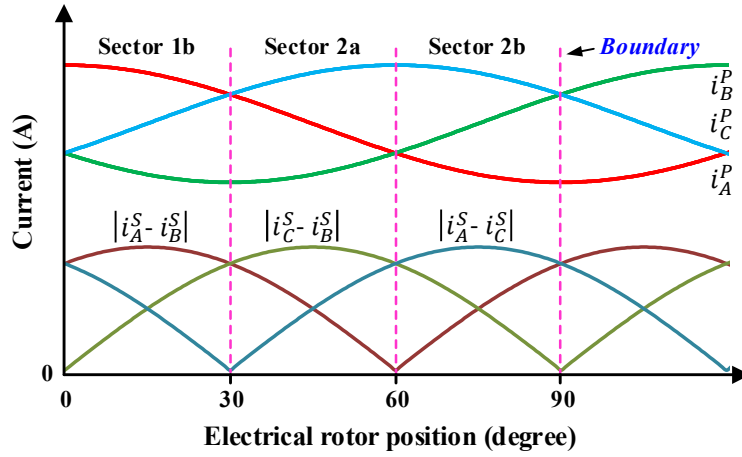


Fig. 3.11. Three-phase primary current response and secondary current response difference against rotor position.

Furthermore, according to TABLE 3.1, it is known that for each boundary case two secondary current responses are compared and used to estimate the rotor position. Hence, Fig. 3.11 is modified to Fig. 3.12 by highlighting the difference used for each boundary cases. It can be seen in Fig. 3.12 the highlighted difference is in black and defined as  $|\Delta i|$ . Then, based on Fig. 3.12, the difference  $|\Delta i|$  can be approximately represented as:

$$|\Delta i| \approx \begin{cases} k\theta_r & 15^\circ > \theta_r \geq 0^\circ \\ |\Delta i|_{max} - k(\theta_r - 15) & 30^\circ > \theta_r \geq 15^\circ \\ \theta_r = \text{mod}(\theta_r, 30^\circ) & \end{cases} \quad (3.6)$$

where  $k = |\Delta i|_{max}/15$ ,  $|\Delta i|_{max}$  is the maximum value of  $|\Delta i|$ . Clearly, at the boundary, the current difference  $|\Delta i|$  is zero.

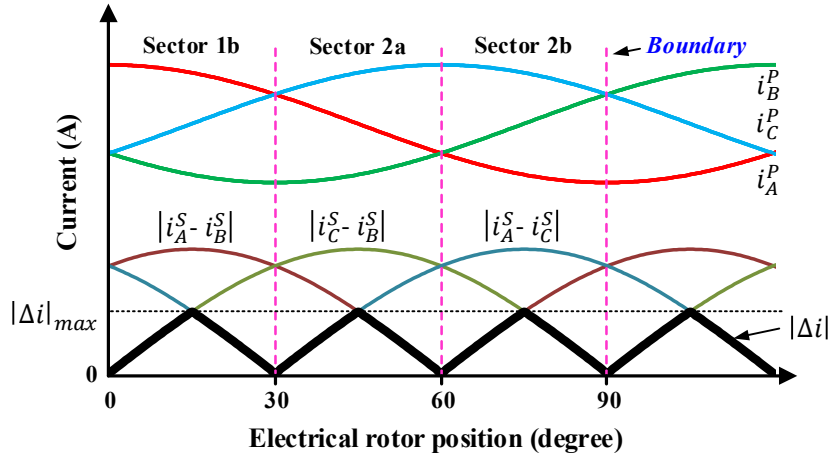


Fig. 3.12. Highlighted secondary current response difference against rotor position.

### B. Boundary width

A so called ‘boundary width’ i.e.  $\theta_w$  is defined as the angle span of the boundary shown in Fig. 3.13. As aforementioned,  $\Delta I_{th}$  is determined from noise. Apart from that,  $\Delta I_{th}$  can be

further determined based on the boundary width  $\theta_w$ . Besides, the "boundary width"  $\theta_w$  can be associated with the aforementioned current difference  $|\Delta i|$ , which is shown in Fig. 3.14.

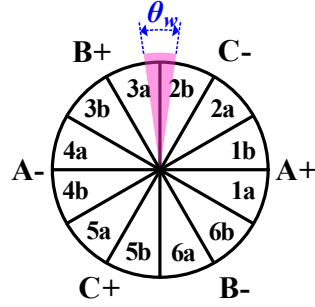


Fig. 3.13. Boundary width associated with estimation sector. [WU20c]

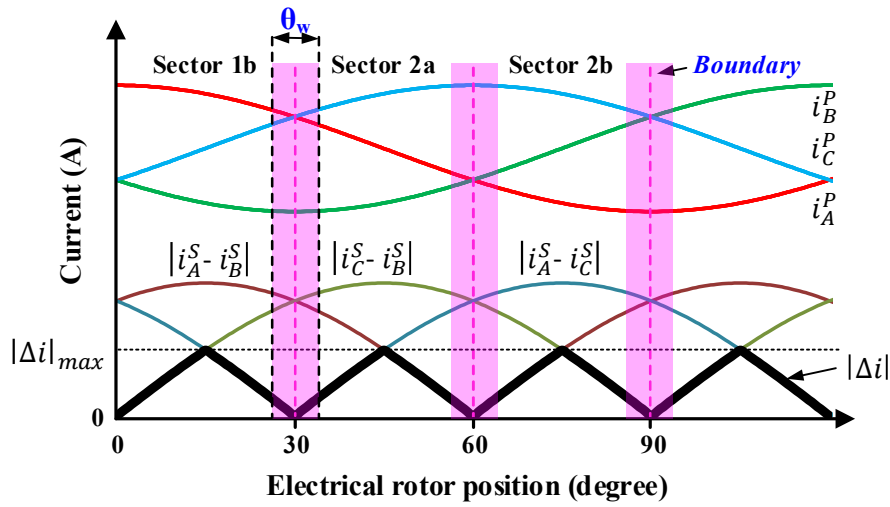


Fig. 3.14. Three-phase current responses and difference against rotor position with boundary width.

Based on Fig. 3.14, the relationship between current difference threshold  $\Delta I_{th1}$  and boundary width  $\theta_w$  can be derived as:

$$\Delta I_{th1} = \frac{|\Delta i|_{max}}{15} \frac{\theta_w}{2} \quad (3.7)$$

where the boundary width  $\theta_w \leq 30^\circ$ . Threshold can be set according to boundary width  $\theta_w$ .

### C. Selection of boundary width

Furthermore,  $\theta_w$  should be selected appropriately so that the estimation performance can be optimized. In Fig. 3.15, different  $\theta_w$  cases are illustrated with measured three-phase current responses against rotor positions.

In the sector charts, the real position  $\theta_{real}$  shown with red arrow is 25 degrees. After applying BDS with a 5-degree  $\theta_w$  as depicted in Fig. 3.15(a), the estimated position  $\hat{\theta}$  shown with blue arrow is 15 degrees with 10 degrees error. Then, by using a 15-degree  $\theta_w$  shown in Fig. 3.15(b), the estimated position  $\hat{\theta}$  is now 30 degrees with only 5 degrees error. For another

case with larger  $\theta_w$  shown in Fig. 3.15(c), the real position  $\theta_{real}$  is 20 degrees. After applying BDS with a 21-degree  $\theta_w$ , the estimated position  $\hat{\theta}$  is 30 degrees with 10 degrees error.

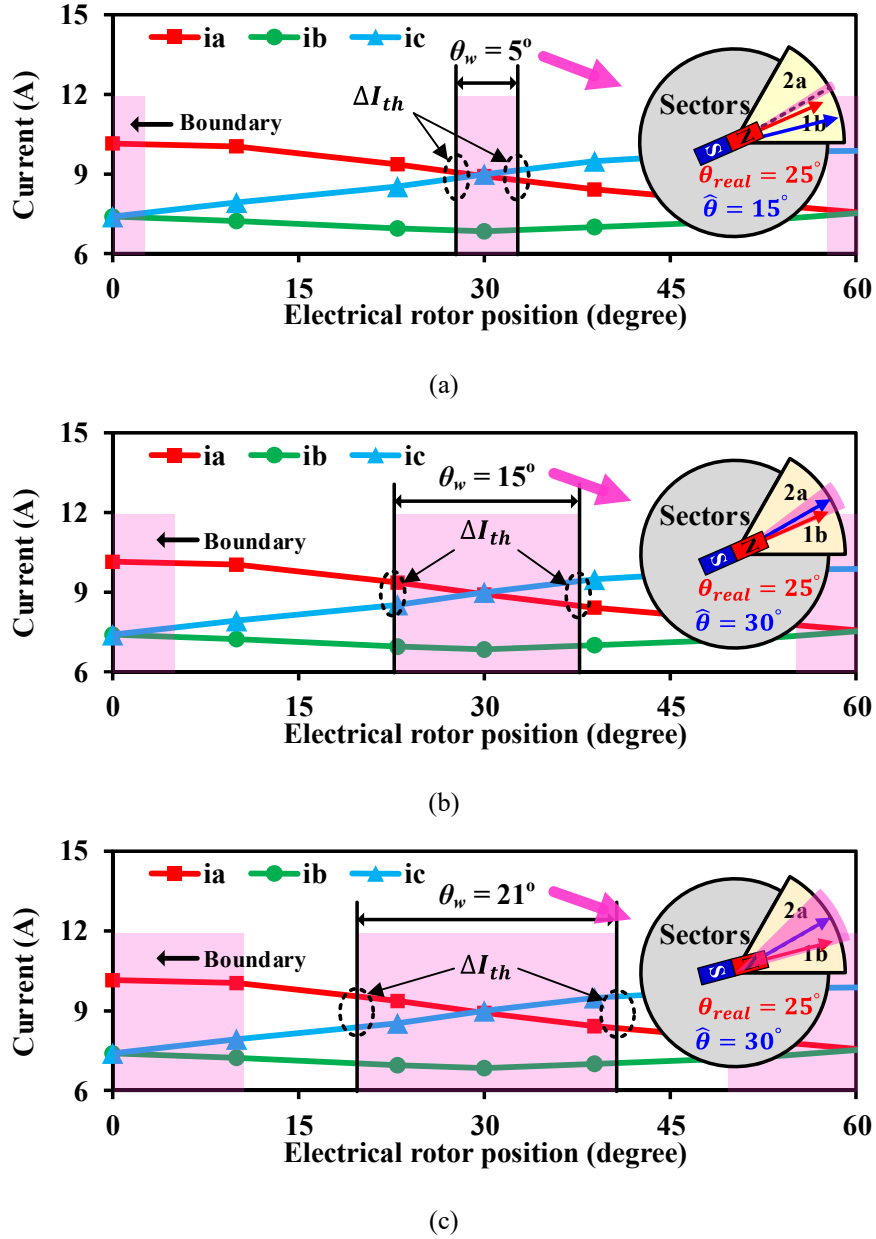


Fig. 3.15. Illustration of boundary width selection. (a) 5-degree boundary width. (b) 15-degree boundary width. (c) 21-degree boundary width. [WU20c]

Therefore, by properly selecting  $\theta_w$ , estimation performance can be optimized. Fig. 3.16 shows the relationship between the maximum estimation error and the boundary width  $\theta_w$ . It is found out that with a 15 degrees boundary width, the estimation performance can be optimized in result of a maximum of 7.5 degrees estimation error.

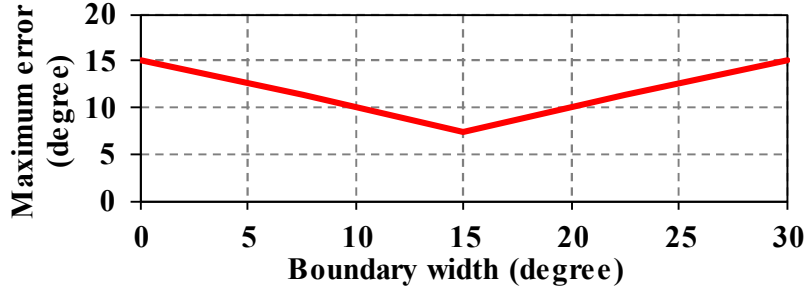


Fig. 3.16. Maximum estimation error against boundary width.

In all, theoretically, by applying the maximum  $\theta_w$  of 15 degrees, the largest estimation error can be reduced from 15 degrees to 7.5 degrees.

#### D. Determination of threshold

The threshold value is determined in the pre-test. After applying a boundary width of 15 degrees, the current difference threshold can be calculated by:

$$\Delta I_{th1} = \frac{|\Delta i|_{max}}{2} \quad (3.8)$$

Therefore, the threshold value can be determined by measuring  $|\Delta i|_{max}$ . According to Fig. 3.12,  $|\Delta i|_{max}$  can be obtained in this pre-test at certain rotor positions, e.g.  $15^\circ$ . For example, at 15 degrees, voltage pulse is injected to phase A and the difference between phase B and phase C currents is recorded and regarded as  $|\Delta i|_{max}$ . In order to reduce the impact from noise  $I_{error}$ , several voltage pulses are injected and the average value is used to calculate the  $\Delta I_{th1}$ .

$$\Delta I_{th1} = \frac{1}{2n} \sum_{k=1}^n |\Delta i(k)|_{max} \quad (3.9)$$

Therefore, the threshold value can be determined through pre-test by measuring the current difference at certain rotor positions.

### 3.5 Experimental Validation

Experiments are carried out to validate the proposed method based on a dSPACE platform. The parameters of the prototype SPM-I are shown in Appendix A. The duration time of voltage pulse applied in this test is 2ms and the magnitude of the voltage pulse is 230V. The duration time and voltage magnitude are chosen to avoid the rotor vibration and movement while the current response is large enough for estimation. Moreover, a longer time interval between each

pulse is used for a clear demonstration. In the experimental section, firstly, an example of rotor initial position estimation is provided to demonstrate the whole estimation process. Then, the overall estimation performance will be presented as well. Moreover, the investigation of the proposed BDS is carried out at last.

### 3.5.1 An Example of Proposed Rotor Initial Position Estimation

At first, an estimation example is provided to validate the effectiveness of the proposed method and for a better illustration of the whole estimation process. The actual electrical rotor position is 41 degrees. The experimental results are demonstrated in Fig. 3.17 and Fig. 3.18. In Fig. 3.17, there are total three current responses corresponding to three applied voltage pulses.

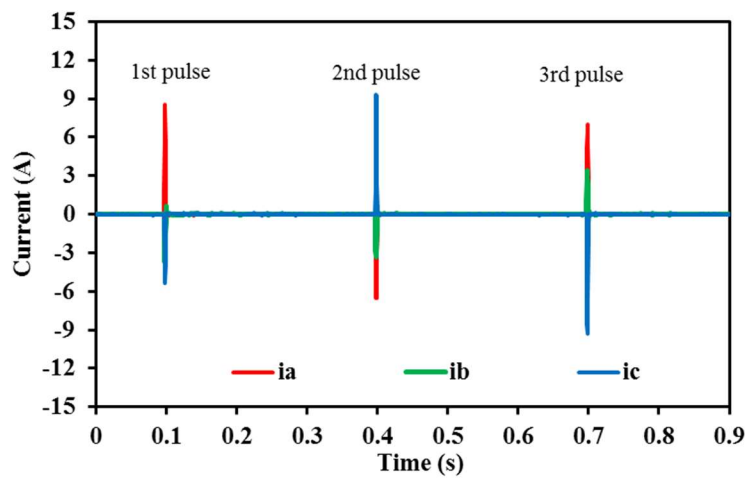
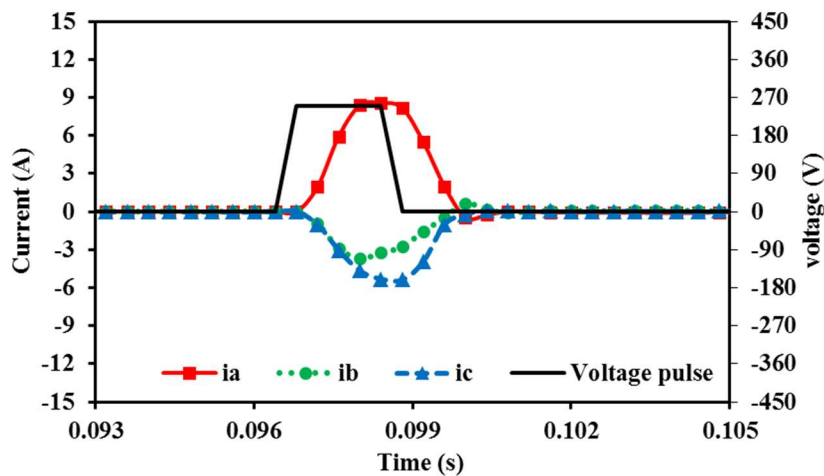
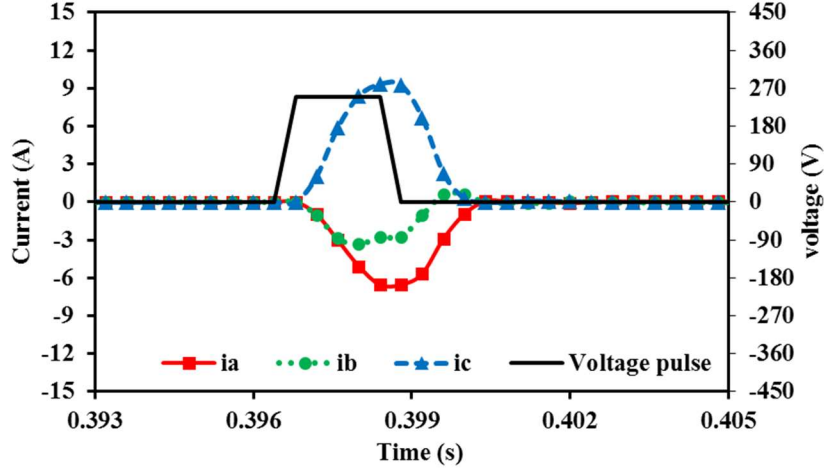


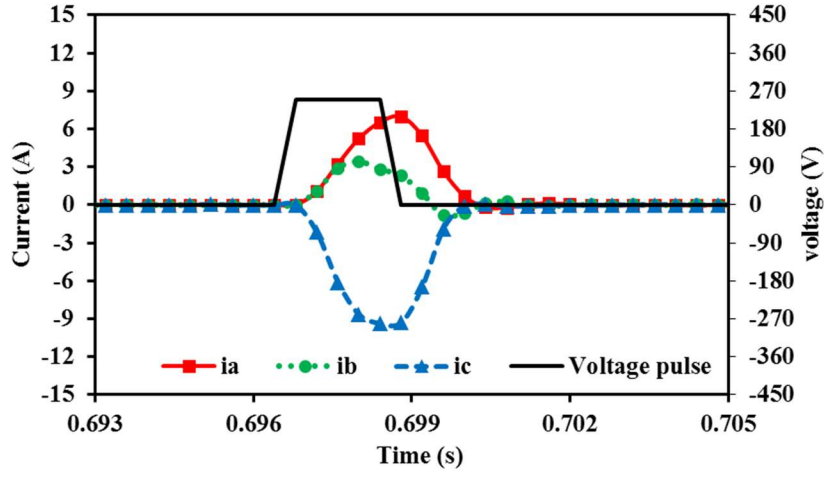
Fig. 3.17. Overall current responses during estimation. [WU20c]



(a)



(b)



(c)

Fig. 3.18. Current responses during estimation. (a) First pulse. (b) Second pulse. (c) Third pulse.

[WU20c]

In Fig. 3.18(a)-(c), the voltage pulse and current responses of each pulse are shown. In addition, each sample point is marked. In Fig. 3.18(a), the current responses of the first voltage pulse show that  $|i_{B1-}| < |i_{C1-}|$ , indicating the rotor magnetic pole is more closer to phase C than phase B. Based on the proposed method, a positive voltage pulse will be injected at phase C in step 2, the current responses are shown in Fig. 3.18(b). It can be seen that  $|i_{B2-}| < |i_{A2-}|$  and  $|i_{A1+}| < |i_{C2+}|$ , and hence, the rotor magnetic pole is closest to phase C. In step 3, a negative voltage pulse is injected at phase C to identify the polarity, as shown in Fig. 3.18(c). The current responses in Fig. 3.18(c) show that  $|i_{C3-}| < |i_{C2+}|$ , and therefore, the rotor north pole is in sector 2. In the last step, the current responses from Fig. 3.18(c) are utilized to upgrade estimation resolution from 60 degrees to 30 degrees. It is shown that  $|i_{B3+}| < |i_{A3+}|$ . Therefore,

the rotor magnetic pole is closer to phase A, indicating the rotor north pole is in sector 2a, which is the same as the actual rotor position.

### 3.5.2 Overall Rotor Initial Position Estimation Performance

For further illustration, the proposed method is tested over the whole range of rotor positions. During the tests, some random initial positions within the whole rotor position range are selected for estimation at standstill. The estimation results and estimation errors are shown in Fig. 3.19. The rotor initial position can be detected over the whole range of rotor positions. Majority of results are within 15 degrees. However, there are some cases that the errors are larger than 15 degrees due to smaller difference of current responses. Subsequently, the proposed boundary detection is applied and analysed in the next part.

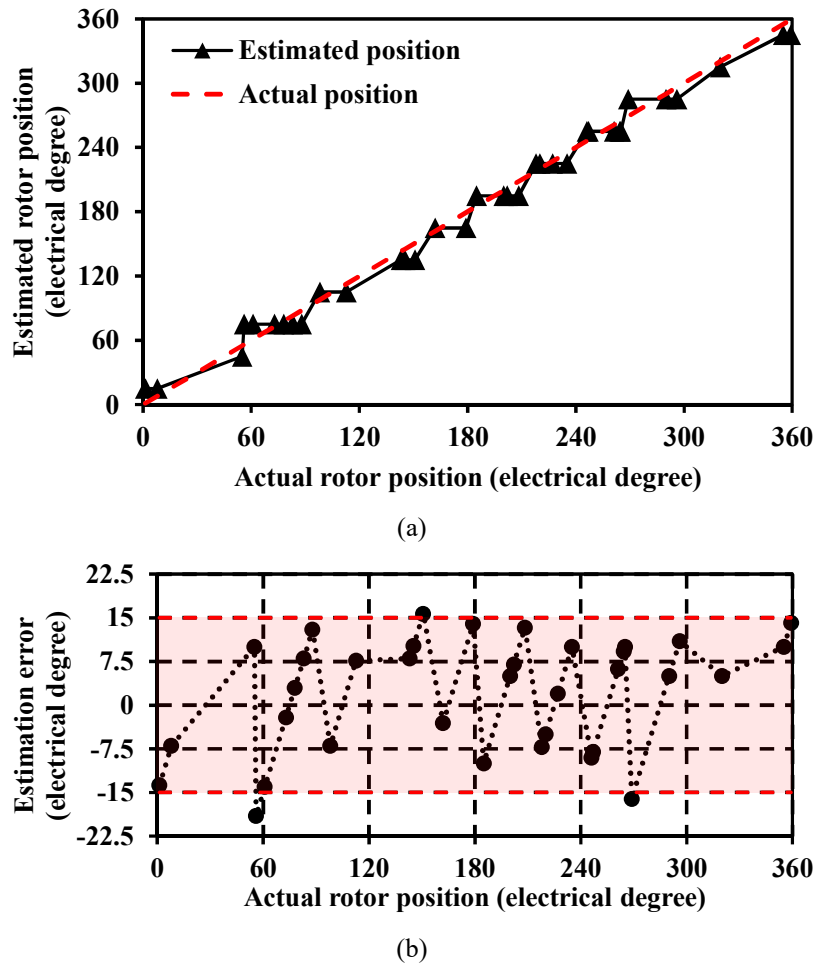


Fig. 3.19. Initial rotor position estimation results without applying BDS. (a) Estimated position against actual rotor position. (b) Estimation error. [WU20c]

### 3.5.3 Boundary Detection Performance

An example of the boundary case during estimation is shown in Fig. 3.20 and Fig. 3.21 for a better illustration.

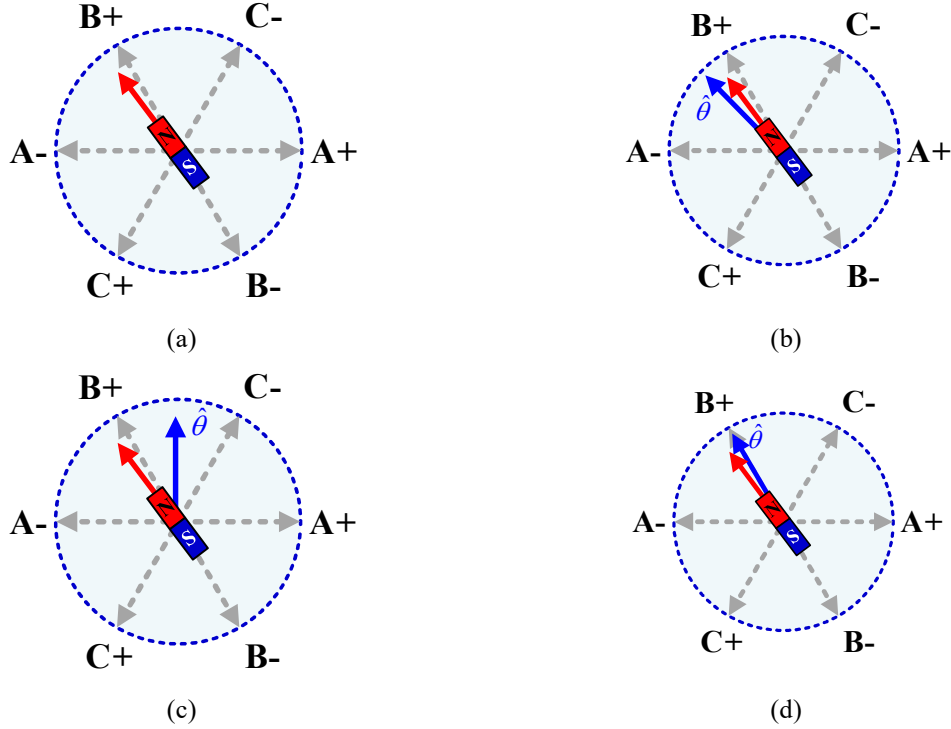


Fig. 3.20. Illustration of boundary case during estimation. (a) Actual rotor initial position. (b) Correct estimation without BDS under ideal condition. (c) Wrong estimation without BDS under practical condition. (d) Enhanced estimation with BDS under practical condition. [WU20c]

In Fig. 3.20(a), the real rotor position is at 122 degrees. In this case, the magnitude of the current in phase A should be larger than that of the current in phase C. Thus, under the ideal condition without any noises, the north pole of rotor should be estimated at 135 degrees shown in Fig. 3.20(b). However, since the rotor north pole is around the boundary between two adjacent sectors, the two current responses have very similar magnitudes. Due to the existence of measurement error and noise, the recorded phase A current has a smaller magnitude than that of the current in phase C as shown in Fig. 3.21. In this case, the estimation is deteriorated as shown in Fig. 3.20(c), the estimation resolution drops from 30 degrees to 60 degrees. Then, estimation with BDS is shown in Fig. 3.20(d). Obviously, the estimation performance is enhanced and the error is only 3 degrees.

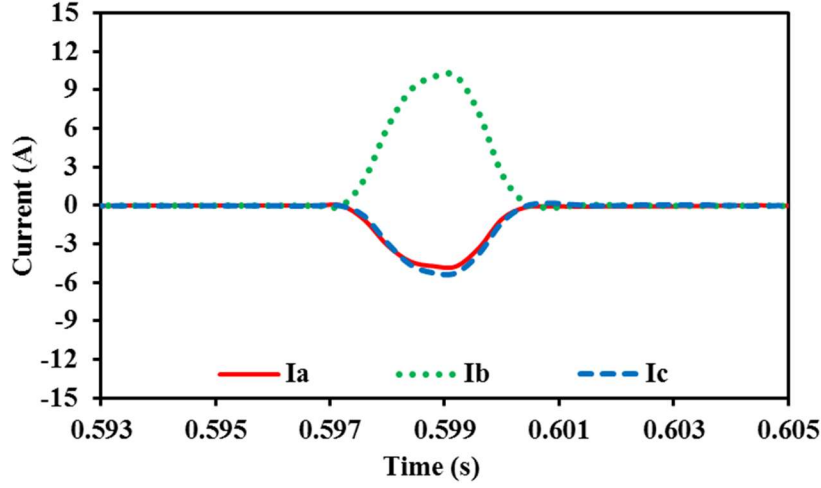
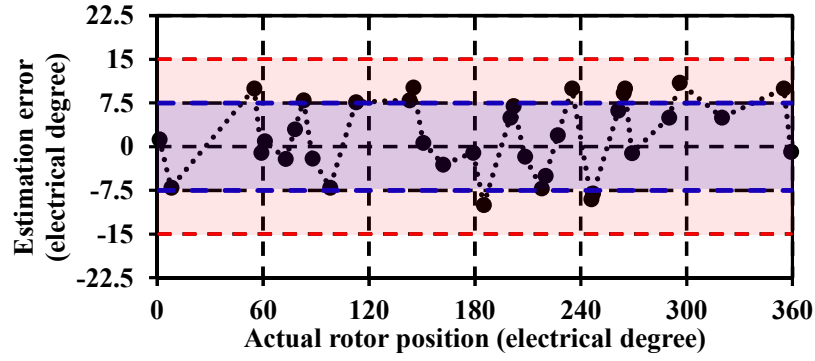
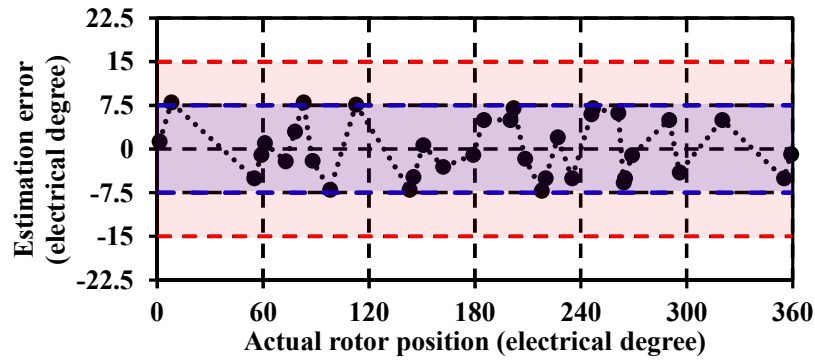


Fig. 3.21. Current responses during the boundary case. [WU20c]

For the overall range of rotor initial position estimation shown in Fig. 3.19(b), there are some boundary cases that the estimation errors are larger than 15 degrees. After applying BDS during estimation, the improved results are shown in Fig. 3.22(a) and (b).



(a)



(b)

Fig. 3.22. Initial rotor position estimation results with BDS. (a)  $\Delta I_{th}$  considering noise only. (b)  $\Delta I_{th}$  considering noise and maximum boundary width. [WU20c]

In Fig. 3.22(a),  $\Delta I_{th}$  is determined as 0.1A considering only the noise in current sampling. Then, in Fig. 3.22(b), by considering the maximum boundary width  $\theta_w$  of 15 degrees and noise

together, according to (3.8),  $\Delta I_{th1}$  is determined as 0.7A in the pre-test. The maximum estimation error is further reduced to around 7.5 degrees. It can be concluded that by using BDS with a proper boundary width  $\theta_w$  and the associated threshold  $\Delta I_{th1}$ , the estimation performance can be enhanced.

### 3.6 Conclusion

In this chapter, a new short-pulse-injection-based rotor initial position estimation method for SPMs is proposed. Different from conventional rotor initial position estimation methods, the required voltage pulses for the proposed method are reduced to three pulses only, with a 30-degree estimation resolution at no cost of extra voltage or current sensors. While for conventional methods, either extra voltage and current sensors or more voltage pulses are necessary to achieve at most 30-degree estimation resolution. The proposed method with fewer pulses can save the execution time, reduce the induced losses and reduce the cost. Moreover, a simple boundary detection strategy is proposed. The impact of current sampling noise on position estimation is reduced. Meanwhile, by selecting a proper boundary width, the estimation accuracy is improved from 30-degree to 15-degree estimation resolution. The proposed method is verified by experimental results. Furthermore, the proposed method is compared with several conventional methods. The overall comparison is shown in TABLE 3.2. The proposed method shows a comparative performance compared with conventional methods.

TABLE 3.2  
OVERALL COMPARISON

Method	[SCH97]	[NAK00]	[LAI03]	[LEE06]	[CHA09]	Proposed
Estimation resolution (degree)	24	30	60	30	30	15
Maximum error (degree)	15	18	30	15	15	7.5
Required pulses	6	21	4	5	3	3
Current sensor	3	3	0	1	1	3
Voltage sensor	0	0	3	0	2	0
PWM Modulation	No	Yes	No	No	No	No
Cost-effective index	392.4	1377	540	112.5	202.5	101.25

# CHAPTER 4

## ROTOR INITIAL POSITION ESTIMATION METHOD BASED ON DC-LINK VOLTAGE

### 4.1 Introduction

For conventional methods, phase current [MAT96][SCH97][NAK00], DC-link current [LEE06] or terminal phase voltage [LAI03][CHA09] are normally used for position estimation. In this chapter, a new simple rotor initial position estimation method is presented. Different from conventional methods, only one DC-link voltage sensor is utilized to estimate the rotor initial position and a 30-degree estimation resolution can be achieved. Besides, practical issues are considered including DC-link voltage measurement errors, DC-link resistance, DC-link capacitance and DC-link voltage ripples. In order to obtain a more reliable estimation performance, a guideline of voltage pulse selection is also presented based on practical considerations.

In this chapter, firstly the basic principle of utilizing DC-link voltage is explained. Then, a specific excitation configuration approach is presented and compared with conventional ones. Furthermore, by using the specific excitation configuration, a so-called ‘equivalent injection position’ is derived so that the estimation process could be simplified. Next, the overall injection procedure and estimation process are illustrated. Moreover, the impact of practical issues on rotor initial position estimation is analysed. Experimental results are provided to verify the effectiveness of the proposed method. At last, the estimation performance comparison between the proposed method and the conventional method is given and followed by the conclusion.

This chapter is based on the papers:

[WU19a] X. M. Wu and Z. Q. Zhu, “A novel rotor initial position detection method utilizing dc-link voltage sensor,” *2019 IEEE International Electric Machines & Drives Conference (IEMDC)*, San Diego, CA, USA, 2019, pp. 1093-1098.

[WU20d] X. M. Wu, Z. Q. Zhu, and Z. Y. Wu, “A novel rotor initial position detection method utilizing DC-link voltage sensor,” submitted to *IEEE Transactions on Industry Applications*.

## 4.2 Utilization of DC-link Voltage

Different from conventional methods by using measured current responses after applying voltage pulses, the variation of DC-link voltage is measured and used to estimate the rotor initial position for the proposed method. The principle of utilizing DC-link voltage variation is demonstrated in this section.

Firstly, the DC-link voltage source can be approximately regarded as one internal DC-link resistor  $R_{dc}$  and a controlled voltage source  $V_c$  in series as shown in Fig. 4.1. Next, an equivalent circuit during voltage pulse injection is also shown in Fig. 4.1, where  $R_{eq}$  and  $L_{eq}$  are the equivalent resistance and inductance in the circuit during excitation.

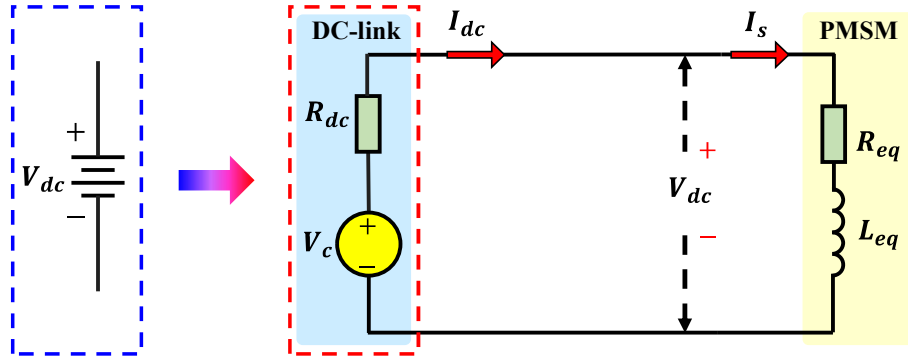


Fig. 4.1. Illustration of DC-link voltage utilization. [WU20d]

Based on Fig. 4.1, after injection of voltage pulse, there is a current  $I_{dc}$  flowing through the circuit and the measured DC-link voltage  $V_{dc}$  can be represented by:

$$V_{dc} = V_c - I_{dc}R_{dc} \quad (4.1)$$

During the excitation, it can be seen that there is a voltage drop on the DC-link resistor, i.e.  $I_{dc}R_{dc}$  causing a variation on the DC-link voltage, i.e.  $\Delta V_{dc}$ . As introduced in Section 2.2, the induced current response  $I_{dc}$  reflects the rotor initial position, i.e.  $I_{dc}(\theta)$ , so that the DC-link voltage variation also contains the rotor initial position information, i.e.  $\Delta V_{dc}(\theta)$ . Therefore, rotor initial position can be estimated by utilizing DC-link voltage. It is worth noting that the value of DC-link resistance  $R_{dc}$  can be regarded as the gain of DC-link voltage variation which will influence the estimation performance. Therefore, the influence of this DC-link resistance will be discussed in Section 4.5 and investigated by experiments in Section 4.6 as well.

## 4.3 Excitation Configuration Investigation

In this section, the excitation configuration of conventional methods is firstly investigated and a specific excitation configuration for the developed method is then introduced and compared with the conventional ones.

### 4.3.1 Three-phase Based Excitation Configuration

For conventional methods[SCH97][NAK00][LAI03][LEE06], both three-phase windings are connected and excited during excitation. An example is given in Fig. 4.2.

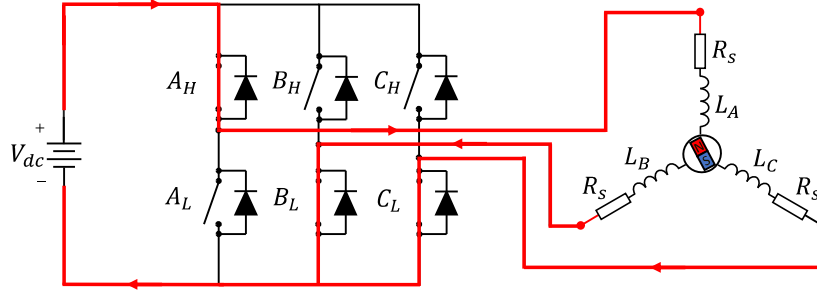


Fig. 4.2. Conventional excitation configuration. [WU20d]

For the conventional excitation configuration shown in Fig. 4.2, the equivalent inductance during injection is:

$$L_{eq} = L_A + \frac{L_C L_B}{L_C + L_B} \quad (4.2)$$

It is worth mentioning that the resistance part and mutual inductance part are relatively small and thus neglected in the derivation of equivalent inductance. Besides, the three-phase self-inductances are represented as:

$$\begin{aligned} L_A &= L_0 + L_2 \cos(2\theta_r) \\ L_B &= L_0 + L_2 \cos\left(2\left(\theta_r - \frac{2\pi}{3}\right)\right) \\ L_C &= L_0 + L_2 \cos\left(2\left(\theta_r + \frac{2\pi}{3}\right)\right) \end{aligned} \quad (4.3)$$

where  $L_{ABC}$  is the three-phase self-inductance,  $L_0$  and  $L_2$  are the DC component and the 2<sup>nd</sup> order harmonic component of the self-inductance, respectively.

### 4.3.2 Two-phase Based Excitation Configuration

For the proposed method, different from conventional methods shown in Fig. 4.2, only two phases in series are excited during each voltage pulse injection, which means that only two legs of inverter are operating during each voltage pulse injection. The upper and lower switches on the other leg are both turned off, and thus, the two excited phases are in series. In case of Fig. 4.3, phases A and B are in series and excited at the same time. The upper and lower switches on inverter leg of phase C are both turned off.

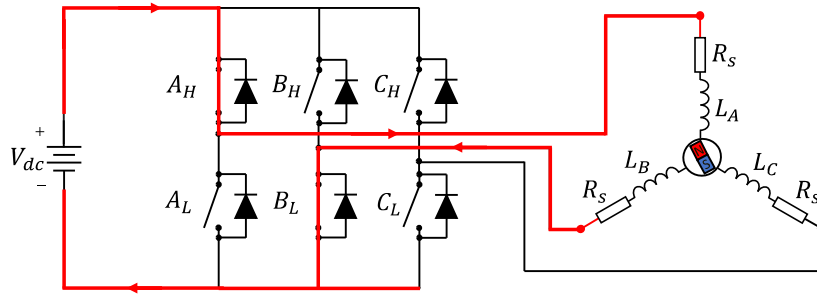


Fig. 4.3. Proposed excitation configuration. [WU20d]

For the proposed excitation configuration shown in Fig. 4.3, the equivalent inductance is:

$$L_{eq} = L_A + L_B \quad (4.4)$$

### 4.3.3 Comparison Between Three-phase and Two-phase Excitation

It is known that due to magnetic saturation, a 2<sup>nd</sup> harmonic component appears in the inductance. Clearly, a larger magnitude of  $L_2$  makes the estimation performance better. Since the equivalent inductances are different due to different excitation configurations as shown in (4.2) and (4.4), a different value of the 2<sup>nd</sup> harmonic component in the equivalent inductance is also expected.

Based on (4.2) and (4.4), the per-unit values of the 2<sup>nd</sup> order harmonic component in the equivalent inductance with different excitation configurations are given in Fig. 4.4. The original value of the 2<sup>nd</sup> order harmonic component in phase A self-inductance is also given for comparison. It can be seen that compared with conventional one, the proposed excitation configuration has a larger magnitude of the 2<sup>nd</sup> order harmonic component in the equivalent inductance which can obviously result in a better performance.

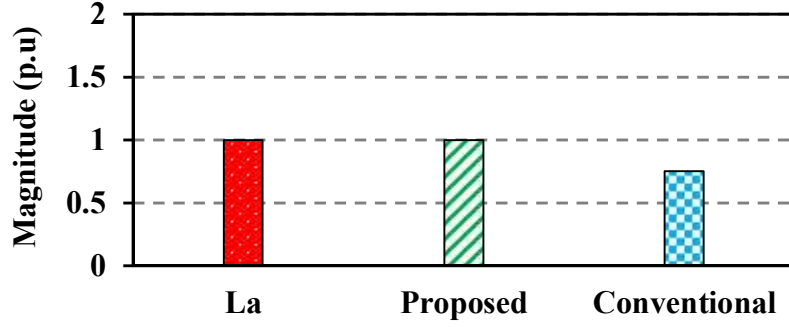


Fig. 4.4. Comparison of magnitude of 2nd order harmonic component in the inductance. [WU20d]

#### 4.3.4 Equivalent Injection Position

In case of the proposed excitation configuration, two phases in series are excited together, representing a sum of the two phase inductances, the rotor initial position information may not be obtained directly by comparing the sums. Thus, an equivalent injection position is derived based on the excited two phases, which simplifies the analysis process.

Fig. 4.6 shows an example when a voltage pulse is injected to A+ and C- phases which are 0 and 60 degrees respectively and the equivalent injection position can be obtained by sum of these two vectors as shown in Fig. 4.6. Hence, the equivalent injection position is 30 degrees.

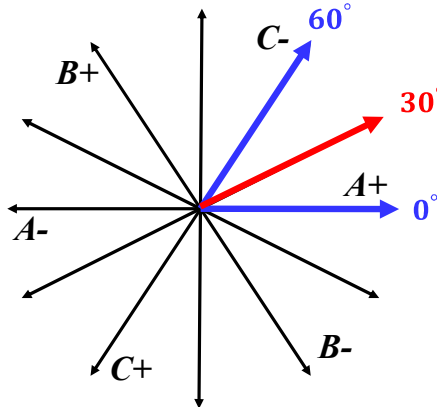


Fig. 4.5. An example of equivalent injection position. [WU20d]

Furthermore, the equivalent injection position can be explained mathematically. In this injection case, the equivalent inductance is:

$$L_{eq} = L_A + L_C \quad (4.5)$$

(4.5) can be modified by substituting (4.3) as:

$$L_{eq} = 2L_0 - L_2 \cos \left( 2\left(\theta_r - \frac{\pi}{6}\right) \right) \quad (4.6)$$

Clearly, the equivalent inductance in (4.6) also aligns with the equivalent injection position of 30 degrees.

Moreover, all the 6 equivalent injection positions are shown in Fig. 4.6 marking with red and described in TABLE 4.1 as well.

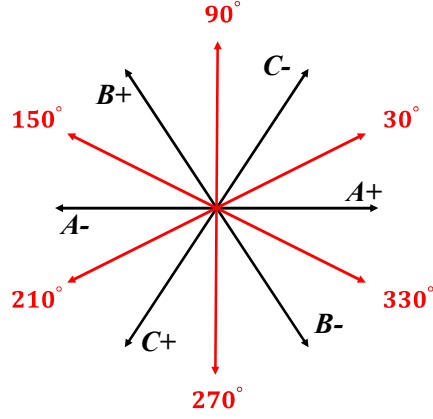


Fig. 4.6. Overall equivalent injection positions. [WU20d]

TABLE 4.1  
EQUIVALENT INJECTION POSITION OF EACH PULSE

Voltage pulse number	Excited phases	Equivalent Inductance $L_{eq}$	Equivalent injection position (degree) <sup>a</sup>
1	A+, C-	$L_{A+} + L_{C-}$	30
2	B+, C-	$L_{B+} + L_{C-}$	90
3	A-, B+	$L_{A-} + L_{B+}$	150
4	A-, C+	$L_{A-} + L_{C+}$	210
5	B-, C+	$L_{B-} + L_{C+}$	270
6	A+, B-	$L_{A+} + L_{B-}$	330

## 4.4 Voltage Pulse Injection Process

For the proposed method, 6 voltage pulses are injected to 6 equivalent positions in total. Then, the DC-link voltage variations are recorded. Based on the principle described before, the maximum DC-link voltage variation indicates where the north pole of rotor is closest to. Then, the rotor can be located in sectors of 60-degree resolution shown in Fig. 4.7.

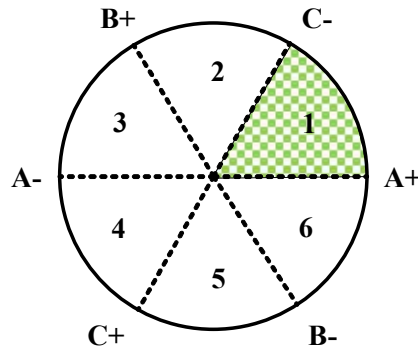


Fig. 4.7. 60 degrees resolution sector. [WU20d]

Up to now, a 60-degree estimation resolution can be acquired. Next, the estimation resolution is improved to 30 degrees. An example is given here for a clear illustration which is shown as green areas in Fig. 4.8.

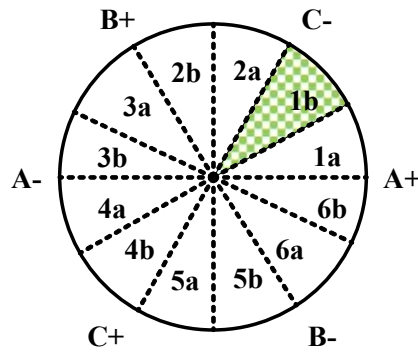


Fig. 4.8. Sector demonstration. (a) 60-degree resolution estimation. (b) 30-degree resolution estimation. [WU20d]

If the rotor position is estimated at 30 degrees, i.e. sector 1, then by comparing two adjacent DC-link voltage variations of voltage pulses injected in 90 degrees and 330 degrees. Supposing the variation of 90 degrees is larger than that of 330 degrees, rotor position is then estimated at 45 degrees (sector 1b), otherwise it is 15 degrees (sector 1a), and other cases are similar. By doing this, a 30-degree estimation resolution can be obtained at last. The overall estimation process flow chart is given in Fig. 4.9.

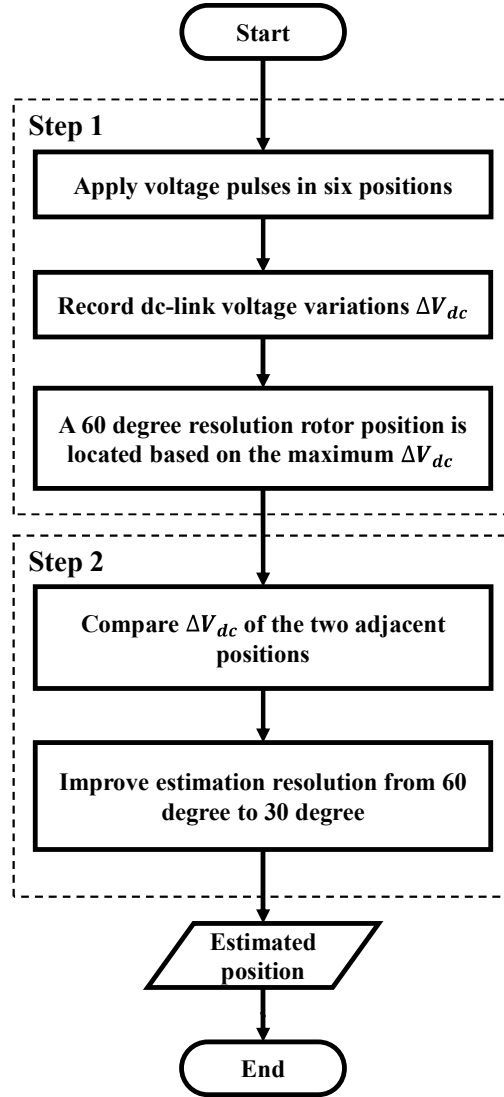


Fig. 4.9. Overall estimation process flow chart. [WU20d]

## 4.5 Consideration of Practical Issues

As described in Section 4.4, 6 voltage pulses are injected and the corresponding 6 DC-link voltage variations are recorded and compared to obtain the rotor initial position. Hence, the differences between them are important to acquire the correct position information. However, the analyses of the proposed method in Section 4.3 are based on a simplified and ideal model. In practical applications, there are several factors including DC-link voltage measurement errors, DC-link capacitance, DC-link resistance and DC-link voltage ripples which may have impacts on DC-link voltage responses and the estimation results accordingly.

Therefore, in this section, the impacts of these factors are investigated. By considering these factors, selection of voltage pulse is also discussed. For DC-link capacitance, due to the

limitation of hardware system, it is mainly demonstrated by simulation. For the influence of DC-link resistance, both simulation and experiment results are provided. Both simulation and experiment share the same parameters given in Appendix. In the tests, the proposed method is executed. As described in Section 4.4, 6 voltage pulses are injected and 6 DC-link voltage variations are recorded.

#### 4.5.1 DC-link Measurement Errors

For both conventional and the proposed method, due to existing errors during measurement including scaling error and offset error, the estimation performance may be deteriorated.

For the proposed method, an example is given here for illustration. Two measured DC-link voltage variations  $\Delta V_{dc1}$  and  $\Delta V_{dc}$  are shown in (4.7) and (4.8), their difference is given in (4.9).

$$\Delta V_{dc1} = (1 + \varepsilon_{scale})\Delta V_{dc1_o} + \varepsilon_{offset} \quad (4.7)$$

$$\Delta V_{dc2} = (1 + \varepsilon_{scale})\Delta V_{dc2_o} + \varepsilon_{offset} \quad (4.8)$$

$$\Delta V_{dc1} - \Delta V_{dc2} = (1 + \varepsilon_{scale})(\Delta V_{dc1_o} - \Delta V_{dc2_o}) \quad (4.9)$$

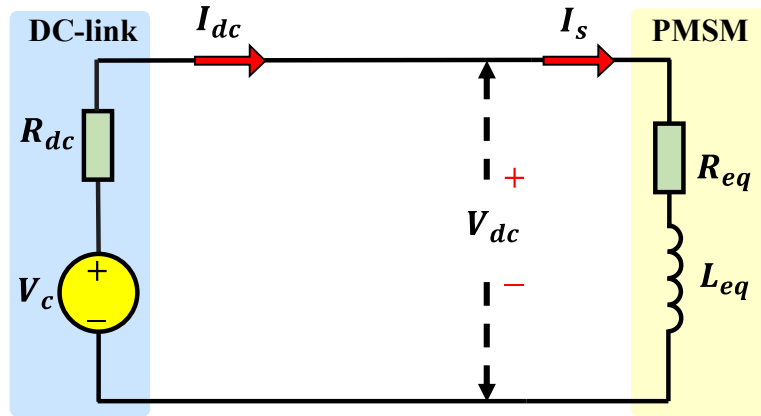
where  $\Delta V_{dc\_o}$  and  $\Delta V_{dc2_o}$  are the original values of DC-link voltage variation,  $\varepsilon_{scale}$  and  $\varepsilon_{offset}$  are scaling and offset errors in the DC-link voltage measurement.

For the proposed method, since only one DC-link voltage sensor is used, each response after excitation shares the same offset and scaling errors with each other. As shown in (4.9), the difference between two voltage responses is not affected by measurement errors. However, for conventional methods that using 2 or more sensors [SCH97][ANK00][LAI03][CHA09], the offsets and scaling errors can be different in different sensors, and therefore, the difference between different responses will be affected, leading to a deteriorated estimation. It is obvious that the proposed method shows the capability of being insensitive to DC-link voltage measurement errors.

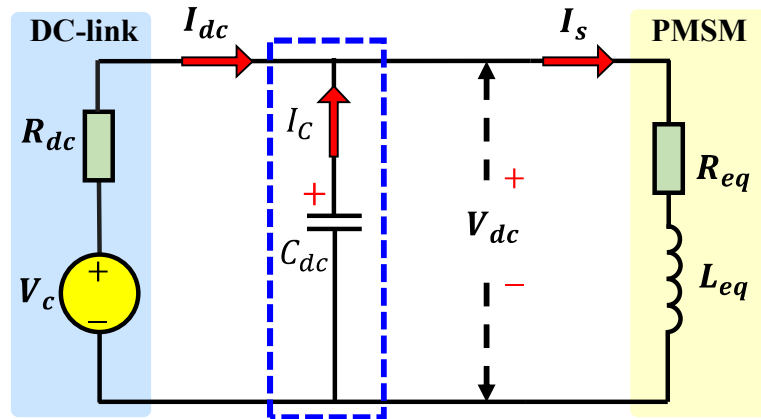
#### 4.5.2 DC-link Capacitance

In Fig. 4.10(a), the basic principle of the proposed method is demonstrated. However, as depicted in Fig. 4.10(b), in practical system, a DC-link capacitor is normally required in the DC

power supply. The DC-link capacitor and the DC-link resistor together form a RC type low pass filter (LPF). Therefore, the influence of this LPF is discussed in this section.



(a)



(b)

Fig. 4.10. Equivalent circuit during excitation. (a) Without DC-link capacitor. (b) With DC-link capacitor. [WU20d]

Firstly, as depicted in Fig. 4.10(a), without considering DC-link capacitor, the DC-link voltage variation during excitation is given as:

$$\Delta V_{dc} = I_s R_{dc} \quad (4.10)$$

where  $I_s = I_{dc}$ .

Then, by considering the DC-link capacitor as shown in Fig. 4.10(b), the DC-link voltage variation given in (8) should be modified to:

$$\Delta V_{dc}(s) = \frac{1}{1 + R_{dc} C_{dc} s} \cdot I_s(s) R_{dc} \quad (4.11)$$

where  $I_s = I_{dc} + I_c$  and  $C_{dc}$  is the DC-link capacitance.

According to (4.11), after considering the DC-link capacitor, the induced DC-link voltage response  $\Delta V_{dc}$  is filtered by the RC LPF. Moreover, referring to (4.11), the cut-off frequency of this RC LPF can be represented as:

$$f_c = \frac{1}{2\pi R_{dc} C_{dc}} \quad (4.12)$$

Apparently, this cut-off frequency depends on the values of DC-link capacitance and DC-link resistance together. It is worth noting that the magnitude of the DC-link voltage response may be decayed after filtering, resulting in a deteriorated estimation.

Fig. 4.11 shows the simulation results of DC-link voltage variation by considering different value of  $C_{dc}$ , i.e. cut-off frequency  $f_c$ . The DC-link resistance is kept same as 0.5ohm. Clearly, the increase of  $C_{dc}$  results in a more decayed voltage response in magnitude.

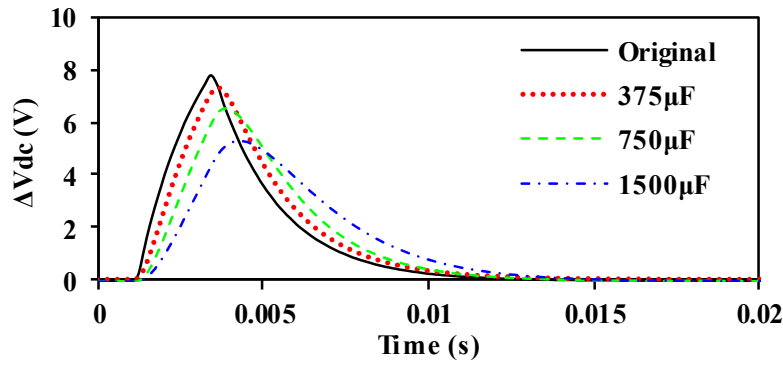


Fig. 4.11. DC-link voltage variation against different DC-link capacitance. [WU20d]

Furthermore, considering two DC-link voltage variations and their differences that are recorded, their filtered values and the original values are presented in Fig. 4.12. Apparently, as  $C_{dc}$  increases, the responses and difference are reduced compared with original values.

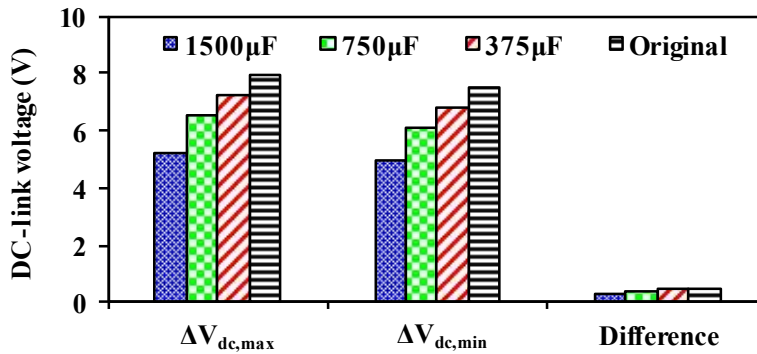


Fig. 4.12. DC-link voltage variations and the difference against different DC-link capacitance.

[WU20d]

In other words, if  $f_c$  is lower, the difference between two voltage variations becomes smaller, which will become vulnerable to noises and disturbances. Under this circumstance, the estimation may become unreliable.

### 4.5.3 DC-link Resistance

As mentioned in Section 4.2, the variation of DC-link voltage  $\Delta V_{dc}(\theta)$  is proportional to DC-link resistance  $R_{dc}$  given in (4.10) without DC-link capacitance  $C_{dc}$ . In the simulation, considering different DC-link resistance, the proposed method using  $\Delta V_{dc}$  and the conventional method using current response  $I_{dc}$  [LEE06] are compared. The conventional method is introduced in Chapter 2. For both methods, after injecting 6 pulses into six positions, the differences between the maximum and minimum of DC-link voltage variations and current responses are compared in Fig. 4.13. Obviously, a larger difference indicates a better estimation performance.

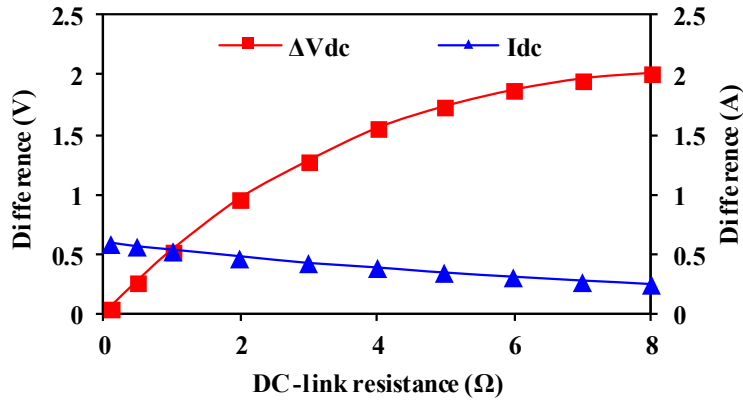


Fig. 4.13. Simulation results of DC-link resistance influence on response difference without DC-link capacitor. [WU20d]

From Fig. 4.13, it is noticed that as DC-link resistance increases, the conventional method utilizing current responses becomes worse due to the decreased current response difference. For the proposed method utilizing DC-link voltage variations, the difference between two DC-link voltage responses increases with DC-link resistance, and thus, a better estimation performance is expected with a larger DC-link resistance. It is worth noting that for some applications, the DC-link resistance is smaller than 1ohm. In this case, an external resistor can be added to the circuit and be switched off after estimation.

However, as earlier mentioned, due to the existence of DC-link capacitance, the variation of DC-link voltage should be modified to (4.11). According to (4.11) and (4.12), as DC-link resistance increases, the cut-off frequency of the LPF decreases correspondingly. Fig. 4.14

shows both the simulation and experiment results of the DC-link voltage variation differences considering  $C_{dc}$ .

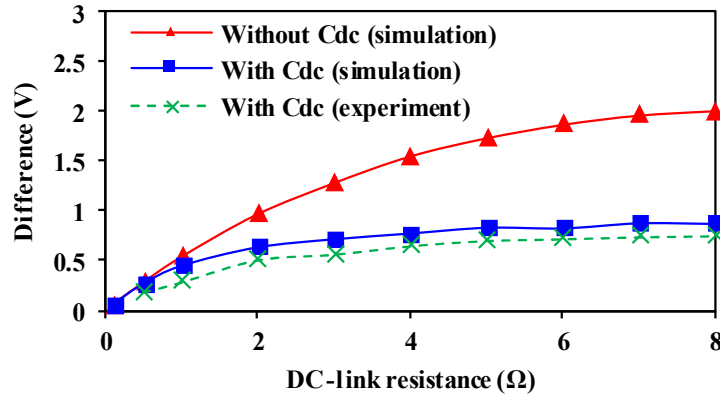


Fig. 4.14. Simulation and experiment results of DC-link resistance influence on response difference with DC-link capacitor. [WU20d]

Obviously, with  $C_{dc}$ , the induced voltage variation differences become smaller compared to the results without  $C_{dc}$ . Moreover, as  $R_{dc}$  increases, the difference of  $\Delta V_{dc}$  firstly increases and then starts to saturate, due to the reduction of cut-off frequency leading to a more decayed magnitude of DC-link voltage response. Although after considering  $C_{dc}$ , the difference of  $\Delta V_{dc}$  becomes smaller compared to that without considering  $C_{dc}$ , generally, a larger DC-link resistance still contributes to a larger difference and is beneficial to position estimation.

#### 4.5.4 DC-link Voltage Ripple

In some applications, there are some ripples existing in the DC-link voltage [LEE14][TAU17][ZHA17]. An example is given in Fig. 4.15, for a diode-based rectifier system, there could be a fluctuation in the DC-link voltage.

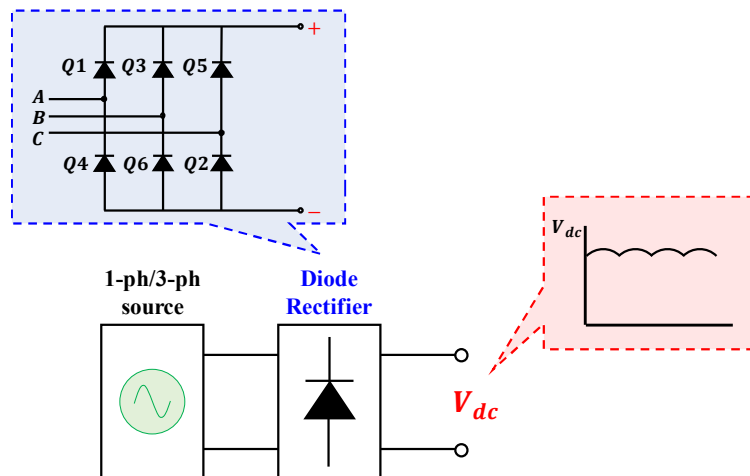


Fig. 4.15. Diode rectifier bridge with ripple in the DC-link voltage. [WU20d]

Meanwhile, some other noises may also cause ripples in the DC-link voltage. For the experimental platform in this chapter, ripples also exist in the DC-link voltage, the measurement

results are depicted in Fig. 4.16. After measurement, the peak-to-peak value of the DC-link voltage ripple is approximately 75mV.

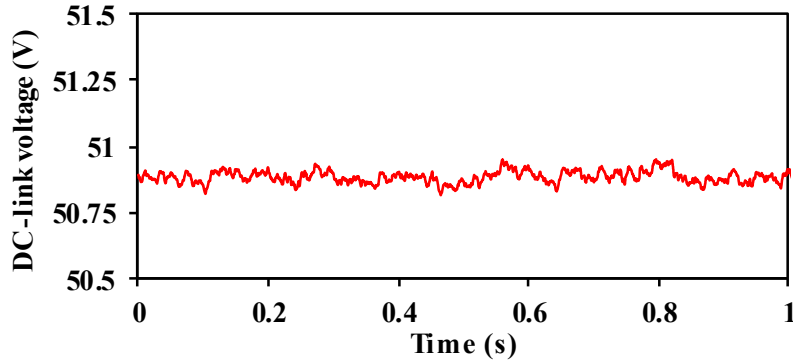


Fig. 4.16. Experiment results of DC-link voltage ripple. [WU20d]

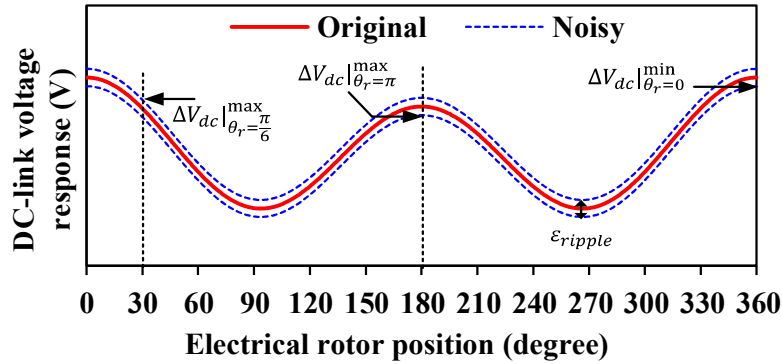


Fig. 4.17. Analytical results of DC-link voltage responses against electrical rotor position. [WU20d]

Since DC-link voltage variation is utilized in this chapter, ripples and noises in DC-link voltage may affect the estimation performance. Clearly, since DC-link voltage variation is utilized, ripples and noises in DC-link voltage may affect the estimation performance. The peak to peak value of the DC-link voltage ripple is defined by  $\varepsilon_{Ripple}$ . Assuming the DC-link voltage ripple exists, the analytical DC-link voltage responses against electrical rotor position can be drawn as shown in Fig. 4.17. The red line shows the ideal DC-link voltage response without any ripples. When considering ripples, the sampled DC-link voltage responses may vary within  $\left(-\frac{\varepsilon_{Ripple}}{2}, \frac{\varepsilon_{Ripple}}{2}\right)$ . Hence, the blue lines are the upper and lower limits of the noisy DC-link voltage responses. The width of upper and lower limits is  $\varepsilon_{Ripple}$ .

Ideally, without considering the DC-link voltage ripple, in order to obtain a 30 degree estimation resolution, the DC-link voltage response should meet two requirements as given by:

$$\Delta V_{dc}|_{\theta_r=0} - \Delta V_{dc}|_{\theta_r=\pi} > 0 \quad (4.13)$$

$$\Delta V_{dc}|_{\theta_r=0} - \Delta V_{dc}|_{\theta_r=\frac{\pi}{6}} > 0 \quad (4.14)$$

(4.13) is used to guarantee that the coil excitation is enough so that the polarity identification result is reliable, otherwise there will be a 180-degree estimation error leading to startup failure or reversal. Furthermore, (4.14) guarantees the estimation resolution within 30 degrees. However, due to the existence of voltage ripples, for each sampled DC-link voltage response, it can vary within the blue lines as demonstrated in Fig. 17. Considering voltage ripples, the requirements of (4.13) and (4.14) are now modified as:

$$\Delta V_{dc}|_{\theta_r=0}^{\min} - \Delta V_{dc}|_{\theta_r=\pi}^{\max} > 0 \quad (4.15)$$

$$\Delta V_{dc}|_{\theta_r=0}^{\min} - \Delta V_{dc}|_{\theta_r=\frac{\pi}{6}}^{\max} > 0 \quad (4.16)$$

Requirements of (14) and (15) can be fulfilled by selecting voltage pulses which will be discussed in the following section. Moreover, it is worth mentioning that for some lower cost applications using passive rectifier with small film DC-link capacitor, the DC-link voltage ripples become significant. It becomes unfeasible to estimate the rotor initial position.

#### 4.5.5 Duration and Magnitude Selection of Voltage Pulse

As discussed before, in practical applications, DC-link resistance, DC-link capacitance and DC-link voltage ripple have influence on the measured DC-link voltage response, which may affect the estimation performance. Therefore, in order to obtain reliable estimation results, magnitude and duration of voltage pulse should be selected appropriately. The basic goal of selection voltage pulse is to guarantee DC-link voltage responses are observable against rotor position while minimizing the induced movement. Besides, enough coil excitation is necessary to produce a difference between south and north poles for polarity identification.

Duration of voltage pulse can be selected according to [LEE09]. In order to obtain a maximum response difference after excitation, an optimal duration of voltage pulse is suggested as around the electrical time constant of the machine as:

$$T_p \approx \frac{L_{eq}}{R_{eq}} \quad (4.17)$$

Furthermore, in the off-line test, this duration should be shortened if the rotor rotates. In this chapter, duration  $T_p$  is initially selected as electrical time constant of the prototype machine.

On the other hand, enough magnitude  $V_p$  of the voltage pulse is necessary to obtain reliable estimation results. As aforementioned, due to existence of DC-link capacitance, DC-link resistance and DC-link voltage ripple, errors exhibit in the measured DC-link voltage. Hence, the measured DC-link voltage variation can be modified as:

$$\Delta V_{dc} = K_{LPF} * \Delta V_{dc0} + \varepsilon_{Ripple} + \varepsilon_{Noise} \quad (4.18)$$

where  $K_{LPF}$  is the decay ratio due to LPF filtering and  $K_{LPF} \leq 1$ ,  $\Delta V_{dc0}$  is the original DC-link voltage variation,  $\varepsilon_{ripple}$  is the error caused by DC-link voltage ripple,  $\varepsilon_{Noise}$  is the error caused by noise during sampling.

Based on (4.15), (4.16) and (4.18), considering both noises and voltage ripples, two modified requirements for selecting voltage pulse in the off-line test are given in (4.19) and (4.20). In (4.19) and (4.20), due to the existence of noise, multiple injections are taken and the average value of voltage responses are calculated.

$$\Delta V_{dc}|_{\Delta\theta_r=0}^{ave} - \Delta V_{dc}|_{\Delta\theta_r=\pi}^{ave} > \varepsilon_{Ripple} + \varepsilon_{Noise} \quad (4.19)$$

$$\Delta V_{dc}|_{\Delta\theta_r=0}^{ave} - \Delta V_{dc}|_{\Delta\theta_r=\frac{\pi}{6}}^{ave} > \varepsilon_{Ripple} + \varepsilon_{Noise} \quad (4.20)$$

Firstly, the polarity identification is considered by (4.19) and sufficient coil excitation should be guaranteed. As shown in (4.19), two opposite pulses with 180 degrees difference are injected. The difference should be large enough to guarantee the polarity identification result as given in (4.19). Secondly, in order to achieve a 30-degree resolution estimation, another requirement should be met as expressed in (4.20). As illustrated by (4.20), two voltage pulses with 30 degrees difference are injected and the difference should fulfill the requirement of (4.20).

In all, in the off-line test, duration  $T_p$  and magnitude  $V_p$  should be adjusted properly to ensure that the difference between different DC-link voltage variations is large enough for position estimation.

## 4.6 Experimental Validation

Experiments are carried out to verify the effectiveness of the proposed method. The experiment is based on a dSPACE system. The parameters of prototype SPM-I are shown in Appendix A. Besides, the parameters of experimental platform is also provided in Appendix. In this section, firstly, based on the hardware system, magnitude and duration of voltage pulse are selected. Then, the rotor initial position estimation process is demonstrated via one example, followed by the overall estimation against different rotor positions. At last, estimation performance against different DC-link resistance and comparison with conventional method using current responses are investigated.

### 4.6.1 Voltage Pulse Selection

As illustrated in Section 4.5, during the selection of voltage pulse, several practical issues should be considered including the DC-link resistance, DC-link capacitance and the DC-link voltage ripples. Therefore, magnitude and duration should be selected properly to make sure the estimation reliable. Based on the experimental platform, the error in the sampled DC-link voltage is measured as 37.5mV, then the difference between voltage variations should be at least larger than 75mV. The cut-off frequency of RC LPF is calculated as 212.2Hz.

After testing, two different sets of the amplitude and duration of the voltage pulse are selected as 100V, 5ms and 230V, 3ms. Hence, the rotor movement or vibration is minimized and a large enough DC-link voltage response is also obtained for rotor initial position estimation.

### 4.6.2 An Estimation Example

An example of rotor initial position estimation with the proposed method is shown in Fig. 4.18.

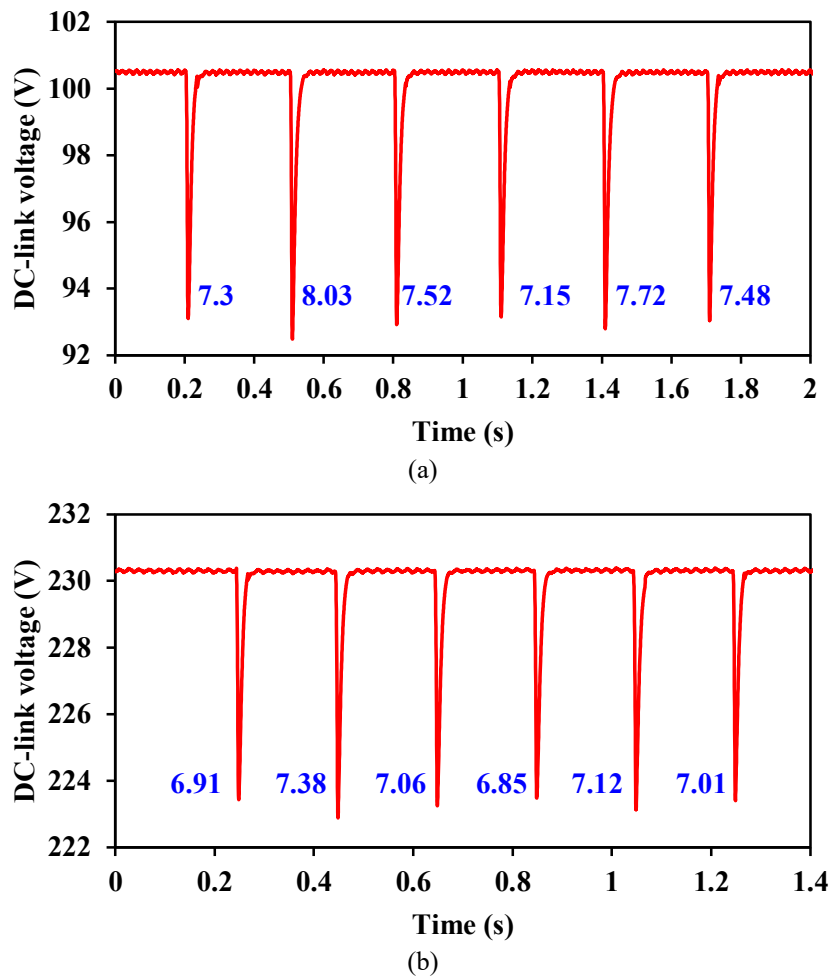
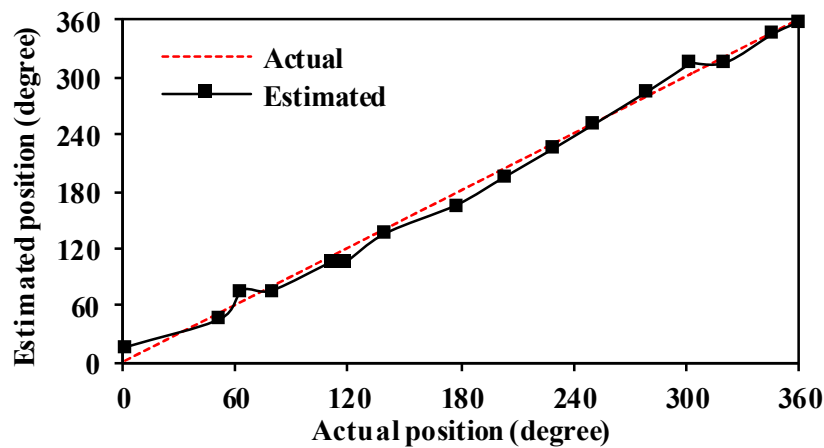


Fig. 4.18. Example of estimation. (a) 100V, 5ms. (b) 230V, 3ms. [WU20d]

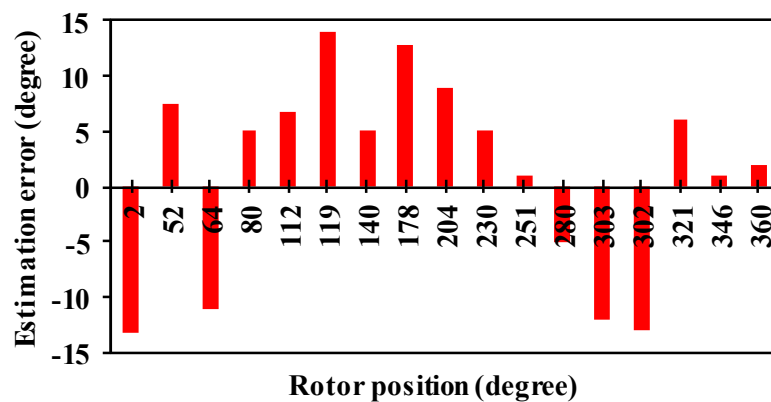
The actual rotor position is at 103 degrees. Six voltage pulses are injected at first, following by injection sequence of 30, 90, 150, 210, 270 and 330 degrees. The DC-link voltage variations are recorded and compared. For both Figs. 4.18(a) and (b), it is found that the largest one is the 2<sup>nd</sup> pulse indicating the rotor locates at 90 degrees. By now, a 60-degree resolution is obtained and the next step is to increase the estimation resolution by comparing the two neighbour voltage variations, i.e. the 1<sup>st</sup> and 3<sup>rd</sup> pulses, it is obvious that the 3<sup>rd</sup> one is larger than the 1<sup>st</sup> one, and therefore the rotor is closer to the position of the 3<sup>rd</sup> one. Hence, the new updated estimation position is 105 degrees. Compared with the actual position, the error is smaller than 15 degrees, and therefore, a 30-degree resolution is obtained at last.

#### 4.6.3 Overall Rotor Initial Position Estimation Performance

The overall estimation performance over different rotor positions of the developed method is illustrated in Fig. 4.19(a) and (b). As can be seen, all the estimation errors of different positions are within 15 degrees, and therefore, a 30-degree resolution is acquired.



(a)



(b)

Fig. 4.19. Overall estimation performance. (a) Position. (b) Error. [WU20d]

#### 4.6.4 Comparison with Estimation Using Current Responses

In this part, conventional estimation method [LEE06] using current response and the proposed estimation using DC-link voltage variation are compared considering different DC-link resistance. 6 voltage pulses are injected to 6 positions, the peak values of phase current responses and the DC-link voltage variations are both recorded. In the test, 100V and 5ms voltage pulse is selected and the real rotor position is fixed at 90 degrees. The peak values of each case are presented in TABLE 4.2,  $\Delta$  represents the difference between maximum and minimum values among the 6 responses in each case. A larger  $\Delta$  indicates a better performance in terms of measurement noises or sensor resolution. In other words, a smaller  $\Delta$  is more sensitive to measurement errors including noises and resolution.

From TABLE 4.2, it can be concluded that as DC-link resistance increases, a larger difference is obtained with the proposed method and a better estimation performance is obtained compared with conventional current response based methods.

TABLE 4.2  
PEAK VALUE COMPARISON BETWEEN PHASE CURRENT AND DC-LINK VOLTAGE VARIATION

Injection position (degree)		30	90	150	210	270	330	$\Delta$
0.5 $\Omega$	$I(A)$	8.027	8.771	8.104	8.043	8.464	8.036	<b>0.75</b>
	$\Delta V_{dc}(V)$	3.58	3.94	3.6	3.59	3.81	3.58	<b>0.36</b>
1 $\Omega$	$I(A)$	7.895	8.614	7.899	7.906	8.291	7.9	<b>0.72</b>
	$\Delta V_{dc}(V)$	7.06	7.85	7.09	7.10	7.53	7.06	<b>0.79</b>
2 $\Omega$	$I(A)$	7.811	8.509	7.887	7.841	8.235	7.888	<b>0.682</b>
	$\Delta V_{dc}(V)$	9.49	10.58	9.56	9.60	10.26	9.6	<b>1.09</b>
5 $\Omega$	$I(A)$	7.725	8.381	7.777	7.736	8.152	7.799	<b>0.656</b>
	$\Delta V_{dc}(V)$	12.2	13.32	12.25	12.04	13.12	12.13	<b>1.12</b>

#### 4.7 Conclusion

In this chapter, a new simple rotor initial position estimation method is presented, which can be used for surface mounted PM machines including brushless dc machines and PMSMs. Different from the conventional methods using phase current sensors or phase voltage sensors,

only one DC-link voltage sensor is utilized. The method provides a 30-degree estimation resolution with maximum error of  $\pm 15^\circ$ . For the proposed method, a specific excitation approach is used to enhance the performance and a so-called ‘equivalent injection position’ is developed to simplify the estimation. Practical issues in the real hardware system are analysed. It is shown that the proposed method is insensitive to sensor measurement errors and shows a better performance with a larger DC-link resistance compared with conventional methods. Finally, the proposed method is verified by experimental results.

# **CHAPTER 5**

## **ROTOR INITIAL POSITION ESTIMATION CONSIDERING PARAMETER ASYMMETRY**

### **5.1 Introduction**

Based on the magnetic saturation effect, several short-pulse-injection-based rotor initial position estimation methods [MAT96][SCH97][NAK00][LAI03][LEE06] [CHA09] are proposed. However, most of the existing methods are based on the symmetrical machine parameters including three-phase inductances and resistances. However, in practical, the three-phase resistances or inductances can be asymmetric. Specifically, resistance asymmetry can be caused by cabling, inverter, and stator windings [REI10][XU16c]. For inductance asymmetry, it can be resulted from mechanical manufacturing tolerance, eccentricity, and winding fault [DEG98][XU16c]. However, for the short-pulse-injection-based rotor initial position estimation, the impact of machine parameter asymmetry is rarely investigated.

Therefore, in this chapter, the rotor initial position estimation under both resistance and inductance asymmetries is investigated. Firstly, the mathematical model of current responses under parameter asymmetries is derived. Then, based on the developed model, the impact of parameter asymmetries on position estimation is discussed. Furthermore, an impact indicator called ‘feasible estimation area ratio’ is defined to quantify the impact of parameter asymmetries on position estimation. Moreover, two compensation methods are proposed considering parameter asymmetries. The first method can be used to reduce the impact of resistance asymmetry and the second one can be used for both inductance and resistance asymmetries. The effectiveness of these two methods are examined by simulation results.

### **5.2 Current Response Model**

In this section, the current response model with both symmetrical and asymmetric parameters are derived. Based on the developed model, the impact of parameter asymmetry is then analysed.

### 5.2.1 Parameter Symmetry

For a symmetrical parameter system, the voltage model associating with arbitrary phase current at standstill is given by:

$$V_{DC} = R_{eq,X} i_X + L_{eq,X} \frac{di_X}{dt} \quad (5.1)$$

where  $X$  represent the arbitrary phase,  $L_{eq,X}$  and  $R_{eq,X}$  are equivalent resistance and inductance of the arbitrary injected pulse. According to [MAT96],  $L_{eq,X}$  and  $R_{eq,X}$  of three-phase can be derived as:

$$L_{eq,A} = \frac{4}{9} \frac{L_0^2 - L_2^2}{L_0 + L_2 \cos(2\theta_r)} \quad (5.2)$$

$$L_{eq,B} = \frac{4}{9} \frac{L_0^2 - L_2^2}{L_0 + L_2 \cos(2\theta_r + 2\pi/3)} \quad (5.3)$$

$$L_{eq,C} = \frac{4}{9} \frac{L_0^2 - L_2^2}{L_0 + L_2 \cos(2\theta_r - 2\pi/3)} \quad (5.4)$$

$$R_{eq,A} = R_{eq,B} = R_{eq,C} = \frac{3}{2} R \quad (5.5)$$

where  $L_0$  and  $L_2$  are the amplitudes of DC and the 2<sup>nd</sup> order harmonic components of self-inductance, respectively.  $R$  is the nominal value of phase resistance.

For voltage pulse injection based method, the injected voltage can be assumed as a step input, then the phase current response is given by:

$$i_X(t) = \frac{V_{DC}}{R_{eq,X}} (1 - e^{-\frac{t}{L_{eq,X}/R_{eq,X}}}) \quad (5.6)$$

However, current response in this nonlinear form is difficult for analysis. In order to simplify the analysis, according to [MAT96], three-phase current responses can be modelled as a function of rotor position in (5.7). Furthermore, the current response model considering parameter asymmetry will also be developed based on (5.7).

$$\begin{aligned}
I_A &= I_0 + I_2 \cos(2\theta_r) \\
I_B &= I_0 + I_2 \cos\left(2\left(\theta_r - \frac{2\pi}{3}\right)\right) \\
I_C &= I_0 + I_2 \cos\left(2\left(\theta_r + \frac{2\pi}{3}\right)\right)
\end{aligned} \tag{5.7}$$

where  $I_0$  and  $I_2$  are the amplitudes of DC offset and the 2<sup>nd</sup> order harmonic components of the current response, respectively.

Then, the simulated three-phase current responses with symmetrical parameters are shown in Fig. 5.1.

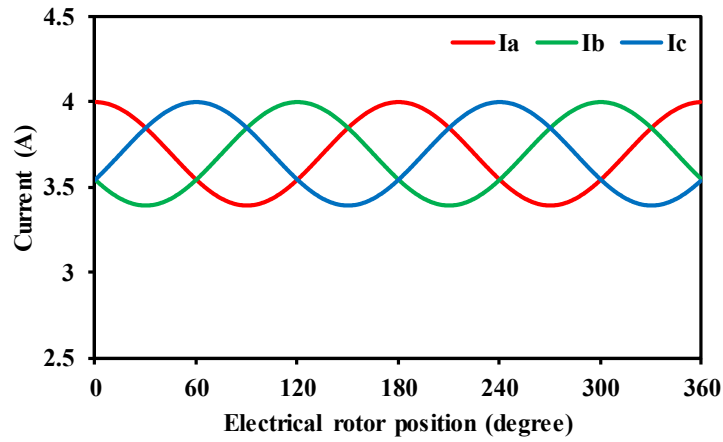


Fig. 5.1. Current responses against electrical rotor position with symmetrical parameters.

Normally, parameters including three-phase resistances and three-phase self-inductances are considered as balanced. Hence, the three-phase current responses are balanced as shown in Fig. 5.1. However, practically, the resistance and inductance may be asymmetric. Hence, the three-phase current responses under both resistance and inductance asymmetries are investigated in the next section.

### 5.2.2 Resistance Asymmetry

Three-phase resistances can be asymmetric due to cabling, inverter, and stator windings. Under asymmetry, the three-phase resistances are represented as:

$$\begin{aligned}
R_A &= R + \Delta R_A \\
R_B &= R + \Delta R_B \\
R_C &= R + \Delta R_C
\end{aligned} \tag{5.8}$$

where  $R_A$ ,  $R_B$  and  $R_C$  are three-phase resistances,  $R$  is the nominal value of three-phase resistances,  $\Delta R_A$ ,  $\Delta R_B$  and  $\Delta R_C$  are the unbalance terms in the three-phase resistances. Then, under resistance asymmetry, the three-phase equivalent resistances in (5.5) are modified as:

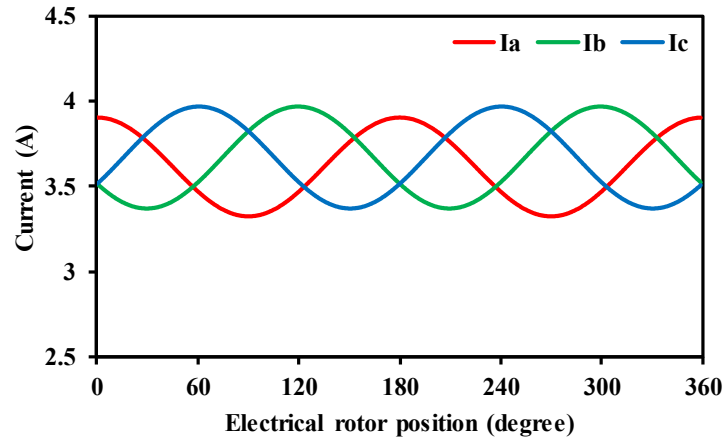
$$R_{eq,A} = R_A + \frac{R_B R_C}{R_B + R_C} = R + \Delta R_A + \frac{(R + \Delta R_B)(R + \Delta R_C)}{2R + \Delta R_B + \Delta R_C} \quad (5.9)$$

$$R_{eq,B} = R_B + \frac{R_A R_C}{R_A + R_C} = R + \Delta R_B + \frac{(R + \Delta R_A)(R + \Delta R_C)}{2R + \Delta R_A + \Delta R_C} \quad (5.10)$$

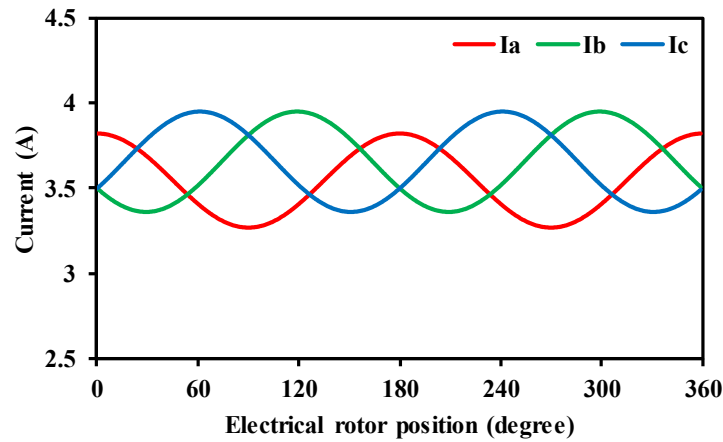
$$R_{eq,C} = R_C + \frac{R_A R_B}{R_A + R_B} = R + \Delta R_C + \frac{(R + \Delta R_A)(R + \Delta R_B)}{2R + \Delta R_A + \Delta R_B} \quad (5.11)$$

Then, simulation considering three-phase resistance asymmetry is carried out. In the simulation, both one-phase and two-phase resistance asymmetric cases are considered. For both cases, different levels of asymmetry are also simulated.

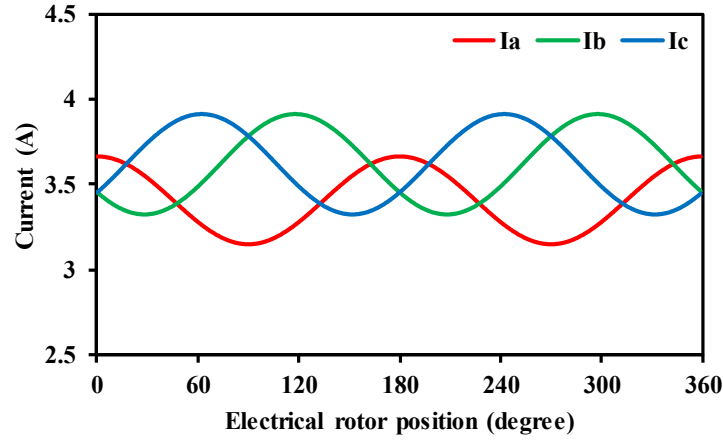
Firstly, one-phase resistance asymmetry is considered. In this test, it is assumed that the unbalance component only exists in phase A. Moreover, different values of  $\Delta R_A$  are simulated ( $\Delta R_A = 1\Omega$  (25% $R$ ),  $2\Omega$  (50% $R$ ),  $4\Omega$  (100% $R$ )). The simulation results of current responses under one-phase resistance asymmetry are shown in Fig. 5.2.



(a)



(b)

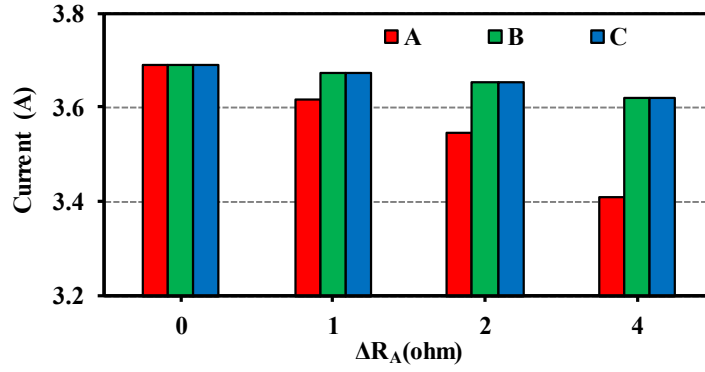


(c)

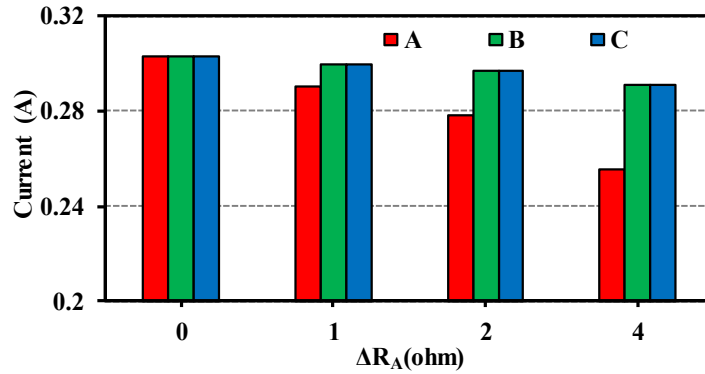
Fig. 5.2. Current responses against electrical rotor position with one-phase resistance asymmetry.

(a)  $\Delta R_A = 1\Omega$  (25% $R$ ). (b)  $\Delta R_A = 2\Omega$  (50% $R$ ). (c)  $\Delta R_A = 4\Omega$  (100% $R$ ).

Then, the harmonic spectra of current responses with different  $\Delta R_A$  are shown in Fig. 5.3.



(a)



(b)

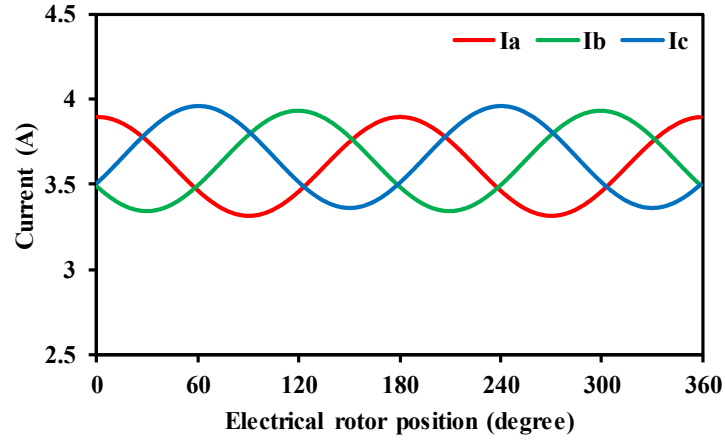
Fig. 5.3. Harmonic spectra of current responses with one-phase resistance asymmetry. (a) DC offset.

(b) 2<sup>nd</sup> order hamronic.

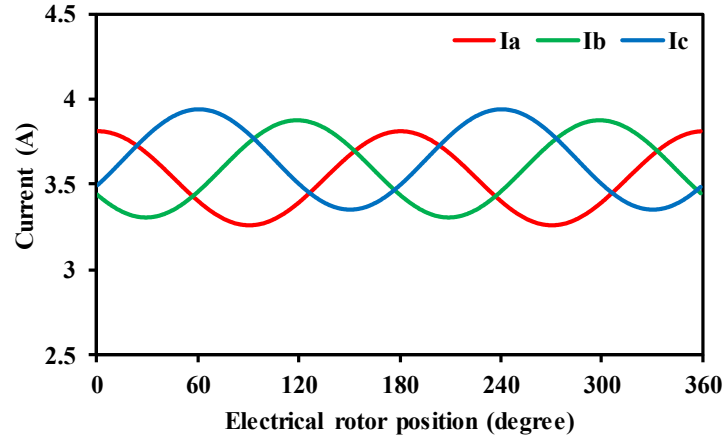
Based on the results in Fig. 5.2 and Fig. 5.3, it is found that for the phase A current response, the amplitudes of DC offset and the 2<sup>nd</sup> order harmonic decrease as  $\Delta R_A$  becomes larger.

Next, two-phase resistance asymmetry is considered. In the test, unbalance components exist in both phase A and B. Different values of  $\Delta R_A$  and  $\Delta R_B$  are simulated ( $\Delta R_A =$

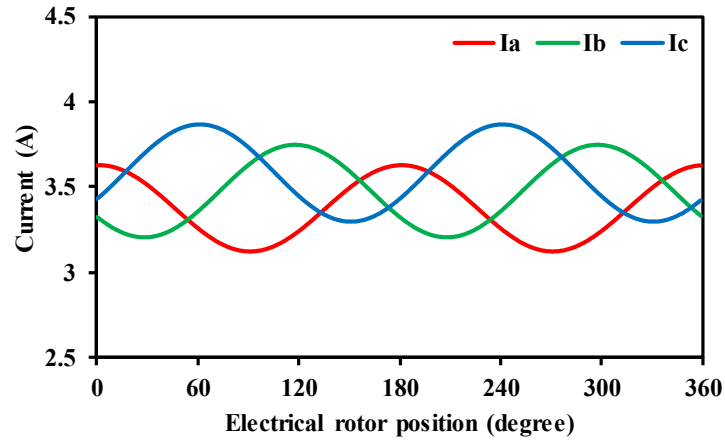
$1\Omega$  (25% $R$ ),  $\Delta R_B = 0.5\Omega$  (12.5% $R$ ) ,  $\Delta R_A = 2\Omega$  (50% $R$ ),  $\Delta R_B = 1\Omega$  (25% $R$ ) ,  $\Delta R_A = 4\Omega$  (100% $R$ ),  $\Delta R_B = 2\Omega$  (50% $R$ )). The simulation results of current responses under two-phase resistance asymmetry are shown Fig. 5.4.



(a)



(b)



(c)

Fig. 5.4. Current responses against electrical rotor position with two-phase resistance asymmetry. (a)  $\Delta R_A = 1\Omega$  (25% $R$ ),  $\Delta R_B = 0.5\Omega$  (12.5% $R$ ). (b)  $\Delta R_A = 2\Omega$  (50% $R$ ),  $\Delta R_B = 1\Omega$  (25% $R$ ). (c)  $\Delta R_A = 4\Omega$  (100% $R$ ),  $\Delta R_B = 2\Omega$  (50% $R$ ).

Then, the harmonic spectra of current response with different  $\Delta R_A$  and  $\Delta R_B$  are shown in Fig. 5.5.

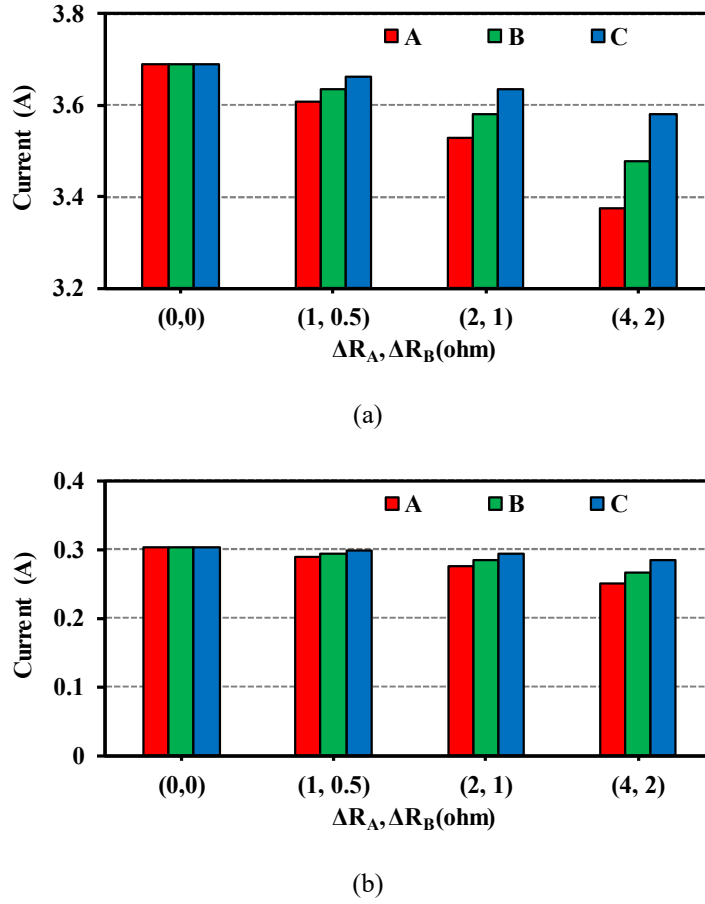


Fig. 5.5. Harmonic spectra of current responses with two-phase resistance asymmetry. (a) DC offset. (b) 2<sup>nd</sup> order harmonic.

Based on the results shown in Fig. 5.4 and Fig. 5.5, the conclusions are similar to the one phase case. Higher unbalance level decreases the amplitudes of DC offset and the 2<sup>nd</sup> order harmonic in the unbalanced phase current response.

Based on the simulation results, the current response model in (5.7) is modified considering resistance asymmetry. The equivalent mathematical model of the three-phase current responses under resistance asymmetry is derived as:

$$\begin{aligned}
 I_A &\approx \Delta I_{RA} + I_0 + K_{\Delta RA} \cdot I_2 \cos(2\theta_r) \\
 I_B &\approx \Delta I_{RB} + I_0 + K_{\Delta RB} \cdot I_2 \cos\left(2\left(\theta_r - \frac{2\pi}{3}\right)\right) \\
 I_C &\approx \Delta I_{RC} + I_0 + K_{\Delta RC} \cdot I_2 \cos\left(2\left(\theta_r + \frac{2\pi}{3}\right)\right)
 \end{aligned} \tag{5.12}$$

where  $\Delta I_{RA}$ ,  $\Delta I_{RB}$  and  $\Delta I_{RC}$  are DC offsets in the current responses due to resistance asymmetry.  $K_{\Delta RA}$ ,  $K_{\Delta RB}$  and  $K_{\Delta RC}$  are the gains of current responses due to resistance asymmetry. Besides, for  $\Delta I_{RA}$ ,  $\Delta I_{RB}$ ,  $\Delta I_{RC}$ ,  $K_{\Delta RA}$ ,  $K_{\Delta RB}$  and  $K_{\Delta RC}$ , their relationship with  $\Delta R_A$ ,  $\Delta R_B$  and  $\Delta R_C$  are given by:

$$\begin{aligned}\Delta I_{RA} &\approx k_{R0} \cdot \Delta R_A \\ \Delta I_{RB} &\approx k_{R0} \cdot \Delta R_B \\ \Delta I_{RC} &\approx k_{R0} \cdot \Delta R_C\end{aligned}\tag{5.13}$$

$$\begin{aligned}K_{\Delta RA} &\approx k_{R2}/\Delta R_A \\ K_{\Delta RB} &\approx k_{R2}/\Delta R_B \\ K_{\Delta RC} &\approx k_{R2}/\Delta R_C\end{aligned}\tag{5.14}$$

where  $k_{R0}$  is the equivalent gain of DC offset in current response due to resistance asymmetry and  $k_{R0} < 0$ .  $k_{R2}$  is the equivalent gain of the 2<sup>nd</sup> order harmonic in current response due to resistance asymmetry.

### 5.2.3 Inductance Asymmetry

Apart from resistance, inductance can also be asymmetric due to mechanical manufacturing tolerance, machine eccentricity and winding fault. Assuming that three-phase self-inductances are asymmetric and the inductance matrix can be expressed as:

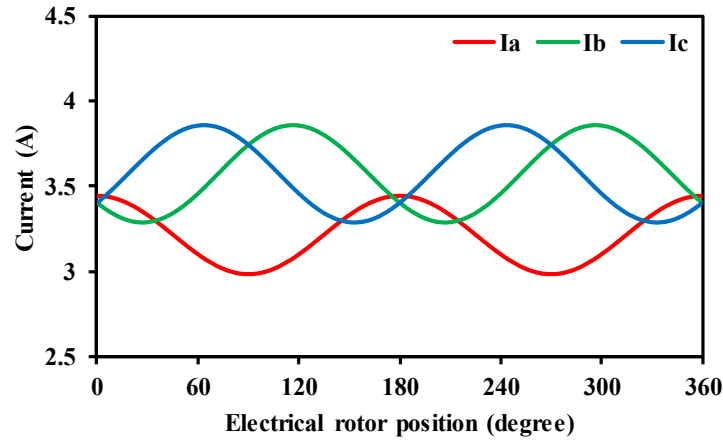
$$L(a, b, c) = \begin{bmatrix} L_{AA} & M_{AB} & M_{AC} \\ M_{BA} & L_{BB} & M_{BC} \\ M_{CA} & M_{CB} & L_{CC} \end{bmatrix} + \begin{bmatrix} \Delta L_A & 0 & 0 \\ 0 & \Delta L_B & 0 \\ 0 & 0 & \Delta L_C \end{bmatrix}\tag{5.15}$$

$$\begin{aligned}L_{AA} &= L_0 - L_2 \cos(2\theta_r) & M_{AB} &= M_{BA} = \frac{1}{2}L_0 - L_2 \left(2(\theta_r + \frac{2\pi}{3})\right) \\ L_{BB} &= L_0 - L_2 \cos\left(2(\theta_r - \frac{2\pi}{3})\right) & M_{BC} &= M_{CB} = \frac{1}{2}L_0 - L_2 \cos(2\theta_r) \\ L_{CC} &= L_0 - L_2 \left(2(\theta_r + \frac{2\pi}{3})\right) & M_{CA} &= M_{AC} = \frac{1}{2}L_0 - L_2 \left(2(\theta_r - \frac{2\pi}{3})\right)\end{aligned}\tag{5.16}$$

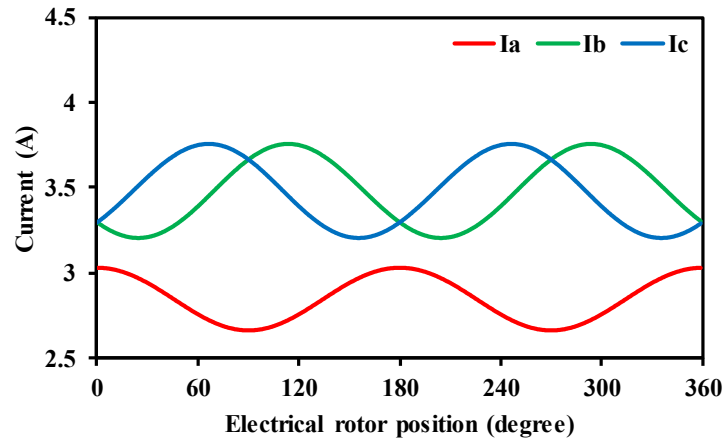
where  $L_{AA}$ ,  $L_{BB}$  and  $L_{CC}$  are three-phase self-inductances.  $M_{AB}$ ,  $M_{BA}$ ,  $M_{BC}$ ,  $M_{CB}$ ,  $M_{CA}$  and  $M_{AC}$  are the three-phase mutual inductances.  $\Delta L_A$ ,  $\Delta L_B$  and  $\Delta L_C$  are the unbalanced terms in three-phase self-inductances. Similar to the resistance case, simulation is firstly carried out by considering different cases of inductance asymmetry. Based on the results, an equivalent mathematical model of current response under inductance asymmetry is then summarized.

Since the self-inductance is much larger than the mutual-inductance, the analysis is mainly based on self-inductance. Hence, one-phase and two-phase self-inductance asymmetric cases are considered.

Firstly, one-phase self-inductance asymmetry case is simulated. In this case, unbalance component only exists in phase A. Different values of  $\Delta L_A$  are simulated ( $\Delta L_A = 4mH(25\%L_0)$ ,  $\Delta L_A = 8mH(50\%L_0)$ ). The simulation results of current responses under inductance asymmetry are shown in Fig. 5.6.



(a)



(b)

Fig. 5.6. Current responses against electrical rotor position with one-phase self-inductance asymmetry. (a)  $\Delta L_A = 4mH (25\%L_0)$ . (b)  $\Delta L_A = 8mH (50\%L_0)$ .

Then, the harmonic spectra of current responses with different  $\Delta L_A$  are shown in Fig. 5.7.

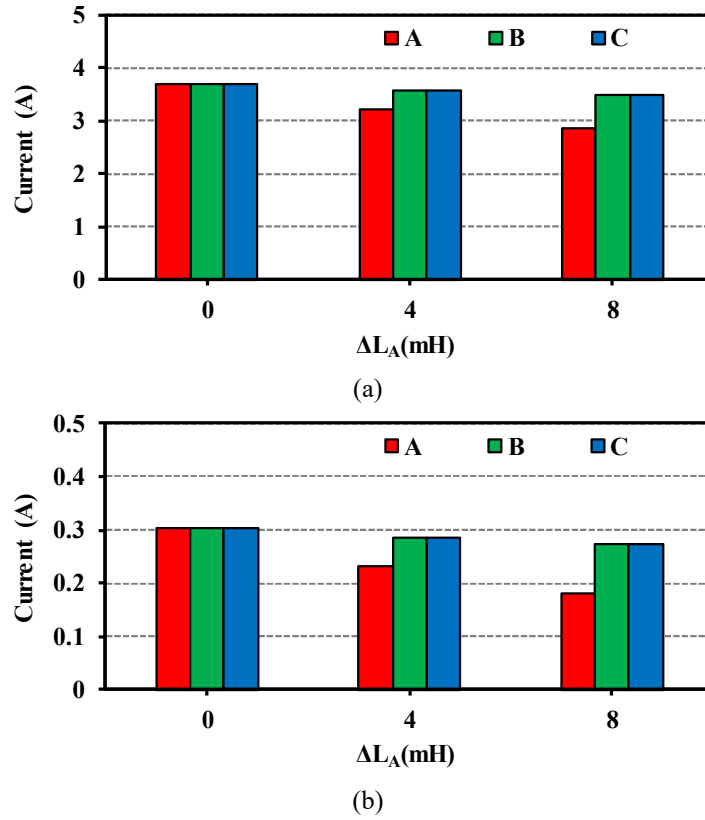
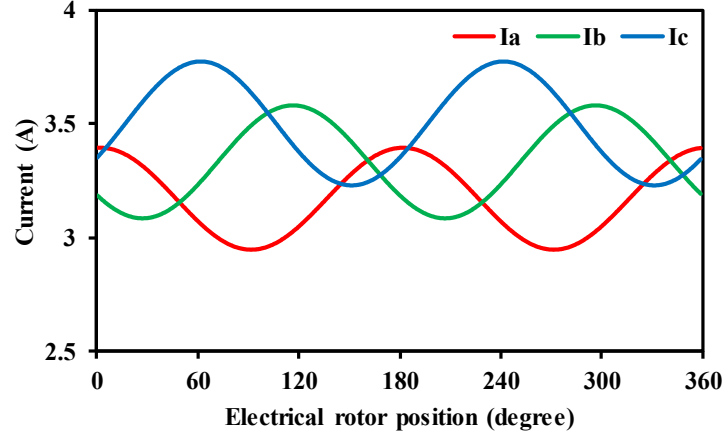


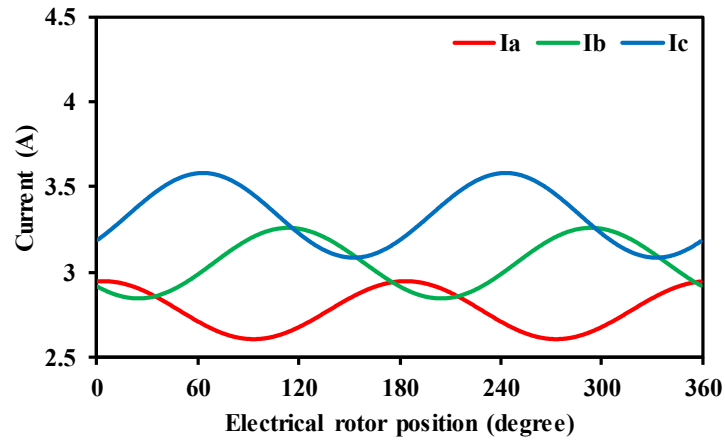
Fig. 5.7. Harmonic spectra of current responses with one-phase self-inductance asymmetry. (a) DC offset. (b) 2<sup>nd</sup> order harmonic.

Based the results shown in Fig. 5.6 and Fig. 5.7, the conclusions are similar to the resistance asymmetry case. A higher unbalance level decreases the DC offset and the 2<sup>nd</sup> order harmonic of the unbalanced phase current response. Besides, as shown in Fig. 5.6, if  $\Delta L_A$  is large enough, phase A current will be always smaller than the other two phase currents. Phase A current will be completely masked by the other two phase current responses in the estimation. Consequently, the estimation in the sectors related to phase A will be incorrect.

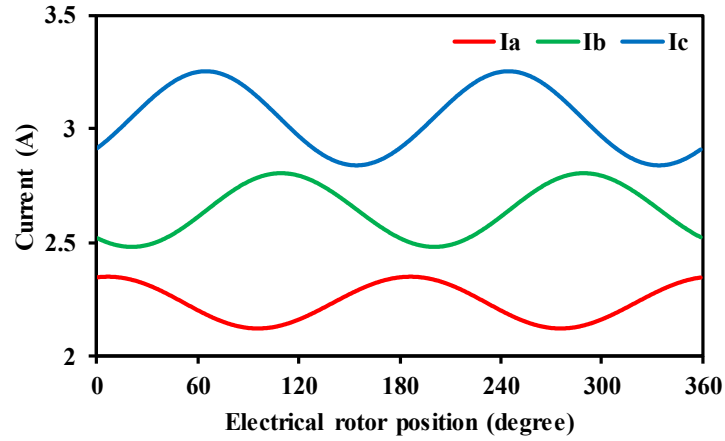
Next, two-phase self-inductance asymmetric case is considered. In this case, unbalance components exist in both phase A and phase B. Different values of  $\Delta L_A$  and  $\Delta L_B$  are simulated ( $\Delta L_A = 4\text{mH}$  (25% $L_0$ ),  $\Delta L_B = 2\text{mH}$  (12.5% $L_0$ ),  $\Delta L_A = 8\text{mH}$  (50% $L_0$ ),  $\Delta L_B = 4\text{mH}$  (25% $L_0$ ),  $\Delta L_A = 16\text{mH}$  (100% $L_0$ ),  $\Delta L_B = 8\text{mH}$  (50% $L_0$ )). The simulation results of current responses under two-phase self-inductance asymmetry are shown in Fig. 5.8.



(a)



(b)



(c)

Fig. 5.8. Current responses against electrical rotor position with two-phase self-inductance asymmetry. (a)  $\Delta L_A = 4mH$  ( $25\%L_0$ ),  $\Delta L_B = 2mH$  ( $12.5\%L_0$ ). (b)  $\Delta L_A = 8mH$  ( $50\%L_0$ ),  $\Delta L_B = 4mH$  ( $25\%L_0$ ). (c)  $\Delta L_A = 16mH$  ( $100\%L_0$ ),  $\Delta L_B = 8mH$  ( $50\%L_0$ ).

Then, the harmonic spectra of current response with different  $\Delta L_A$  and  $\Delta L_B$  are shown in Fig. 5.7.

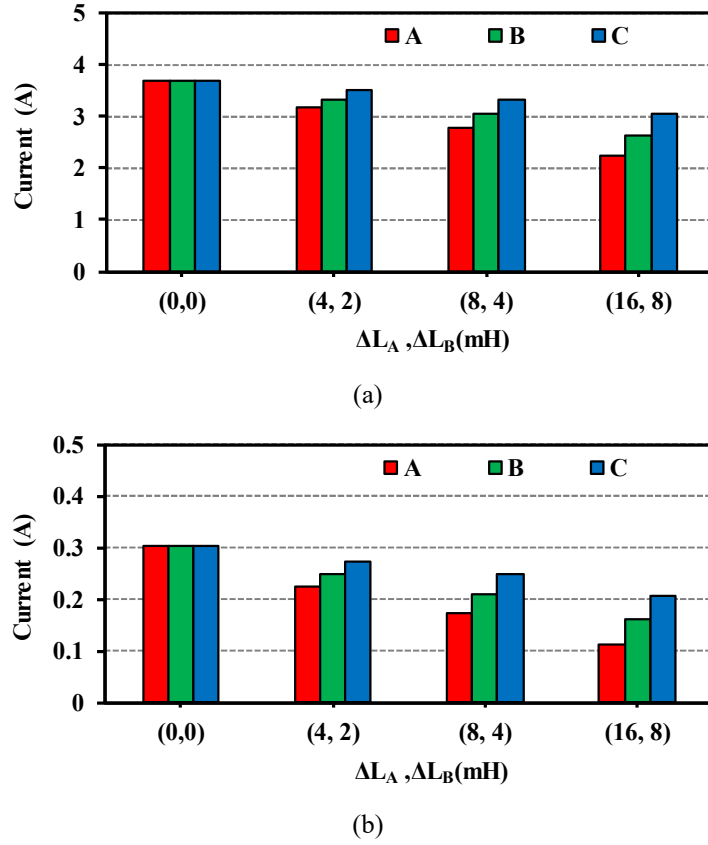


Fig. 5.9. Harmonic spectra of current responses with two-phase self-inductance asymmetry. (a) DC offset. (b) 2<sup>nd</sup> order harmonic.

For the two-phase inductance asymmetric case, higher unbalance component will make the DC offset and the 2<sup>nd</sup> order harmonic of the current response decrease in the unbalanced phase. Same as the one-phase case, when  $\Delta L_A$  and  $\Delta L_B$  are large enough, phases A and B currents will be always smaller than phase C current. The estimation in sectors related to phase A and B will be incorrect.

Based on the phenomena of inductance asymmetry, the equivalent mathematical model of three-phase current responses under inductance asymmetry can be derived as:

$$\begin{aligned}
 I_A &\approx \Delta I_{L_A} + I_0 + K_{\Delta L_A} I_2 \cos(2\theta_r) \\
 I_B &\approx \Delta I_{L_B} + I_0 + K_{\Delta L_B} I_2 \cos\left(2\left(\theta_r - \frac{2\pi}{3}\right)\right) \\
 I_C &\approx \Delta I_{L_C} + I_0 + K_{\Delta L_C} I_2 \cos\left(2\left(\theta_r + \frac{2\pi}{3}\right)\right)
 \end{aligned} \tag{5.17}$$

where  $\Delta I_{L_A}$ ,  $\Delta I_{L_B}$  and  $\Delta I_{L_C}$  are the DC offsets in the current responses due to inductance asymmetry.  $K_{\Delta L_A}$ ,  $K_{\Delta L_B}$  and  $K_{\Delta L_C}$  are the gains of the current responses due to inductance asymmetry. Besides, for  $\Delta I_{R_A}$ ,  $\Delta I_{R_B}$ ,  $\Delta I_{R_C}$ ,  $K_{\Delta L_A}$ ,  $K_{\Delta L_B}$  and  $K_{\Delta L_C}$ , they can be represented as:

$$\begin{aligned}
\Delta I_{L_A} &\approx k_{L0} \cdot \Delta L_A \\
\Delta I_{L_B} &\approx k_{L0} \cdot \Delta L_B \\
\Delta I_{L_C} &\approx k_{L0} \cdot \Delta L_C
\end{aligned} \tag{5.18}$$

$$\begin{aligned}
K_{\Delta L_A} &\approx k_{L2}/\Delta L_A \\
K_{\Delta L_B} &\approx k_{L2}/\Delta L_B \\
K_{\Delta L_C} &\approx k_{L2}/\Delta L_C
\end{aligned} \tag{5.19}$$

where  $k_{L0}$  is the equivalent gain of DC offset in current response due to inductance asymmetry and  $k_{L0} < 0$ .  $k_{L2}$  is the equivalent gain of the 2<sup>nd</sup> order harmonic in current response due to inductance asymmetry.

## 5.2.4 Summary

Based on the current responses under resistance and inductance asymmetries, the general current response model under parameter asymmetry can be derived as:

$$\begin{aligned}
I_A &\approx (\Delta I_{R_A} + \Delta I_{L_A}) + I_0 + (K_{\Delta R_A} \cdot K_{\Delta L_A}) \cdot I_2 \cos(2\theta_r) \\
I_B &\approx (\Delta I_{R_B} + \Delta I_{L_B}) + I_0 + (K_{\Delta R_B} \cdot K_{\Delta L_B}) \cdot I_2 \cos\left(2\left(\theta_r - \frac{2\pi}{3}\right)\right) \\
I_C &\approx (\Delta I_{R_C} + \Delta I_{L_C}) + I_0 + (K_{\Delta R_C} \cdot K_{\Delta L_C}) \cdot I_2 \cos\left(2\left(\theta_r + \frac{2\pi}{3}\right)\right)
\end{aligned} \tag{5.20}$$

Then, (5.20) can be simplified as:

$$\begin{aligned}
I_A &\approx I_{A0}^u + I_{A2}^u \cos(2\theta_r) \\
I_B &\approx I_{B0}^u + I_{B2}^u \cos\left(2\left(\theta_r - \frac{2\pi}{3}\right)\right) \\
I_C &\approx I_{C0}^u + I_{C2}^u \cos\left(2\left(\theta_r + \frac{2\pi}{3}\right)\right)
\end{aligned} \tag{5.21}$$

$$\begin{aligned}
I_{A0}^u &= I_0 + \Delta I_{R_A} + \Delta I_{L_A} \\
I_{B0}^u &= I_0 + \Delta I_{R_B} + \Delta I_{L_B} \\
I_{C0}^u &= I_0 + \Delta I_{R_C} + \Delta I_{L_C}
\end{aligned} \tag{5.22}$$

$$\begin{aligned}
I_{A2}^u &= K_{\Delta R_A} \cdot K_{\Delta L_A} \cdot I_2 \\
I_{B2}^u &= K_{\Delta R_B} \cdot K_{\Delta L_B} \cdot I_2 \\
I_{C2}^u &= K_{\Delta R_C} \cdot K_{\Delta L_C} \cdot I_2
\end{aligned} \tag{5.23}$$

where  $I_{A0}^u$ ,  $I_{B0}^u$  and  $I_{C0}^u$  are the DC offsets in three-phase current responses under parameter asymmetries,  $I_{A2}^u$ ,  $I_{B2}^u$  and  $I_{C2}^u$  are the amplitudes of the 2<sup>nd</sup> order harmonic in three-phase current responses under parameter asymmetries.

In summary, for both resistance and inductance asymmetries, the unbalanced phase will have reduced amplitudes of DC and the 2<sup>nd</sup> order harmonic. As the unbalance level increases,

there is more reduction. If the unbalanced level keeps increasing, the unbalanced phase current will be always smaller than other phase currents. The estimation in the sectors related to unbalanced phase will be incorrect in this case.

### 5.3 Position Estimation under Parameter Asymmetries

In this section, the impacts of parameter asymmetries on the rotor initial position estimation are investigated. The investigation is firstly based on a conventional method presented in [SCH97] by simulation.

Firstly, voltage pulses are injected into 6 positions by selecting 6 voltage vectors of a 3-phase voltage inverter (V1~V6), as shown in Fig. 2.5. Then, the estimated sector is determined by looking at the largest current response. For the conventional method, the estimation sectors are shown in Fig. 5.11.

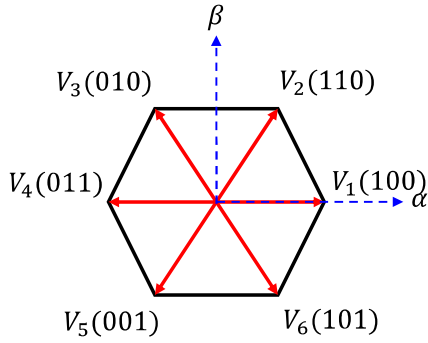


Fig. 5.10. Voltage vectors.

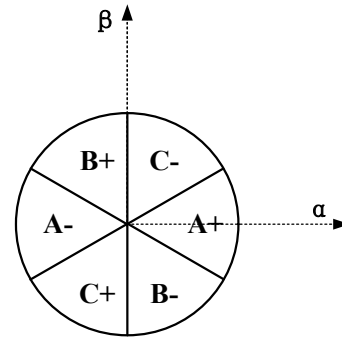


Fig. 5.11. Estimation sectors.

Then, the current responses against rotor position associated with the estimation sectors are shown in Fig. 5.12.

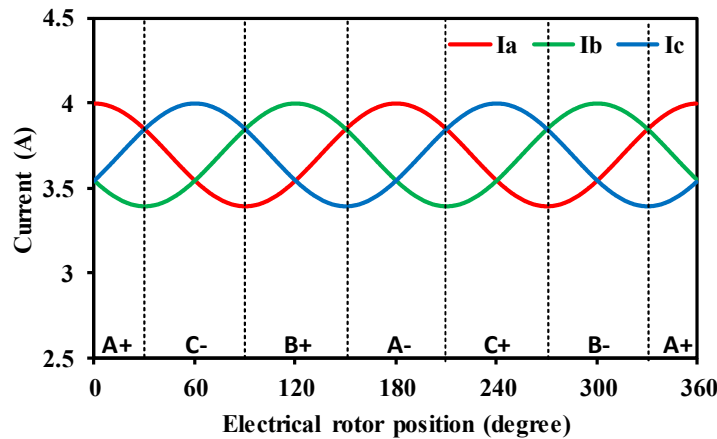


Fig. 5.12. Current responses against electrical rotor position with symmetrical parameters.

In Fig. 5.12, the black dotted lines indicate the ideal evenly distributed boundaries between

sectors. If the parameters are symmetrical, the estimation sectors are distributed evenly by 60 degrees for each sector. In each sector, only one phase current should be the largest so that the rotor initial position can be determined at the correct sector.

Furthermore, the position estimation performance with symmetrical parameters is shown in Fig. 5.13. Under ideal condition, the maximum position estimation error is 30 degrees.

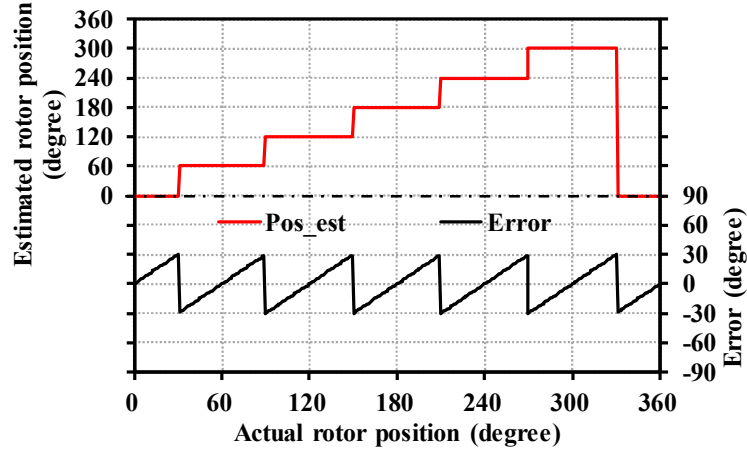
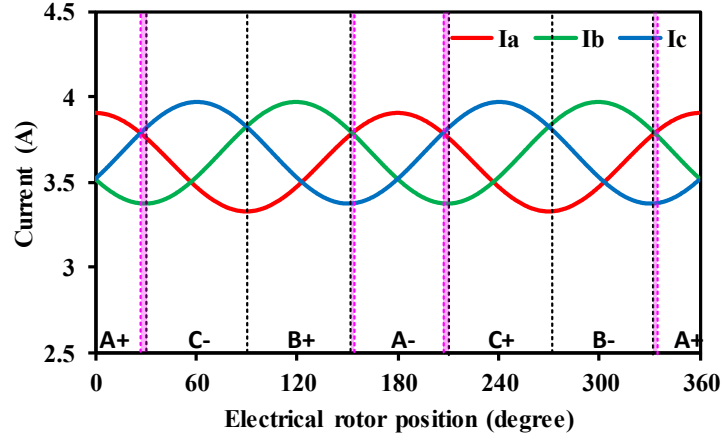


Fig. 5.13. Current responses against electrical rotor position with parameter symmetry.

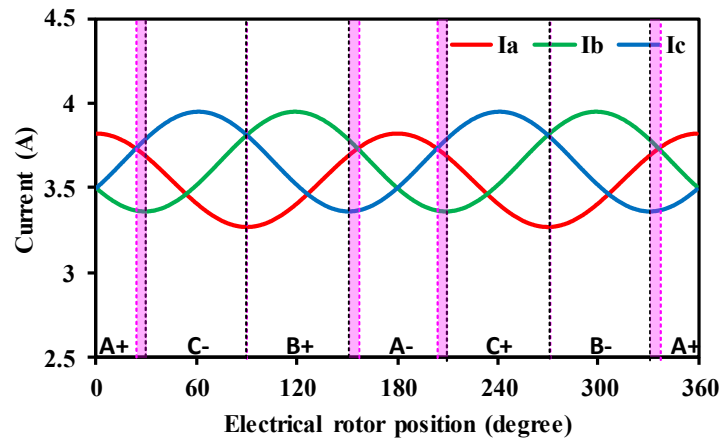
However, under parameter asymmetries, as discussed in Section 5.2, the three-phase current responses are unbalanced. Therefore, the estimation sectors become unevenly distributed and the position estimation performance will be affected. In the following sections, the resistance and inductance asymmetry impact on position estimation will be investigated based on the simulation in this section. Moreover, an indicator called ‘feasible estimation area ratio’ is defined and used to simply quantify the impact of parameter asymmetry on position estimation.

### 5.3.1 Resistance Asymmetry

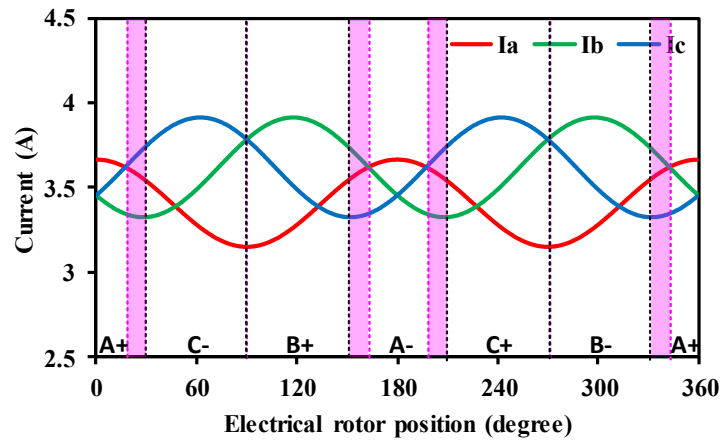
Firstly, the impact of resistance asymmetry on position estimation is investigated. Both one-phase and two-phase resistance asymmetric cases are considered. In Fig. 5.14, three-phase current responses under one-phase resistance asymmetry are shown first. Besides, the estimation performance is shown in Fig. 5.15. In Fig. 5.14, the pink dotted lines are the boundaries between unevenly distributed sectors due to parameter asymmetries. The interaction area between the black and pink lines is highlighted as pink blocks. If the rotor initial position locates in these pink block areas, the estimation will go wrong. The total angle span of all these pink block areas is defined as  $A_{Est\_wrong}$  (degree). Clearly, as  $A_{Est\_wrong}$  increases, the estimation performance will be more deteriorated, Fig. 5.15.



(a)



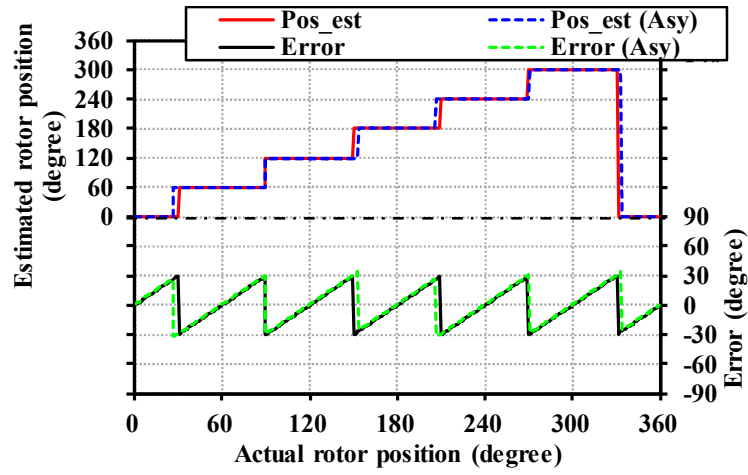
(b)



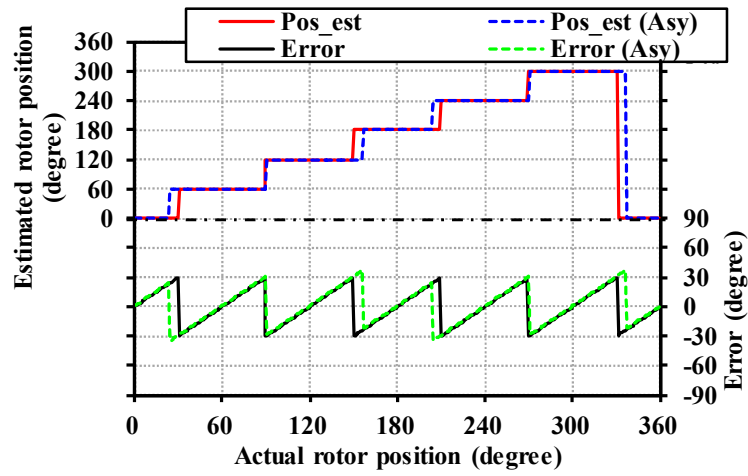
(c)

Fig. 5.14. Current responses against electrical rotor position with one-phase resistance asymmetry.

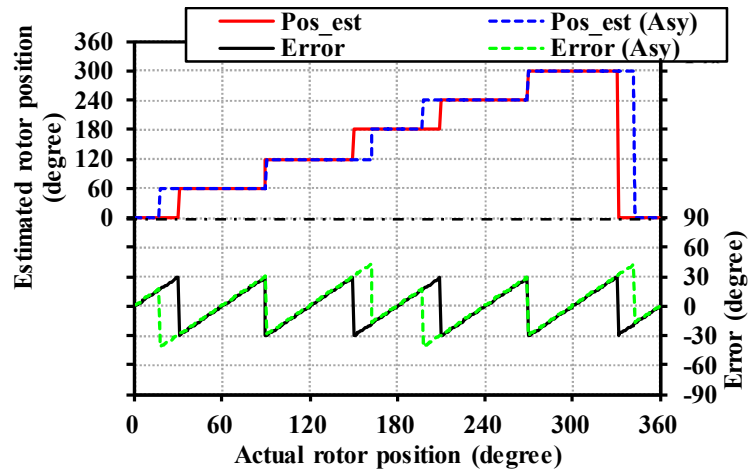
(a)  $\Delta R_A = 1\Omega$  (25% $R$ ). (b)  $\Delta R_A = 2\Omega$  (50% $R$ ). (c)  $\Delta R_A = 4\Omega$  (100% $R$ )



(a)



(b)



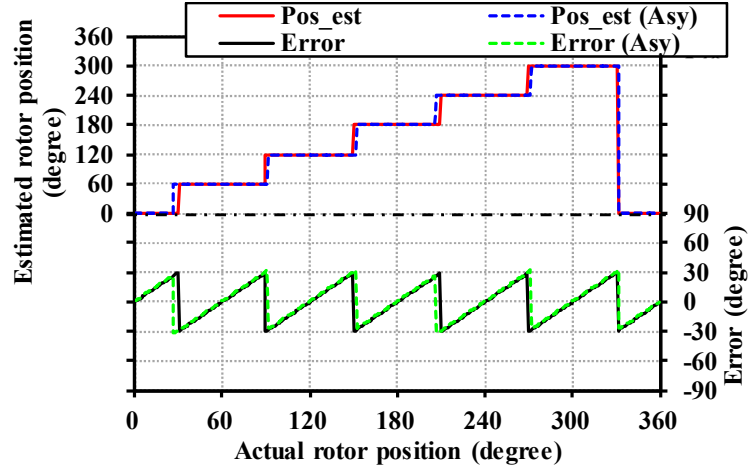
(c)

Fig. 5.15. Rotor position estimation with one-phase resistance asymmetry. (a)  $\Delta R_A = 1\Omega$  (25% $R$ ).

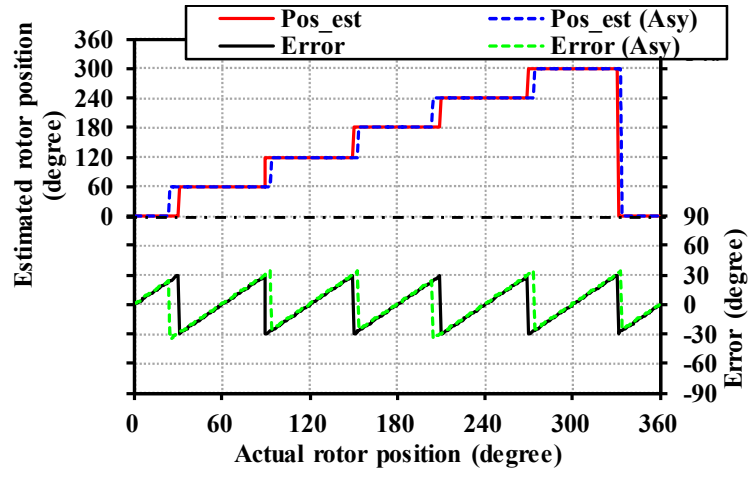
(b)  $\Delta R_A = 2\Omega$  (50% $R$ ). (c)  $\Delta R_A = 4\Omega$  (100% $R$ )

Then, in Fig. 5.16, three-phase current responses under two-phase resistance asymmetry are given. The estimation performance is shown in Fig. 5.17.

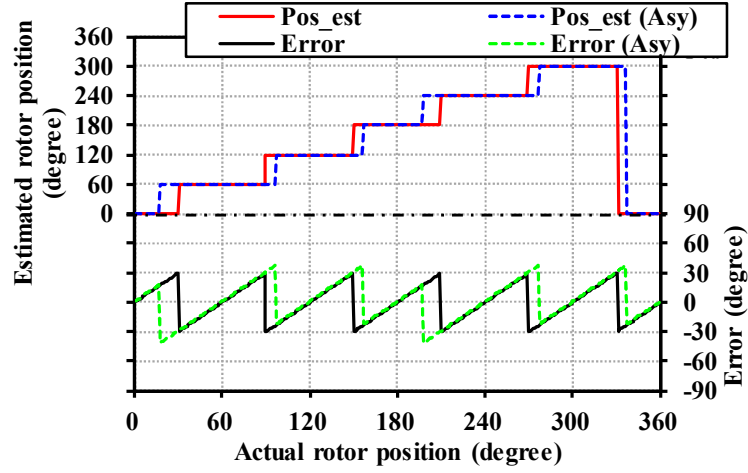




(a)



(b)



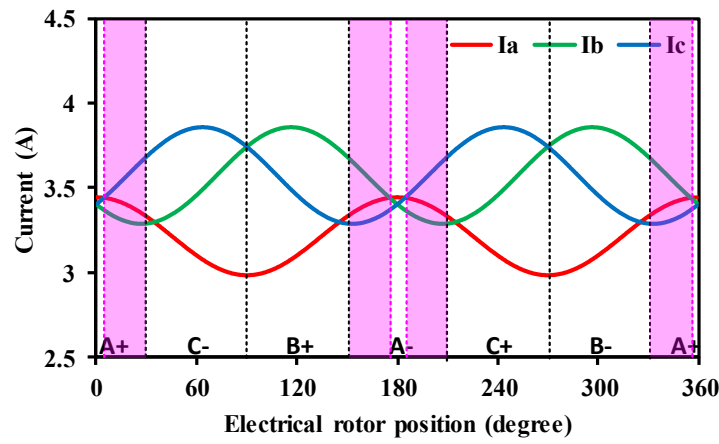
(c)

Fig. 5.17. Rotor position estimation with two-phase resistance asymmetry. (a)  $\Delta R_A = 1\Omega$  (25% $R$ ),  $\Delta R_B = 0.5\Omega$  (12.5% $R$ ). (b)  $\Delta R_A = 2\Omega$  (50% $R$ ),  $\Delta R_B = 1\Omega$  (25% $R$ ). (c)  $\Delta R_A = 4\Omega$  (100% $R$ ),  $\Delta R_B = 2\Omega$  (50% $R$ ).

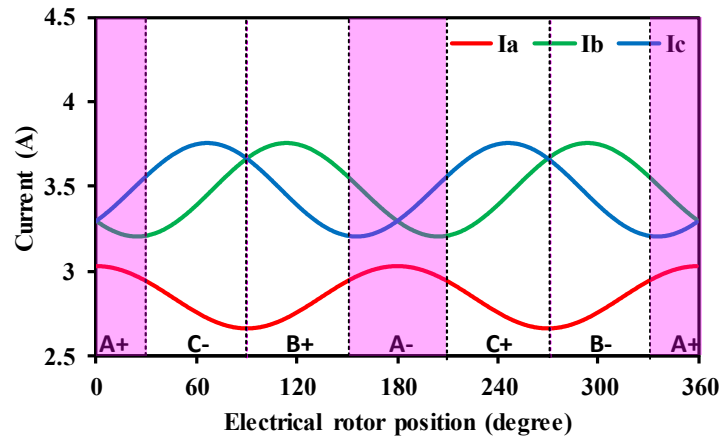
Clearly, for both one-phase and two-phase resistance asymmetric cases, as the resistance unbalance level goes higher,  $A_{Est\_wrong}$  becomes larger and therefore the position estimation performance is more affected.

### 5.3.2 Inductance Asymmetry

Similarly, the inductance asymmetry impact is also investigated. Both one-phase and two-phase self-inductance asymmetric cases are considered. Firstly, in Fig. 5.18, three-phase current responses under one-phase self-inductance asymmetry are shown. Besides, the estimation performance is shown in Fig. 5.20.

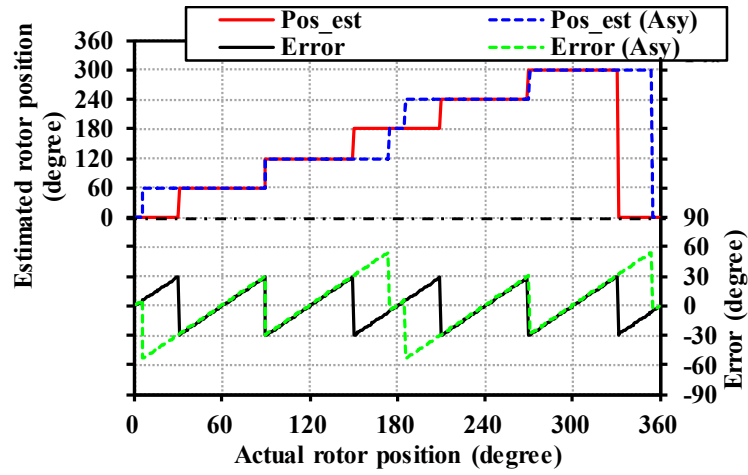


(a)

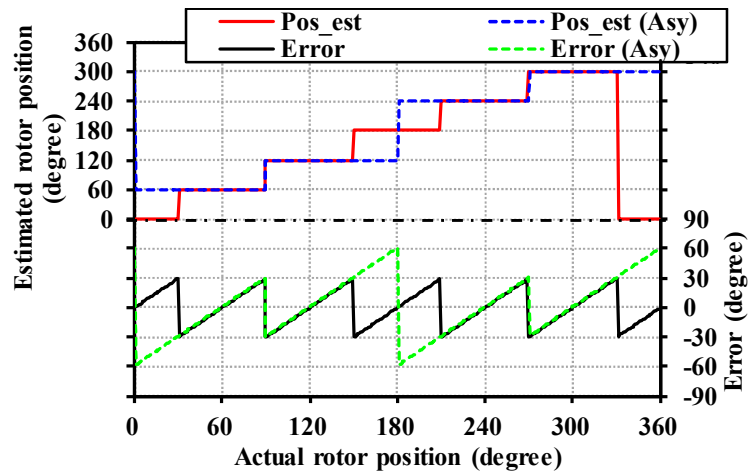


(b)

Fig. 5.18. Current responses against electrical rotor position with one-phase self-inductance asymmetry. (a)  $\Delta L_A = 4mH$  ( $50\%L_0$ ). (b)  $\Delta L_A = 8mH$  ( $50\%L_0$ ).



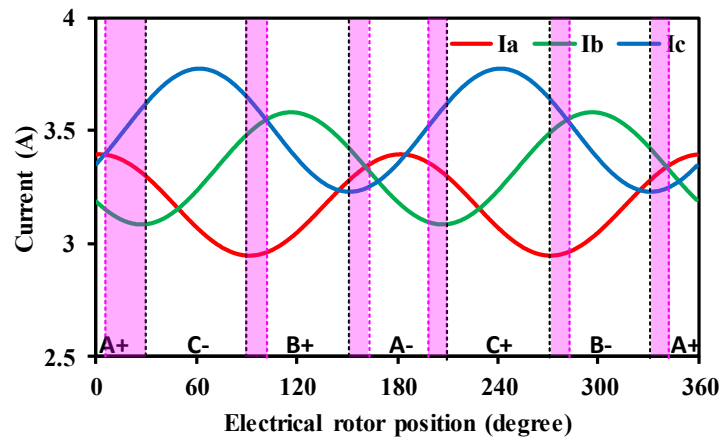
(a)



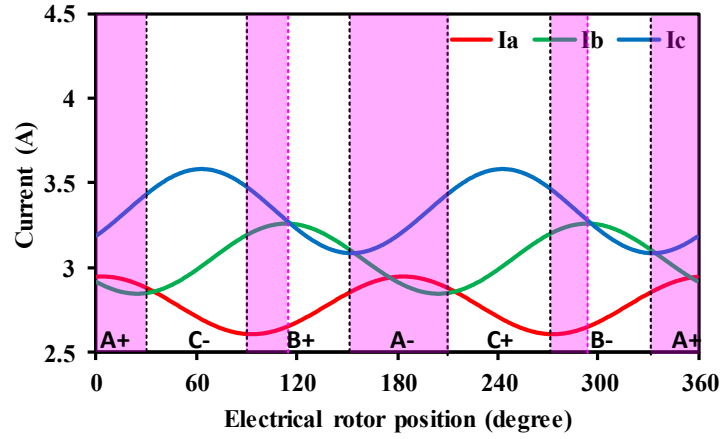
(b)

Fig. 5.19. Rotor position estimation with one-phase self-inductance asymmetry. (a)  $\Delta L_A = 4mH$  ( $50\%L_0$ ). (b)  $\Delta L_A = 8mH$  ( $50\%L_0$ ).

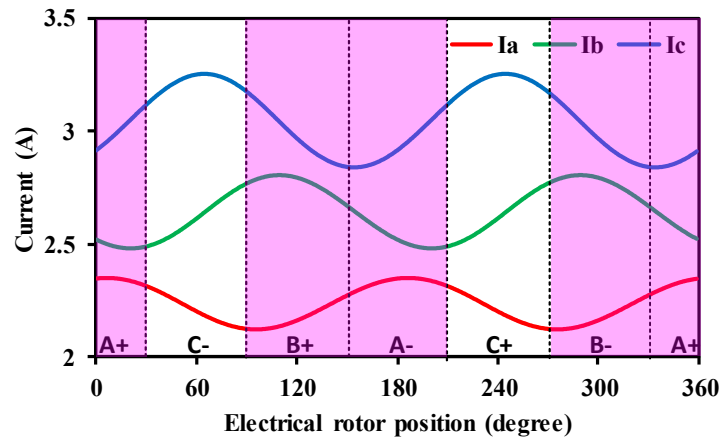
Then, in Fig. 5.20, three-phase current responses under two-phase self-inductance asymmetry are given. The estimation performance is shown in Fig. 5.21.



(a)

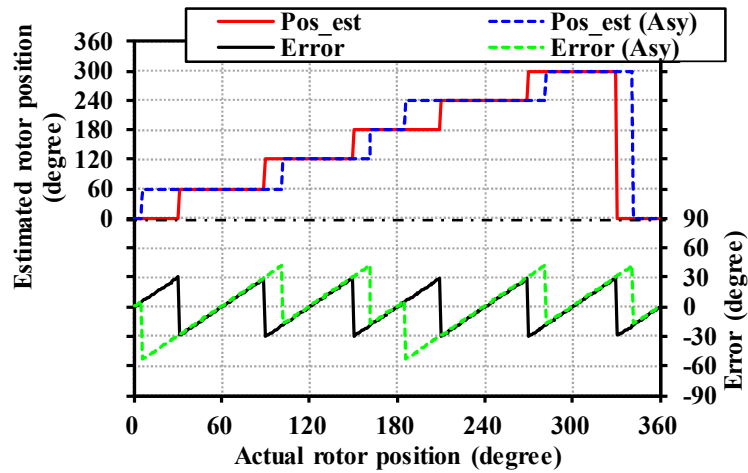


(b)



(c)

Fig. 5.20. Current responses against electrical rotor position with two-phase self-inductance asymmetry. (a)  $\Delta L_A = 4mH$  ( $25\%L_0$ ),  $\Delta L_B = 2mH$  ( $12.5\%L_0$ ). (b)  $\Delta L_A = 8mH$  ( $50\%L_0$ ),  $\Delta L_B = 4mH$  ( $25\%L_0$ ). (c)  $\Delta L_A = 16mH$  ( $100\%L_0$ ),  $\Delta L_B = 8mH$  ( $50\%L_0$ ).



(a)

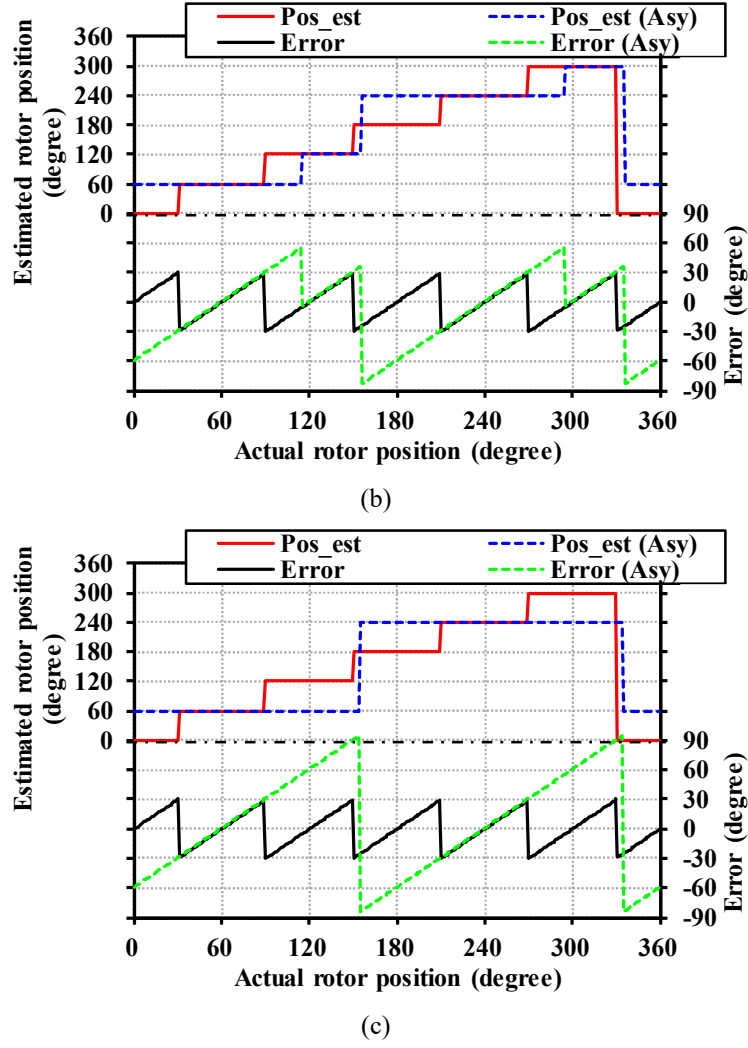


Fig. 5.21. Rotor position estimation with two-phase self-inductance asymmetry. (a)  $\Delta L_A = 4mH$  (25% $L_0$ ),  $\Delta L_B = 2mH$  (12.5% $L_0$ ). (b)  $\Delta L_A = 8mH$  (50% $L_0$ ),  $\Delta L_B = 4mH$  (25% $L_0$ ). (c)  $\Delta L_A = 16mH$  (100% $L_0$ ),  $\Delta L_B = 8mH$  (50% $L_0$ ).

Same as the resistance asymmetry, for both one-phase and two-phase self-inductance asymmetric cases, as the inductance unbalance level goes higher,  $A_{Est\_wrong}$  becomes larger and the position estimation performance is more deteriorated.

### 5.3.3 Feasible Estimation Area Ratio

Based on  $A_{Est\_wrong}$ , an indicator called ‘feasible estimation area ratio’, i.e.  $\alpha_E$ , is introduced and defined in (5.24). This ratio  $\alpha_E$  is used to quantify the influence of parameter asymmetry on position estimation performance.

$$\alpha_E = \frac{360^\circ - A_{Est\_wrong}}{360^\circ} \times 100\% \quad (5.24)$$

Clearly, for symmetrical case, the feasible estimation area ratio  $\alpha_E$  is 100%. Then, the feasible estimation area ratio  $\alpha_E$  considering different resistance and inductance asymmetric cases are calculated and shown in Fig. 5.22 and Fig. 5.23, respectively.

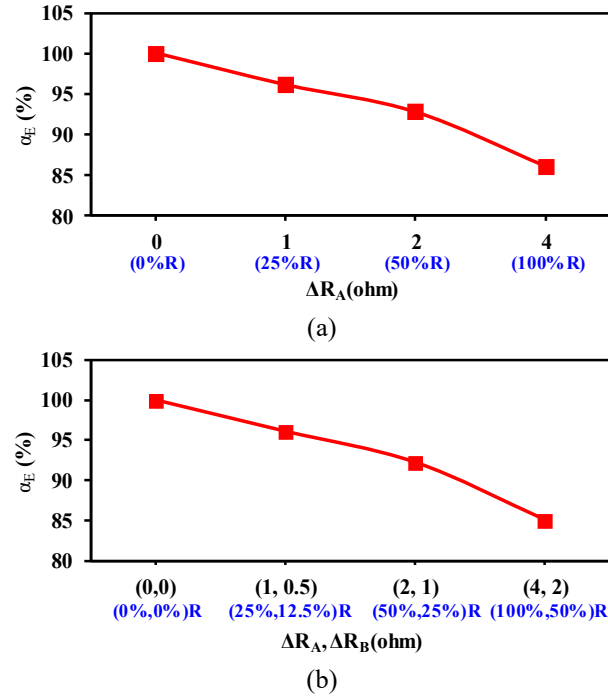


Fig. 5.22. Feasible estimation area ratio with resistance symmetry. (a) One-phase resistance asymmetry. (b) Two-phase resistance asymmetry.

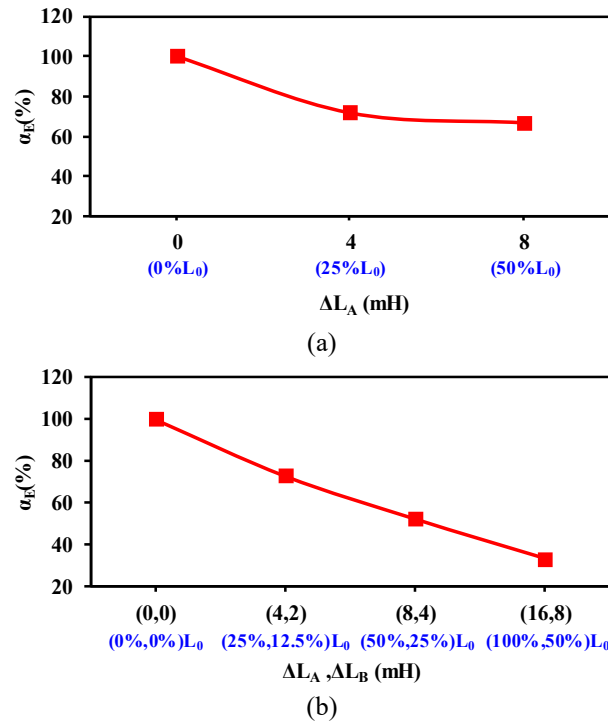


Fig. 5.23. Feasible estimation area ratio with inductance symmetry. (a) One-phase self-inductance asymmetry. (b) Two-phase self-inductance asymmetry.

Clearly, for both resistance and inductance asymmetric cases, the feasible estimation area ratio decreases as the unbalanced level becomes higher. If the unbalanced level keeps increasing, the unbalanced phase current will be always smaller than the other phase currents. The estimation in the sectors related to unbalanced phase will be incorrect. The least  $\alpha_E$  is 66.7% for one-phase asymmetry and 33.3% for two-phase asymmetry.

### 5.3.4 Summary

Based on the results, several conclusions under parameter asymmetries can be drawn. Firstly, in parameter symmetrical case, the estimation sectors should be evenly distributed by 60 degrees. However, in parameter asymmetric case, the estimation sectors are no longer evenly distributed. These uneven distributed sectors will cause position estimation error. Moreover, a higher level of asymmetry will decrease the feasible estimation area ratio  $\alpha_E$ . For one-phase asymmetric case, the least  $\alpha_E$  is 66.7% and for two-phase asymmetry case, the least  $\alpha_E$  is 33.3%.

## 5.4 Compensation Methods for Parameter Asymmetries

Discussed in the previous sections, parameter asymmetries will cause position errors for conventional methods. Hence, in this section, two compensation methods for rotor initial position estimation are proposed considering parameter asymmetries.

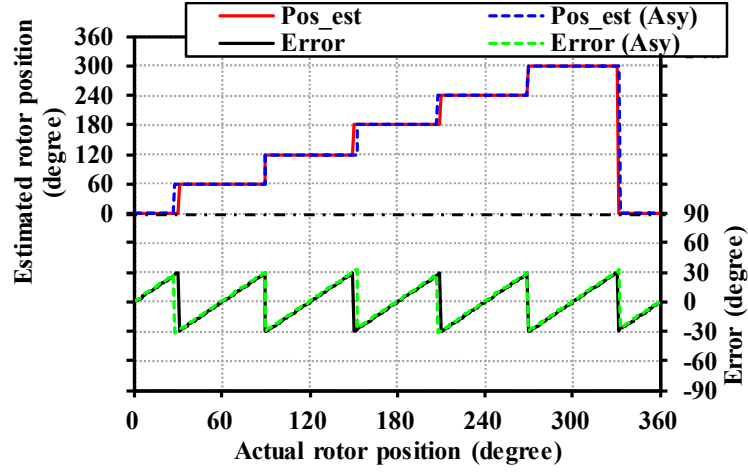
### 5.4.1 Adjustment of Voltage Pulse Duration

According to the results in Section 5.3, it is found that the influence of inductance asymmetry is more significant than the resistance asymmetry. This is due to the short duration of voltage pulse leading to a large current change. Hence, the voltage drop on inductance is much more than the resistance one as shown in (5.25).

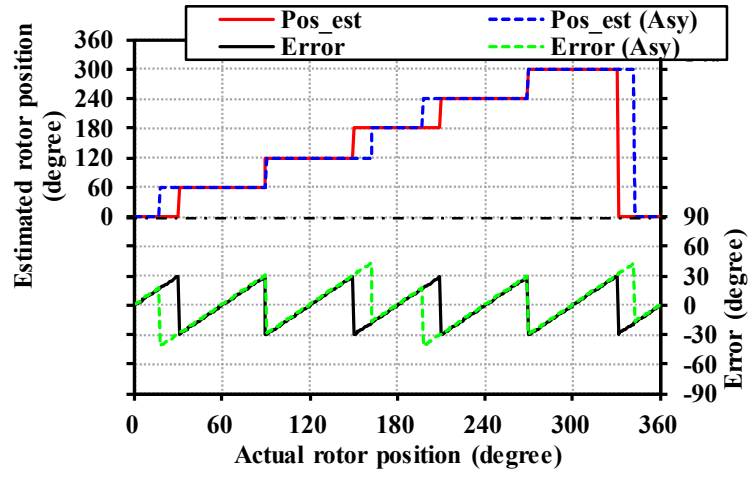
$$V_{DC} = R_{eq,X}i_X + L_{eq,X}\frac{di_X}{dt} \quad (5.25)$$

Therefore, the influence of resistance asymmetry on position estimation can be reduced by simply adjusting the duration of voltage pulse. Simulation results are given to verify the effectiveness of the proposed method.

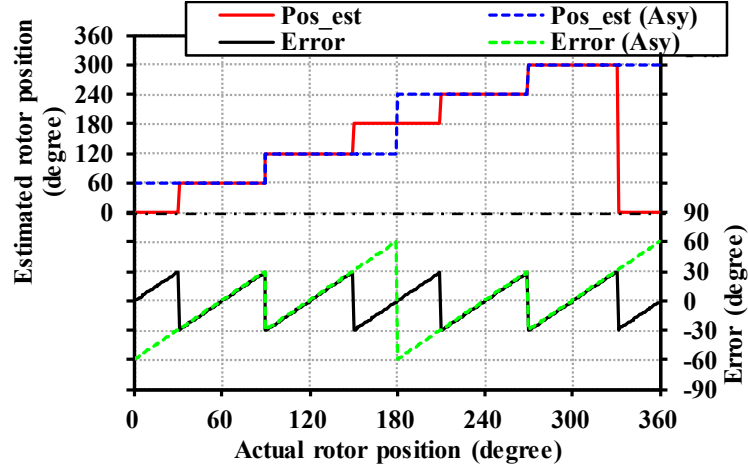
Firstly, under resistance asymmetry, the estimation performances with different voltage pulse durations are shown in Fig. 5.24. Then, the results for inductance asymmetric case are also shown in Fig. 5.25 for comparison with resistance asymmetric case.



(a)



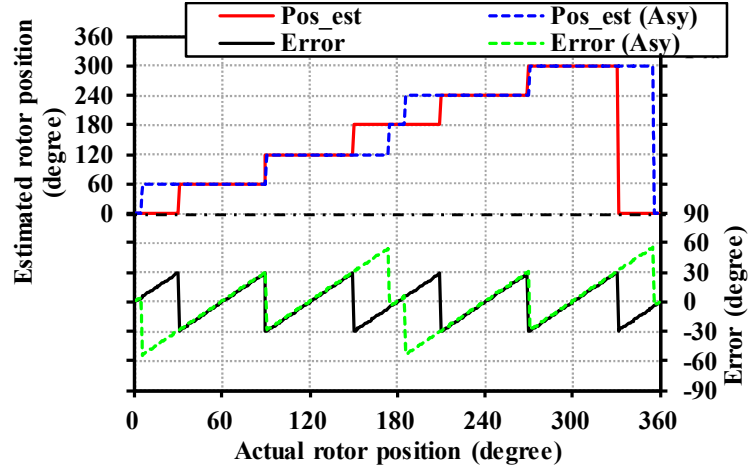
(b)



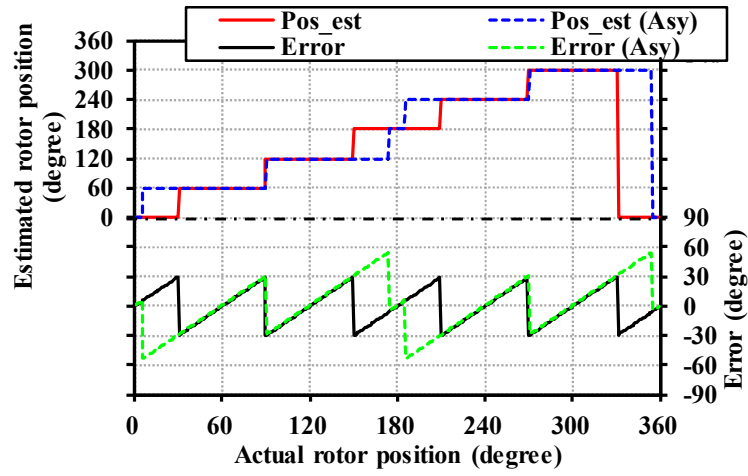
(c)

Fig. 5.24. Rotor position estimation with one-phase resistance asymmetry ( $\Delta R_A = 4\Omega$ ) with different voltage pulse durations. (a)  $T_P = 0.25\text{ms}$ . (b)  $T_P = 1\text{ms}$ . (c)  $T_P = 3\text{ms}$ .

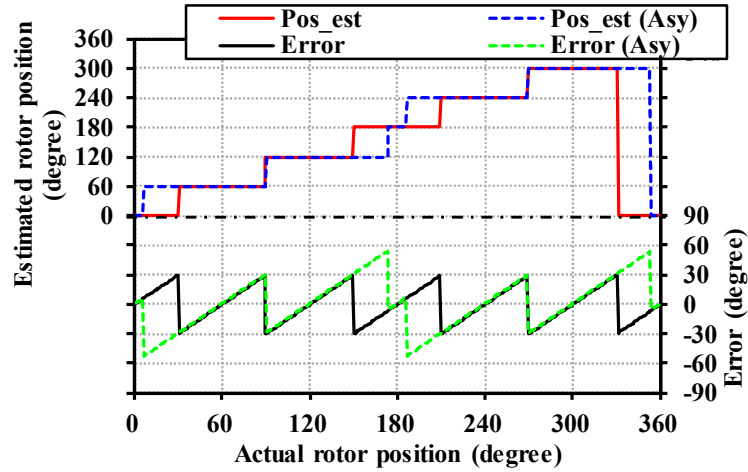
As shown in Fig. 5.24, as the duration increases, the impact of resistance asymmetry becomes more significant. Then, the inductance asymmetric case is shown in Fig. 5.25.



(a)



(b)



(c)

Fig. 5.25. Rotor position estimation with one-phase resistance asymmetry ( $\Delta L_A = 4\text{mH}$ ) with different voltage pulse durations. (a)  $T_P = 0.25\text{ms}$ . (b)  $T_P = 1\text{ms}$ . (c)  $T_P = 3\text{ms}$ .

From the results shown in Fig. 5.25, it can be seen that the duration has negligible influence on inductance asymmetry. Furthermore, the feasible estimation area ratio  $\alpha_E$  of both resistance and inductance asymmetric cases with different durations are calculated and shown in Fig. 5.26.

Compared with inductance asymmetry, the position estimation performance is less influenced by resistance asymmetry. By reducing the duration, the influence of resistance asymmetry on position estimation can be suppressed, while there is almost no effect on inductance asymmetry. Hence, only the impact of resistance asymmetry can be reduced by adjusting voltage pulse duration.

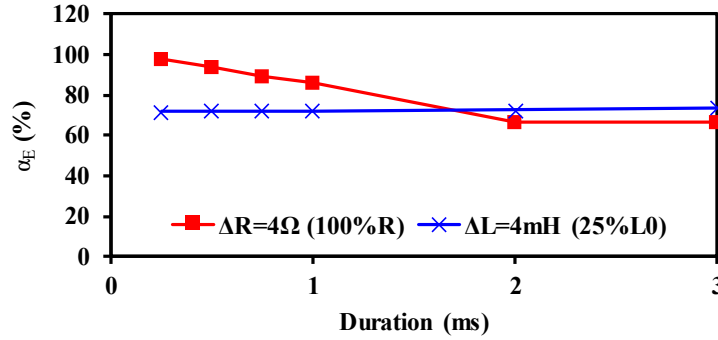


Fig. 5.26. Feasible estimation area ratio with different voltage pulse duration.

Then, considering different resistance asymmetry cases, simulation results of  $\alpha_E$  with different durations are shown in Fig. 5.27 and Fig. 5.28. Clearly, under resistance asymmetry, by reducing the duration of voltage pulse,  $\alpha_E$  can be increased effectively.

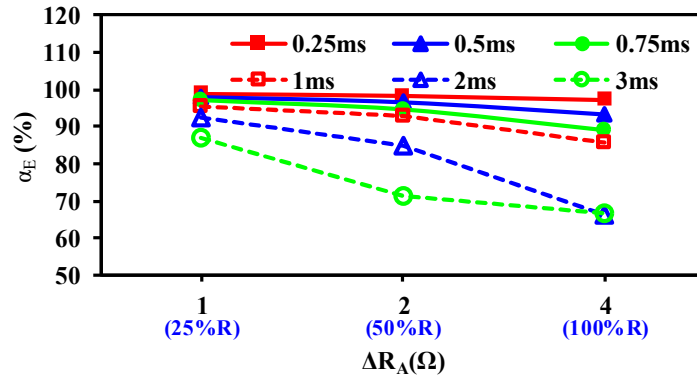


Fig. 5.27. Feasible estimation area ratio with different voltage pulse duration under one-phase resistance asymmetry.

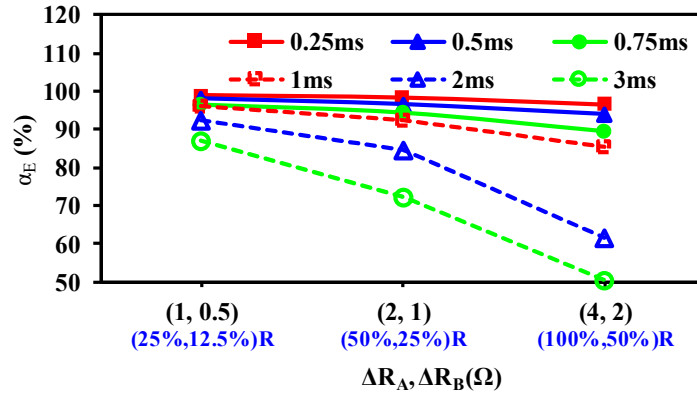


Fig. 5.28. Feasible estimation area ratio with different voltage pulse duration under two-phase resistance asymmetry.

In summary, adjustment of voltage pulse duration can be used to compensate for resistance asymmetry. The impact of resistance asymmetry can be reduced by using a shorter duration pulse. However, reducing the duration indicates a smaller number of sample points of the current response. A higher sampling rate might be required. Thus, this compensation method may become unfeasible in some applications due to the limited sampling rate.

### 5.4.2 Current Response Compensation Method

In Section 5.2, the current response models under resistance and inductance asymmetries are derived. Based on these models, a general current response model considering both resistance and inductance asymmetries can be given by:

$$\begin{aligned} I_A &\approx (\Delta I_{R_A} + \Delta I_{L_A}) + I_0 + (K_{\Delta R_A} \cdot K_{\Delta L_A}) \cdot I_2 \cos(2\theta_r) \\ I_B &\approx (\Delta I_{R_B} + \Delta I_{L_B}) + I_0 + (K_{\Delta R_B} \cdot K_{\Delta L_B}) \cdot I_2 \cos\left(2\left(\theta_r - \frac{2\pi}{3}\right)\right) \\ I_C &\approx (\Delta I_{R_C} + \Delta I_{L_C}) + I_0 + (K_{\Delta R_C} \cdot K_{\Delta L_C}) \cdot I_2 \cos\left(2\left(\theta_r + \frac{2\pi}{3}\right)\right) \end{aligned} \quad (5.26)$$

Then, (5.26) can be simplified as:

$$\begin{aligned} I_A &\approx I_{A0}^u + I_{A2}^u \cos(2\theta_r) \\ I_B &\approx I_{B0}^u + I_{B2}^u \cos\left(2\left(\theta_r - \frac{2\pi}{3}\right)\right) \\ I_C &\approx I_{C0}^u + I_{C2}^u \cos\left(2\left(\theta_r + \frac{2\pi}{3}\right)\right) \end{aligned} \quad (5.27)$$

$$\begin{aligned} I_{A0}^u &= I_0 + \Delta I_{R_A} + \Delta I_{L_A} \\ I_{B0}^u &= I_0 + \Delta I_{R_B} + \Delta I_{L_B} \\ I_{C0}^u &= I_0 + \Delta I_{R_C} + \Delta I_{L_C} \end{aligned} \quad (5.28)$$

$$\begin{aligned} I_{A2}^u &= K_{\Delta R_A} \cdot K_{\Delta L_A} \cdot I_2 \\ I_{B2}^u &= K_{\Delta R_B} \cdot K_{\Delta L_B} \cdot I_2 \\ I_{C2}^u &= K_{\Delta R_C} \cdot K_{\Delta L_C} \cdot I_2 \end{aligned} \quad (5.29)$$

where  $I_{A0}^u$ ,  $I_{B0}^u$  and  $I_{C0}^u$  are the DC offsets in three-phase current responses under parameter asymmetries,  $I_{A2}^u$ ,  $I_{B2}^u$  and  $I_{C2}^u$  are the amplitudes of the 2<sup>nd</sup> order harmonics in three-phase current responses under parameter asymmetries.

Based on (5.30), a current response compensation method is developed. Current responses against rotor position are firstly measured in the pre-test. Then, the coefficients  $I_{A0}^u$ ,  $I_{B0}^u$ ,  $I_{C0}^u$ ,  $I_{A2}^u$ ,  $I_{B2}^u$  and  $I_{C2}^u$  in (5.30) are calculated and used to compensate for the unbalanced three-phase current responses. The compensated three-phase current responses are given by:

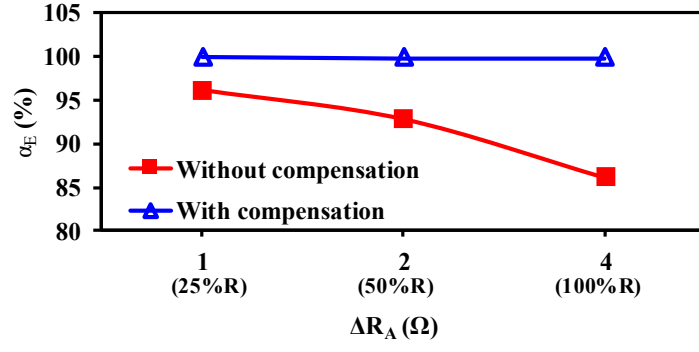
$$\begin{aligned} I_A^c &= (I_A - I_{A0}^u) \cdot \frac{I_{2\_AVE}}{I_{A2}^u} + I_{0\_AVE} \\ I_B^c &= (I_B - I_{B0}^u) \cdot \frac{I_{2\_AVE}}{I_{B2}^u} + I_{0\_AVE} \\ I_C^c &= (I_C - I_{C0}^u) \cdot \frac{I_{2\_AVE}}{I_{C2}^u} + I_{0\_AVE} \end{aligned} \quad (5.30)$$

$$\begin{aligned} I_{0\_AVE} &= \frac{I_{A0}^u + I_{B0}^u + I_{C0}^u}{3} \\ I_{2\_AVE} &= \frac{I_{A2}^u + I_{B2}^u + I_{C2}^u}{3} \end{aligned} \quad (5.31)$$

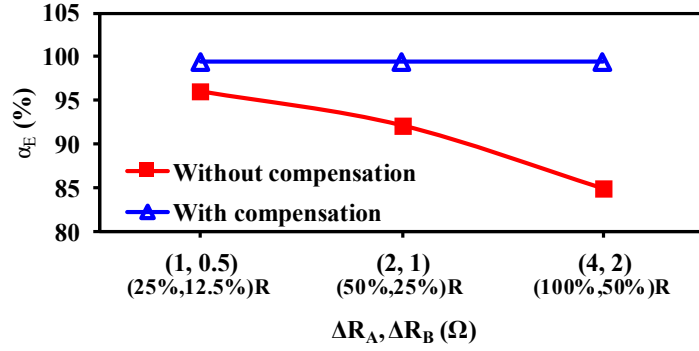
After compensation, the three-phase current responses become symmetrical and given by:

$$\begin{aligned} I_A^c &= I_0 + I_2 \cos(2\theta_r) \\ I_B^c &= I_0 + I_2 \cos\left(2\left(\theta_r - \frac{2\pi}{3}\right)\right) \\ I_C^c &= I_0 + I_2 \cos\left(2\left(\theta_r + \frac{2\pi}{3}\right)\right) \end{aligned} \quad (5.32)$$

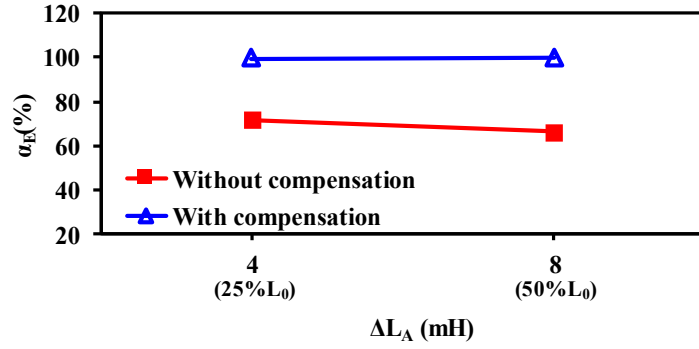
Then, the proposed compensation method is validated by simulation. The simulation results are shown in Fig. 5.29. In Fig. 5.29, different asymmetry scenarios are considered. It can be seen that for both asymmetry cases, the feasible estimation area ratios  $\alpha_E$  are largely increased to 100% after compensation.



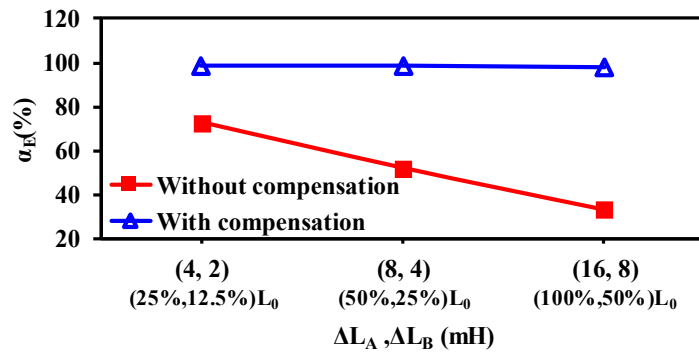
(a)



(b)



(c)



(d)

Fig. 5.29. Feasible estimation area ratio with different voltage pulse duration. (a) One-phase resistance asymmetry. (b) Two-phase resistance asymmetry. (c) One-phase self-inductance asymmetry. (d) Two-phase self-inductance asymmetry.

Besides, different from the first compensation method, the second compensation method can be used without the limitation of duration. As discussed before, the impact of resistance asymmetry can be significantly influenced by voltage pulse durations. Therefore, an example of compensation performance under one-phase resistance asymmetry ( $\Delta R_A = 4\Omega$ , 100% $R$ ) is shown in Fig. 5.30. In the example, different voltage pulse durations are considered. Clearly, the second method shows no change in compensation effects regarding different durations. For the second current response compensation method, the three-phase current responses against rotor position are measured in the pre-test by injecting voltage pulses. In order to guarantee the compensation performance, in the position estimation, the magnitude and duration of the injected voltage pulse should be identical to the one used in the pre-test.

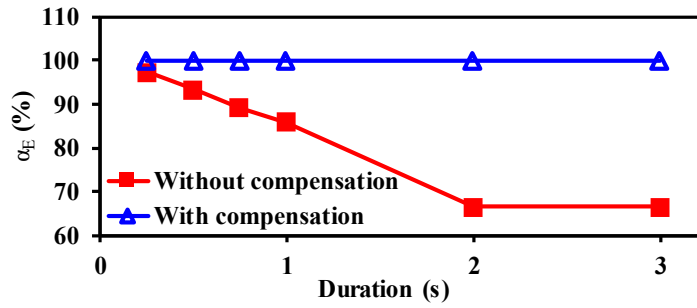


Fig. 5.30. Feasible estimation area ratio with different voltage pulse duration under one-phase resistance asymmetry ( $\Delta R_A = 4\Omega$ , 100% $R$ ).

In summary, by doing pre-test measurement of three-phase current responses against the rotor position, the unbalanced three-phase current responses can be compensated to be balanced again. The effectiveness of this compensation method is verified by simulation results. This method can be used for both resistance and inductance asymmetric cases. However, the main limitation of this method is the requirement of pre-test measurement of three-phase current responses.

## 5.5 Conclusion

In this chapter, rotor initial position estimation under both machine resistance and inductance asymmetries is investigated. The model of current responses under parameter asymmetries is developed and the impact of parameter asymmetries on position estimation is investigated. It is found that the current response of the unbalanced phase will have decreased amplitudes of both DC offset and the 2<sup>nd</sup> order harmonic component compared with the other phases. For one-phase asymmetric case, the least feasible estimation area ratio  $\alpha_E$  is 66.7%. For

two-phase asymmetric case, the least feasible estimation area ratio  $\alpha_E$  is only 33.3%. Moreover, two compensation methods are proposed which effectively reduce the impact of parameter asymmetries. Both methods are verified by simulation results. The first method relies on reducing the duration of voltage pulse so that the resistance impact is suppressed. Thus, this method is only suitable for compensating for the resistance asymmetry, not for the inductance asymmetry. As shown by simulation results, a satisfied compensation performance can be obtained with a very short duration of voltage pulse. However, shorter duration requires a higher sampling frequency, which can be limited in some applications. For the second method, based on the general model of current response under parameter asymmetry, a direct current response compensation method is developed. The current responses are measured in the pre-test and the asymmetry coefficients are obtained and used to compensate for the asymmetric three-phase current responses. After compensation, the three-phase current responses become symmetrical again. Therefore, the second method shows a satisfied compensation performance for both inductance and resistance asymmetries. However, this method requires pre-test measurement of the three-phase current responses.

# **CHAPTER 6**

## **A NEW SIMPLIFIED FUNDAMENTAL MODEL BASED SENSORLESS CONTROL FOR SURFACE- MOUNTED PERMANENT MAGNET SYNCHRONOUS MACHINES**

### **6.1 Introduction**

Basically, sensorless techniques can be divided into fundamental model based techniques and saliency tracking based techniques. Fundamental model based methods utilizing back-EMF or flux-linkage have a good performance at middle and high speeds. Back-EMF and flux-linkage can be estimated simply using phase-locked loop (PLL) or other observers including adaptive observer [PII08][YOO09a], sliding-mode observer (SMO) [CHI09] [KIM11], and extended Kalman filter (EKF) [BOL99]. However, the magnitude of back-EMF is proportional to the rotor speed, these methods present poor performance and cannot be employed in the zero and low speed range. In terms of saliency tracking based methods, which are more suitable in the zero and low speed range. Discrete voltage pulses [HOL05], PWM excitation [KIM12], or continuous carrier signal injection based methods [JAN95] [BRI04] are proposed and show effectiveness in the zero and low speed range. However, in case of surface-mounted permanent magnet synchronous machines, due to geometric characteristics, the inductance saliency is insufficient or none. Hence, saliency tracking based methods may not be employed for the SPMSM. Therefore, it is still a challenge for sensorless control of SPMSM at zero and low speed.

Conventionally, in order to employ sensorless control techniques on SPMSM, an open-loop start-up process [WU91][FAT08][IEP12] is adopted to help the machine firstly reaching at a certain high speed so that the magnitude of back-EMF is large enough for position tracking. However, with load or load variations, the operation may become unstable so that the machine will lose its synchronism. A reverse rotation or oscillation can also happen during starting. In addition, the starting torque is not guaranteed to be its maximum value, which will significantly slow down the starting process. Moreover, extra control strategies are required to achieve a smooth transition from open-loop control to closed-loop control.

In this chapter, a solution is proposed for SPMSM sensorless control considering the starting process and low speed operation. In this chapter, a simplified fundamental model based sensorless control method for SPMSM is proposed. Based on the simplified model, the stator currents in the stationary reference frame can be directly utilized for position estimation, without the need of parameter and voltage information. Different from conventional fundamental model based methods calculating back-EMF or flux-linkage, the proposed method utilizes the rotor position information contained in the stator current. The stator currents are directly measured from the current sensors, and in the low speed range, sensorless control performance can be improved. For the starting part, obtaining the accurate rotor initial position or sector information before starting is favourable in order to avoid the reverse rotation and oscillation issues that could possibly happen during starting [BOL99][JAN06]. Methods based on magnetic saturation effect could be used [MAT96] [SCH97] [TUR03] [WAN10]. In this chapter, a rotor initial position detection method in [SCH97] is adopted, which guarantees a satisfied estimation performance at standstill, especially for SPMSM. With the knowledge of rotor initial position, the proposed method is able to start the machine from standstill against different load conditions without reverse rotation. The influence of inverter nonlinearity on the proposed rotor position estimation method is also discussed and the corresponding compensation is considered.

This chapter is organized as follows: Firstly, the fundamental model of PMSM and conventional sensorless control methods are introduced. Then, the proposed method is illustrated including the mathematical model derivation, influence of inverter-nonlinearity and starting procedure. The proposed method is implemented on the dSPACE platform and its effectiveness is verified by the experiment results on two prototype SPMSMs. Moreover, the proposed method is applied to the Siemens wind power system and is verified by hardware-in-loop (HIL) simulation.

This chapter is based on the paper:

[WU20e] X. M. Wu, Z. Q. Zhu, and Z. Y. Wu, “A new simplified fundamental model-based sensorless control method for surface-mounted permanent magnet synchronous machines,” submitted to *IET Electric Power Applications*.

## 6.2 Conventional Fundamental Model Based Sensorless Control

### Methods

It is known that saliency tracking based methods cannot be applied to SPMSM due to the lack of rotor saliency, fundamental model based methods are the main way to realize sensorless control of SPMSM. For the fundamental model based sensorless control methods, rotor position estimation is based on calculating either back-EMF or flux-linkage. Hence, in this section, the basic approaches of utilizing back-EMF and flux-linkage for position estimation are demonstrated.

#### 6.2.1 Back-EMF Based Sensorless Control Methods

For back-EMF based sensorless control methods, back-EMF can be calculated based on the stationary reference frame or the estimated synchronous reference frame. Then, two different reference frames based sensorless methods for SPMSM are introduced in this part.

##### *A. Stationary reference frame*

The voltage equation for SPMSM in the stationary reference frame is given as:

$$\begin{bmatrix} v_\alpha \\ v_\beta \end{bmatrix} = \begin{bmatrix} R_s + pL_s & 0 \\ 0 & R_s + pL_s \end{bmatrix} \begin{bmatrix} i_\alpha \\ i_\beta \end{bmatrix} + \omega_r \psi_m \begin{bmatrix} -\sin\theta_r \\ \cos\theta_r \end{bmatrix} \quad (6.1)$$

The right hand side term represents the back-EMF that contains the rotor position and speed information. Back-EMF terms can be calculated as:

$$\begin{bmatrix} e_\alpha \\ e_\beta \end{bmatrix} = \begin{bmatrix} v_\alpha \\ v_\beta \end{bmatrix} - \begin{bmatrix} R_s + pL_s & 0 \\ 0 & R_s + pL_s \end{bmatrix} \begin{bmatrix} i_\alpha \\ i_\beta \end{bmatrix} \quad (6.2)$$

Then, the back-EMF terms are given as:

$$\begin{bmatrix} e_\alpha \\ e_\beta \end{bmatrix} = \omega_r \psi_m \begin{bmatrix} -\sin\theta_r \\ \cos\theta_r \end{bmatrix} \quad (6.3)$$

The rotor position can be calculated by:

$$\theta_r = \arctan \left( -\frac{e_\alpha}{e_\beta} \right) \quad (6.4)$$

It is worth noting that in the implementation, since voltage information is not available, the reference voltage value  $v_\alpha^*$  and  $v_\beta^*$  are used instead.

### B. Estimated synchronous reference frame

Rotor position can also be estimated based on calculating back-EMF in the estimated synchronous reference frame. [MOR02] and [CHE03] introduced the Extended Back-EMF based method, i.e.  $E_{ex}$ , by which the voltage equation is given as:

$$\begin{bmatrix} v_d \\ v_q \end{bmatrix} = \begin{bmatrix} R_s + pL_d & -\omega_r L_q \\ \omega_r L_q & R_s + pL_d \end{bmatrix} \begin{bmatrix} i_d \\ i_q \end{bmatrix} + \begin{bmatrix} 0 \\ E_{ex} \end{bmatrix} \quad (6.5)$$

where  $v_d$  and  $v_q$  are the d-q axis stator voltages,  $i_d$  and  $i_q$  are the d-q axis stator currents,  $L_d$  and  $L_q$  are the d-q axis inductances respectively.  $E_{ex} = \omega_r \psi_m + (L_d - L_q)(\omega_r i_d - p i_q)$ . It is worth noting that for SPMSM,  $L_s = L_d = L_q$ . Then, (1.34) is modified as:

$$\begin{bmatrix} v_d \\ v_q \end{bmatrix} = \begin{bmatrix} R_s + pL_s & -\omega_r L_s \\ \omega_r L_s & R_s + pL_s \end{bmatrix} \begin{bmatrix} i_d \\ i_q \end{bmatrix} + \begin{bmatrix} 0 \\ \omega_r \psi_m \end{bmatrix} \quad (6.6)$$

For a sensorless control system, the actual rotor position is unknown. Therefore, the above equations should be transformed into the estimated synchronous reference frame with the transformation matrix given by:

$$T(\Delta\theta_r) = \begin{bmatrix} \cos(\Delta\theta_r) & \sin(\Delta\theta_r) \\ -\sin(\Delta\theta_r) & \cos(\Delta\theta_r) \end{bmatrix} \quad (6.7)$$

$$T^{-1}(\Delta\theta_r) = \begin{bmatrix} \cos(\Delta\theta_r) & -\sin(\Delta\theta_r) \\ \sin(\Delta\theta_r) & \cos(\Delta\theta_r) \end{bmatrix} \quad (6.8)$$

where  $\Delta\theta_r$  is the rotor position error between the estimation and actual values. Besides, the relationship between the synchronous reference frame and the estimated synchronous reference frame is shown in Fig. 6.1.

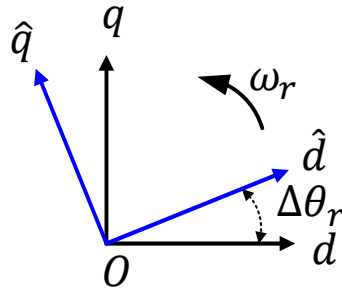


Fig. 6.1. Relationship between ABC reference frame and synchronous reference frame.

Then, the voltage equation in the estimated synchronous reference frame is given by:

$$\begin{bmatrix} \hat{v}_d \\ \hat{v}_q \end{bmatrix} = \begin{bmatrix} R_s + pL_d & -\omega_r L_q \\ \omega_r L_q & R_s + pL_d \end{bmatrix} \begin{bmatrix} \hat{i}_d \\ \hat{i}_q \end{bmatrix} + \begin{bmatrix} \hat{E}_d \\ \hat{E}_q \end{bmatrix} \quad (6.9)$$

$$\begin{bmatrix} \hat{E}_d \\ \hat{E}_q \end{bmatrix} = E_{ex} \begin{bmatrix} -\sin\Delta\theta_r \\ \cos\Delta\theta_r \end{bmatrix} + \Delta\omega_r L_d \begin{bmatrix} \hat{i}_q \\ -\hat{i}_d \end{bmatrix} \quad (6.10)$$

The superscript sign ‘^’ indicates the variables are in the estimated synchronous reference frame.  $\Delta\omega_r$  is the rotor speed error between estimation and actual values, respectively. For SPMSM, (1.36) and (1.37) are modified as:

$$\begin{bmatrix} \hat{v}_d \\ \hat{v}_q \end{bmatrix} = \begin{bmatrix} R_s + pL_s & -\omega_r L_s \\ \omega_r L_s & R_s + pL_s \end{bmatrix} \begin{bmatrix} \hat{i}_d \\ \hat{i}_q \end{bmatrix} + \begin{bmatrix} \hat{E}_d \\ \hat{E}_q \end{bmatrix} \quad (6.11)$$

$$\begin{bmatrix} \hat{E}_d \\ \hat{E}_q \end{bmatrix} = \omega_r \psi_m \begin{bmatrix} -\sin\Delta\theta_r \\ \cos\Delta\theta_r \end{bmatrix} + \Delta\omega_r L_d \begin{bmatrix} \hat{i}_q \\ -\hat{i}_d \end{bmatrix} \quad (6.12)$$

Then, the position error can be expressed in the following equations:

$$\Delta\theta_r = \tan^{-1}\left(-\frac{\hat{E}_d}{\hat{E}_q}\right) \quad (6.13)$$

Subsequently, as shown in Fig. 1.17, a position observer is applied to adjust the estimation position to minimize the position estimation error  $\Delta\theta_r$  to make the estimated reference fame align with actual one. It is worth noting that in the implementation, since voltage information is not available, the reference voltage value  $v_d^*$  and  $v_q^*$  are used instead.

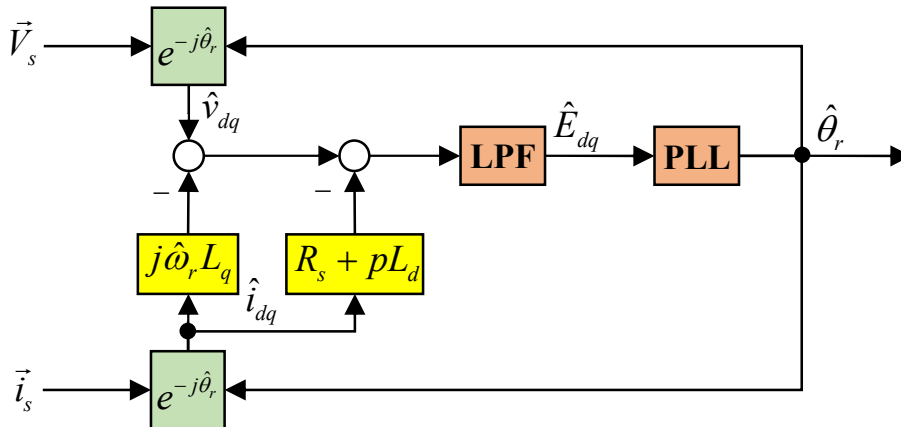


Fig. 6.2. Extended Back-EMF based position observer. [CHE03]

## 6.2.2 Flux-linkage Based Sensorless Control Methods

For flux-linkage based sensorless control methods, rotor position can also be estimated in the stationary reference frame or the estimated synchronous reference frame. Therefore, two different flux-linkage sensorless methods are introduced in this part.

### A. Stationary reference frame

In the stationary reference frame, the flux-linkage can be calculated as follows,

$$\psi_{m,\alpha\beta} = \int (v_{\alpha\beta} - R_s i_{\alpha\beta}) dt - L_s i_{\alpha\beta} \quad (6.14)$$

The flux-linkages are given as

$$\begin{bmatrix} \psi_{m\alpha} \\ \psi_{m\beta} \end{bmatrix} = \psi_m \begin{bmatrix} \cos\theta_r \\ \sin\theta_r \end{bmatrix} \quad (6.15)$$

Hence, the rotor position can be obtained as

$$\theta_r = \arctan \frac{\psi_{m\beta}}{\psi_{m\alpha}} \quad (6.16)$$

It is worth noting that in the implementation any dc offset or current measurement error will be continuously amplified by the pure integration until saturation. Therefore, a high-pass filter (HPF) is normally applied to the variables to be integrated. Since the transfer function of the pure integration is  $1/s$ , the equivalent replacement of pure integrator is same as a low-pass filter (LPF).

### B. Estimated synchronous reference frame

Besides, rotor position can be estimated based on the flux-linkage in the estimated synchronous reference frame. [BOL08] proposed a so called ‘Active Flux’ concept. The active flux (AF) is defined as:

$$\psi_{AF} = \psi_m + (L_d - L_q) i_d \quad (6.17)$$

For SPMSM, since  $L_d = L_q$ , the active flux is modified to:

$$\psi_{AF} = \psi_m \quad (6.18)$$

With the active flux, the flux equation can be generalized as:

$$\begin{bmatrix} \psi_d \\ \psi_q \end{bmatrix} = \begin{bmatrix} L_d & 0 \\ 0 & L_q \end{bmatrix} \begin{bmatrix} i_d \\ i_q \end{bmatrix} + \begin{bmatrix} \psi_{AF} \\ 0 \end{bmatrix} \quad (6.19)$$

Since the rotor position is unknown in the practical sensorless control system, the flux-linkage should be transformed into the estimated reference frame:

$$\begin{bmatrix} \hat{\psi}_d \\ \hat{\psi}_q \end{bmatrix} = \begin{bmatrix} L_d & 0 \\ 0 & L_q \end{bmatrix} \begin{bmatrix} \hat{i}_d \\ \hat{i}_q \end{bmatrix} + \begin{bmatrix} \hat{\psi}_{AFd} \\ \hat{\psi}_{AFq} \end{bmatrix} \quad (6.20)$$

where  $[\hat{\psi}_{AFd} \ \hat{\psi}_{AFq}]^T$  is the projected AF defined as  $[\hat{\psi}_{AFd} \ \hat{\psi}_{AFq}]^T = \psi_{AF}[\cos\Delta\theta_r \ \sin\Delta\theta_r]^T$ . Based on (1.48), the rotor speed and position can be estimated by an observer. The overall control scheme is shown in Fig. 1.21.

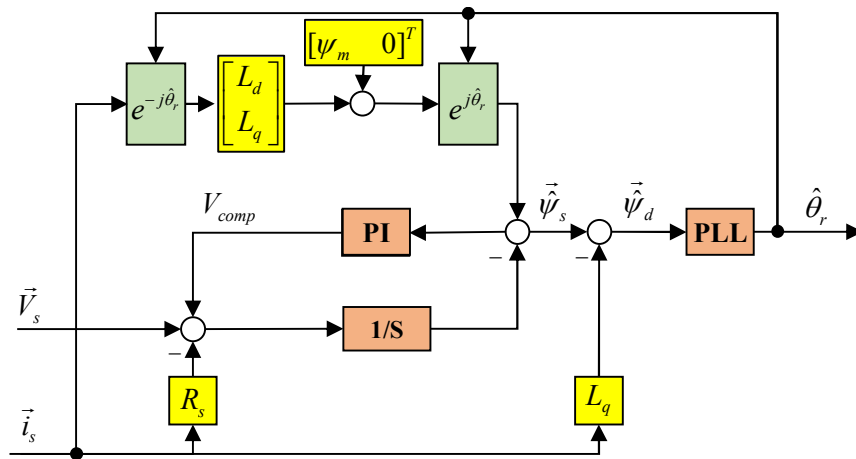


Fig. 6.3. Active flux based position observer. [BOL08]

### 6.2.3 Summary

It is known that the conventional methods based on the fundamental model offer good performance in the middle and high-speed ranges. While in zero and low speed range, back-EMF and flux-linkage are unobservable, besides there are also some other factors affecting the sensorless control performance including the parameter mismatch, inverter non-linearity, etc. Therefore, the conventional fundamental model based methods normally cannot be used in zero and low speed range. In order to solve this issue, a new sensorless control method based on the simplified fundamental model is proposed and introduced in the following section.

## 6.3 Proposed Simplified Fundamental Model Based Method for Starting and Low Speed Operation

Based on the fundamental model in Section 6.2, a new simplified fundamental model based sensorless control method is introduced in this section. Instead of calculating back-EMF or flux-linkage in conventional ways, only the measured stator currents are directly used to extract the rotor position information in the proposed method. Since currents are measured from physical sensors, comparing with conventional direct utilization of back-EMF or flux-linkage, the sensorless control performance can be improved in starting and low speed range. In this section, the mathematical model derivation of the proposed simplified fundamental model is provided at first and including the demonstration of how to utilize stator current to estimate the rotor position. Furthermore, the influence of inverter nonlinearity is discussed as well. The overall sensorless control block diagram is illustrated in Fig. 6.4.

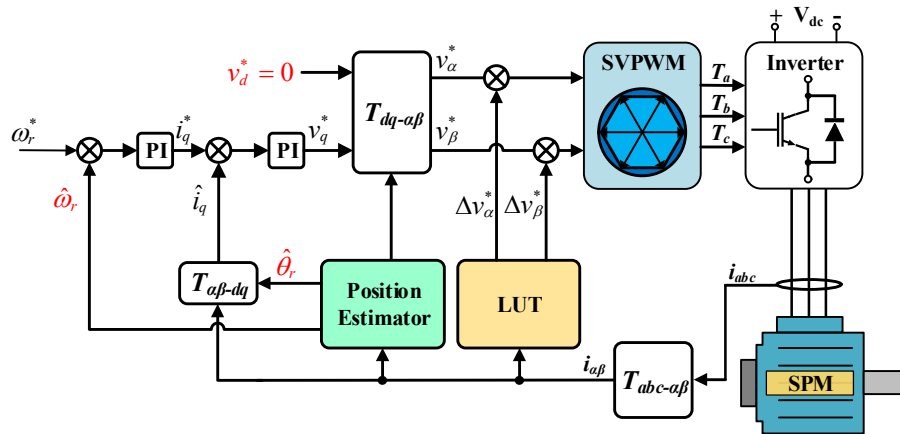


Fig. 6.4. Overall sensorless control block diagram. [WU20e]

### 6.3.1 Simplified Model

The proposed method is based on the fundamental model in the stationary reference frame. Firstly, re-arranging the voltage equations by moving current terms to the left side and the current terms are represented as:

$$\begin{bmatrix} R_s + pL_s & 0 \\ 0 & R_s + pL_s \end{bmatrix} \begin{bmatrix} i_\alpha \\ i_\beta \end{bmatrix} = \begin{bmatrix} v_\alpha \\ v_\beta \end{bmatrix} - \omega_r \psi_m \begin{bmatrix} -\sin\theta_r \\ \cos\theta_r \end{bmatrix} \quad (6.21)$$

Besides, the stator voltages in the stationary reference frame can be represented as:

$$\begin{bmatrix} v_\alpha \\ v_\beta \end{bmatrix} = \begin{bmatrix} \cos\theta_r & -\sin\theta_r \\ \sin\theta_r & \cos\theta_r \end{bmatrix} \cdot \begin{bmatrix} v_d \\ v_q \end{bmatrix} = \begin{bmatrix} -V_m \sin(\theta_r - \theta_v) \\ V_m \cos(\theta_r - \theta_v) \end{bmatrix} \quad (6.22)$$

where  $v_d$  and  $v_q$  are the d- and q-axis voltages in the synchronous reference frame,  $V_m$  is the amplitude of stator voltage and  $\theta_v = \arctan(v_d/v_q)$ .

Substitute (6.22) into (6.21) and using Laplace transform to obtain the solution of stator currents shown in (6.23).

$$\begin{aligned} \begin{bmatrix} i_\alpha \\ i_\beta \end{bmatrix} &= \frac{\omega_r \psi_m}{\sqrt{R_s^2 + \omega_r^2 L_s^2}} \begin{bmatrix} \sin(\theta_r - \theta_p) \\ -\cos(\theta_r - \theta_p) \end{bmatrix} + \frac{V_m}{\sqrt{R_s^2 + \omega_r^2 L_s^2}} \begin{bmatrix} -\sin(\theta_r - \theta_v - \theta_p) \\ \cos(\theta_r - \theta_v - \theta_p) \end{bmatrix} + \\ &\omega_r \psi_m e^{-\frac{R_s}{L_s} t} \begin{bmatrix} \frac{\omega_r L_s}{R_s^2 + \omega_r^2 L_s^2} \\ \frac{R_s}{R_s^2 + \omega_r^2 L_s^2} \end{bmatrix} - \frac{V_m}{\sqrt{R_s^2 + \omega_r^2 L_s^2}} e^{-\frac{R_s}{L_s} t} \begin{bmatrix} \sin(\theta_v + \theta_p) \\ \cos(\theta_v + \theta_p) \end{bmatrix} \end{aligned} \quad (6.23)$$

From (6.23), it can be seen that the last two terms containing the transient part, i.e.  $e^{-(R_s/L_s \cdot t)}$ . In the steady-state, this term can be neglected. In the transient state, during low speed or starting operation, there can be influenced only under the condition of  $L_s \gg R_s$ . Hence, these two terms are neglected in this section. Then (6.23) is simplified to (6.24).

$$\begin{bmatrix} i_\alpha \\ i_\beta \end{bmatrix} = \frac{\omega_r \psi_m}{\sqrt{R_s^2 + \omega_r^2 L_s^2}} \begin{bmatrix} \sin(\theta_r - \theta_p) \\ -\cos(\theta_r - \theta_p) \end{bmatrix} + \frac{V_m}{\sqrt{R_s^2 + \omega_r^2 L_s^2}} \begin{bmatrix} -\sin(\theta_r - \theta_v - \theta_p) \\ \cos(\theta_r - \theta_v - \theta_p) \end{bmatrix} \quad (6.24)$$

where  $\theta_p = \arctan(\omega_r L_s / R_s)$ ,  $\theta_v = \arctan(v_d/v_q)$ .

Obviously, in (6.24), there are two angles  $\theta_v$  and  $\theta_p$  introducing errors in position estimation when directly using stator currents to estimate the rotor position. As a consequence, in order to utilize the stator currents to estimate the rotor position, these two angles are necessary to be considered.

As seen from (6.24), each term on the right side has the error angel  $\theta_p$ . Therefore, it is much more convenient to use the transformation method to compensate for this error angle. The transformation matrix and its inverse constituted by  $\theta_p$  are given in (6.25) and (6.26). The transformation is illustrated in Fig. 6.5.

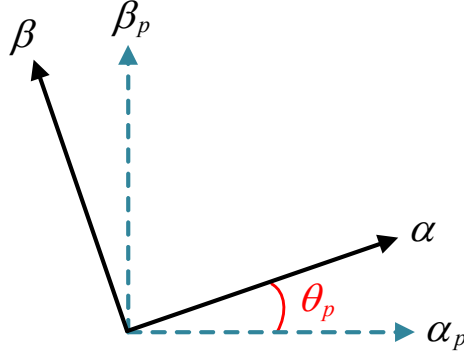


Fig. 6.5. Reference frame transformation. [WU20e]

By applying (6.25) to (6.24), the influence of  $\theta_p$  can be easily eliminated.

$$T(\theta_p) = \begin{bmatrix} \cos\theta_p & \sin\theta_p \\ -\sin\theta_p & \cos\theta_p \end{bmatrix} \quad (6.25)$$

$$T(\theta_p)^{-1} = \begin{bmatrix} \cos\theta_p & -\sin\theta_p \\ \sin\theta_p & \cos\theta_p \end{bmatrix} \quad (6.26)$$

After transformation, (6.24) becomes (6.27), and the stator currents are transformed from the conventional  $\alpha\beta$  stationary reference frame to a new so-called  $\alpha_p\beta_p$  reference frame.

$$\begin{bmatrix} i_{\alpha_p} \\ i_{\beta_p} \end{bmatrix} = \frac{1}{\sqrt{R_s^2 + \omega_r^2 L_s^2}} \begin{bmatrix} -V_m \sin(\theta_r - \theta_v) \\ V_m \cos(\theta_r - \theta_v) \end{bmatrix} - \omega_r \psi_m \begin{bmatrix} -\sin\theta_r \\ \cos\theta_r \end{bmatrix} \quad (6.27)$$

As shown in (6.27), in order to directly utilize stator currents to acquire rotor position information, the left error angle  $\theta_v$  is to be compensated. According to (6.22),  $\theta_v$  is directly controlled to zero by controlling the d-axis voltage to zero, i.e.  $v_d = 0$ . The control diagram of this part is shown in Fig. 6.4, a zero command is given to the d-axis voltage. Initially, there may be an error between the estimated and actual positions, and therefore, the following derivation can be based on the estimated reference frame.

The d-axis voltage in the estimation reference frame can be represented as:

$$\hat{v}_d = R_s \hat{i}_d + L_s \frac{d\hat{i}_d}{dt} - \omega_r L_s \hat{i}_q - \omega_r \psi_m \sin\Delta\theta_r \quad (6.28)$$

In the control system, as illustrated by Fig. 6.4, the d-axis voltage in the estimation reference frame, i.e.  $\hat{v}_d$ , is controlled to zero, neglecting the transient part which is relatively small. Then, the equation in (6.28) becomes:

$$R_s \hat{i}_d - \omega_r L_s \hat{i}_q = \omega_r \psi_m \sin \Delta \theta_r = E \sin \Delta \theta_r \quad (6.29)$$

With the definition of  $\theta_p$  in (6.24), the left side of (6.29) can be re-arranged as:

$$\cos \theta_p \hat{i}_d - \sin \theta_p \hat{i}_q = A \sin \Delta \theta_r \quad (6.30)$$

where  $A = \frac{E}{\sqrt{R_s^2 + \omega_r^2 L_s^2}}$ .

Utilizing the transformation matrix in (6.25), (6.30) can be transformed into (6.31).

$$i_{\alpha_p} \cos \hat{\theta}_r + i_{\beta_p} \sin \hat{\theta}_r = A \sin \Delta \theta_r \quad (6.31)$$

In (6.31),  $\hat{\theta}_r$  is the estimated rotor position. Obviously, it can be seen that when  $i_{\alpha_p}$  and  $i_{\beta_p}$  are the input of a phase-locked loop (PLL), the right side of (6.31) is equal to the error signal  $\varepsilon_{PLL}$  of the PLL whose block diagram is shown in Fig. 6.6.

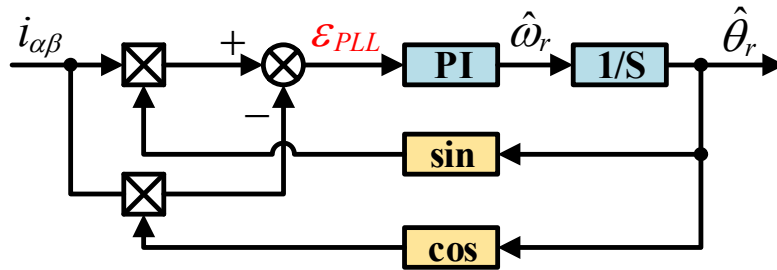


Fig. 6.6. Block diagram of the Phase-locked Loop. [WU20e]

The PLL used here is a conventional and common way to extract phase and frequency information from input signals. Now, (6.31) is represented as:

$$i_{\alpha_p} \cos \hat{\theta}_r + i_{\beta_p} \sin \hat{\theta}_r = \varepsilon_{PLL} \quad (6.32)$$

After the error  $\varepsilon_{PLL}$  converges to zero, the position will be correctly tracked and position estimation error is zero, i.e.  $\Delta \theta_r = 0$ . Then, combining the model in (6.27), the inputs of the PLL,  $i_{\alpha_p}$  and  $i_{\beta_p}$  can be represented as:

$$\begin{bmatrix} i_{\alpha_p} \\ i_{\beta_p} \end{bmatrix} = \frac{V_m - \omega_r \psi_m}{\sqrt{R_s^2 + \omega_r^2 L_s^2}} \cdot \begin{bmatrix} -\sin\theta_r \\ \cos\theta_r \end{bmatrix} \quad (6.33)$$

Since only the low speed range is concerned in this section, then (6.33) can be finalized as a simplified model in (6.34). Because when the rotor speed is low, it is assuming that  $R_s \gg \omega_r L_s$ . According to (6.24), the influence of  $\theta_p$  can be ignored, i.e.  $\theta_p \approx 0$ .

$$\begin{bmatrix} i_{\alpha} \\ i_{\beta} \end{bmatrix} = \frac{V_m - \omega_r \psi_m}{\sqrt{R_s^2 + \omega_r^2 L_s^2}} \cdot \begin{bmatrix} -\sin\theta_r \\ \cos\theta_r \end{bmatrix} \quad (6.34)$$

The final simplified model in (6.34) states that the rotor position information can be directly extracted from stator current at low speed through a PLL or other observers. Clearly, the current information is provided by the current sensor. No parameters and voltage information is required. Thus, a good estimation performance is expected, especially in the low speed range. This benefit makes this proposed method effective and capable of position estimation in the low speed range and even starting from the standstill.

### 6.3.2 Phase-locked Loop

As discussed in Section 6.3.1, a quadrature PLL is used to track the rotor position information from the stator currents. Based on (6.34), the equivalent block diagram of PLL is shown in Fig. 6.7.

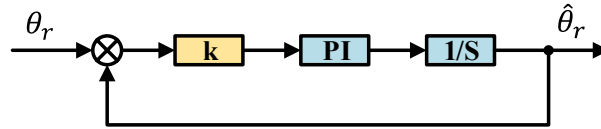


Fig. 6.7. Equivalent block diagram of the phase-locked loop. [WU20e]

In Fig. 6.7,  $k = \sqrt{i_{\alpha}^2 + i_{\beta}^2}$  which varies with different conditions. In order to fix the poles of the PLL transfer function at different conditions, it is necessary to normalize the input signals by dividing  $k$ . Then the normalized input error signal of PLL can be expressed as:

$$\varepsilon_{PLL,N} = \frac{1}{\sqrt{i_{\alpha}^2 + i_{\beta}^2}} (i_{\alpha} \cos \hat{\theta}_r + i_{\beta} \sin \hat{\theta}_r) \quad (6.35)$$

Therefore, the closed loop transfer function of the PLL can be given by:

$$H(s) = \frac{K_p s + K_i}{s^2 + K_p s + K_i} \quad (6.36)$$

(6.36) can be re-arranged as:

$$H(s) = \frac{2\xi\omega_n s + \omega_n^2}{s^2 + 2\xi\omega_n s + \omega_n^2} \quad (6.37)$$

where  $\omega_n = \sqrt{K_i}$ ,  $\xi = \frac{K_p}{2} \sqrt{\frac{1}{K_i}}$ .  $\omega_n$  is the natural frequency and can be used as the bandwidth of PLL.  $\xi$  is the damping factor. A higher damping factor can reduce the overshoot but also sacrifice the dynamic performance. Then, the parameters of PLL can be initially designed. Furthermore, the stability of PLL should also be considered after determining the parameters of PLL. Since the PLL used in the chapter is a typical second-order PLL, according to [GAR05], this type of PLL is unconditionally stable for all positive values of parameters.

### 6.3.3 Speed Estimator

Speed feedback is essential for the closed-loop speed control of PMSM drives. Normally, rotor speed is calculated by differentiating the estimated rotor position. However, calculation of speed from the differential of rotor position may be inappropriate for the feedback in the closed-loop system. Since the noise will be amplified by the differential operation.

The rotor speed calculated from the differential of the estimated rotor position is given by:

$$\hat{\omega}_r = \frac{\hat{\theta}_r(k) - \hat{\theta}_r(k-1)}{\Delta T_s} \quad (6.38)$$

where  $\hat{\theta}_r(k)$  and  $\hat{\theta}_r(k-1)$  are the instantaneous estimated rotor position at the starts of the  $k$ th and  $(k-1)$ th sample periods.  $\Delta T_s$  is the duration of one sample period. However, this estimated speed  $\hat{\omega}_r$  cannot be directly used in the speed feedback, since the noise  $w(k)$  in the estimated rotor position will be amplified with a small  $\Delta T_s$  as shown by (6.39).

$$\hat{\omega}_r = \frac{\hat{\theta}_r(k) - \hat{\theta}_r(k-1)}{\Delta T_s} + \frac{w(k)}{\Delta T_s} \quad (6.39)$$

Therefore, the estimated speed should be filtered by a low-pass filter (LPF) as:

$$\hat{\omega}_{r\_LPF} = LPF(\hat{\omega}_r) = \frac{1}{T_s + 1} \hat{\omega}_r \quad (6.40)$$

where  $\hat{\omega}_{r\_LPF}$  is the estimated speed after filtering and  $T$  is the time constant of the low-pass filter. The block diagram of the speed estimator is shown in Fig. 6.8.

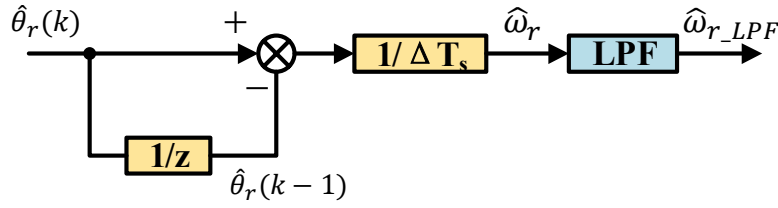


Fig. 6.8. Block diagram of speed estimator.

### 6.3.4 Inverter Nonlinearity Effect

As mentioned in Section 6.3.1, in order to make  $\theta_v$  zero, a zero command is given to d-axis voltage, which is shown in Fig. 6.4. However, it is worth noting that in practice, the output voltage of the inverter may be different from the reference voltage due to inverter-nonlinearity, of which the dead-time is the main contribution to the output voltage error. In this chapter, two machines are tested and take SPM-I as the example, the influence of inverter-nonlinearity on the proposed position estimation method is investigated.

According to [JEO91][RAU10][GON11], the relationship between phase voltage error and phase current can be obtained due to inverter-nonlinearity. Then, the phase voltage error against the phase current is measured and shown in Fig. 6.9. It can be seen that the voltage error is relatively small compared to the rated terminal voltage of the tested SPMSM as shown in the Appendix. This is due to that the dead-time effect is less with a lower switching frequency. The sampling frequency and dead time settings of the test rig are 2.5 kHz and  $2\mu s$ , respectively.

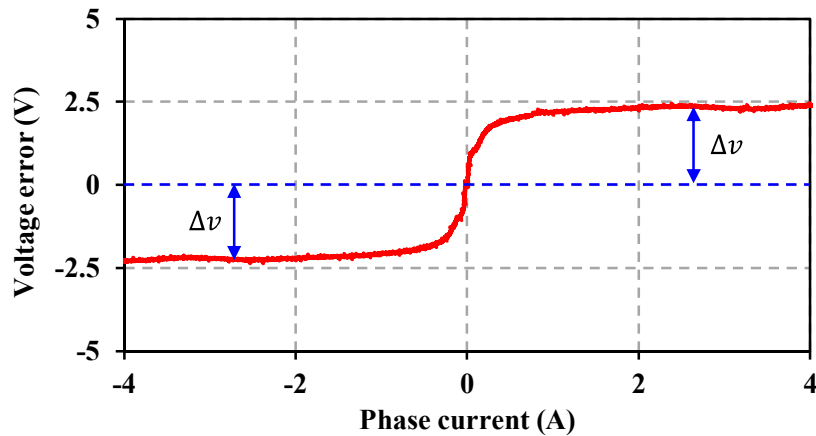


Fig. 6.9. Measured voltage error against phase current. [WU20e]

Equation (6.41) illustrates that the actual d-axis voltage is different from the reference due to inverter-nonlinearity.

$$v_d^* = v_d + \Delta v_d \quad (6.41)$$

As mentioned in Part A before,  $\theta_v$  is controlled to zero. Due to the existence of  $\Delta v_d$ , an error is therefore introduced in the angle  $\theta_v$ , which is shown in (6.42).

$$\Delta \theta_v = \arctan \frac{\Delta v_d}{v_q} \quad (6.42)$$

Based on the simplified mathematical model presented, a non-zero  $\theta_v$  will cause a position estimation error. However, it is obviously seen from (6.42) that a slight difference in  $v_d$  can be minimized by dividing  $v_q$ . In all, as shown in Fig. 6.10, with the original settings of dead time and switching frequency, position estimation error caused by this inverter nonlinearity can be ignored. Therefore, the compensation of inverter-nonlinearity may be unnecessary.

However, if the inverter-nonlinearity effect becomes more significant, then the estimation error will increase so that it cannot be ignored as before. Therefore, corresponding compensations are necessary. In Fig. 6.10, the dead-time is intentionally increased to investigate its influence on position estimation error. Clearly, it can be seen that position error increases as the dead-time becomes larger.

There are many methods [JEO91] [RAU10][GON11][PAR12][WAN14a] to solve the influence of inverter-nonlinearity effect, with which the influence can be solved properly. Based on the relationship between the measured voltage errors against current shown in Fig. 6.9, a compensation look-up table (LUT) is generated to solve the position estimation error due to inverter nonlinearity. According to [WAN14a], the generated compensation LUT can be represented as a nonlinear function between the output phase voltage error and the phase current, viz.,

$$\Delta v_{error-x} = f(i_x) = 2\Delta U \left( \frac{1}{1 + e^{-ki_x}} - \frac{1}{2} \right) \quad (6.43)$$

where  $\Delta v_{error-x}$  and  $i_x$  are the arbitrary phase distortion voltage and phase current, respectively.  $\Delta U$  and  $k$  are the distortion voltage model parameters. A larger dead-time contributes to a larger  $\Delta U$ . Then, the voltage command is modified to:

$$v^{**} = v^* + f(i_x) \quad (6.44)$$

The block diagram of the compensation is shown in Fig. 6.4. Fig. 6.10 shows that after compensation, the position error caused by inverter-nonlinearity is eliminated apparently.

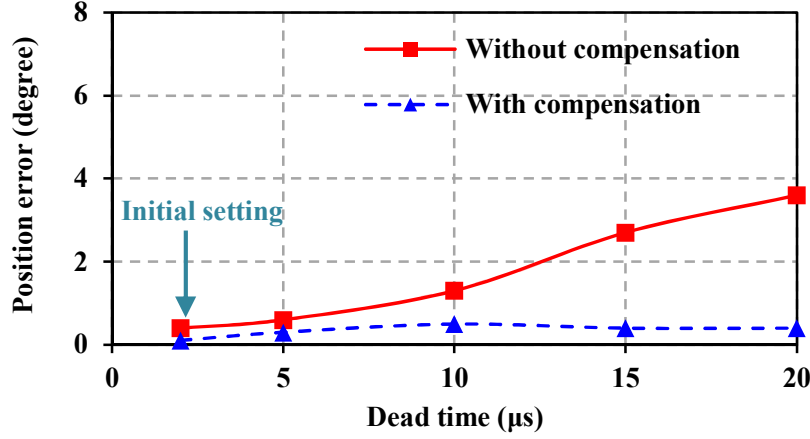


Fig. 6.10. Position estimation error against dead-times. [WU20c]

### 6.3.5 Starting Procedure

For conventional fundamental model based methods, zero and low speed sensorless control performance is poor due to non-observable back-EMF. For the proposed method, the stator currents are directly used to estimate the position, the low speed sensorless control performance could be improved. Although for the proposed method, zero speed rotor position estimation is unfeasible, it is still possible to start the machine as long as the observer can quickly converge to the actual position after an initial rotation movement is produced. However, starting without the knowledge of rotor initial position information, the starting performance may not be satisfied and become even worse, e.g. reverse rotation issue [BOL99][JAN06], which is not allowed by some applications. In [BOL99], a countermeasure to reverse rotation during starting is proposed by looking at the estimated speed, a 180-degree compensation angle is compensated during reverse rotation. However, a large q-axis current impulse will be produced during the correction, producing harmful torque. Hence, before starting the rotor initial position information is obtained to improve the starting performance and prevent the reverse rotation. Rotor initial position estimation methods based on magnetic saturation effect [MAT96][SCH97][TUR03][WAN10][WU20c] are a satisfactory alternative and are employed in the section.

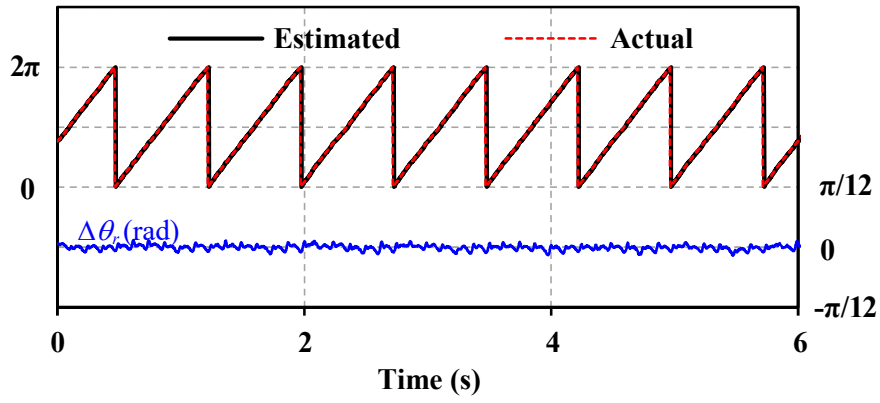
In this section, the method in [WU20c] is adopted to estimate the rotor initial sector. By using [WU20c], initial rotor position can be estimated with a maximum error of 15 degrees. With the knowledge of the rotor initial position sector, a more reliable starting performance can be achieved without reverse rotation, which will be verified by experimental results.

### 6.3.6 Experimental Validation

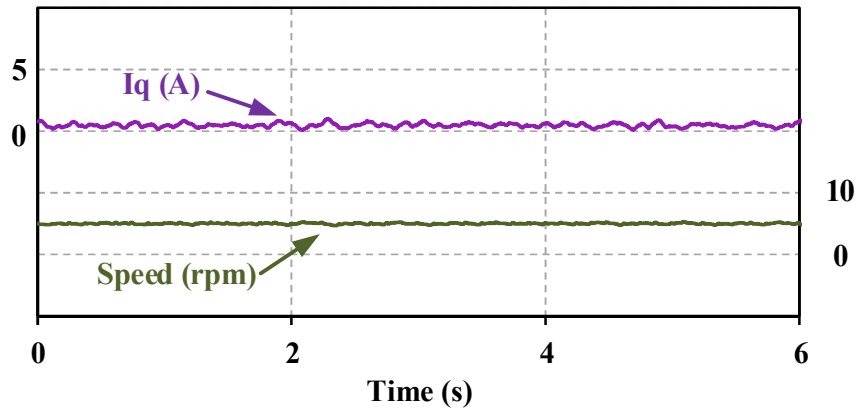
The experiments are implemented on a dSPACE platform to validate the effectiveness of the proposed method on two prototype SPMSMs, i.e. SPM-I and SPM-II (their parameters are shown in Appendix A). Although SPM-I has a larger PM flux-linkage, the large inertia makes it more difficult to start up. SPM-II has a much smaller inertia but its PM flux-linkage is also much smaller than SPM-I. For SPM-I, a torque motor is connected to the test SPMSM through the shaft. The torque motor is operated in torque control mode to provide the desired load to the SPM-I. Both steady-state and dynamic performances are investigated. Moreover, the starting performance test is carried out.

#### *A. Steady-state Performance*

The steady-state sensorless control performance with the proposed method is illustrated in Fig. 6.11 and Fig. 6.12. The position estimation error is  $\Delta\theta_r$ . In the test, SPM-I and SPM-II are controlled at 5rpm and 25rpm, respectively, which are approximately the minimum speeds that give the reliable performance. Fig. 6.11 and Fig. 6.12 are the steady-state estimation performance with no-load and Fig. 6.13 and Fig. 6.14 are the ones with the full-load. It can be seen that the proposed method provides good performance with different load conditions at a low speed. Besides, the steady-state position estimation performance against different load conditions is also considered and illustrated in Fig. 6.15, together with the DC component of the position estimation error. It can be seen that there is a small increase in the position error with more load. This is due to the simplification of the model from (6.33) to (6.34). Besides, SPM-II has slightly larger error than SPM-I. According to (6.24), this is due to a smaller resistance of SPM-II. Besides, a slight larger inverter non-linearity effect of SPM-II platform also increases the error. Nevertheless, the error is so small that can be ignored.

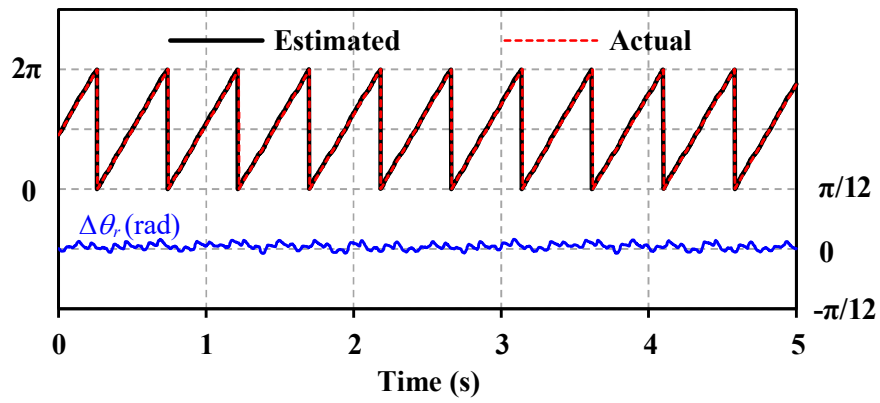


(a)

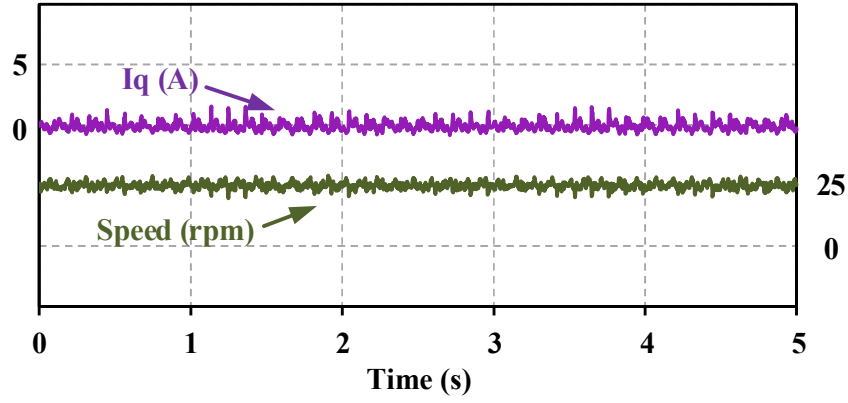


(b)

Fig. 6.11. No load steady-state performance at 5 rpm. (SPM-I) (a) Rotor position estimation. (b) Rotor speed and q-axis current. [WU20e]

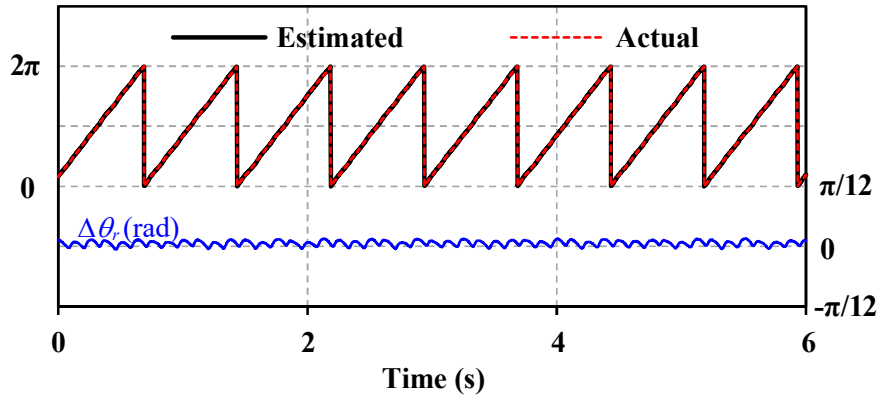


(a)

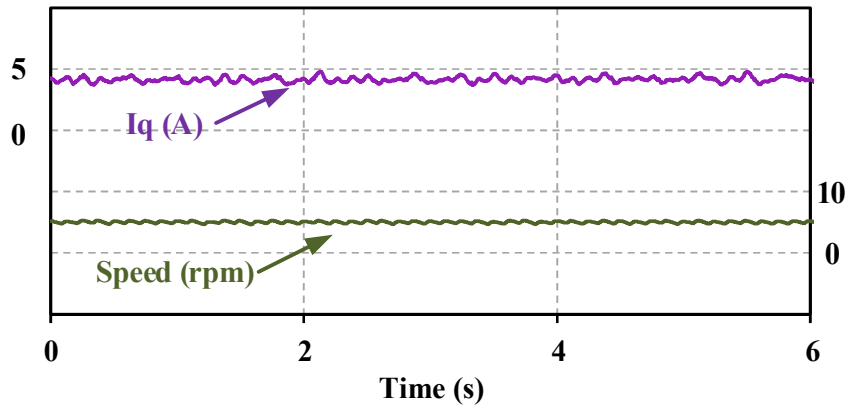


(b)

Fig. 6.12. No load steady-state performance at 25 rpm. (SPM-II) (a) Rotor position estimation. (b) Rotor speed and q-axis current. [WU20e]

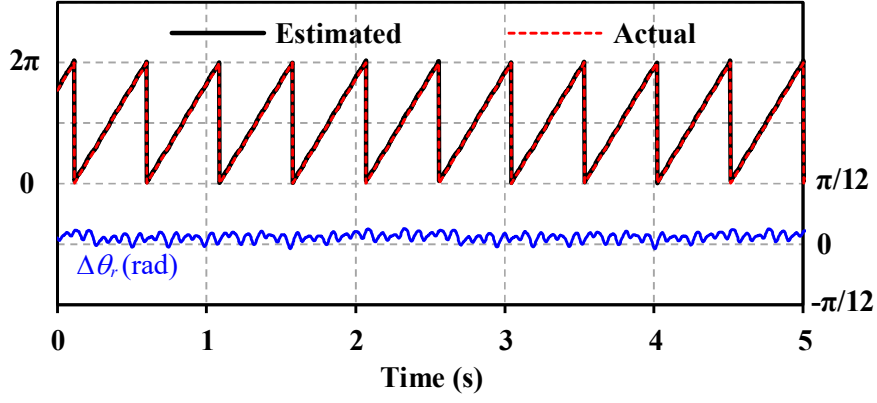


(a)

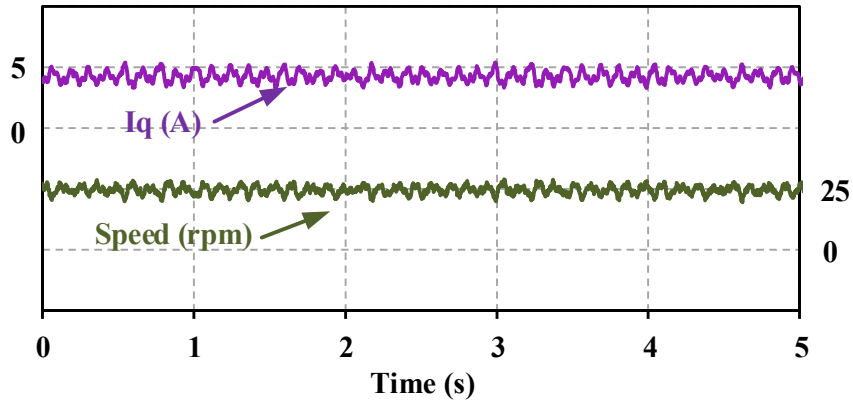


(b)

Fig. 6.13. Full load steady-state performance at 5 rpm. (SPM-I) (a) Rotor position estimation. (b) Rotor speed and q-axis current. [WU20e]



(a)



(b)

Fig. 6.14. Full load steady-state performance at 25 rpm. (SPM-II) (a) Rotor position estimation. (b) Rotor speed and q-axis current. [WU20e]

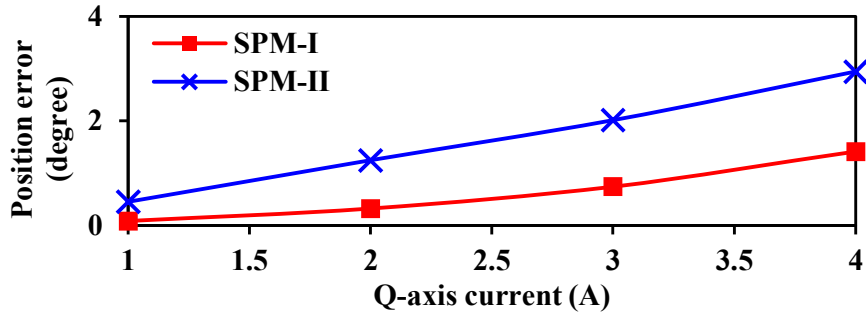


Fig. 6.15. DC component of position error against different load conditions. [WU20e]

### B. Dynamic-state performance

The dynamic performance of the proposed method is also presented in this part. For both SPM-I and SPM-II, step speed and step load tests are carried out. For the step speed test on SPM-I in Fig. 6.16, the speed reference is given as 0-10-20rpm. For the step speed test on SPM-II in Fig. 6.17, the speed reference is given as 20-50-100-200rpm. From the result, it can be

observed that the rotor is able to start from standstill well and then follow the given speed reference properly with the proposed method.

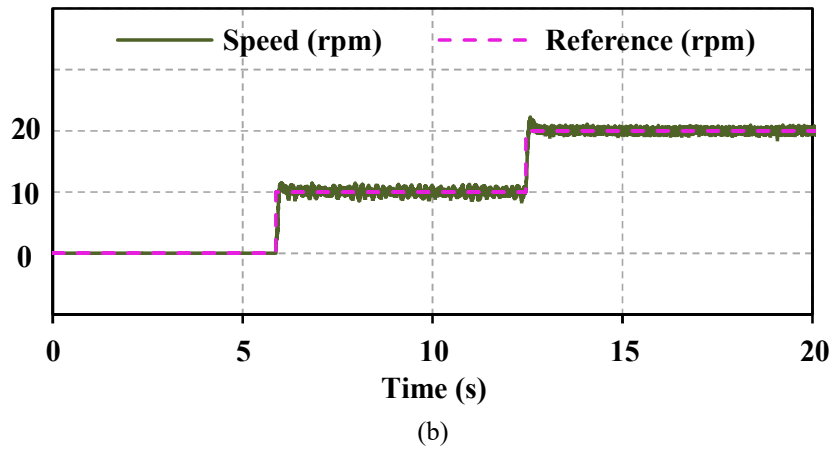
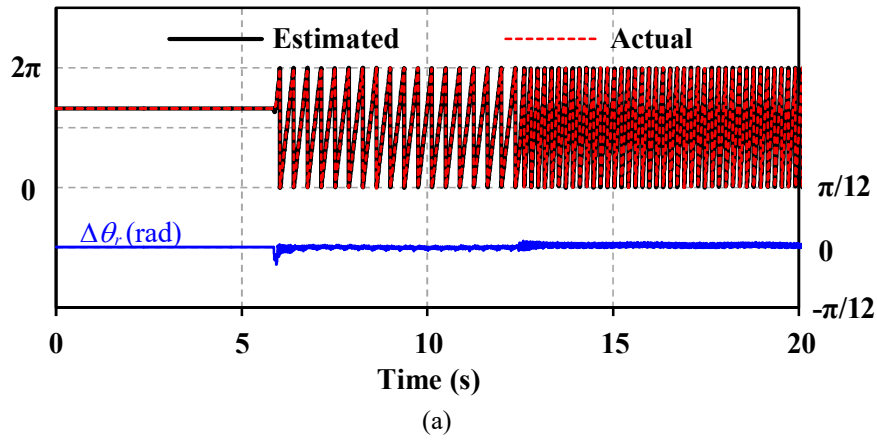
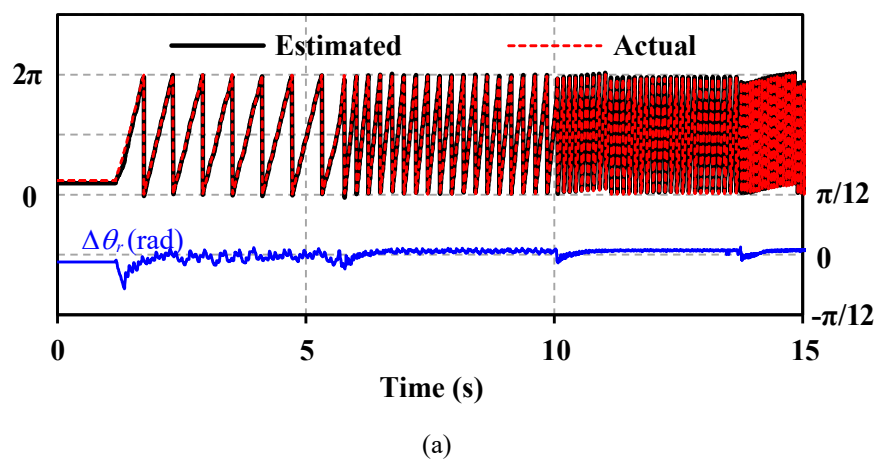
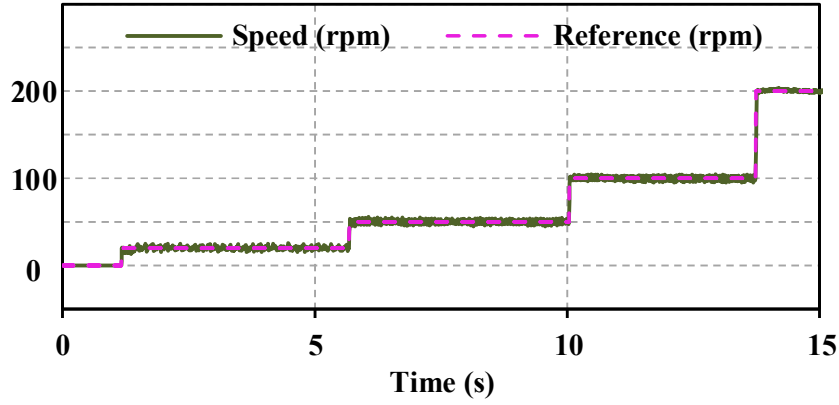


Fig. 6.16. Dynamic performance under step speed. (SPM-I) (a) Rotor position estimation. (b) Rotor speed and speed reference. [WU20e]

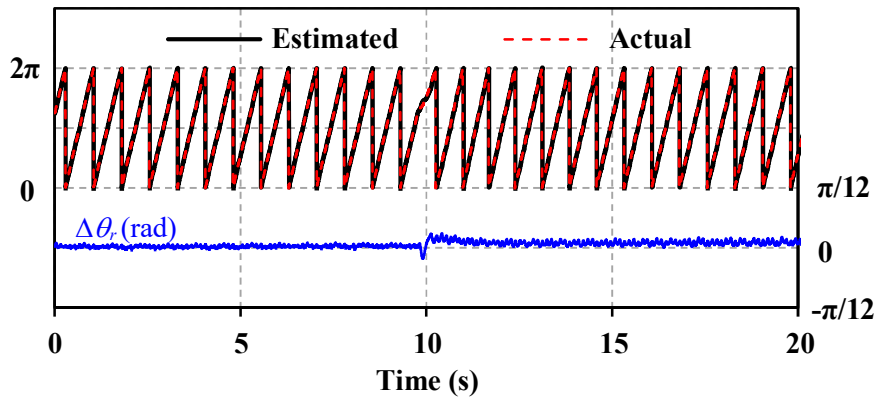




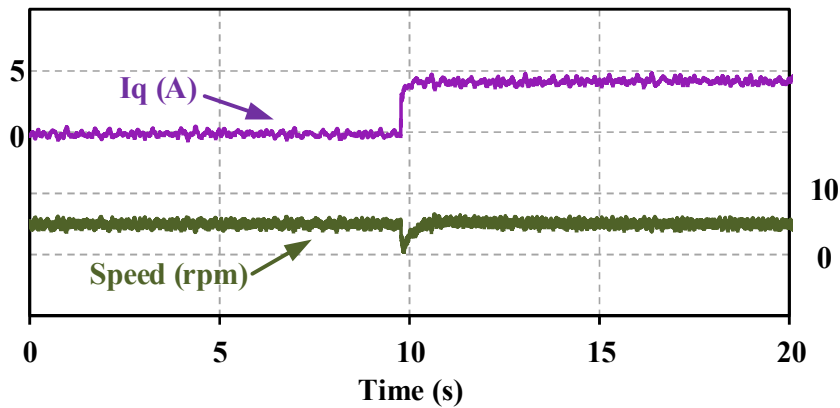
(b)

Fig. 6.17. Dynamic performance under step speed. (SPM-II) (a) Rotor position estimation. (b) Rotor speed and speed reference. [WU20e]

The step load test of both SPM-I and SPM-II are shown in Fig. 6.18 and Fig. 6.19, it is shown that the proposed method gives a good position tracking performance when q-axis current changes rapidly from no-load to full-load.

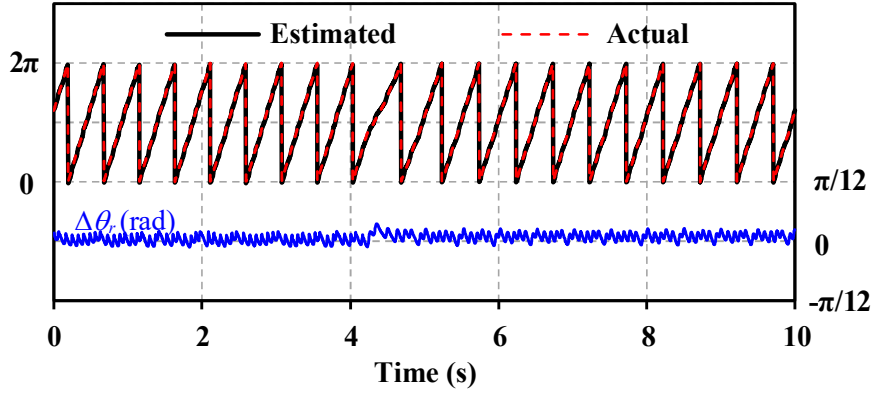


(a)

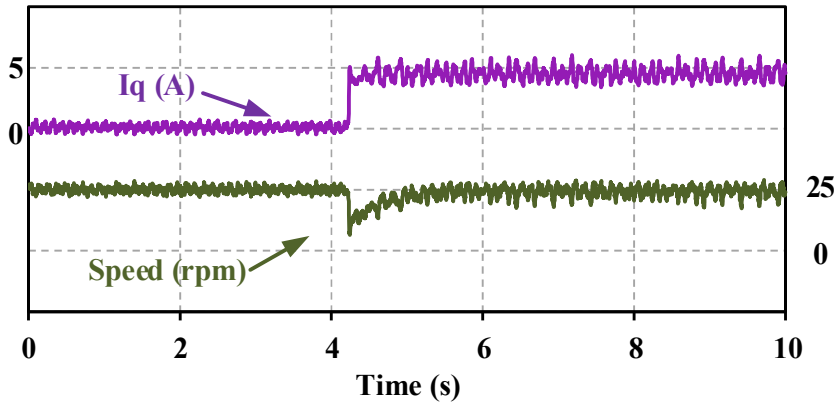


(b)

Fig. 6.18. Dynamic performance under step load. (SPM-I) (a) Rotor position estimation. (b) Rotor speed and q-axis current. [WU20e]



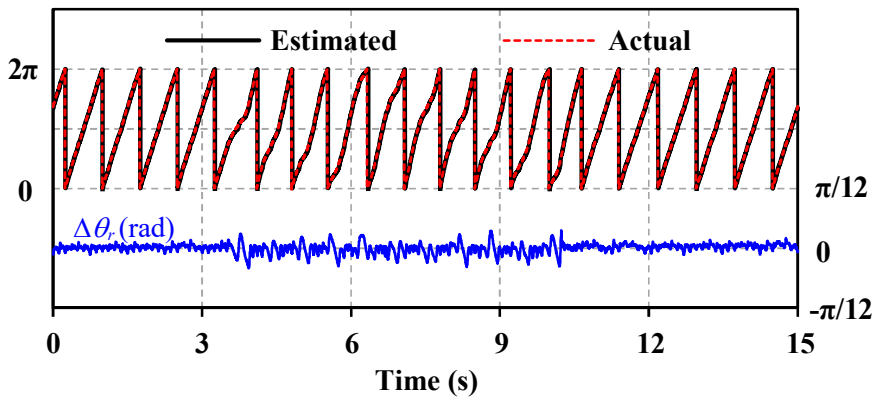
(a)



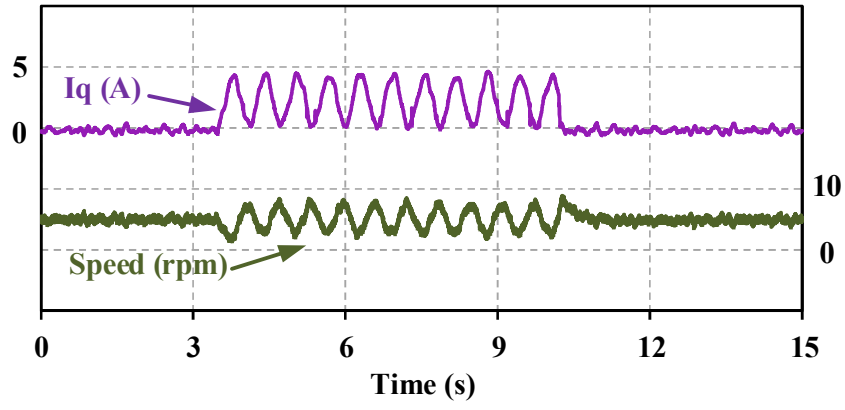
(b)

Fig. 6.19. Dynamic performance under step load. (SPM-II) (a) Rotor position estimation. (b) Rotor speed and q-axis current. [WU20e]

Moreover, a variable load test at 5rpm and 10rpm are considered in Fig. 6.20 and Fig. 6.21. Due to hardware limitation, the variable load test is only carried out on SPM-I. A time-varying load is applied to the SPM-I. The load changes from no-load to full-load. It can be seen that a stable position tracking performance is achieved at both 5rpm and 10rpm. Therefore, it can be concluded that the proposed position estimation method presents a good dynamic performance.

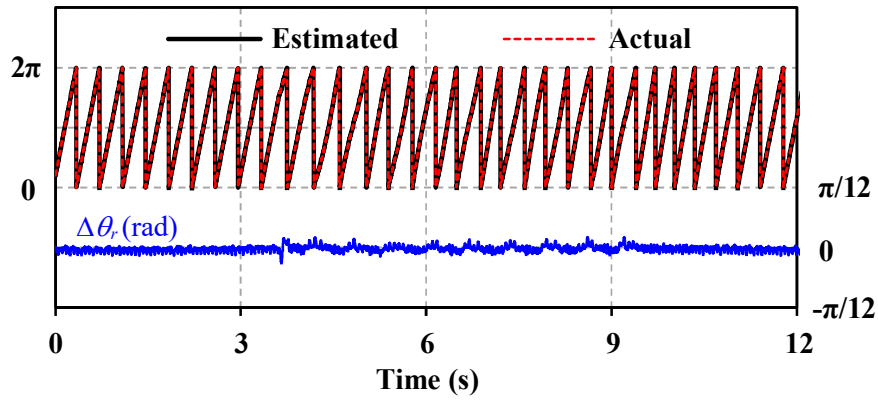


(a)

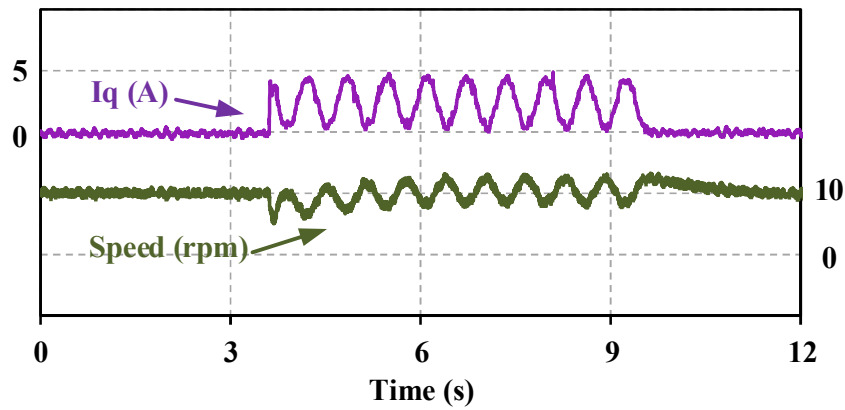


(b)

Fig. 6.20. Dynamic performance under variable load at 5rpm. (SPM-I) (a) Rotor position estimation. (b) Rotor speed and q-axis current. [WU20e]



(a)



(b)

Fig. 6.21. Dynamic performance under variable load at 10rpm. (SPM-I) (a) Rotor position estimation. (b) Rotor speed and q-axis current. [WU20e]

### C. Starting Performance

In this part, starting performance is examined. Firstly, in Fig. 6.22, a starting failure using the conventional back-EMF based method [CHE03] is shown. Next, as discussed in Section 6.3.4, the rotor initial sector information can be favourable in a reliable starting performance. Fig. 6.23 shows the starting performance without the knowledge of rotor initial sector information, it can be seen that a reverse starting happens.

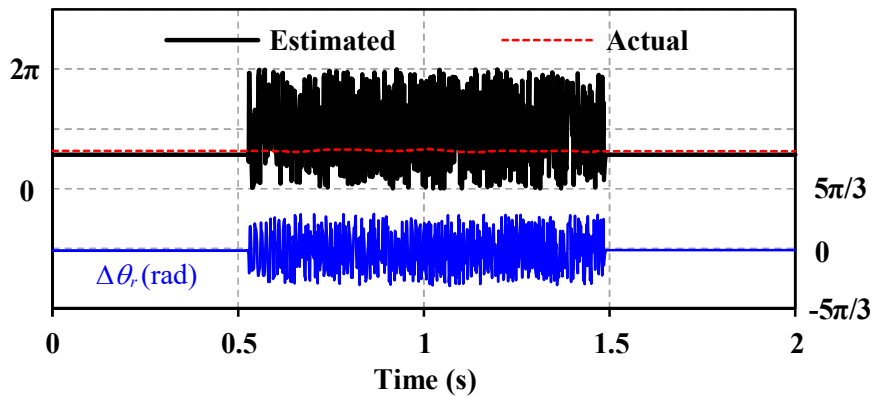


Fig. 6.22. Starting failure with the conventional back-EMF method [CHE03]. [WU20e]

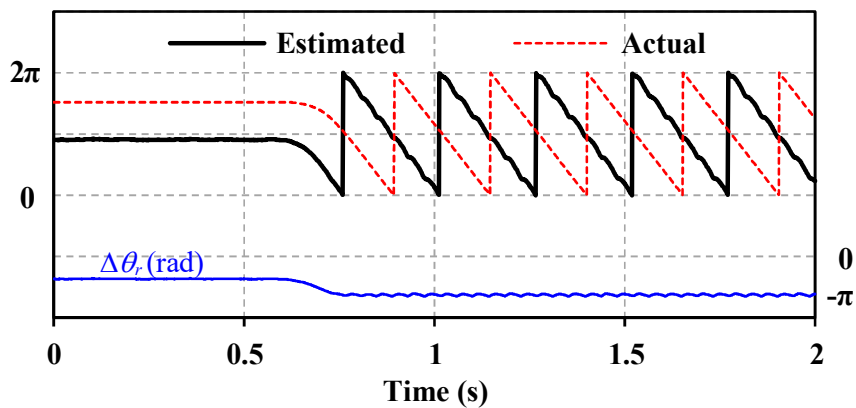
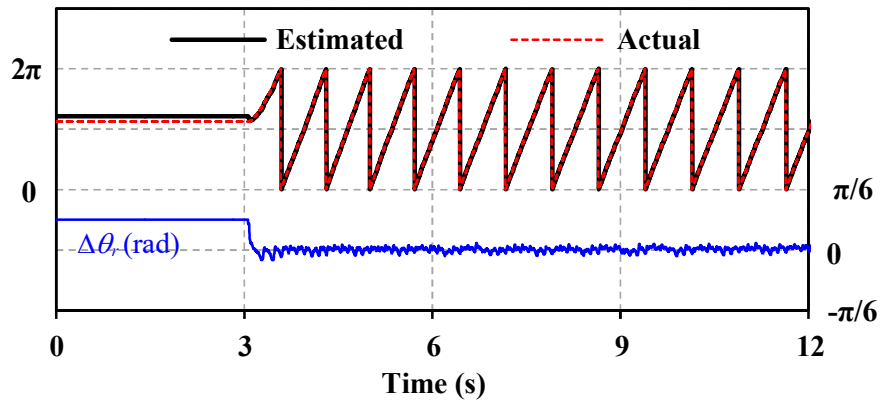


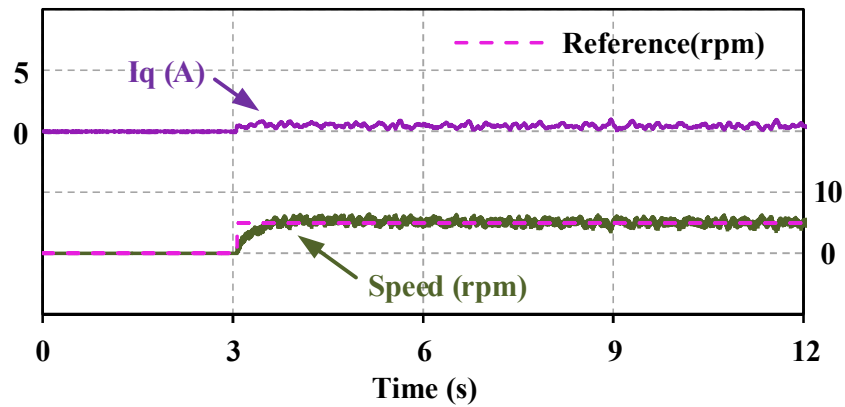
Fig. 6.23. Reverse rotation during starting, without knowledge of rotor initial sector information. [WU20e]

In contrast, with the knowledge of rotor initial sector, starting performance is tested. Rotor initial sector is firstly estimated based on [WU20c]. The maximum initial position error is 15 degrees. Therefore, in this part, the machine starts from standstill with 15 degrees initial position error. Fig. 6.24 and Fig. 6.26 show the starting performance with the proposed method considering no-load and full-load conditions. For the no-load test, on both SPM-I and SPM-II, it can be seen that the position can be tracked quickly and gives a satisfying starting

performance. In case of starting with full-load, due to hardware limitation, the test is only carried out on SPM-I. The torque motor is set as zero speed with a 91Nm torque limit which is the rated torque of the prototype SPMSM. As long as the prototype SPMSM can provide a proper torque that is larger than 91Nm during starting, the machine can start to accelerate to the reference speed. As shown in Fig. 6.26 the proposed method is able to start the machine from standstill with full-load.

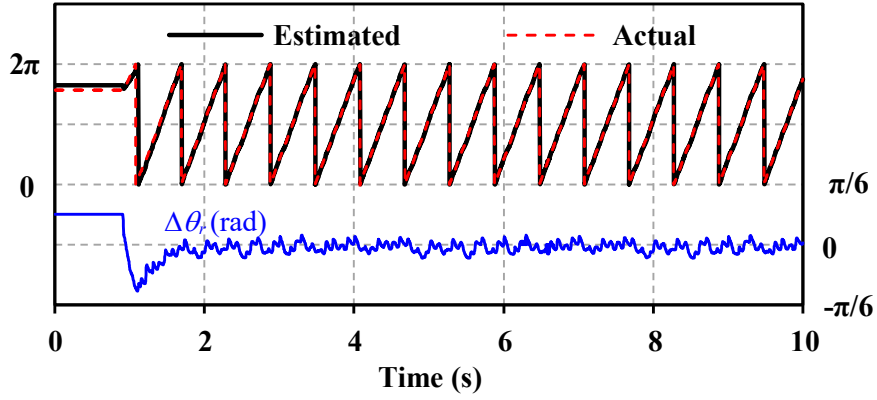


(a)

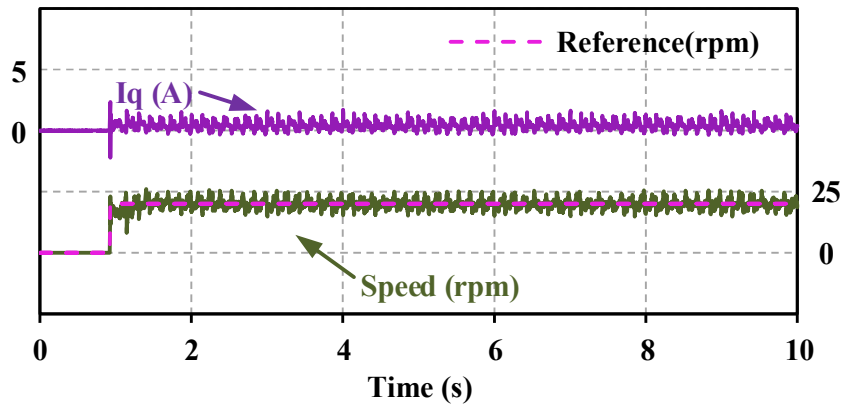


(b)

Fig. 6.24. Starting performance with no-load, with knowledge of rotor initial sector information. (SPM-I) (a) Rotor position estimation. (b) Rotor speed and q-axis current.

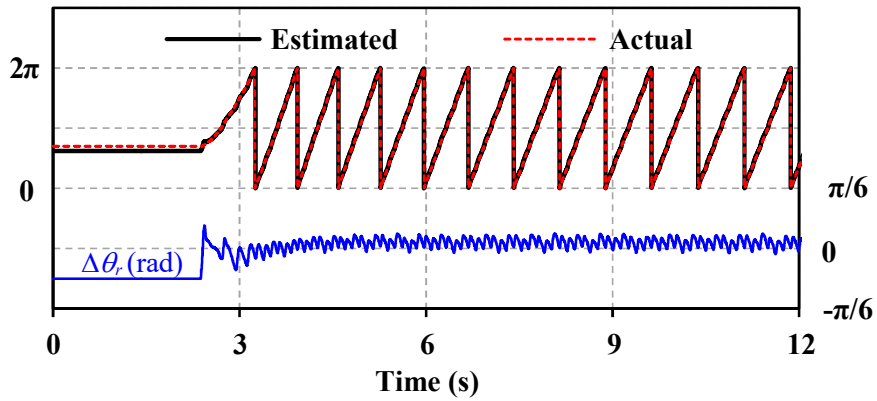


(a)

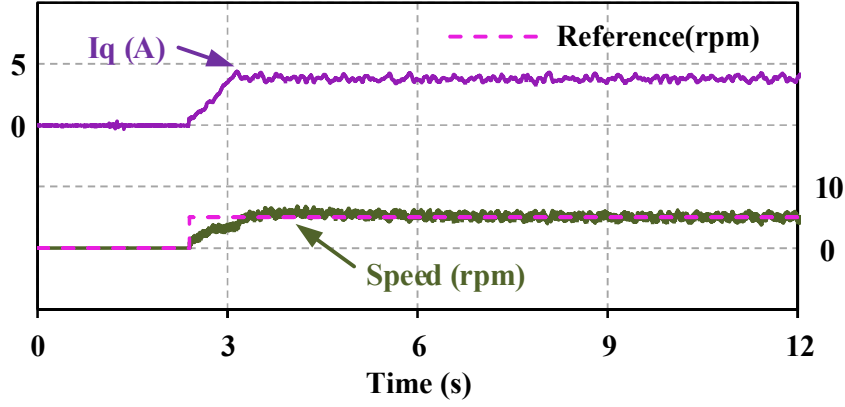


(b)

Fig. 6.25. Starting performance with no-load, with knowledge of rotor initial sector information.  
(SPM-II) (a) Rotor position estimation. (b) Rotor speed and q-axis current.



(a)



(b)

Fig. 6.26. Starting performance with the full-load, with knowledge of rotor initial sector information. (a) Rotor position estimation. (b) Rotor speed and q-axis current. [WU20e]

## 6.4 Application of Proposed Simplified Fundamental Model Based Method in Wind Power System

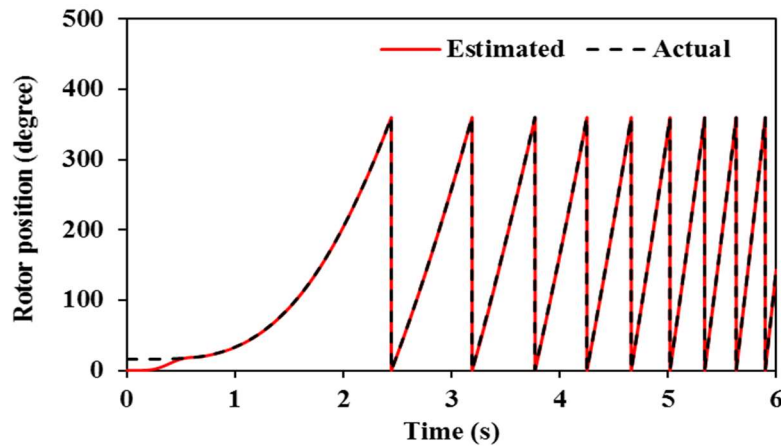
For wind power systems, both generating and motoring modes are necessary. In generating mode, the zero and low speed region may not be operated. However, in the motoring mode, starting operation is necessary. Especially, in the Siemens wind power system, a so-called “motoring test mode” is required since the turbines need to be tested in the motoring mode before installation. In the motoring test mode, the turbine is required to start from standstill to the rated speed or the overspeed under no load but with a very large inertia. For turbines with low or no saliency, high-frequency signal injection methods cannot be used to start the turbine. Currently, open-loop control method, i.e. VVVF(variable voltage variable frequency), is used but a large torque oscillation may occur during the starting. Hence, the proposed method is applied to the wind turbine in the motoring test mode to achieve a closed-loop sensorless starting operation.

### 6.4.1 Starting Performance

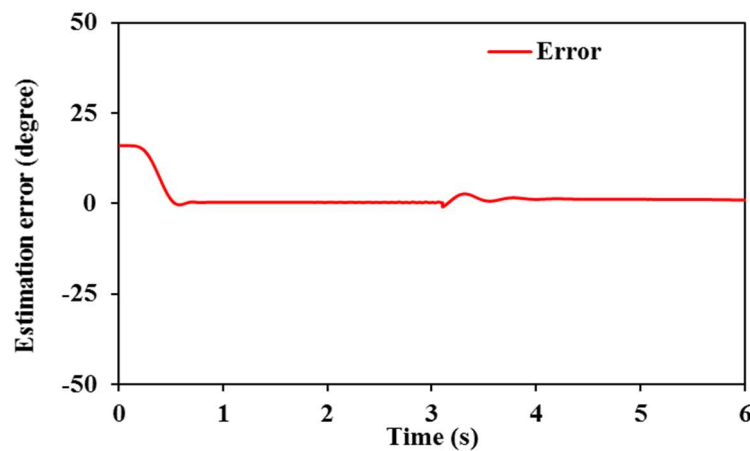
Due to the limitation of the practical test platform, only hardware-in-loop (HIL) simulation test is carried out based on the Siemens 3MW SPMSM wind turbine system and the turbine is operating in the motoring test mode. The turbine starts from 0 to 5 rpm under no load. Besides, it is worth mentioning that the induced q-axis current should be limited within 100A (2% rated current) by following the industrial requirements. Besides, in this part the starting performance is investigated with and without applying the rotor initial position estimation.

### A. With rotor initial position estimation

Firstly, the rotor initial position estimation method based on magnetic saturation introduced in Chapter 2 is applied at standstill. Then, the maximum rotor initial position error can be limited within  $\pm 15$  degrees. In this case, the starting performance is shown in Fig. 6.27. It can be seen that the turbine can start smoothly and there is no oscillation in the actual speed. Besides, during starting the induced q-axis current is within 50A which is smaller than the limitation.

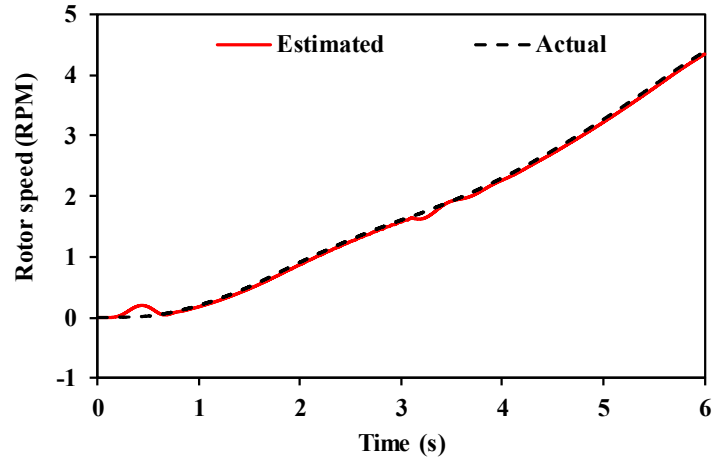


(a)

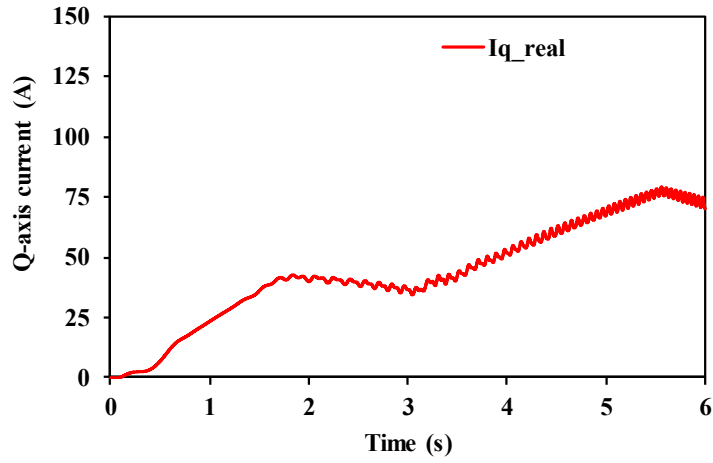


(b)

Fig. 6.27. Starting performance with rotor initial position error of 15 degrees. (a) Rotor position. (b) Position estimation error.



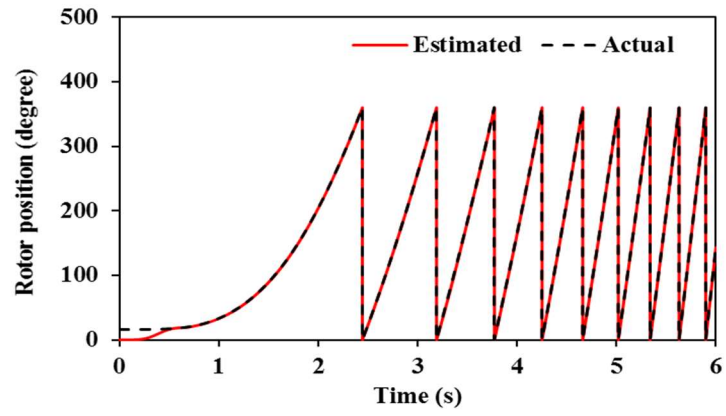
(a)



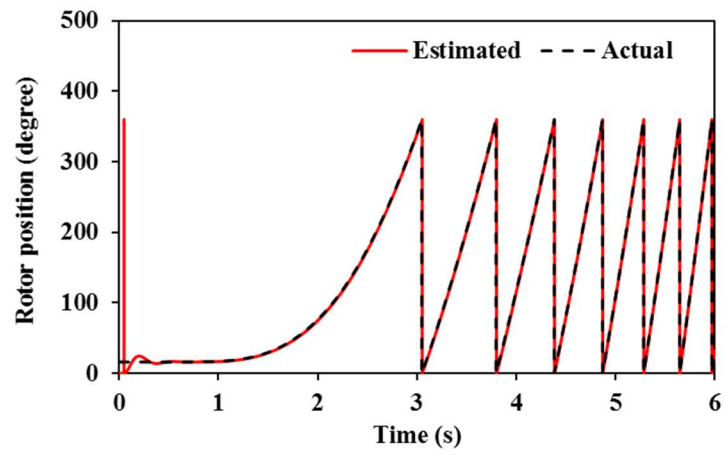
(b)

Fig. 6.28. Starting performance with rotor initial position error of 15 degrees. (a) Rotor speed. (b) Q-axis current.

Furthermore, the starting performance of the proposed method is compared with high frequency injection method. The high-frequency injection method used here is the conventional pulsating signal injection method. Both methods are tested with a 15-degree initial position error. The estimated position comparison is firstly shown in Fig. 6.29 and the estimation errors are given in Fig. 6.30. For both methods, the rotor position is estimated successfully and the turbine starts from standstill smoothly.

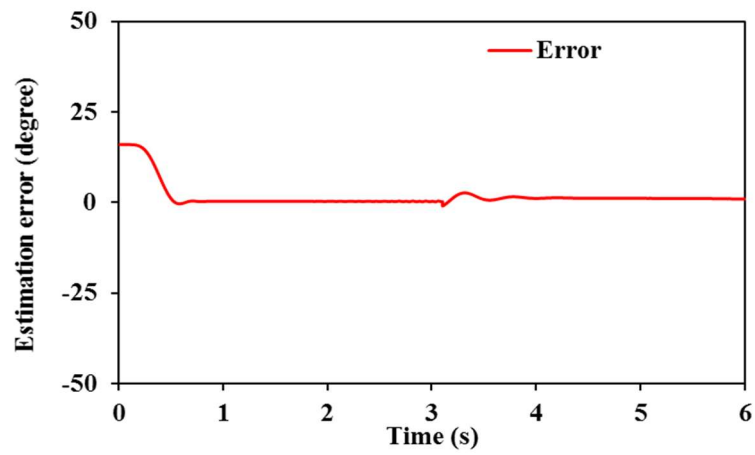


(a)



(b)

Fig. 6.29. Rotor position estimation comparison. (a) Proposed method. (b) High frequency injection method.



(a)

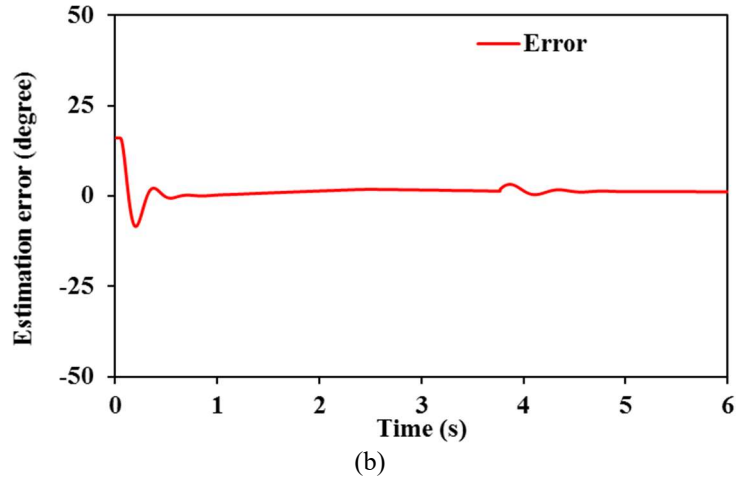


Fig. 6.30. Rotor position estimation error comparison. (a) Proposed method. (b) High frequency injection method.

Then, the rotor speed comparison is shown in Fig. 6.31. Obviously, by applying both methods the turbine is able to start successfully and rotate in the correct direction.

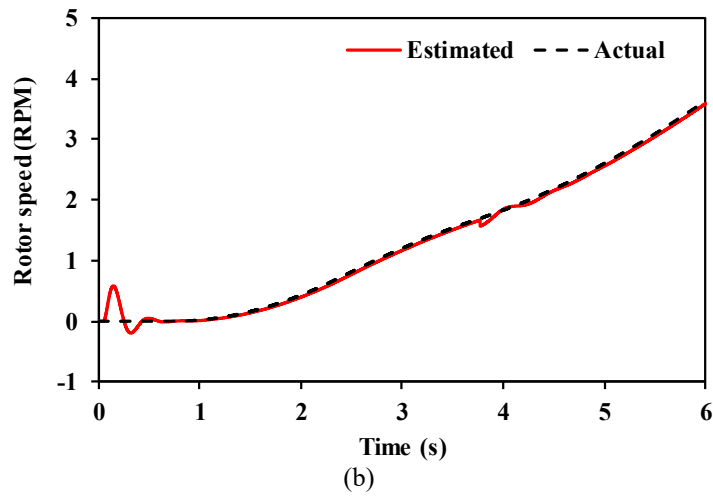
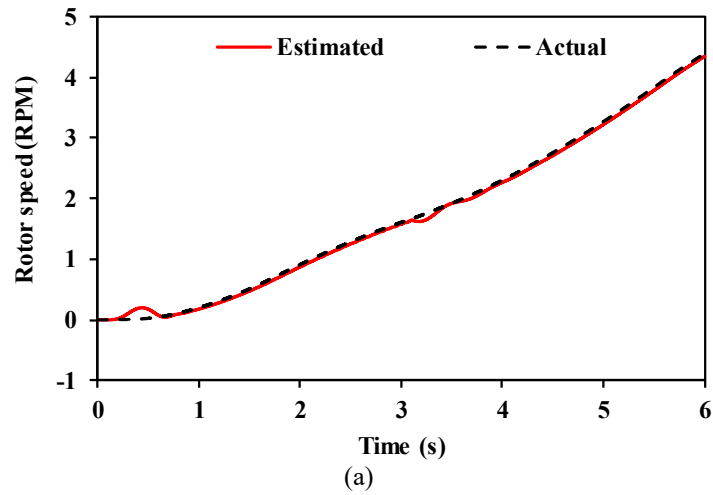


Fig. 6.31. Rotor speed comparison. (a) Proposed method. (b) High frequency injection method.

Fig. 6.32 shows the actual q-axis currents during the starting. It can be seen that for both methods, the q-axis current impulses during starting are within the limitation.

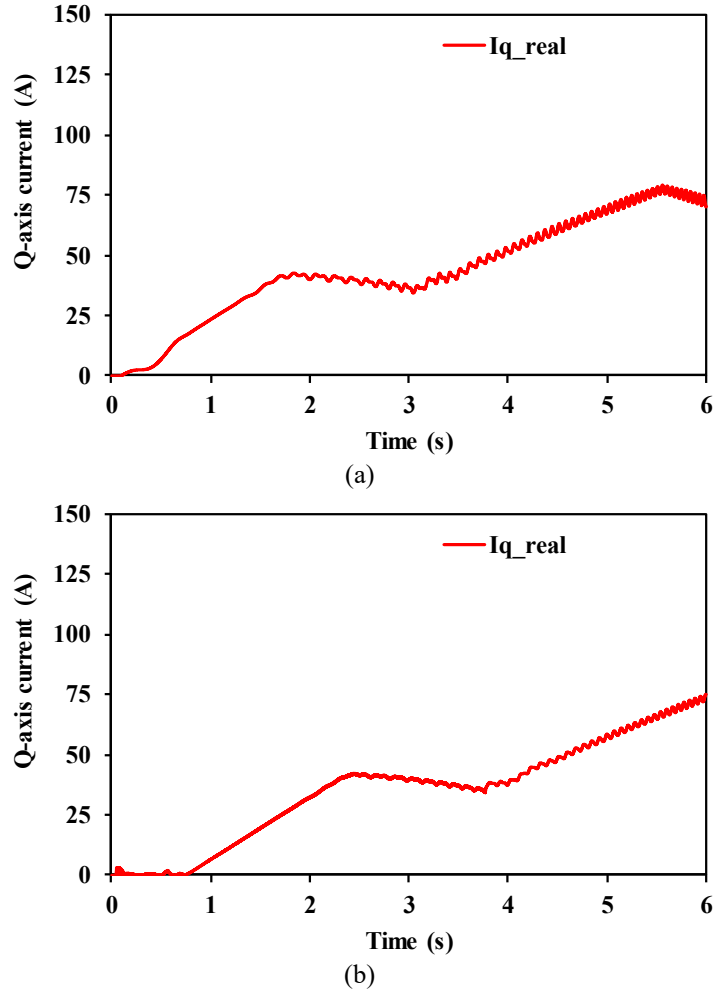


Fig. 6.32. Q-axis current comparison. (a) Proposed method. (b) High frequency injection method.

In summary, with the knowledge of rotor initial position, the starting performance of the proposed method is satisfied as the high frequency signal injection method.

### ***B. Without rotor initial position estimation***

As introduced in Chapter 2, in the rotor initial position estimation, voltage pulses are required and a certain amount of current response is necessary to saturate the iron core and therefore obtain reliable estimation performance. Inevitably, there will be current impulses in q-axis causing torque and noise, which may be limited by industrial requirement. Hence, in this part the proposed method is also tested without the rotor initial position estimation.

As shown in Fig. 6.33, by applying the proposed method the turbine is able to start with a maximum of rotor initial position error of 90 degrees. It is worth noting that although estimated speed goes negative at beginning, the actual speed is not and does not have any oscillation. This will be further investigated in the next section.

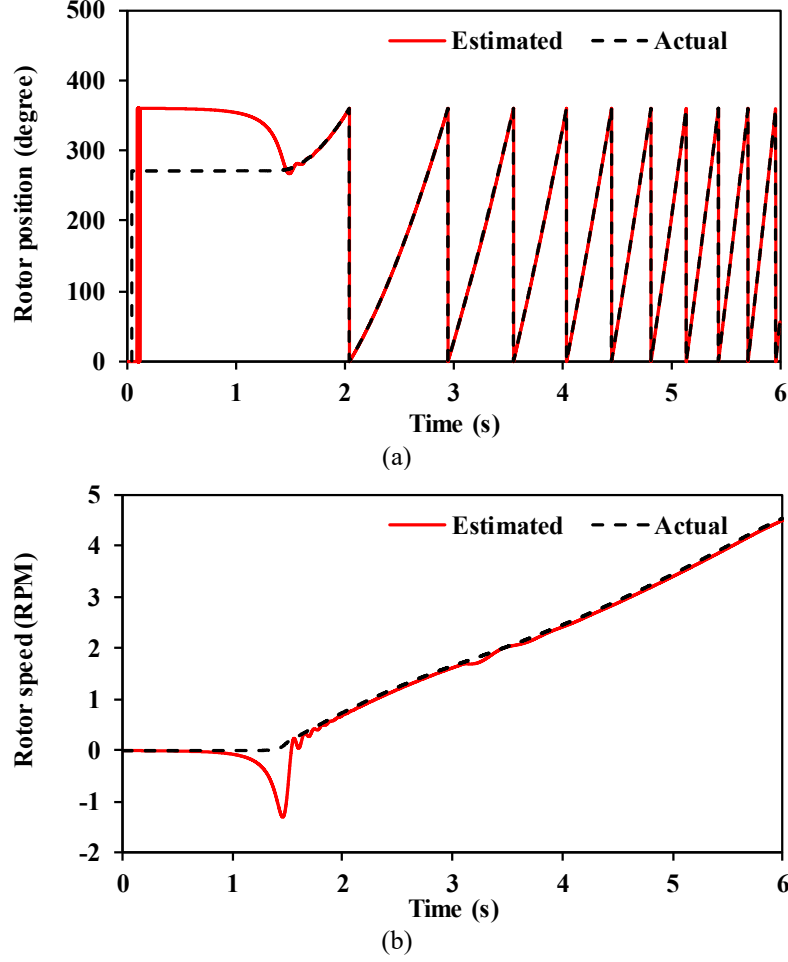


Fig. 6.33. Starting performance with rotor initial position error of 90 degrees. (a) Rotor position. (b) Rotor speed.

However, if the rotor initial position error is larger than 90 degrees, reverse rotation happens during starting. The reverse rotation can be explained in two aspects:

Firstly, as introduced in Section 6.3.1, a conventional quadrature PLL is used to estimate the rotor position. The input error signal  $\varepsilon_{PLL}$  of PLL can be represented as:

$$\varepsilon_{PLL} = K_m \sin \theta_r \cos \hat{\theta}_r - K_m \cos \theta_r \sin \hat{\theta}_r = K_m \sin(\theta_r - \hat{\theta}_r) \approx K_m \Delta\theta_r \quad (6.45)$$

where  $K_m$  is the amplitude of input error signal  $\varepsilon_{PLL}$ . According to [ZHA16], there are two equilibrium points for the PLL, i.e. 0 and 180 degrees. When the initial position error is larger than 90 degrees, the PLL input error signal will be converged to 180 degrees [OLI12].

Secondly, for SPMSMs, the output torque is only produced by q-axis current which is given by:

$$T_e = \frac{3}{2} p \psi_m i_q \quad (6.46)$$

Currents in the estimated synchronous reference frame can be transformed into actual synchronous reference frame as given by:

$$\begin{bmatrix} i_d \\ i_q \end{bmatrix} = \begin{bmatrix} \cos\Delta\theta_r & -\sin\Delta\theta_r \\ \sin\Delta\theta_r & \cos\Delta\theta_r \end{bmatrix} \cdot \begin{bmatrix} \hat{i}_d \\ \hat{i}_q \end{bmatrix} \quad (6.47)$$

Then, the actual q-axis current can be represented as:

$$i_q = \hat{i}_d \sin \Delta\theta_r + \hat{i}_q \cos \Delta\theta_r \quad (6.48)$$

Since  $\hat{i}_d$  is close to zero and can be neglected, (6.48) can be simplified as:

$$i_q \approx \hat{i}_q \cos \Delta\theta_r \quad (6.49)$$

Then, the electromagnetic torque is also simplified as:

$$T_e \approx \frac{3}{2} P \psi_m \hat{i}_q \cos \Delta\theta_r \quad (6.50)$$

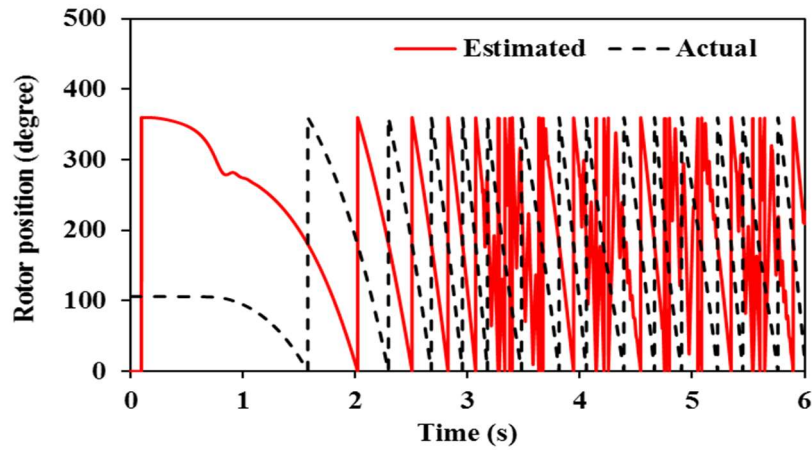
Considering different values of  $\Delta\theta_r$ , the output electromagnetic torque is given by:

$$T_e = \begin{cases} +T & -90^\circ < \Delta\theta_r < 90^\circ \\ 0 & \Delta\theta_r = \pm 90^\circ \\ -T & 90^\circ < \Delta\theta_r < 270^\circ \end{cases} \quad (6.51)$$

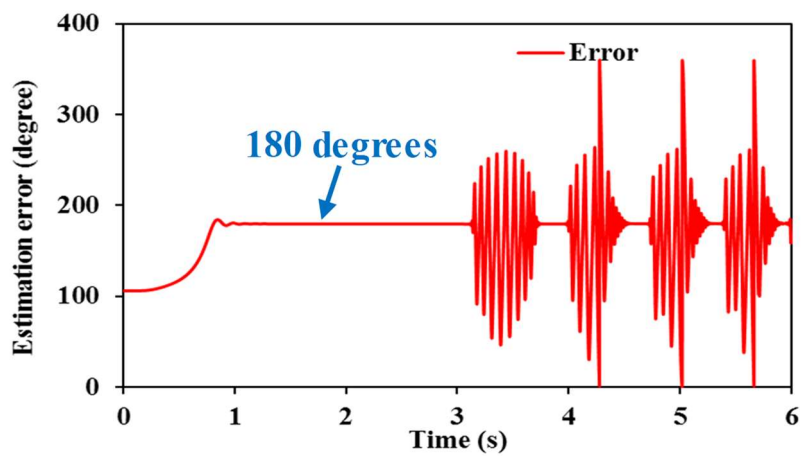
Obviously, a negative torque is produced when the position error is larger than 90 degrees, i.e.  $90^\circ < \Delta\theta_r < 270^\circ$ , which also aligns with [BOL99].

In summary, if the rotor initial position error is larger than 90 degrees, after starting the PLL will converge to its 180 degrees equilibrium point causing a 180 degrees position error. In this case, a negative torque will be produced and the rotor rotates reversely.

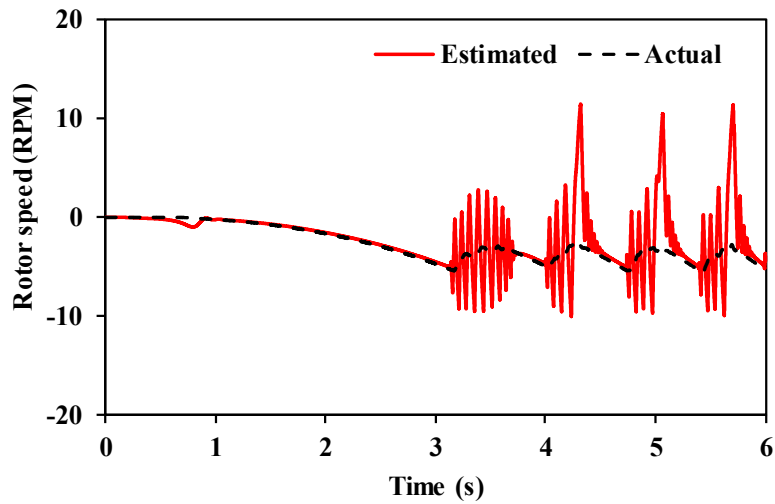
As shown in Fig. 6.34, the turbine starts to rotate reversely when the rotor initial position error is larger than 90 degrees. Both the actual speed and the q-axis current go negative. The position estimation error is 180 degrees during the reverse rotation. In this case, a reverse rotation compensation strategy should be developed to correct the rotation direction during the reversal, as will be shown in the next section.



(a)



(b)



(c)

Fig. 6.34. Starting performance with rotor initial position error larger than 90 degrees. (a) Rotor position. (b) Estimation error. (c) Rotor speed.

## 6.4.2 Reverse Rotation Compensation Strategy

As described in the previous section, by applying the proposed method without the knowledge of rotor initial position, reverse rotation happens when rotor initial position error is large, i.e.  $90^\circ < \Delta\theta_r < 270^\circ$ . Hence, a reverse rotation compensation strategy is developed in this section.

### A. Estimated speed detection

During the reverse rotation, the rotor speed is shown in Fig. 6.35.

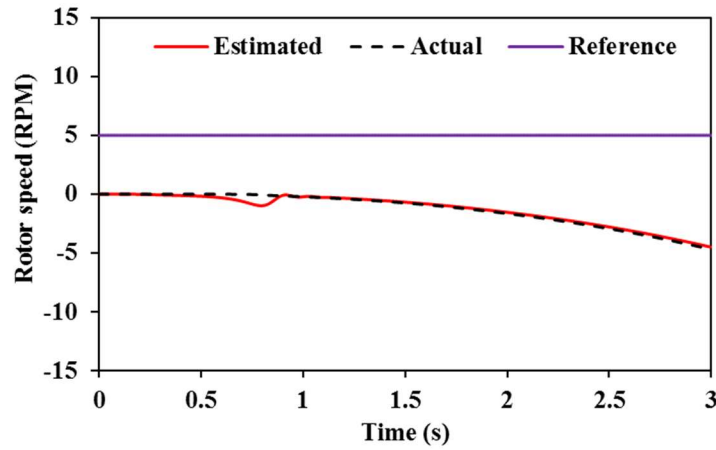


Fig. 6.35. Rotor speed during reverse rotation.

It can be seen that during the reverse rotation, the estimated speed is the same as the actual one. Furthermore, according to Section 6.3, the estimated speed can be obtained by:

$$\hat{\omega}_r = \frac{\hat{\theta}_r(k) - \hat{\theta}_r(k-1)}{\Delta T_s} \quad (6.52)$$

During the reverse rotation, the estimated position has a constant 180 degrees error. Hence, as given by (6.53) the estimated speed is the same as the actual speed.

$$\hat{\omega}_r = \frac{(\hat{\theta}_r(k) + \pi) - (\hat{\theta}_r(k-1) + \pi)}{\Delta T_s} = \frac{\hat{\theta}_r(k) - \hat{\theta}_r(k-1)}{\Delta T_s} \quad (6.53)$$

Based on this, reverse rotation can be detected by observing the sign of the estimated speed.

### B. Observer convergence detection

The estimated speed is used for detection of reverse rotation. However, during starting, there will be a dynamic stage for the observer to converge (Stage 1) as shown in Fig. 6.36. In this

stage, the sign of the estimated speed can be negative even if the rotor rotates correctly afterwards (Stage 2).

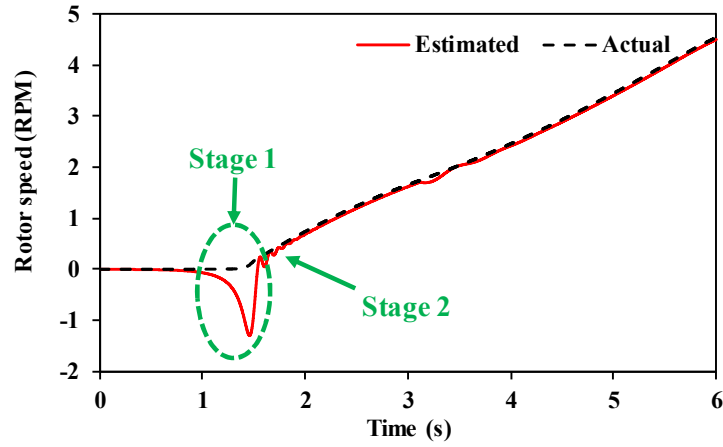


Fig. 6.36. Rotor speed during reverse rotation.

Clearly, only after the convergence period of the observer (Stage 2), the sign of the estimated speed can be used for detecting reverse rotation. Thus, an additional detection of the convergence period is required.

For the proposed method, the Phase-locked Loop (PLL) is used as the observer to estimate the rotor position and speed as shown in Fig. 6.6 and the input error signal of the PLL is  $\varepsilon_{PLL}$ .

During the starting, considering different rotor initial position error, there are 4 different cases in total as given by:

$$\begin{cases} 180^\circ < \Delta\theta_r < 270^\circ & \text{Reversal case 1} \\ 90^\circ < \Delta\theta_r < 180^\circ & \text{Reversal case 2} \\ 0^\circ < \Delta\theta_r < 90^\circ & \text{Correct case 1} \\ 270^\circ < \Delta\theta_r < 360^\circ & \text{Correct case 2} \end{cases} \quad (6.54)$$

The input error signals of PLL under different cases are shown in Fig. 6.37.

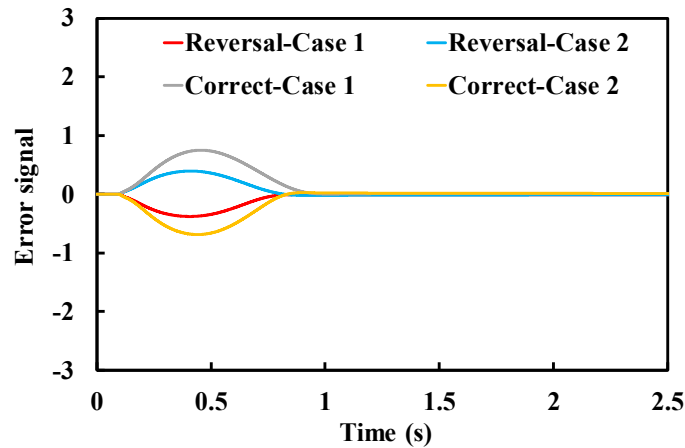


Fig. 6.37. Error signals of Phase-locked Loop under different cases.

Clearly, for both cases, after the convergence period the input error signal  $\varepsilon_{PLL}$  will be minimized. Therefore, the input error signal of PLL  $\varepsilon_{PLL}$  can be used to detect the end of convergence. As given by (6.55), a threshold value is set, if  $\varepsilon_{PLL}$  is smaller than the value then the convergence is regarded as finished.

$$|\varepsilon_{PLL}| < Threshold \quad (6.55)$$

After that, the sign of the estimated speed is then detected to justify the rotation direction. If the estimated speed is negative, an angle of 180 degrees is compensated. The compensation flow chart is shown in Fig. 6.38.

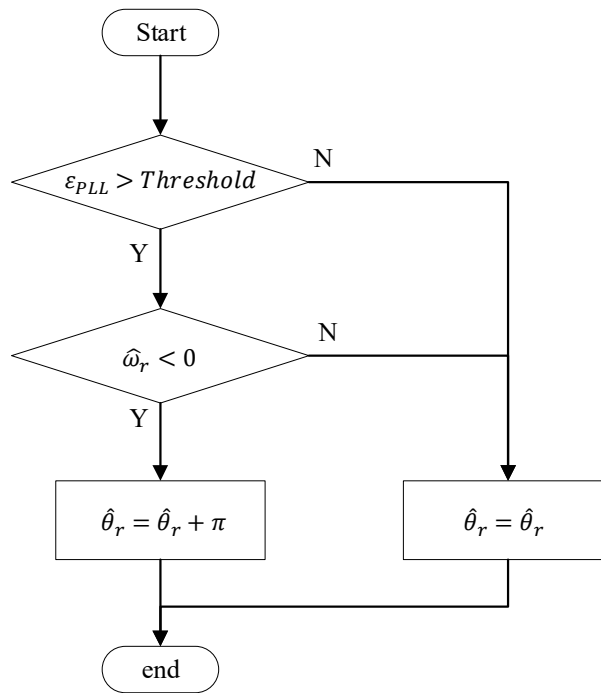


Fig. 6.38. Flow chart of reverse rotation compensation strategy.

### C. Compensation performance

Fig. 6.39 shows the compensation performance of the presented strategy. In the test, the rotor rotates reversely at first with an error of 180 degrees. Then, the estimated position is compensated with 180 degrees and the rotation direction is corrected afterwards.

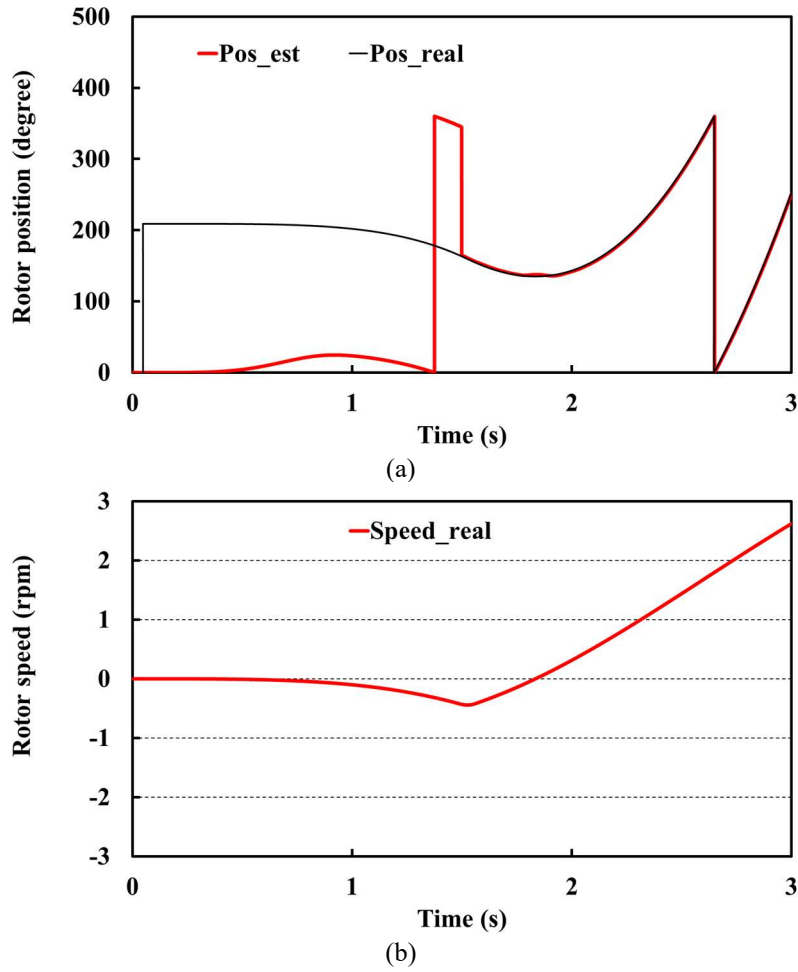


Fig. 6.39. Reverse rotation compensation performance (a) Rotor position. (b) Rotor speed.

#### D. Q-axis current step mitigation

Firstly, the compensation strategy is verified in Fig. 6.40.

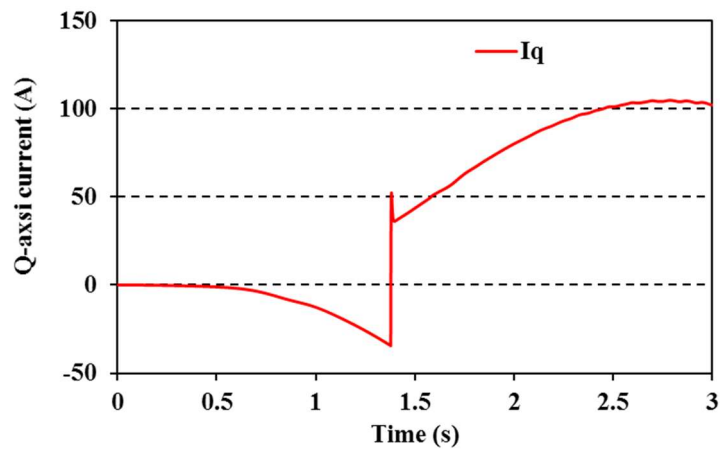


Fig. 6.40. Q-axis current step during reverse rotation compensation.

However, as shown in Fig. 6.40, during the correction of reverse rotation there will be a large q-axis current step which should be limited according to industrial requirements. Hence a q-axis current step mitigation strategy is further developed to avoid the large q-axis current step.

Fig. 6.41 shows the original q-axis current reference change during the reverse rotation compensation. Clearly, the step change of the q-axis current reference will cause a step in the q-axis current. Therefore, the q-axis current reference can be adjusted to avoid the q-axis current step.

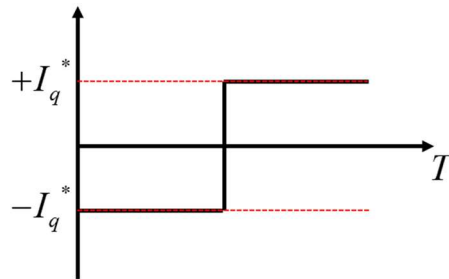


Fig. 6.41. Original q-axis current demand during reverse rotation compensation.

As shown in Fig. 6.42, a ramp demand of the q-axis current is applied instead of step change. Hence, the step of q-axis current can be avoided.

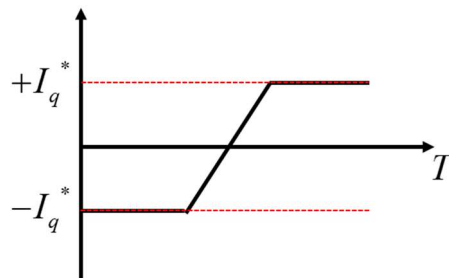


Fig. 6.42. Improved q-axis current demand during reverse rotation compensation.

By using the ramp demand of q-axis current, the q-axis current during the reverse rotation compensation is shown in Fig. 6.43. It can be seen that the q-axis current step change is now replaced by a ramp increase.

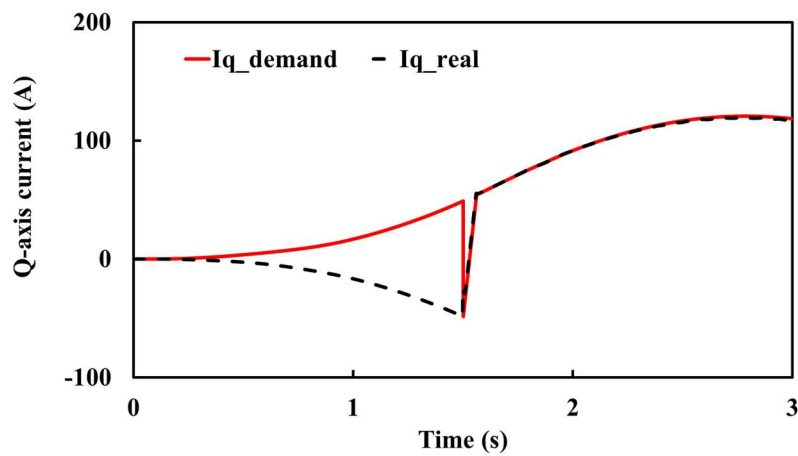


Fig. 6.43. Q-axis current ramp during reverse rotation compensation.

## 6.5 Conclusion

This chapter introduced a simplified fundamental model based sensorless control method for SPMSM in low speed range and considering the starting process. Instead of calculating back-EMF or flux-linkage as conventional methods, this proposed method directly uses stator currents in the stationary reference frame for rotor position estimation, providing a more effective way to estimation the rotor position. A good position estimation performance at low speed is achieved since the current information is directly obtained from the current sensors. Moreover, with the knowledge of the rotor initial position information before starting, the proposed method is able to provide a satisfied starting performance even with the load. The influence of inverter nonlinearity is also discussed and the corresponding compensation shows a satisfied performance when the inverter nonlinearity effect gets larger. The proposed methods are verified through experimental results, showing good position estimation performance under different operations. Furthermore, the proposed method is applied to Siemens wind power system to start the turbine from standstill. With the rotor initial position information, the proposed method shows a satisfied performance as conventional high frequency signal injection method. When rotor initial position information is not available, a reverse rotation compensation strategy is developed to guarantee a reliable starting performance. The proposed method is verified by hardware-in-loop (HIL) simulation of Siemens wind turbine.

# CHAPTER 7

## SENSORLESS CONTROL OF PERMANENT MAGNET SYNCHRONOUS MACHINES CONSIDERING ROTOR ECCENTRICITY

### 7.1 Introduction

Basically, sensorless techniques can be divided into fundamental model based techniques [MOR02][CHE03][BOL08][YOO09a] and saliency tracking based techniques [JAN95][DEG98][BRI04][XU16a]. Fundamental model based methods utilizing back-EMF have a good performance at middle and high speeds. However, the magnitude of back-EMF is proportional to the rotor speed, these methods present poor performance and cannot be employed in zero and low speed regions. In terms of saliency tracking based methods, they are more suitable in zero and low speed ranges.

However, most of the researches are based on a healthy condition of PMSM. On the contrary, in this chapter, sensorless control of PMSM under rotor eccentricity (RE) is considered. Caused by many sources [KRA04][RAJ07][ROU07][EBR09][DOR10] [HON12a] including manufacture tolerance, structure deformation and bearing wear, rotor eccentricity is an unavoidable issue, especially in mass production and real operation. Besides, it is prone to exist in large machines, such as wind turbine PM generators. The influence and principle of rotor eccentricity are exploited by a lot of researches [HON12b] [HSI13] [ZHU13] [LI15] [LIU17] [SON17]. Generally, PMSM characteristics including back-EMF, inductance, torque etc. can be influenced by rotor eccentricity. Hence, under rotor eccentricity, there exhibit parameter variation, unbalance and harmonics. For conventional fundamental model based sensorless control methods under rotor eccentricity, these undesired changes could affect the position estimation performance.

Hence, in this chapter, the effect of rotor eccentricity on PMSM characteristics and its impacts on conventional fundamental model based sensorless control methods are investigated firstly. Combined with the conclusion in [WU19b], under rotor eccentricity, there will be mechanical frequency ripple in torque and power signals, unbalance in three-phase back-EMFs, flux-linkages and inductances and variations in inductance value. Then, impacts of these undesired phenomena on conventional fundamental model based sensorless control methods

are investigated. It is found that there will be mechanical frequency and the 2<sup>nd</sup> order harmonic exist in the position estimation error due to rotor eccentricity. For conventional back-EMF based sensorless control method, the phase-locked loop (PLL) technique is a suitable choice to extract the position from input [WAN14a]. However, since the bandwidth of PLL is generally designed widely in consideration of dynamic performance, it is difficult to effectively eliminate these low order harmonics. Therefore, an adaptive notch filter introduced in [WAN14a] is applied to a conventional back-EMF based sensorless control method [MOR02] [CHE03] to suppress these undesired harmonics.

In this chapter, the rotor eccentricity is firstly explained and the experimental setup of rotor eccentricity is described. Then, the impacts of the rotor eccentricity on PMSM characteristics are summarized and demonstrated. Moreover, the impact of these undesired changes on sensorless control performance are analysed based on the conventional back-EMF based sensorless control method. Then, the adaptive notch filter is introduced and the modified back-EMF based position estimator is demonstrated. Finally, rotor eccentricity effects on PMSM characteristics are examined by measurement results, and the modified back-EMF based sensorless control method is implemented on a dSPACE platform and its effectiveness are verified by experiments.

This chapter is based on the papers:

[WU19b] X. M. Wu, and Z. Q. Zhu, "A simple mechanical rotor position estimation method based on rotor eccentricity," *2019 IEEE International Electric Machines and Drives Conference (IEMDC)*, San diego, CA, 2019.

[WU20f] X. M. Wu, Z. Q. Zhu, and Z. Y. Wu, "Analysis and Suppression of Rotor Eccentricity Effects on Fundamental Model Based Sensorless Control of Permanent Magnet Synchronous Machine," *IEEE Transactions on Industry Applications*, In press.

## 7.2 Rotor Eccentricity

In this section, the rotor eccentricity is firstly defined. Then, the experimental setup of rotor eccentricity is described including the modelling, measurement and tuning of the airgap length.

### 7.2.1 Definition

Rotor eccentricity is caused by many reasons, such as manufacture tolerance, structure deformation and bearing wear which are unavoidable, especially in mass production and real operation. The principle and impact of rotor eccentricity are already exploited by a lot of researches. Basically, there are two types of eccentricity, static eccentricity (SE) and dynamic eccentricity (DE), which are illustrated in Fig. 7.1. For a healthy motor, the geometric and rotating centers of the rotor are aligned with the stator bores as illustrated in Fig. 7.1(a). For SE, the rotor rotates around its own geometry center,  $O_r$ , which is shifted in parallel to that of the stator, i.e.  $O_s$ , as illustrated in Fig. 7.1(b). For DE shown in Fig. 7.1(c), the geometry center of the rotor is also shifted but the rotor rotates around the geometry center of the stator,  $O_s$ . Commonly, in real applications, these two types of eccentricities both exist at the same time, and both have impacts on machine characteristics leading to deteriorated sensorless control performance.

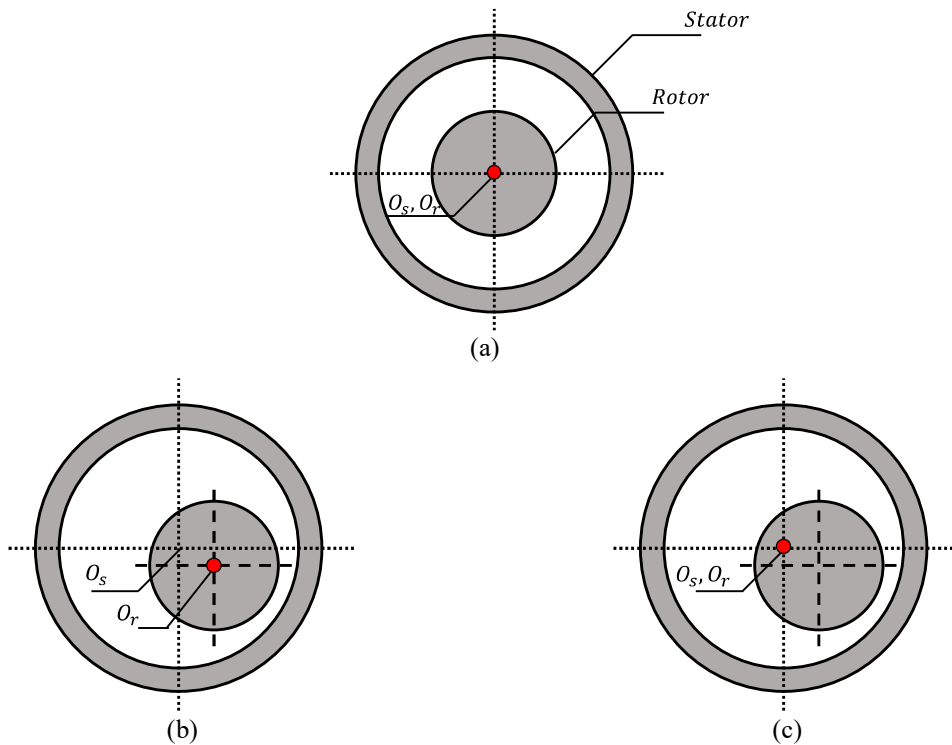


Fig. 7.1. Illustration of rotor eccentricity. (a) Concentric. (b) Static eccentric. (c) Dynamic eccentric.

[WU20f]

### 7.2.2 Experimental Setup

The experimental setup of rotor eccentricity is then demonstrated in this part. A designated test platform with adjustable rotor eccentricity is shown in Appendix A. The rotor SE level can be adjusted and then fixed. However, during the operation, the prototype machine may also exhibit DE and hence a mixed eccentricity. Therefore, a rotor air-gap model under rotor eccentricity is defined firstly to quantify the level of SE and DE, independently.

Based on [SON17], the air gap mathematic model is given by:

$$g(\theta_x, \theta_M) = g_0 + g_{DE} \cos(\theta_x - \theta_M + \varphi_{DE}) + g_{SE} \cos(\theta_x + \varphi_{SE}) \quad (7.1)$$

$$\varepsilon_{DE} = \frac{g_{DE}}{g_0} \times 100\%, \varepsilon_{SE} = \frac{g_{SE}}{g_0} \times 100\% \quad (7.2)$$

where  $g$  is the air gap with mixed rotor eccentricity,  $g_0$  is the length of the air gap,  $g_{DE}$  is the magnitude of dynamic eccentricity,  $g_{SE}$  is the magnitude of static eccentricity,  $\theta_x$  is the geometric angle from x-axis,  $\theta_M$  is the rotating angle of the motor,  $\varphi_{DE}$  is the phase shift of dynamic rotor eccentricity and  $\varphi_{SE}$  is the phase shift of static rotor eccentricity,  $\varepsilon_{SE}$  and  $\varepsilon_{DE}$  are the relative magnitudes of static and dynamic eccentricities with respect to the length of air gap.

By measuring air-gap length at multiple positions against  $\theta_x$  and  $\theta_m$ , all the coefficients in (7.1) and (7.2) can be derived including the level of SE and DE. The coefficients are shown in TABLE 7.1.

TABLE 7.1  
AIRGAP MODEL COEFFICIENTS

Parameter	Value
$g_0$	1.557mm
$g_{DE}$	0.1564mm
$\varepsilon_{DE}$	10%
$g_{SE}$	0.4486mm
$\varepsilon_{SE}$	28.81%
$\varphi_{DE}$	13.16°
$\varphi_{SE}$	177.6°

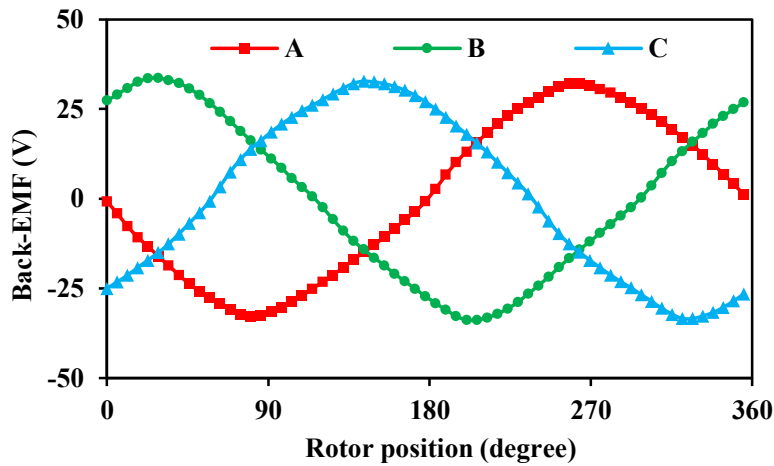
After measurement, the relative magnitude of dynamic eccentricity  $\varepsilon_{DE}$  is 10%. The relative magnitude of static eccentricity  $\varepsilon_{SE}$  is tuned from 0% to 45% in the test afterwards.

## 7.3 Rotor Eccentricity Effects on PMSMs

In this section, the influence of rotor eccentricity on PMSM characteristics are generally discussed including three-phase back-EMF, flux-linkages, inductance and torque ripple. Besides, the mathematic model of PMSM under rotor eccentricity is derived. These impacts of rotor eccentricity on PMSM characteristics are demonstrated by examples of measurement results. More detailed measurement results are given in the experimental section.

### 7.3.1 Back-EMF and Flux-linkages

Referring to [ZHU13] and [LI15], due to existence of rotor eccentricity including both static and dynamic ones, there will be unbalance in the three-phase back-EMF. Moreover, the unbalance level mainly depends on the machine configurations. Machines with rotating asymmetric winding has larger unbalance level than that of rotating symmetrical one [ZHU13], [LI15]. The rotating symmetry means that the machine configuration repeats every certain amount of angle. Fig. 7.2(a) shows one example of the measured three phase back-EMF waveforms of the prototype machine which is rotating symmetrical under a mixed rotor eccentricity (20% SE, 10% DE). Fig. 7.2(b) shows its harmonic spectrum which proves that there is unbalance in the three phase back-EMF waveforms under rotor eccentricity.



(a)

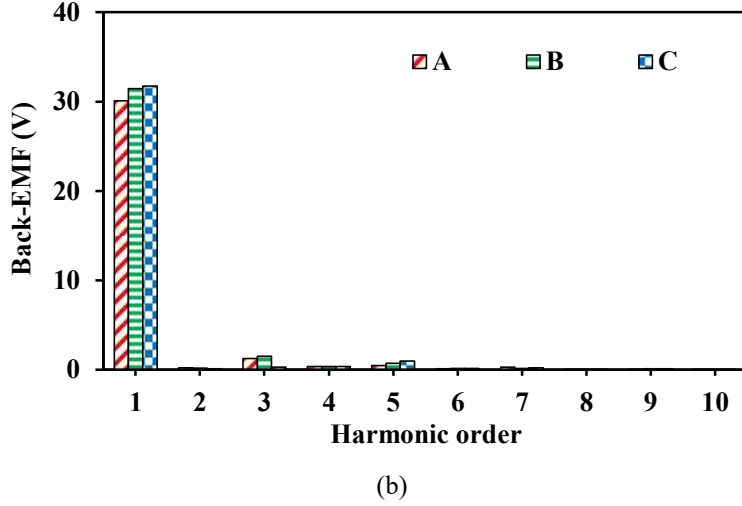


Fig. 7.2. Three-phase back-EMFs with rotor eccentricity (20% SE, 10% DE). (a) Waveforms. (b) Spectra. [WU20f]

The example in Fig. 7.2 demonstrates the existence of unbalance in the three-phase back-EMF waveforms under rotor eccentricity. For unbalance case, the amplitudes of three-phase back-EMFs can be different. Then, the three-phase back-EMFs in ABC reference frame are given by:

$$\begin{aligned}
 E_a &= -\omega_r(\psi_m + \Delta\psi_A) \sin \theta_r \\
 E_b &= -\omega_r(\psi_m + \Delta\psi_B) \sin(\theta_r - \frac{2\pi}{3}) \\
 E_c &= -\omega_r(\psi_m + \Delta\psi_C) \sin(\theta_r + \frac{2\pi}{3})
 \end{aligned} \tag{7.3}$$

where  $\Delta\psi_A$ ,  $\Delta\psi_B$  and  $\Delta\psi_C$  represent the undesired unbalance flux-linkage terms caused by rotor eccentricity,  $\omega_r$  is the rotor speed,  $\theta_r$  is the rotor position,  $\psi_m$  is the PM flux-linkage. Then, the unbalanced back-EMFs in the actual synchronous reference frame can be derived as:

$$\begin{aligned}
 \begin{bmatrix} E_d^u \\ E_q^u \end{bmatrix} &= \begin{bmatrix} E_d \\ E_q \end{bmatrix} + \underbrace{\frac{\omega_r}{3} \begin{bmatrix} 0 \\ \Delta\psi_A + \Delta\psi_B + \Delta\psi_C \end{bmatrix}}_{DC} \\
 &\quad - \underbrace{\frac{\omega_r}{3} \begin{bmatrix} \Delta\psi_A \sin(2\theta_r) - \Delta\psi_B \sin(2\theta_r - \frac{\pi}{3}) - \Delta\psi_C \sin(2\theta_r + \frac{\pi}{3}) \\ \Delta\psi_A \cos(2\theta_r) - \Delta\psi_B \cos(2\theta_r - \frac{\pi}{3}) - \Delta\psi_C \cos(2\theta_r + \frac{\pi}{3}) \end{bmatrix}}_{2nd Harmonic}
 \end{aligned} \tag{7.4}$$

$$\begin{bmatrix} E_d \\ E_q \end{bmatrix} = \omega_r \psi_m \begin{bmatrix} 0 \\ 1 \end{bmatrix} \tag{7.5}$$

where  $E_d^u$  and  $E_q^u$  are unbalanced back-EMFs in the synchronous reference frame,  $E_d$  and  $E_q$  are the original components of back-EMFs in the synchronous reference frame. Besides, in sensorless control system, the real rotor position is unknown, (7.4) should be transformed into the estimated synchronous reference frame by using the matrix below:

$$T(\Delta\theta_r) = \begin{bmatrix} \cos\Delta\theta_r & \sin\Delta\theta_r \\ -\sin\Delta\theta_r & \cos\Delta\theta_r \end{bmatrix} \quad (7.6)$$

where  $\Delta\theta_r$  is the position error. After transformation, (7.4) is modified to (7.7).

$$\begin{aligned} & \begin{bmatrix} \hat{E}_d^u \\ \hat{E}_q^u \end{bmatrix} \\ &= \begin{bmatrix} \hat{E}_d \\ \hat{E}_q \end{bmatrix} + \frac{\omega_r}{3} \underbrace{\left[ (\Delta\psi_A + \Delta\psi_B + \Delta\psi_C) \begin{bmatrix} -\sin\Delta\theta_r \\ \cos\Delta\theta_r \end{bmatrix} \right]}_{DC} \\ & \quad - \frac{\omega_r}{3} \underbrace{\begin{bmatrix} -\Delta\psi_A \sin(\Delta\theta_r - 2\theta_r) + \Delta\psi_B \sin\left(\Delta\theta_r - 2\theta_r + \frac{\pi}{3}\right) + \Delta\psi_C \sin\left(\Delta\theta_r - 2\theta_r - \frac{\pi}{3}\right) \\ \Delta\psi_A \cos(\Delta\theta_r - 2\theta_r) - \Delta\psi_B \cos\left(\Delta\theta_r - 2\theta_r + \frac{\pi}{3}\right) - \Delta\psi_C \cos\left(\Delta\theta_r - 2\theta_r - \frac{\pi}{3}\right) \end{bmatrix}}_{2nd \text{ Harmonic}} \end{aligned} \quad (7.7)$$

$$\begin{bmatrix} \hat{E}_d \\ \hat{E}_q \end{bmatrix} = \omega_r \psi_m \begin{bmatrix} -\sin\Delta\theta_r \\ \cos\Delta\theta_r \end{bmatrix} \quad (7.8)$$

where  $\hat{E}_d^u$  and  $\hat{E}_q^u$  are the unbalanced back-EMFs in the estimated synchronous reference frame.  $\hat{E}_d$  and  $\hat{E}_q$  are the original components of back-EMFs in the estimated synchronous reference frame. It can be seen from (7.4) and (7.7) that there are extra DC and the 2<sup>nd</sup> order harmonic components in the estimated back-EMFs.

Furthermore, according to [ZHU13], the ideal relationship between additional flux-linkages  $\Delta\psi_A$ ,  $\Delta\psi_B$  and  $\Delta\psi_C$  caused by eccentricity can be derived as:

$$\begin{bmatrix} \Delta\psi_B \\ \Delta\psi_C \end{bmatrix} = \Delta\psi_A \cdot \begin{bmatrix} \frac{\cos(\theta_x - 120^\circ)}{\cos\theta_x} \\ \frac{\cos(\theta_x + 120^\circ)}{\cos\theta_x} \end{bmatrix} \quad (7.9)$$

From (7.9), it is also known that:

$$\Delta\psi_A + \Delta\psi_B + \Delta\psi_C = 0 \quad (7.10)$$

Then, by substituting (7.9) into (7.7), the back-EMFs under rotor eccentricity are now given by:

$$\begin{bmatrix} \hat{E}_d^u \\ \hat{E}_q^u \end{bmatrix} = \begin{bmatrix} \hat{E}_d \\ \hat{E}_q \end{bmatrix} - \frac{\omega_r \Delta\psi_A}{2\cos\theta_x} \underbrace{\begin{bmatrix} -\sin(\Delta\theta_r - 2\theta_r - \theta_x) \\ \cos(\Delta\theta_r - 2\theta_r - \theta_x) \end{bmatrix}}_{2nd \text{ Harmonic}} \quad (7.11)$$

Apparently, according to (7.11), the additional DC component in back-EMF can be neglected under rotor eccentricity. Therefore, it is mainly the 2<sup>nd</sup> order harmonic that exists in the back-EMF due to rotor eccentricity.

Clearly, for flux-linkages, they are the same as the back-EMFs. The unbalanced flux-linkages in the estimated reference frame are given by:

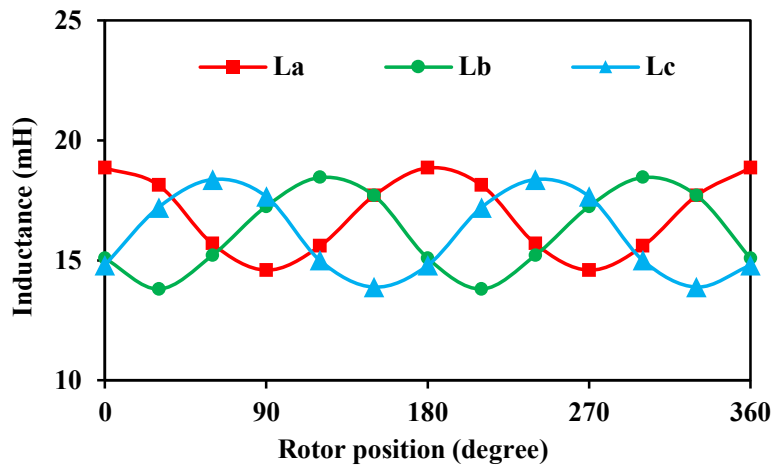
$$\begin{bmatrix} \hat{\psi}_{md}^u \\ \hat{\psi}_{mq}^u \end{bmatrix} = \underbrace{\begin{bmatrix} \hat{\psi}_{md} \\ \hat{\psi}_{mq} \end{bmatrix}}_{\text{original}} + \frac{\Delta\psi_A}{2\cos\theta_x} \underbrace{\begin{bmatrix} \Delta\psi_A \cos(\Delta\theta_r - 2\theta_r - \theta_x) \\ \Delta\psi_A \sin(\Delta\theta_r - 2\theta_r - \theta_x) \end{bmatrix}}_{\text{2nd Harmonic}} \quad (7.12)$$

$$\begin{bmatrix} \hat{\psi}_{md} \\ \hat{\psi}_{mq} \end{bmatrix} = \psi_m \begin{bmatrix} \cos\Delta\theta_r \\ \sin\Delta\theta_r \end{bmatrix} \quad (7.13)$$

where  $\hat{\psi}_{md}^u$  and  $\hat{\psi}_{mq}^u$  are the unbalanced PM flux-linkages in the estimated synchronous reference,  $\hat{\psi}_{md}$  and  $\hat{\psi}_{mq}$  are the original PM flux-linkages in the estimated synchronous reference. Similar to unbalanced back-EMFs, it is mainly the 2<sup>nd</sup> order harmonic component appear in the estimated PM flux-linkages.

### 7.3.2 Inductance

Under rotor eccentricity, unbalance also exists in three-phase inductances [DEG98], [XU16]. By way of example, Fig. 7.3(a) shows the measurement results of three-phase self-inductance under rotor eccentricity. The three-phase self-inductances are measured by an LCR meter at different electrical rotor positions. Clearly, there is an unbalance component in phase A which has a dc-offset compared with other two phases. It is also confirmed by harmonic spectra in Fig. 7.3(b). It is clear that the average values of three-phase inductances are different.



(a)

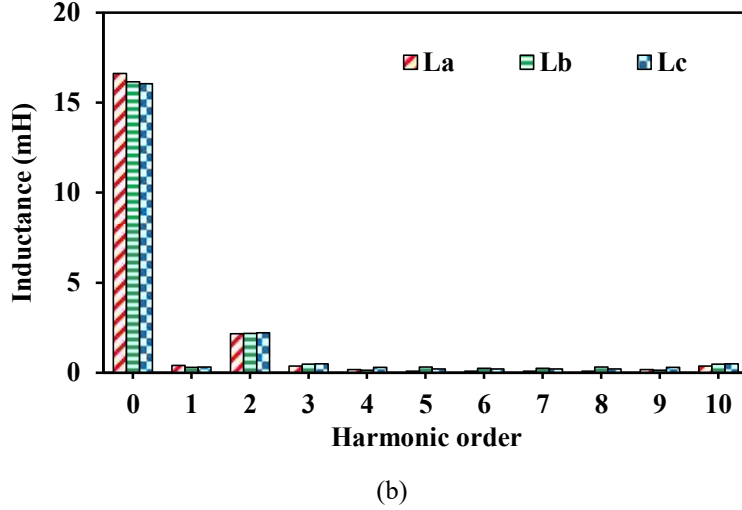


Fig. 7.3. Three-phase self-inductances under rotor eccentricity. (a) Waveforms. (b) Harmonic spectra. [WU20f]

Similar to back-EMFs, the unbalanced inductances in synchronous reference frame can be simply modelled as:

$$\begin{bmatrix} L_d^u \\ L_q^u \end{bmatrix} = \underbrace{\begin{bmatrix} L_d \\ L_q \end{bmatrix}}_{\text{Original}} + \underbrace{\begin{bmatrix} \Delta L_{d\_DC} \\ \Delta L_{q\_DC} \end{bmatrix}}_{DC} + \Delta L_{2h} \underbrace{\begin{bmatrix} \cos 2\theta_r \\ -\cos 2\theta_r \end{bmatrix}}_{\text{2nd Harmonic}} \quad (7.14)$$

where  $L_d^u$  and  $L_q^u$  are the unbalanced d-q inductances in the estimated synchronous reference,  $L_d$  and  $L_q$  are the original d-q inductances.  $\Delta L_{d\_DC}$  and  $\Delta L_{q\_DC}$  are the DC offsets caused by unbalance.  $\Delta L_{2h}$  is the amplitude of the 2<sup>nd</sup> order harmonic due to unbalanced inductance. It is worth mentioning that similar to back-EMFs, any change in one phase will often shift the other two phases in reverse direction. Therefore, the DC offset in (7.14) can be neglected and the unbalanced inductances are now given by:

$$\begin{bmatrix} L_d^u \\ L_q^u \end{bmatrix} \approx \underbrace{\begin{bmatrix} L_d \\ L_q \end{bmatrix}}_{\text{Original}} + \Delta L_{2h} \underbrace{\begin{bmatrix} \cos 2\theta_r \\ -\cos 2\theta_r \end{bmatrix}}_{\text{2nd Harmonic}} \quad (7.15)$$

Furthermore, under rotor eccentricity the value of inductance also varies [HON12a] [HON12b] [LIU17] due to magnetic saturation. According to [HON12a], the d-axis inductance will decrease as level of rotor eccentricity becomes higher while for q-axis inductance, its change under rotor eccentricity will be much less than d-axis inductance. Experimental measurement will be given in Section 7.5 to verify this phenomenon. In summary, the d-q axis inductances under rotor eccentricity are given by:

$$\begin{bmatrix} L_d^{RE} \\ L_q^{RE} \end{bmatrix} \approx \underbrace{\begin{bmatrix} L_d \\ L_q \end{bmatrix}}_{\text{Original}} + \underbrace{\begin{bmatrix} \Delta L_{d\_DC} \\ 0 \end{bmatrix}}_{DC} + \Delta L_{2h} \underbrace{\begin{bmatrix} \cos 2\theta_r \\ -\sin 2\theta_r \end{bmatrix}}_{2nd \text{ Harmonic}} \quad (7.16)$$

where  $L_d^{RE}$  and  $L_q^{RE}$  are the d-q inductances under rotor eccentricity. Clearly, under rotor eccentricity, there will be DC offset and 2<sup>nd</sup> order harmonic differences between the nominal value and the actual value of the inductance.

### 7.3.3 Mechanical Frequency Torque Ripple

According to [RAJ07] and [WU19b], due to the existence of dynamic eccentricity, there is a mechanical frequency component ripple in the output electromagnetic torque, which is shown in Fig. 7.4. As shown in Appendix A, the output torque is measured by a torque transducer mounted on the shaft.

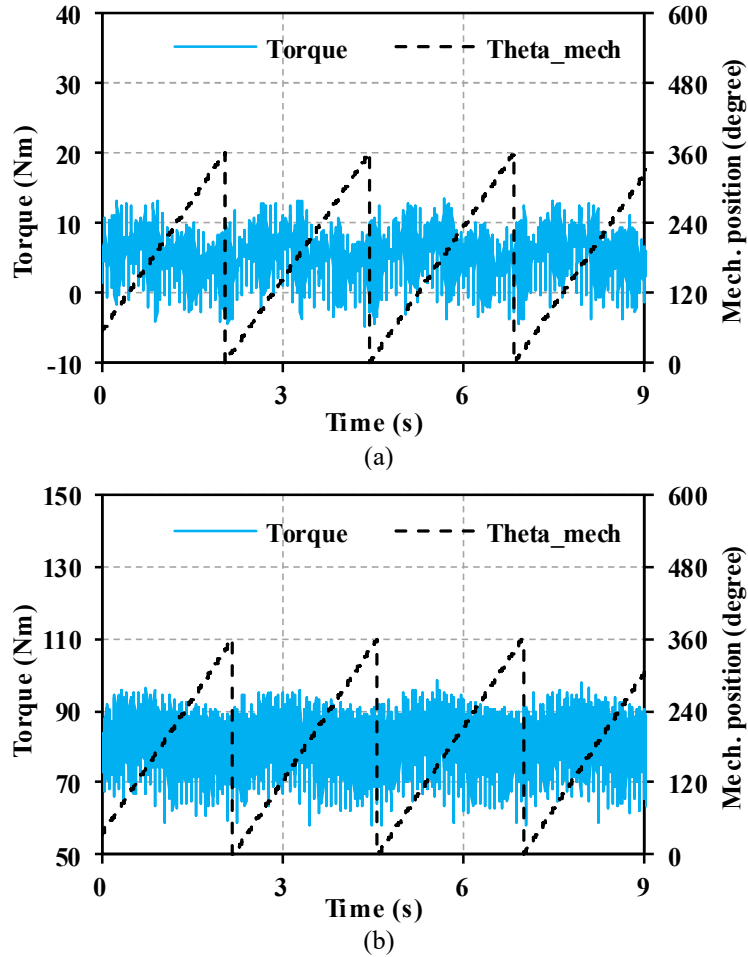


Fig. 7.4. Output torque against rotor mechanical position. (a) No load. (b) Full load. [WU19b]

In Fig. 7.4, with a 10% DE, the measured torque curves against mechanical rotor position under no load and full load are provided. Furthermore, harmonic spectra of torque in Fig. 7.5

show the existence of torque component at rotor mechanical frequency  $f_m$ . Moreover, it can be seen from Fig. 7.4 and Fig. 7.5 that the load influence on mechanical frequency order component of torque can be ignored.

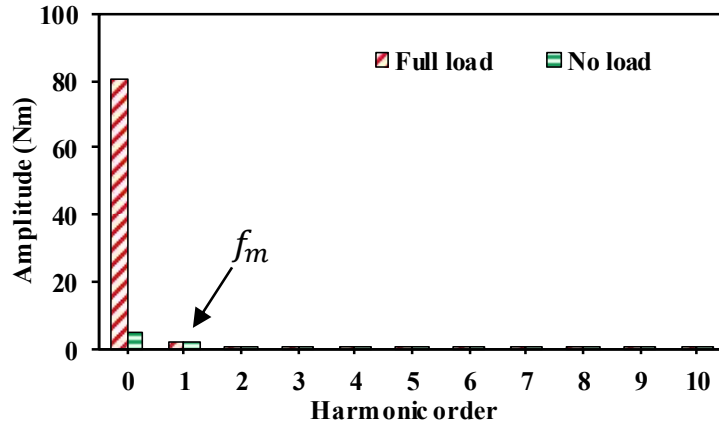


Fig. 7.5. Spectra of no load and full load output torques. [WU19b]

Besides, the torque ripple will also be reflected in the instantaneous power signal. The instantaneous real power  $P_1$  can be calculated from stator voltages and currents by:

$$P_1 = \frac{3}{2}(v_\alpha i_\alpha + v_\beta i_\beta) \quad (7.17)$$

Then,  $P_1$  can be approximately represented as:

$$P_1 = P_0 + P_m \quad (7.18)$$

where  $P_m$  is the mechanical frequency order component and the left components are represented as  $P_0$ .  $P_m$  is the required component that needs to be extracted from  $P_1$ . The original real power signal against rotor mechanical position is shown in Fig. 7.6. The harmonic spectra in Fig. 7.7 indicate the existence of mechanical frequency order component in the power signal.

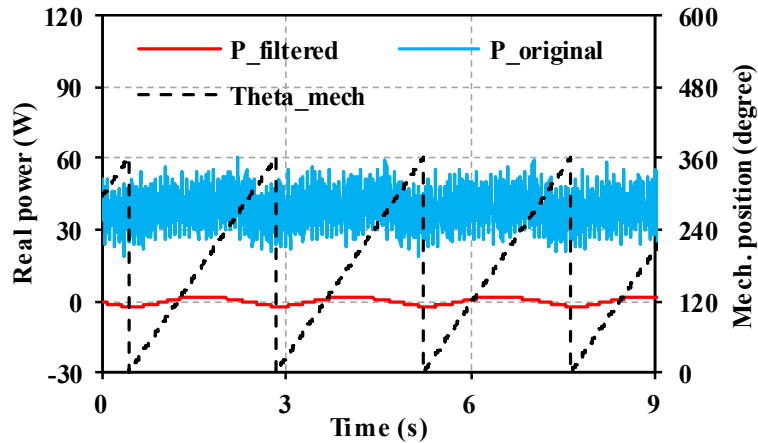


Fig. 7.6. Real power signal against rotor mechanical position. [WU19b]

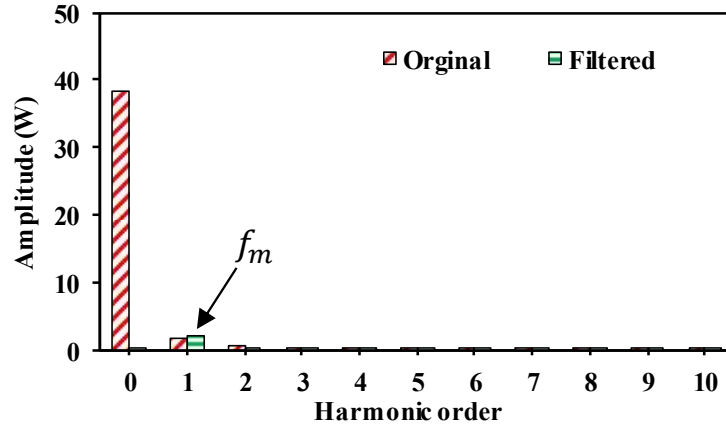


Fig. 7.7. Spectra of original and filtered real power signals. [WU19b]

In order to simplify the analysis, this mechanical frequency ripple in power signal is assumed to be an equivalent harmonic in the back-EMF as given by:

$$P_m = \Delta e_m I_s \quad (7.19)$$

$$P_m = I_s E_m \cos(\theta_m + \varphi_m) \quad (7.20)$$

where  $\Delta e_m$  is the equivalent mechanical frequency order harmonic component in the back-EMF,  $E_m$  is the amplitude,  $\theta_m$  is the mechanical angular position and  $\varphi_m$  is the phase angle. Therefore, this mechanical frequency ripple is regarded as the back-EMF harmonics in this chapter. Moreover, although this chapter focuses on the rotor eccentricity effects, it is still worth mentioning that apart from DE, mechanical load imbalance may also cause the mechanical frequency ripple in the torque and power signal [RAJ07]. Besides, according to [RAJ07], mechanical load imbalance may also cause additional eccentricity effects.

### 7.3.4 Summary

In conclusion, under rotor eccentricity, unbalance appears in three phase back-EMFs, flux-linkages and inductances. Besides, value of inductance changes as well. Besides, mechanical frequency torque ripple exists. These undesired phenomena together will produce position estimation errors for fundamental model based sensorless control methods. Therefore, in the next section position estimation error associated with rotor eccentricity and corresponding suppression strategy are shown.

## 7.4 Rotor Eccentricity Effects on Fundamental Model Based Sensorless Control

Considering conventional fundamental model based sensorless control methods, normally flux-linkage [BOL08], [YOO09a] and back-EMF are used for position estimation. Thus, in this chapter, the analysis is based on the typical back-EMF based method [MOR02], [CHE03]. According to [MOR02], [CHE03], machine parameters are required by fundamental model based sensorless control methods for rotor position estimation. Apparently, any parameter mismatch will affect the sensorless control performance. Besides, any distortion in back-EMF and flux-linkage will also affect the performance. Hence, based on the analysis of rotor eccentricity effects on PMSM characteristics, the impacts on fundamental sensorless control methods is derived in this section.

### 7.4.1 Conventional Back-EMF Sensorless Control

[MOR02] and [CHE03] introduced the extended Back-EMF based method, i.e.  $E_{ex}$ , by which the voltage equation is given by:

$$\begin{bmatrix} v_d \\ v_q \end{bmatrix} = \begin{bmatrix} R_s + pL_d & -\omega_r L_q \\ \omega_r L_q & R_s + pL_d \end{bmatrix} \begin{bmatrix} i_d \\ i_q \end{bmatrix} + \begin{bmatrix} 0 \\ E_{ex} \end{bmatrix} \quad (7.21)$$

where  $v_d$  and  $v_q$  are the d-q axis stator voltages,  $i_d$  and  $i_q$  are the d-q axis stator currents,  $L_d$  and  $L_q$  are the d-q axis inductances, respectively.  $E_{ex} = \omega_r \psi_m + (L_d - L_q)(\omega_r i_d - p i_q)$ .

For a sensorless control system, the actual rotor position is unknown. Therefore, the above equations should be transformed into the estimated synchronous reference frame:

$$\begin{bmatrix} \hat{v}_d \\ \hat{v}_q \end{bmatrix} = \begin{bmatrix} R_s + pL_d & -\omega_r L_q \\ \omega_r L_q & R_s + pL_d \end{bmatrix} \begin{bmatrix} \hat{i}_d \\ \hat{i}_q \end{bmatrix} + \begin{bmatrix} \hat{E}_d \\ \hat{E}_q \end{bmatrix} \quad (7.22)$$

$$\begin{bmatrix} \hat{E}_d \\ \hat{E}_q \end{bmatrix} \approx E_{ex} \begin{bmatrix} -\sin\Delta\theta_r \\ \cos\Delta\theta_r \end{bmatrix} \quad (7.23)$$

where the superscript sign ‘ $\wedge$ ’ indicates the variables in the estimated synchronous reference frame. Then, the estimated position error can be expressed in the following equations:

$$\Delta\hat{\theta}_r = \tan^{-1}\left(-\frac{\hat{E}_d}{\hat{E}_q}\right) \quad (7.24)$$

Subsequently, as shown in Fig. 7.8, a position observer, such as the phase-locked loop (PLL), is normally applied to adjust the estimated position to minimize the estimated position error  $\Delta\hat{\theta}_r$  to make the estimated reference frame align with the actual one.

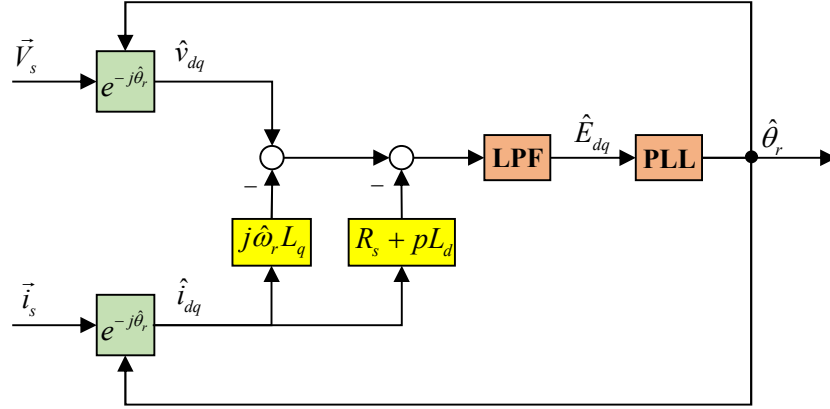


Fig. 7.8. Real power signal against rotor mechanical position [MOR02], [CHE03].

#### 7.4.2 Rotor Eccentricity Effects on Position Estimation

Clearly, any parameter mismatch or harmonics in back-EMF will cause errors in (7.24). Based on the analysis in Section 7.3, under rotor eccentricity there will be errors in the estimated position error as given by:

$$\Delta\hat{\theta}_r = \tan^{-1}\left(-\frac{\hat{E}_d + \Delta E_d}{\hat{E}_q + \Delta E_q}\right) \quad (7.25)$$

where  $\Delta\hat{\theta}_r$  is the estimated position error,  $\Delta E_d$  and  $\Delta E_q$  are errors in the estimated back-EMFs.

According to [LEE15], regardless of the algorithms, the main goal of them is to nullify the estimated position error  $\Delta\hat{\theta}_r$  in (7.25). Since (7.25) is an arctangent function, nullifying  $\Delta\hat{\theta}_r$  is equal to ' $\hat{E}_d + \Delta E_d = 0$ '. Based on this conclusion, the steady-state position estimation error  $\Delta\theta_r$  caused by rotor eccentricity can be derived as:

$$\Delta\theta_r = \sin^{-1}\left(\frac{-\hat{\omega}_r \Delta L_{q2h} \hat{i}_q + \Delta e_{d2} + \Delta e_m}{E_{ex}}\right) \quad (7.26)$$

Clearly, it is revealed that rotor eccentricity will cause mainly harmonics in the position estimation. Although d-axis inductance will change under rotor eccentricity, it will not affect the sensorless control position estimation in the steady-state.

Furthermore, as mentioned earlier, a position observer such as the PLL is used to extract the rotor position. PLL is a practical and simple phase and frequency estimation method due to its insensitivity to noise and distortion [WAN14a]. However, in order to fulfil the dynamic performance, the bandwidth of PLL is tuned relatively wide. Hence, the low-order harmonics in (7.26) may be difficult to be eliminated effectively.

Therefore, in the next section, according to (7.26), an adaptive notch filter (ANF) is applied to the typical back-EMF estimator to suppress these harmonic errors in the position estimation.

### 7.4.3 Suppression of Rotor Eccentricity Effects on Rotor Position

#### Estimation

In this section, an adaptive notch filter introduced in [WAN14a] is used to suppress the undesired harmonics due to rotor eccentricity. The adaptive notch filter is an attractive choice to detect harmonics in power quality mitigation. This adaptive notch filter can be used to eliminate the specified harmonics by self-tuning of filter parameters. The overall control diagram of ANF is given in Fig. 7.9. As described in Fig. 7.9, both the 2nd and mechanical frequency order harmonics are eliminated. In Fig. 7.9, P is the number of pole pairs.

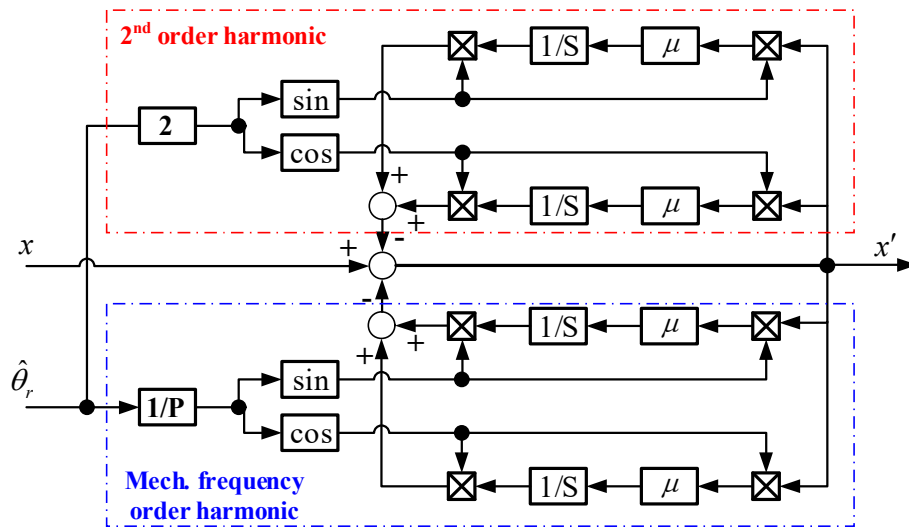


Fig. 7.9. Block diagram of ANF in the position observer. [WU20f]

The transfer function of this ANF is given by:

$$G(s) = \frac{s^2 + \omega_h^2}{s^2 + \mu s + \omega_h^2} \quad (7.27)$$

where  $\omega_h$  is the center frequency of the system, which specifies the order of harmonic to be suppressed. The bandwidth of ANF is  $\mu$ , which is the only parameter to be tuned. This

parameter should be selected carefully, since as  $\mu$  becomes larger, the dynamic response is faster but the steady-state error becomes larger too. The frequency response of ANF is shown in Fig. 7.10.

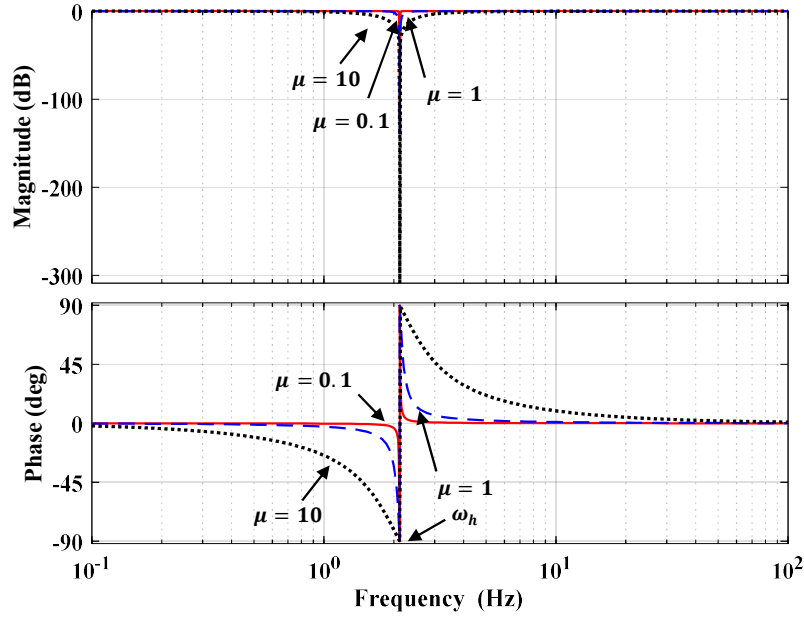


Fig. 7.10. Frequency response of the ANF with different bandwidths [WU20f].

Then, the conventional back-EMF estimation method introduced in Section 7.4.1 is modified by adding an ANF in the position estimation. The overall block diagram of the modified back-EMF estimator is shown in Fig. 7.11.

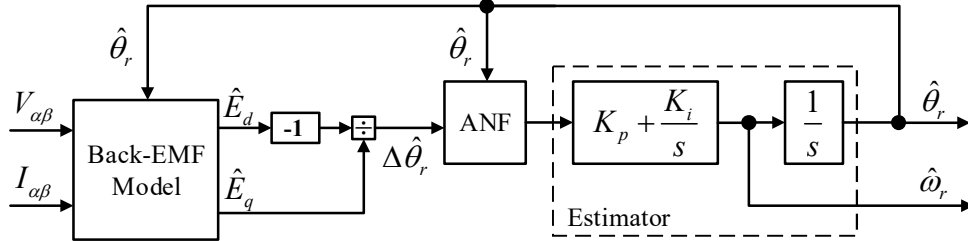


Fig. 7.11. . Block diagram of ANF based position estimator [WU20f].

## 7.5 Experimental Validation

In this experiment section based on SPM-I, the PMSM characteristic changes due to rotor eccentricity are measured and shown at first. As a result of rotor eccentricity, position errors of the conventional back-EMF method are shown. Next, the ANF based back-EMF estimator is examined by eliminating the undesired harmonics in the position error.

### 7.5.1 Machine Parameter Variation under Rotor Eccentricity

Before testing the proposed hybrid sensorless control method, it is worthy to investigate the PMSM characteristic variations under different rotor eccentricity levels. In this part, the static rotor eccentricity level is tuned from 0% to 45%. During the tuning, the eccentricity angle is fixed at 0 degree, i.e.  $\theta_x = 0$ , which aligns with phase A. In this part, considering different levels of SE, the inductance value variation is firstly measured by an LCR meter and then the unbalance level of three-phase inductances and back-EMFs are measured and shown too.

Firstly, the average values and the 2<sup>nd</sup> order harmonic of three-phase self-inductances against SE level are measured and demonstrated in Figs. 12 and 13, respectively.

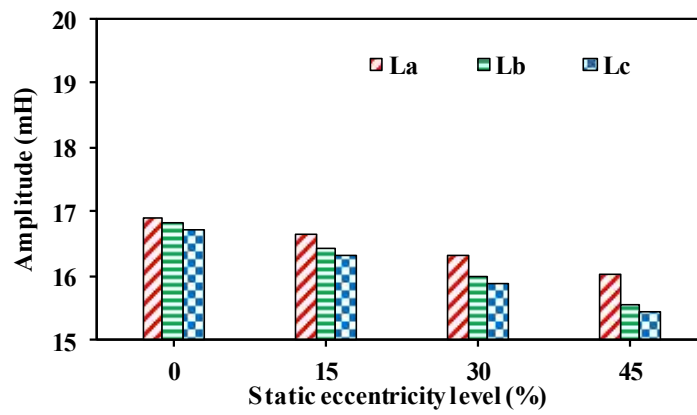


Fig. 7.12. Average value of measured three-phase self-inductances against static eccentricity level.

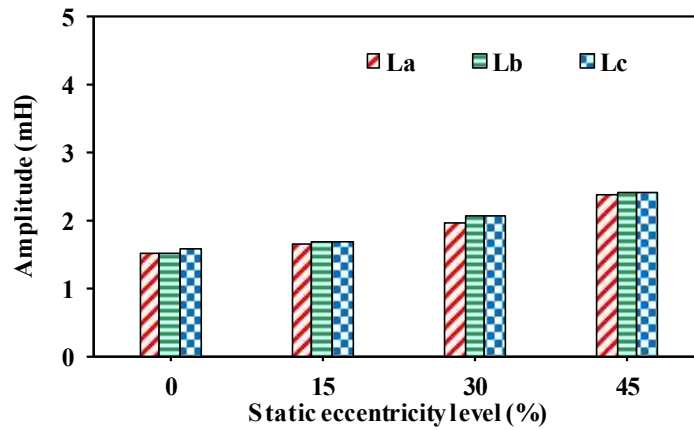


Fig. 7.13. Amplitude of 2<sup>nd</sup> order harmonics of measured three-phase self-inductances against static eccentricity level.

It can be seen that the average value of three-phase self-inductance decreases as the SE level becomes higher, while the 2<sup>nd</sup> order harmonic increases with the SE level. It is worth mentioning here that if the motor operates in the linear magnetic region, the average value of inductance should increase as airgap length decreases, i.e. phase A inductance. However, in

fact, the open-circuit operating point is slightly below the knee of B-H curve. Due to rotor eccentricity, the decreased airgap length will make the stator iron core more saturated so that the inductance will decrease.

Furthermore, the inductances in d-q reference frame are shown in Fig. 7.14.

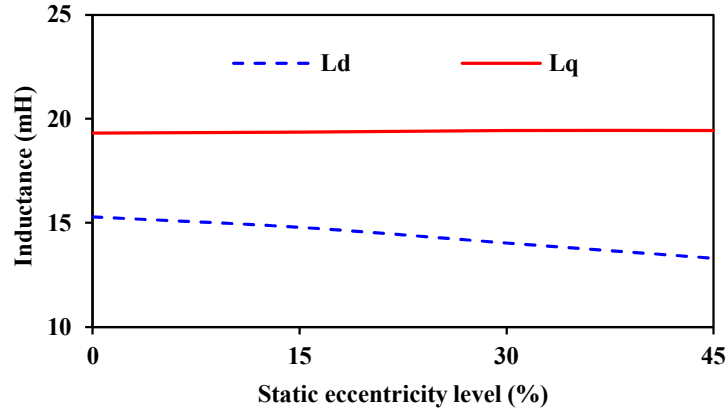


Fig. 7.14. Measured d-q axis inductances against static eccentricity level [WU20f].

Clearly, the d-axis inductance decreases with the SE level and the q-axis inductance only decreases slightly so that can be neglected. This can be explained by (7.28).

$$\begin{cases} L_d = L_0 + M_0 - \frac{3}{2}L_2 \\ L_q = L_0 + M_0 + \frac{3}{2}L_2 \end{cases} \quad (7.28)$$

where  $L_0$  and  $M_0$  are the average values of self- and mutual- inductances,  $L_2$  is the amplitude of the 2<sup>nd</sup> order harmonic of self-inductance. According to Fig. 7.13,  $L_0$  decreases with SE level and  $L_2$  increases with SE level, resulting in the decrease of  $L_d$  and negligible change of  $L_q$ . This is aligned with the conclusion of inductance variation due to rotor eccentricity in Section 7.3.2.

Then, the unbalance level against SE level is investigated. Based on the rotor eccentricity setting mentioned before, the unbalance level of three-phase inductances and back-EMFs are defined as:

$$\frac{X_a - \text{Mean}(X_a, X_b, X_c)}{\text{Mean}(X_a, X_b, X_c)} \times 100\% \quad (7.29)$$

where X can be inductance or back-EMF.

The experimental results of the unbalance level against different SE levels are given in Fig. 7.15. It is obvious that the unbalance levels of both inductance and back-EMF increase with SE

level. Besides, as a result of the existing DE, there is still some unbalance in three-phase inductances and back-EMFs even without SE. Overall, these unbalance levels are quite small since the prototype machine is rotating symmetrical.

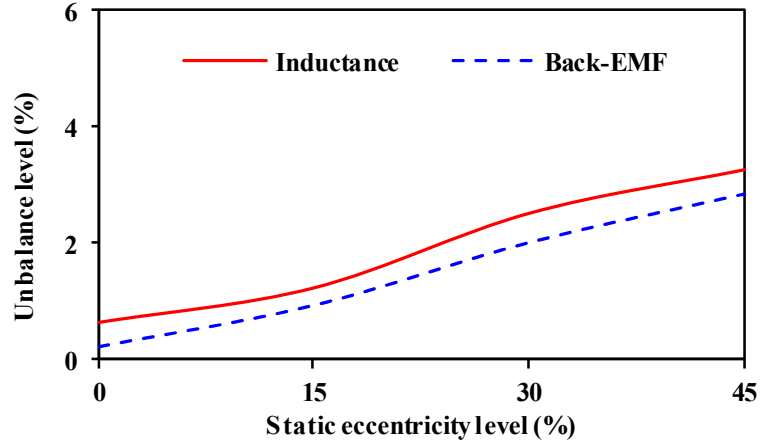


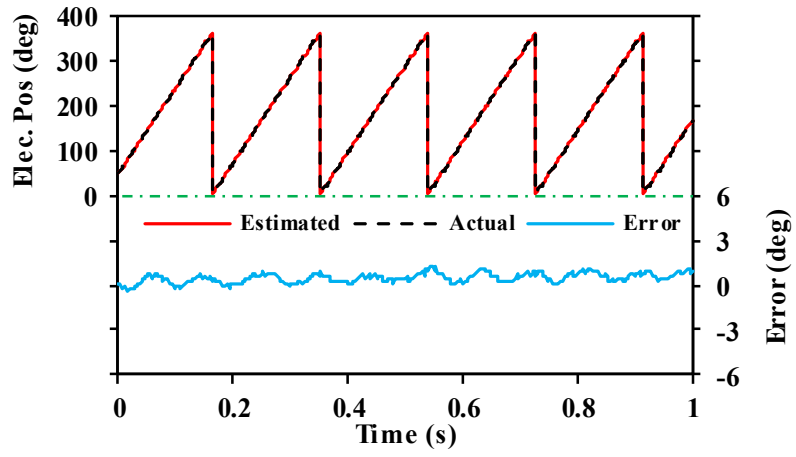
Fig. 7.15. . Unbalance level against static eccentricity. [WU20f]

In conclusion, with higher SE level, the inductance average value decreases while the 2<sup>nd</sup> order harmonic increases. In case of d-q axis inductances, d-axis inductance decreases with SE level and the change in q-axis inductance is negligible. Besides, the unbalance level also goes up with higher SE level.

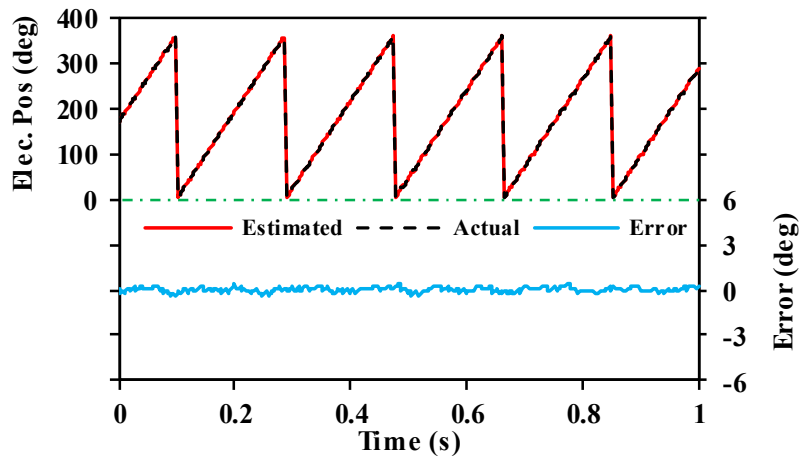
### 7.5.2 Position Estimation under Rotor Eccentricity

In this section, the compensation performance of the modified ANF based position estimation method is shown firstly. Next, considering the different SE levels, position estimation performance of both the conventional method and the modified method are shown. In the test, SE level is tuned from 0% to 45% with a fixed 10% DE level.

An example is firstly given in Fig. 7.16 and Fig. 7.17. In this test, the rotor position is estimated under a 30% SE level. The motor runs at 20rpm at full load condition. At 20rpm, the back-EMF based method can provide a reliable estimation performance.

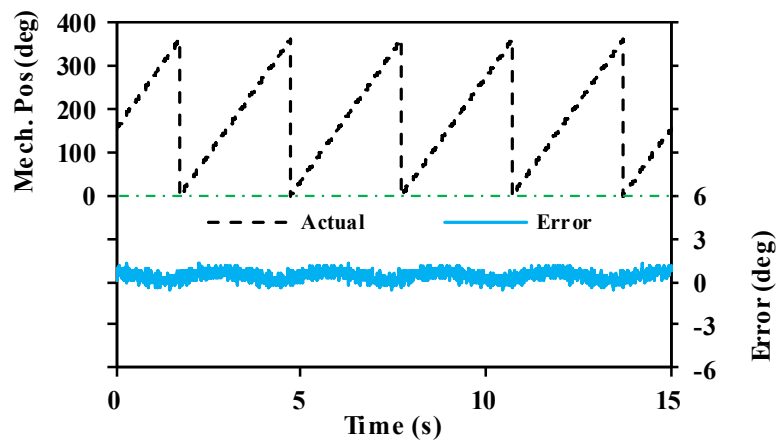


(a)



(b)

Fig. 7.16. The 2<sup>nd</sup> order harmonic errors in position estimation performance. (a) Conventional method. (b) Modified method [WU20f].



(a)

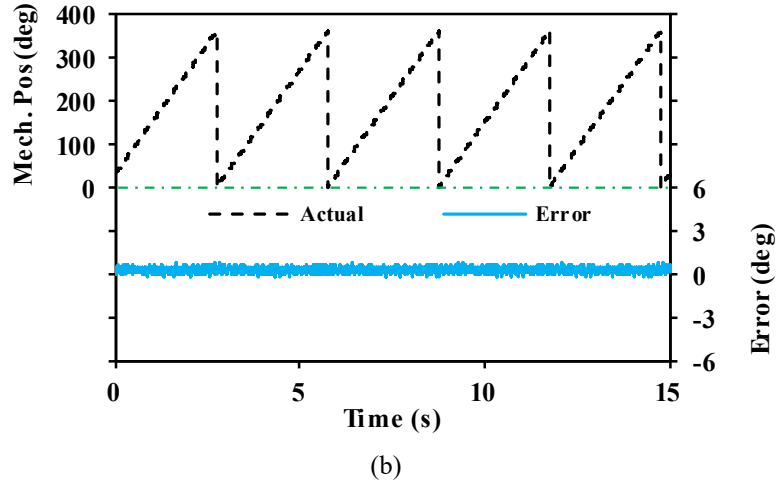
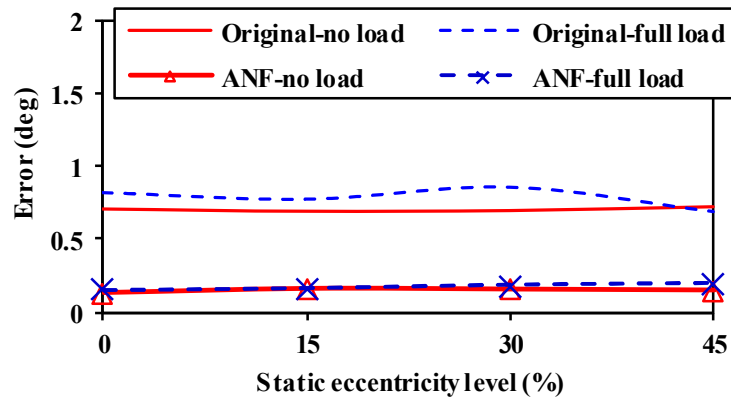
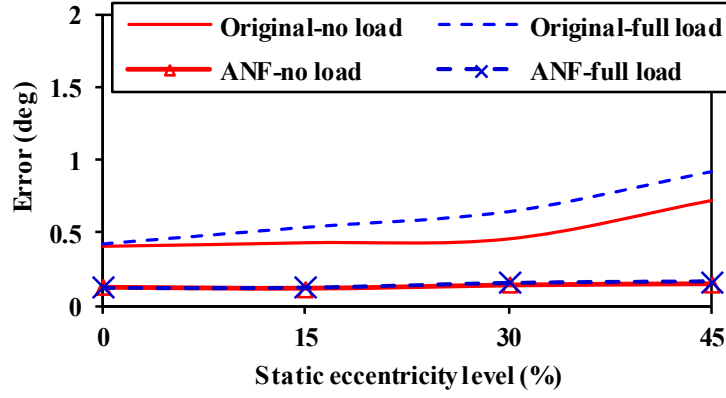


Fig. 7.17. The 2nd order harmonic errors in position estimation performance. (a) Conventional method. (b) Modified method [WU20f].

Estimated results with conventional back-EMF based method are shown in Fig. 7.16(a) and Fig. 7.17(a). Proved by Fig. 7.16(a) and Fig. 7.17(a), there are the 2<sup>nd</sup> order and mechanical frequency order harmonics in the position estimation error due to rotor eccentricity. Then, by applying the modified ANF based position estimator introduced in Section 7.4.3, the estimation performance is shown in Fig. 7.16(b) and Fig. 7.17(b). Clearly, both the 2<sup>nd</sup> order and mechanical frequency harmonics in the position estimation errors are eliminated effectively.

At last, the position errors caused by rotor eccentricity and the compensation performance against different SE level are shown in Fig. 7.18. The mechanical frequency harmonic error is shown in Fig. 7.18(a) and the 2<sup>nd</sup> order harmonic error is shown in Fig. 7.18(b). The motor runs at 20rpm with different load conditions. Clearly, compared with conventional back-EMF based method, the harmonics are suppressed effectively by the modified ANF based position estimator.





(b)

Fig. 7.18. Position errors under different SE levels. (a) Mechanical frequency order harmonic errors.  
(b) 2<sup>nd</sup> order harmonic errors [WU20f].

In Fig. 7.18, it can be seen that there are mechanical frequency and 2<sup>nd</sup> order harmonics exist in the position estimation errors. However, the amplitudes of harmonics in the position error are not very significant. This is due to the prototype machine is rotating symmetrical and the unbalanced level is relatively small as shown in Fig. 7.18. Thus, the induced harmonics in the position error are relatively small for the prototype machine. Nevertheless, for other machines, especially for rotating asymmetric ones, the unbalance level would become much more significant due to rotor eccentricity [ZHU13], [LI15].

## 7.6 Conclusion

This chapter firstly summarized the PMSM characteristic changes due to rotor eccentricity, including unbalanced back-EMFs, flux-linkages and inductances, variation of inductance value and mechanical frequency torque ripple. The rotor eccentricity effect on PMSM characteristics is verified by measurement results with different SE level. Then, mathematical derivation reveals that these rotor eccentricity effect will affect conventional back-EMF based sensorless control performance. It is found that mechanical frequency and the 2<sup>nd</sup> order harmonic errors are introduced in the position estimation. Therefore, an adaptive notch filter is applied to the conventional back-EMF based position estimator. Experiment results are provided showing the existence of mechanical frequency and the 2<sup>nd</sup> order harmonic position errors and these errors are effectively eliminated by the modified position estimator.

Although the main focus of this chapter is on the fundamental model based method, it is worth mentioning that saliency tracking based method can also be affected by rotor eccentricity in way of inductance unbalance induced 2<sup>nd</sup> order harmonic error [XU16c].

# CHAPTER 8

## GENERAL CONCLUSIONS AND FUTURE WORK

### 8.1 Introduction

First of all, the main contributions of this thesis can be grouped by three parts:

- Rotor initial position estimation of SPMSM
- Sensorless start-up operation of SPMSM
- Sensorless control under rotor eccentricity

The research structure linking these three parts is illustrated in Fig. 8.1.

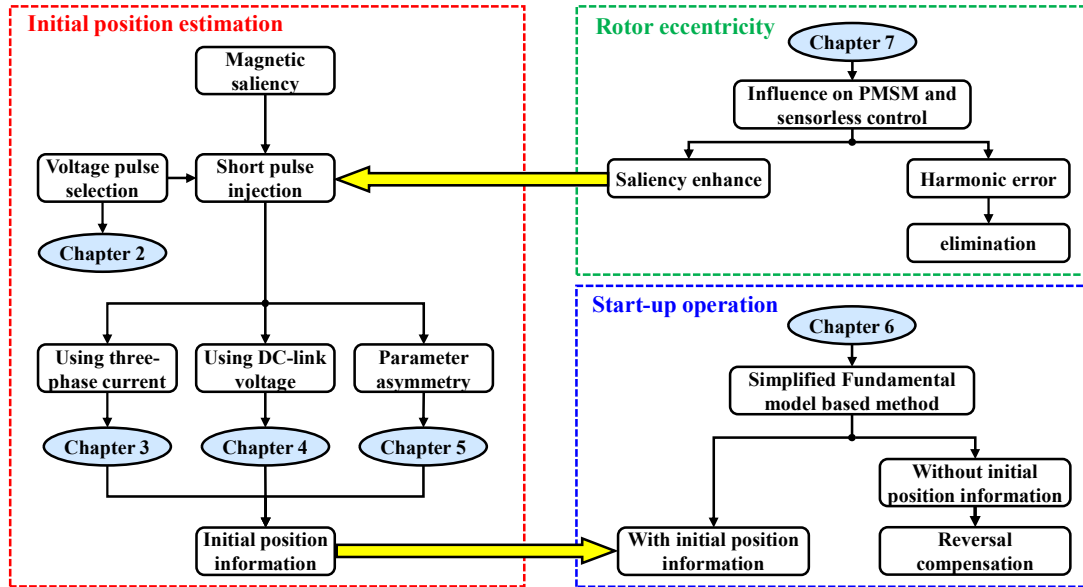


Fig. 8.1. Illustration of research structure.

For the initial position estimation at zero speed, the short pulse injection based method utilizing magnetic saturation effect is extensively investigated in this thesis. With the initial position information, a satisfied sensorless startup operation of SPMSM is achieved by the proposed simplified fundamental model based method in this thesis. Moreover, even without initial position information, sensorless startup operation can be realized with the reverse rotation compensation. Then, the rotor eccentricity effect on PMSMs and conventional fundamental model based sensorless control is investigated. It is found out that the rotor eccentricity can introduce harmonics in position estimation error, and meanwhile, rotor saliency is enhanced under rotor eccentricity which is beneficial to initial position estimation.

## 8.2 Rotor Initial Position Estimation

Based on the magnetic saturation effect, short pulse injection based rotor initial position estimation is systematically investigated in this thesis. The overall structure of the short pulse injection based method can be divided into 4 parts as depicted in Fig. 8.2.

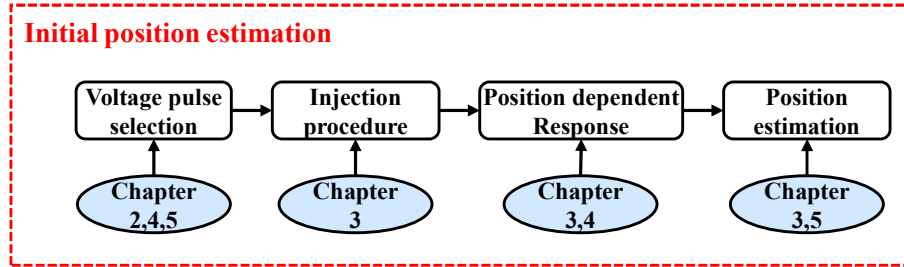


Fig. 8.2. Overall structure of short pulse injection based method.

### *(a) Voltage pulse selection*

Firstly, in order to obtain reliable estimation results, the duration and amplitude of the injected voltage pulse should be selected properly. A simple reliable selection area (RSA) is presented in the thesis. Selection by RSA guarantees a reliable estimation results by considering measurement noise, torque production and rotor movement. For the proposed method utilizing DC-link voltage responses, as discussed in Chapter 4, the pulse selection is additionally influenced by the DC-link capacitance and DC-link resistance which are related to the amplitude of DC-link voltage response. Moreover, for rotor initial position under parameter asymmetries, especially resistance asymmetry, the duration of pulse should be selected as short as possible to minimize the effect of resistance asymmetry. Then, the voltage pulse can be selected according to the proposed extended selection area (ESRA). Since ESRA has a wider and extended selection area which can clearly show if the voltage pulse with shorter duration and higher amplitude is available.

### *(b) Injection procedure*

For the injection procedure, conventional methods inject voltage pulses into several fixed positions and some of them are actually redundant. Hence, in Chapter 3, a novel injection strategy is proposed by selecting injection position based on the previous injection results. The injection strategy has advantages of reducing

- The required injected pulse number
- The total power consumption

- The execution time

***(c) Position dependent response***

For the response part, different position dependent responses are utilized by conventional methods which are shown in TABLE 8.1. For conventional methods utilizing three-phase currents, only the injected phase current response is utilized after injection of voltage pulse. However, the other two phase current responses also contain the position information, and this phenomenon is utilized by the proposed method in Chapter 3, which helps simplify the estimation procedure. Moreover, another novel method is proposed in Chapter 4 which utilizes the DC-link voltage response for position estimation. It is found that the DC-link voltage response is proportional to DC-link resistance. Hence, the estimation performance becomes better as the DC-link resistance increases.

***(d) Position estimation***

Rotor initial position is estimated from the responses at the final step. For conventional methods, peak values of responses are compared and the maximum value indicates where the rotor north pole is. A so-called “boundary case” is introduced in Chapter 3, when the north pole is near or at the boundary between two sectors, the peak values of two responses are very close to each other and become sensitive to measurement noise. Hence, a boundary detection strategy (BDS) is developed which shows the following advantages:

- The estimation error caused by the measurement noise is eliminated and the estimation resolution can be guaranteed at least 30 degrees
- By proper selecting the boundary width, the estimation resolution can be further enhanced from 30 degrees to 15 degrees at least
- The starting torque is increased to at most 99% of the rated value
- The BDS can be applied to all the other existing methods for enhancement

Moreover, considering the cases of parameter asymmetry described in Chapter 5, the three-phase current responses are not symmetrical. Therefore, position estimation is deteriorated. Hence, a compensation strategy by correcting the current responses is proposed in Chapter 5. The three-phase current responses are measured in the offline test. Then, the asymmetric coefficients of the three-phase current responses are measured and calculated. During the estimation, the responses are corrected by these coefficients. Therefore, the influence of parameter asymmetry is eliminated.

For the two proposed methods in Chapters 3 & 4, i.e. [WU20c] and [WU20d], their comparison with conventional methods is shown in TABLE 8.1.

TABLE 8.1  
OVERALL COMPARISON

Method	[SCH97]	[NAK00]	[LEE06]	[LAI03]	[WU20c]	[WU20d]
Response for position estimation	Three-phase current	DQ-axis current	DC-link current	Terminal phase voltage	Three-phase current	DC-link voltage
Consideration of Boundary case	No	No	No	No	<b><u>Yes</u></b>	No
Estimation resolution (degree)	24	30	30	60	<b><u>15</u></b>	30
Maximum estimation error (degree)	15	18	15	30	<b><u>7.5</u></b>	15
Maximum torque reduction (%)	3.41	4.89	3.41	13.4	<b><u>0.86</u></b>	3.41
Required pulses number	6	18	5	4	<b><u>3</u></b>	6
Current sensor	3	3	<b><u>1</u></b>	0	3	0
Voltage sensor	0	0	0	3	0	<b><u>1</u></b>
Requirement of PWM	No	Yes	No	No	No	No

### 8.3 Sensorless Start-up Operation of SPMSM

Sensorless start-up operation is a challenge for SPMSMs. Due to negligible rotor saliency, saliency based methods, e.g. carrier signal injection based methods, cannot be applied. Under this circumstance, a fundamental model based method is a possible solution to realize the start-up operation. In this thesis, a simplified fundamental model based sensorless control method is presented and the start-up operation is achieved even under load. Compared with conventional fundamental model based methods, the proposed method has the following advantages:

- Only the measured stator current is used for position estimation
- Capability of start-up operation under load
- Improved low speed sensorless performance
- Without the need of stator voltage information
- Without the need of machine parameters

Due to simplification of the machine model at low speed, only stator current is used for position estimation, voltage and parameter information are not required. Hence, the estimation performance is enhanced for start-up and low speed operations. The comparison of the proposed method and conventional fundamental model based methods is shown in TABLE 8.2.

TABLE 8.2  
COMPARISON OF FUNDAMENTAL MODEL BASED METHODS

Method	Back-EMF based method	Flux-linkage based method	Proposed method
SPMSM start-up capability	Poor	Poor	Good
Low speed performance	Poor	Poor	Good
Requirement of machine parameter information	Yes	Yes	No
Requirement of stator voltage information	Yes	Yes	No
Requirement of integration	No	Yes	No
Sensitivity to machine parameter variations	High	High	Low
Sensitivity to inverter nonlinearity	High	High	Low

In the start-up operation, since the rotor initial position information is unknown, reverse rotation may happen. Two solutions are proposed in this thesis, including rotor initial position estimation and reverse rotation compensation.

***(a) Rotor initial position estimation***

Based on the magnetic saliency, rotor initial position can be estimated by using the methods introduced in the thesis. Initial position estimation is executed before starting and therefore the reverse rotation is avoided. Since the starting torque is maximized to at least 96% of the rated value, a satisfied start-up even with load can be achieved. Since an extra estimation method is required, overall system complexity is increased.

***(b) Reverse rotation compensation***

A reverse rotation compensation method is presented in the thesis. After rotor rotates reversely, a 180-degree angle is compensated so that the rotation direction is corrected. Clearly, this method is much simpler without the need of magnetic saliency and extra estimation

approach. However, it is limited by some applications of which the reverse rotation is not allowed. Since the starting torque is not guaranteed, the start-up performance under load is poor.

The comparison between these two solutions is given in TABLE 8.3.

TABLE 8.3  
COMPARISON OF SOLUTIONS TO REVERSE ROTATION ISSUE

Method	Rotor initial position estimation	Reverse rotation compensation
Execution timing	Pre	Post
Requirement of magnetic saliency	Yes	No
Maximum starting torque	96% or above	Not guaranteed
Reverse rotation	No	Yes
Complexity	High	Low
Application limitation	Less	More
Performance under load	Good	Poor

## 8.4 Sensorless Control under Rotor Eccentricity

Conventional sensorless control methods are mainly based on a healthy condition of PMSMs. However, the machine is normally non-ideal in reality. Rotor eccentricity, which is a common issue, is considered in the thesis. Under rotor eccentricity, changes in PMSM characteristics are summarized as follows:

- Unbalanced three-phase back-EMF
- Unbalanced three-phase flux-linkage
- Unbalanced three-phase inductance
- Torque ripple
- Change in d-axis inductance amplitude

These undesired effects are shown and discussed in this thesis and approved by experiment measurements. Based on these effects, the influence of rotor eccentricity on sensorless control is also summarized in TABLE 8.4.

TABLE 8.4  
ROTOR ECCENTRICITY EFFECTS ON POSITION ESTIMATION

Methods	Influence on position estimation
Fundamental model based method	<ul style="list-style-type: none"> <li>• 2<sup>nd</sup> order harmonic</li> <li>• Mechanical frequency order harmonic</li> </ul>
Carrier signal injection based method	<ul style="list-style-type: none"> <li>• 2<sup>nd</sup> order harmonic</li> <li>• Increased SNR of current response</li> </ul>
Short pulse injection based method	<ul style="list-style-type: none"> <li>• DC error</li> <li>• Increased SNR of current response</li> </ul>

For fundamental model based method, mainly harmonics are induced in position estimation. Hence, a modified back-EMF estimator by adopting an adaptive notch filter is proposed which eliminates the harmonics effectively.

Besides, the rotor eccentricity effect on saliency based method is also discussed briefly. For carrier signal injection based method, the 2<sup>nd</sup> order harmonic will also appear in the position estimation error due to inductance unbalance. Since only high frequency current response is used and hence the mechanical frequency order harmonic is negligible. For short pulse injection based method, rotor eccentricity will cause inductance asymmetry and hence affect the rotor initial position estimation as demonstrated in Chapter 5. Meanwhile, it is approved that the d-axis inductance is greatly decreased compared with q-axis inductance under rotor eccentricity, which means the saliency is enhanced. Hence, it is potentially beneficial for saliency based methods under the rotor eccentricity.

## 8.5 Future Work

### *A. Magnetic saturation with coil flux only*

In Chapter 2, it is introduced that the magnetic saturation is caused by both PM flux and coil flux. For magnetic saturation effect on SPMSMs, it is normally assumed that the saturation is mainly caused by PM flux and the coil flux is only for polarity detection. However, for some SPMSMs, the air-gap is large or PM flux is weak. Hence, there is negligible magnetic saliency caused by the PM flux. In this situation, only coil flux can be utilized to provide an inductance variation against rotor position. It is worth noting that different from the PM flux, the coil flux will cause an inductance variation with same frequency as one electrical period. Investigation

of this situation can be carried out and the corresponding estimation methods may be developed in the future.

### ***B. Rotor initial position estimation under parameter asymmetries***

In Chapter 5, the short pulse injection based rotor initial position estimation is investigated under resistance and inductance asymmetries. However, the investigation is only done by simulation, experimental verification should be carried out in the future.

### ***C. Consideration of transient part during starting***

In Chapter 6, a simplified fundamental model based method is proposed. Before simplification, the full model is derived as:

$$\begin{bmatrix} i_\alpha \\ i_\beta \end{bmatrix} = \frac{\omega_r \psi_m}{\sqrt{R_s^2 + \omega_r^2 L_s^2}} \begin{bmatrix} \sin(\theta_r - \theta_p) \\ -\cos(\theta_r - \theta_p) \end{bmatrix} + \frac{V_m}{\sqrt{R_s^2 + \omega_r^2 L_s^2}} \begin{bmatrix} -\sin(\theta_r - \theta_v - \theta_p) \\ \cos(\theta_r - \theta_v - \theta_p) \end{bmatrix} +$$

$$\omega_r \psi_m e^{-\frac{R_s t}{L_s}} \begin{bmatrix} \frac{\omega_r L_s}{R_s^2 + \omega_r^2 L_s^2} \\ \frac{R_s}{R_s^2 + \omega_r^2 L_s^2} \end{bmatrix} - \frac{V_m}{\sqrt{R_s^2 + \omega_r^2 L_s^2}} e^{-\frac{R_s t}{L_s}} \begin{bmatrix} \sin(\theta_v + \theta_p) \\ \cos(\theta_v + \theta_p) \end{bmatrix} \quad (8.1)$$

$$\omega_r \psi_m e^{-\frac{R_s t}{L_s}} \begin{bmatrix} \frac{\omega_r L_s}{R_s^2 + \omega_r^2 L_s^2} \\ \frac{R_s}{R_s^2 + \omega_r^2 L_s^2} \end{bmatrix} \quad (8.2)$$

$$\frac{V_m}{\sqrt{R_s^2 + \omega_r^2 L_s^2}} e^{-\frac{R_s t}{L_s}} \begin{bmatrix} \sin(\theta_v + \theta_p) \\ \cos(\theta_v + \theta_p) \end{bmatrix} \quad (8.3)$$

In the thesis, the transient parts, i.e. (8.2) and (8.3), are neglected. However, during the starting operation, these parts may become large, especially (8.2). Hence, it is worthy to investigate the transient parts as a future work.

### ***D. Saliency tracking based method under rotor eccentricity***

The saliency tracking based method under rotor eccentricity is only briefly discussed in this thesis. Investigation of saliency tracking based method under rotor eccentricity should be done experimentally in the future.

### ***E. Zero vector current derivative based method***

For SPMSMs, under the low speed, the fundamental model based methods are mainly affected by the distorted voltage due to inverter nonlinearity. Since the zero vector current

derivative (ZVCD) based method uses the current sampling during zero voltage vector dwelling, stator voltage is not required to estimate the rotor position. Hence, it may be possible to improve the estimation performance at low speed.

## REFERENCES

- [ALM14] A. H. Almarhoon and Z. Q. Zhu, “Influence of back-EMF and current harmonics on position estimation accuracy of permanent magnet synchronous machine”, in *2014 17th International Conference on Electrical Machines and Systems (ICEMS)*, Oct. 2014, pp. 2728–2733.
- [ALM17] A. H. Almarhoon, Z. Q. Zhu, and P. Xu, “Improved pulsating signal injection using zero-sequence carrier voltage for sensorless control of dual three-phase PMSM,” *IEEE Transactions on Energy Conversion*, vol. PP, no. 99, pp. 1–1, 2017.
- [ANT15] R. Antonello, F. Tinazzi, and M. Zigliotto, “Benefits of direct phase voltage measurement in the rotor initial position detection for permanent-magnet motor drives,” *IEEE Transactions on Industrial Electronics*, vol. 62, no. 11, pp. 6719–6726, Nov. 2015.
- [ANT18] R. Antonello, L. Ortombina, F. Tinazzi, and M. Zigliotto, “Enhanced low-speed operations for sensorless anisotropic PM synchronous motor drives by a modified back-EMF observer,” *IEEE Transactions on Industrial Electronics*, vol. 65, no. 4, pp. 3069–3076, Apr. 2018.
- [AYD06] M. Aydin, H. Surong, and T. A. Lipo, “Torque quality and comparison of internal and external rotor axial flux surface-magnet disc machines,” *IEEE Transactions on Industrial Electronics*, vol. 53, no. 3, pp. 822–830, Jun. 2006.
- [AYD07] M. Aydin, Z. Q. Zhu, T. A. Lipo, and D. Howe, “Minimization of cogging torque in axial-flux permanent-magnet machines: design concepts,” *IEEE Transactions on Magnetics*, vol. 43, no. 9, pp. 3614–3622, Sep. 2007.
- [BED15] N. Bedetti, S. Calligaro, and R. Petrella, “Self-commissioning of inverter dead-time compensation by multiple linear regression based on a physical model,” *IEEE Transactions on Industry Applications*, vol. 51, no. 5, pp. 3954–3964, Sep./Oct. 2015.

- [BEN99] A. Benchaib, A. Rachid, E. Audrezet, and M. Tadjine, “Real-time sliding-mode observer and control of an induction motor”, *IEEE Transactions on Industrial Electronics*, vol. 46, no. 1, pp. 128–138, Feb. 1999.
- [BIA05] N. Bianchi, and S. Bolognani, “Influence of rotor geometry of an interior PM motor on sensorless control feasibility,” *Conf. Rec. IEEE-IAS Annu. Meeting*, vol. 4, pp. 2553-2560, 2005.
- [BOL08] I. Boldea, M. C. Paicu, and G. Andreescu, “Active flux concept for motion-sensorless unified AC drives,” *IEEE Transactions on Power Electronics*, vol. 23, no. 5, pp. 2612–2618, Sep. 2008.
- [BOL09] I. Boldea, M. C. Paicu, G. D. Andreescu, and F. Blaabjerg, “Active flux DTFC-SVM sensorless control of IPMSM,” *IEEE Transactions on Energy Conversion*, vol. 24, no. 2, pp. 314-322, 2009.
- [BOL11] S. Bolognani, S. Calligaro, R. Petrella, and M. Sterpellone, “Sensorless control for IPMSM using PWM excitation: Analytical developments and implementation issues,” *Symposium on Sensorless Control for Electrical Drives*, 2011, pp. 64-73.
- [BOL99] S. Bolognani, R. Oboe, and M. Zigliotto, “Sensorless full-digital PMSM drive with EKF estimation of speed and rotor position,” *IEEE Transactions on Industrial Electronics*, vol. 46, no. 1, pp. 184–191, Feb. 1999.
- [BRI01] Briz, F., Degner, M.W., Diez, A., Lorenz, R.D.: 'Measuring, modeling, and decoupling of saturation-induced saliencies in carrier-signal injection-based sensorless AC drives', *IEEE Transactions on Industry Applications*, 2001, 37, (5), pp. 1356–1364.
- [BRI04] F. Briz, M. W. Degner, P. Garcia, and R. D. Lorenz, “Comparison of saliency-based sensorless control techniques for AC machines,” *IEEE Transactions on Industry Applications*, vol. 40, no. 4, pp. 1107–1115, Jul. 2004.
- [BRI05] F. Briz, M. W. Degner, P. Garcia, and J. M. Guerrero, “Rotor position estimation of AC machines using the zero-sequence carrier-signal voltage,”

*IEEE Transactions on Industry Applications*, vol. 41, no. 6, pp. 1637–1646, Nov. 2005.

- [CHA09] P. Champa, P. Somsiri, P. Wipasuramonton, and P. Nakmahachalasint, “Initial rotor position estimation for sensorless brushless dc drives,” *IEEE Transactions on Industry Applications*, vol. 45, no. 4, pp. 1318–1324, Jul. 2009.
- [CHE03] Zhiqian Chen, M. Tomita, S. Doki, and S. Okuma, “An extended electromotive force model for sensorless control of interior permanent-magnet synchronous motors,” *IEEE Transactions on Industrial Electronics*, vol. 50, no. 2, pp. 288–295, Apr. 2003.
- [CHE15] S.-J. Chee, J. Kim, and S.-K. Sul, “Dead-time compensation based on pole voltage measurement,” in *Proc. IEEE Energy Convers. Congr. Expo.*, 2015, pp. 1549–1555.
- [CHE19] G.-R. Chen, J.-Y. Chen, and S.-C. Yang, “Implementation issues of flux linkage estimation on permanent magnet machine position sensorless drive at low speed”, *IEEE Access*, vol. 7, pp. 164641–164649, 2019.
- [CHE20] G.-R. Chen and S.-C. Yang, “Phase voltage measurement for permanent magnet machine sensorless drive using controller capture modulator,” *IEEE Transactions on Industrial Electronics*, vol. 67, no. 1, pp. 49–58, Jan. 2020.
- [CHI09] S. Chi, Z. Zhang, and L. Xu, “Sliding-mode sensorless control of direct-drive PM synchronous motors for washing machine applications,” *IEEE Transactions on Industry Applications*, vol. 45, no. 2, pp. 582–590, Mar./Apr. 2009.
- [CHO17] J. Choi, K. Nam, A. A. Bobtsov, A. Pyrkin, and R. Ortega, “Robust adaptive sensorless control for permanent-magnet synchronous motors,” *IEEE Transactions on Power Electronics*, vol. 32, no. 5, pp. 3989–3997, May 2017.
- [CHU13] W. Q. Chu, “Investigation of torque characteristics of permanent magnet and electrically excited machines,” PhD thesis, University of Sheffield, 2013.

- [COM13] S. Coman and C. Boldișor, “Model reference adaptive control for a DC electrical drive,” *Advanced Materials Research*, vol. 6, no. 2, p. 6, 2013.
- [CON00] A. Consoli, G. Scarcella, and A. Testa, “A new zero-frequency flux-position detection approach for direct-field-oriented-control drives,” *IEEE Transactions on Industry Applications*, vol. 36, no. 3, pp. 797–804, May 2000.
- [CON06] A. Consoli, G. Scarcella, G. Bottiglieri, and A. Testa, “Harmonic analysis of voltage zero-sequence-based encoderless techniques,” *IEEE Transactions on Industry Applications*, vol. 42, no. 6, pp. 1548–1557, Nov. 2006.
- [COR98] M. J. Corley, and R. D. Lorenz, “Rotor position and velocity estimation for a salient-pole permanent magnet synchronous machine at standstill and high speed,” *IEEE Transactions on Industry Applications*, vol.34, no. 4, pp.784–789, 1998.
- [DEG98] M. W. Degner and R. D. Lorenz, “Using multiple saliencies for the estimation of flux, position, and velocity in AC machines,” *IEEE Transactions on Industry Applications*, vol. 34, no. 5, pp. 1097–1104, Sep. 1998.
- [DON12] G. De Donato, F. G. Capponi, G. A. Rivellini, and F. Caricchi, “Integral-slot versus fractional-slot concentrated-winding axial-flux permanent-magnet machines: comparative design, FEA, and experimental tests,” *IEEE Transactions on Industry Applications*, vol. 48, no. 5, pp. 1487-1495, Sep./Oct. 2012.
- [DOR10] D. G. Dorrell, M. Popescu, and D. M. Ionel, “Unbalanced magnetic pull due to asymmetry and low-level static rotor eccentricity in fractional-slot brushless permanent-magnet motors with surface-magnet and consequent-pole rotors,” *IEEE Transactions on Magnetics*, vol. 46, no. 7, pp. 2675–2685, Jul. 2010.
- [EBR09] B. M. Ebrahimi, J. Faiz, and M. J. Roshtkhari, “Static-, dynamic-, and mixed-eccentricity fault diagnoses in permanent-magnet synchronous motors,” *IEEE Transactions on Industrial Electronics*, vol. 56, no. 11, pp. 4727–4739, Nov. 2009.

- [ERT94] N. Ertugrul and P. Acarnley, “A new algorithm for sensorless operation of permanent magnet motors,” *IEEE Transactions on Industry Applications*, vol. 30, no. 1, pp. 126–133, Jan. 1994.
- [FAI06] J. Faiz and S. Pakdelian, “Effect of eccentricity on the accuracy of rotor position estimation techniques in switched reluctance motor drives,” in *2006 IEEE International Magnetism Conference (INTERMAG)*, May 2006, pp. 600–600.
- [FAN15] Y. Fan, L. Zhang, M. Cheng, and K. T. Chau, “Sensorless SVPWM-FADTC of a new flux-modulated permanent-magnet wheel motor based on a wide-speed sliding mode observer,” *IEEE Transactions on Industrial Electronics*, vol. 62, no. 5, pp. 3143–3151, May 2015.
- [FAN94] Fang-Zheng Peng and T. Fukao, “Robust speed identification for speed-sensorless vector control of induction motors,” *IEEE Transactions on Industry Applications*, vol. 30, no. 5, pp. 1234–1240, Sep. 1994.
- [FAT08] M. Fatu, R. Teodorescu, I. Boldea, G. D. Andreescu, and F. Blaabjerg, “I-F starting method with smooth transition to EMF based motion-sensorless vector control of PM synchronous motor/generator,” in *2008 IEEE Power Electronics Specialists Conference*, 2008, pp. 1481–1487.
- [FIS17] M. Fischer and J. Roth-Stielow, “Analysis of the influence of static and dynamic eccentricity on back EMF of a permanent magnet synchronous motor,” in *Innovative Small Drives and Micro-Motor Systems; 11th GMM/ETG-Symposium*, Sep. 2017, pp. 1–6.
- [FOO09] G. Foo, and M. F. Rahman, “Direct torque and flux control of an IPM synchronous motor drive using a back stepping approach,” *IET Electric. Power Appl.*, vol. 3, no. 5, pp. 413–421, 2009
- [FOO10] G. Foo and M. F. Rahman, “Sensorless direct torque and flux-controlled IPM synchronous motor drive at very low speed without signal injection,” *IEEE Transactions on Industrial Electronics*, vol. 57, no. 1, pp. 395–403, Jan. 2010.

- [FUE11] E. Fuentes and R. Kennel, "Sensorless-predictive torque control of the PMSM using a Reduced Order Extended Kalman Filter", in *2011 Symposium on Sensorless Control for Electrical Drives*, Sep. 2011, pp. 123–128.
- [GAD10] S. M. Gadoue, D. Giaouris, and J. W. Finch, "MRAS sensorless vector control of an induction motor using new sliding-mode and fuzzy-logic adaptation mechanisms," *IEEE Transactions on Energy Conversion*, vol. 25, no. 2, pp. 394-402, 2010.
- [GAO07] Q. Gao, G. M. Asher, M. Sumner, and P. Makys, "Position estimation of AC machines over a wide frequency range based on space vector PWM excitation," *IEEE Transactions on Industry Applications*, vol. 43, no. 4, pp. 1001-1011, 2007.
- [GAR05] F. Gardner, "Phaselock technique," (Willey, 2005, 3rd edn.).
- [GAR07] P. Garcia, F. Briz, M. W. Degner, and D. D. Reigosa, "Accuracy, bandwidth, and stability limits of carrier-signal-injection-based sensorless control methods," *IEEE Transactions on Industry Applications*, vol. 43, no. 4, pp. 990–1000, Jul./Aug. 2007.
- [GEN10] F. Genduso, R. Miceli, C. Rando, and G. R. Galluzzo, "Back EMF sensorless-control algorithm for high-dynamic performance PMSM," *IEEE Transactions on Industrial Electronics*, vol. 57, no. 6, pp. 2092–2100, Jun. 2010.
- [GON11] L. M. Gong and Z. Q. Zhu, "A novel method for compensating inverter nonlinearity effects in carrier signal injection-based sensorless control from positive-sequence carrier current distortion," *IEEE Transactions on Industry Applications*, vol. 47, no. 3, pp. 1283–1292, May 2011.
- [GON12] L. Gong, "Carrier signal injection based sensorless control of permanent magnet brushless ac machines", PhD Thesis, Research Group of Electric Machines and Drives, Department of Electronic and Electrical Engineering, University of Sheffield, 2012.
- [GON13] L. M. Gong and Z. Q. Zhu, "Robust initial rotor position estimation of permanent-magnet brushless AC machines with carrier-signal-injection-based

- sensorless control,” *IEEE Transactions on Industry Applications*, vol. 49, no. 6, pp. 2602–2609, Nov. 2013.
- [GON20] C. Gong, Y. Hu, J. Gao, Y. Wang, and L. Yan, “An improved delay-suppressed sliding-mode observer for sensorless vector-controlled PMSM,” *IEEE Transactions on Industrial Electronics*, vol. 67, no. 7, pp. 5913–5923, Jul. 2020.
- [GUE05] J. M. Guerrero, M. Leetmaa, F. Briz, A. Zamarron, and R. D. Lorenz, “Inverter nonlinearity effects in high frequency signal injection-based, sensorless control methods,” *IEEE Transactions on Industry Applications*, vol. 41, no. 2, pp. 618–626, Mar./Apr. 2005.
- [GUG06] P. Guglielmi, M. Pastorelli, and A. Vagati, “Cross-saturation effects in IPM motors and related impact on sensorless control,” *IEEE Transactions on Industry Applications*, vol. 42, no. 6, pp. 1516 – 1522, 2006.
- [HA08] J.-I. Ha, “Analysis of inherent magnetic position sensors in symmetric AC machines for zero or low speed sensorless drives,” *IEEE Transactions on Magnetics*, vol. 44, no. 12, pp. 4689–4696, Dec. 2008.
- [HAM10] W. Hammel, and R. M. Kennel, “Position sensorless control of PMSM by synchronous injection and demodulation of alternating carrier voltage,” *Symposium on Sensorless Control for Electrical Drives*, 2010, pp. 56-63.
- [HAN00] L. Harnefors and H. P. Nee, “A general algorithm for speed and position estimation of AC motors,” *IEEE Transactions on Industrial Electronics*, vol. 47, no. 1, pp. 77–83, Feb. 2000.
- [HAR96] L. Harnefors, “Speed estimation from noisy resolver signals”, in *1996 Sixth International Conference on Power Electronics and Variable Speed Drives (Conf. Publ. No. 429)*, Sep. 1996, pp. 279–282.
- [HEJ11] R. W. Hejny and R. D. Lorenz, “Evaluating the practical low-speed limits for back-EMF tracking-based sensorless speed control using drive stiffness as a

- key metric,” *IEEE Transactions on Industry Applications*, vol. 47, no. 3, pp. 1337–1343, May/Jun. 2011.
- [HEJ11] R. W. Hejny and R. D. Lorenz, “Evaluating the practical low-speed limits for back-EMF tracking-based sensorless speed control using drive stiffness as a key metric,” *IEEE Transactions on Industry Applications*, vol. 47, no. 3, pp. 1337–1343, May/Jun. 2011.
- [HOL03] J. Holtz and Juntao Quan, “Drift- and parameter-compensated flux estimator for persistent zero-stator-frequency operation of sensorless-controlled induction motors”, *IEEE Transactions on Industry Applications*, vol. 39, no. 4, pp. 1052–1060, Jul. 2003.
- [HOL05] J. Holtz and J. Juliet, “Sensorless acquisition of the rotor position angle of induction motors with arbitrary stator windings,” *IEEE Transactions on Industry Applications*, vol. 41, no. 6, pp. 1675-1682, Nov./Dec. 2005.
- [HOL08] J. Holtz, “Acquisition of position error and magnet polarity for sensorless control of PM synchronous machines,” *IEEE Transactions on Industry Applications*, vol. 44, no. 4, pp. 1172–1180, 2008.
- [HON12a] J. Hong, S. Park, D. Hyun, T. Kang, S. B. Lee, C. Karl and A. Haumer, “Detection and classification of rotor demagnetization and eccentricity faults for PM synchronous motors,” *IEEE Transactions on Industry Applications*, vol. 48, no. 3, pp. 923–932, May 2012.
- [HON12b] J. Hong, S. B. Lee, C. Kral, and A. Haumer, “Detection of airgap eccentricity for permanent magnet synchronous motors based on the d-axis inductance,” *IEEE Transactions on Power Electronics*, vol. 27, no. 5, pp. 2605–2612, May 2012.
- [HSI13] M. Hsieh and Y. Yeh, “Rotor eccentricity effect on cogging torque of PM generators for small wind turbines,” *IEEE Transactions on Magnetics*, vol. 49, no. 5, pp. 1897–1900, May 2013.

- [HU98] J. Hu and B. Wu, "New integration algorithms for estimating motor flux over a wide speed range," *IEEE Transactions on Power Electronics*, vol. 13, no. 5, p. 9, 1998.
- [HUA11] Y. Hua, M. Sumner, G. Asher, Q. Gao, and K. Saleh, "Improved sensorless control of a permanent magnet machine using fundamental pulse width modulation excitation," *IET Electric Power Application*, vol. 5, no. 4, pp. 359-370, 2011.
- [HUR94] K. D. Hurst, T. G. Habetler, G. Griva, and F. Profumo, "Speed sensorless field-oriented control of induction machines using current harmonic spectral estimation," in *Proceedings of 1994 IEEE Industry Applications Society Annual Meeting*, Oct. 1994, vol. 1, pp. 601–607 vol.1.
- [HWA01] S. M. Hwang, K. T. Kim, W. B. Jeong, Y. H. Jung, and B. S. Kang, "Comparison of vibration sources between symmetric and asymmetric HDD spindle motors with rotor eccentricity," *IEEE Transactions on Industry Applications*, vol. 37, no. 6, pp. 1727–1731, Dec. 2001.
- [IEP12] L. I. Iepure, I. Boldea, and F. Blaabjerg, "Hybrid I-f starting and observer-based sensorless control of single-phase BLDC-PM motor drives," *IEEE Transactions on Industrial Electronics*, vol. 59, no. 9, pp. 3436–3444, Sep. 2012.
- [JAN03a] J.H. Jang, S.K. Sul, J.I. Ha, K. Ide, and M. Sawamura, "Sensorless drive of surface-mounted permanent-magnet motor by high-frequency signal injection based on magnetic saliency," *IEEE Transactions on Industry Applications*, vol. 39, no. 4, pp. 1031–1039, 2003.
- [JAN03b] J.H. Jang, S.K. Sul, Y.C. Son, "Current measurement issues in sensorless control algorithm using high frequency signal injection method," *Conf. Rec. IEEE-IAS Annual Meeting*, 2003, pp. 1134–1141.
- [JAN06] M. Jansson, L. Harnefors, O. Wallmark, and M. Leksell, "Synchronization at startup and stable rotation reversal of sensorless nonsalient PMSM drives,"

*IEEE Transactions on Industrial Electronics*, vol. 53, no. 2, pp. 379–387, Apr. 2006.

- [JAN95] P. L. Jansen and R. D. Lorenz, “Transducerless position and velocity estimation in induction and salient ac machines,” *IEEE Transactions on Industry Applications*, vol. 31, no. 2, pp. 240–247, Mar./Apr. 1995.
- [JEO05] Y. Jeong, R. D. Lorenz, T. M. Jahns, and S.-K. Sul, “Initial rotor position estimation of an interior permanent-magnet synchronous machine using carrier-frequency injection methods,” *IEEE Transactions on Industry Applications*, vol. 41, no. 1, pp. 38–45, Jan. 2005.
- [JEO91] S.-G. Jeong and M.-H. Park, “The analysis and compensation of dead-time effects in PWM inverters,” *IEEE Transactions on Industrial Electronics*, vol. 38, no. 2, pp. 108–114, Apr. 1991.
- [JIA11] H. Jiang and M. Sumner, “Sensorless torque control of a PM motor using modified HF injection method for audible noise reduction,” in *Proceedings of the 2011 14th European Conference on Power Electronics and Applications*, Aug. 2011, pp. 1–8.
- [JIN05] Jingbo Liu, Jiangang Hu, and Longya Xu, “Sliding mode observer for wide speed range sensorless induction machine drives: considerations for digital implementation”, in *IEEE International Conference on Electric Machines and Drives, 2005.*, May 2005, pp. 300–307.
- [KAN10] J. Kang, “Sensorless control of permanent magnet motors,” *Control Engineering*, vol. 57, no. 4, pp. 1-4, 2010.
- [KARL04] C. Kral, T. G. Habetler, and R. G. Harley, “Detection of mechanical imbalances of induction machines without spectral analysis of time-domain signals,” *IEEE Transactions on Industry Applications*, vol. 40, no. 4, pp. 1101–1106, Jul. 2004.
- [KHL12] A. Khlaief, M. Bendjedia, M. Boussak, and M. Gossa, “A nonlinear observer for high-performance sensorless speed control of IPMSM drive,” *IEEE Transactions on Power Electronics*, vol. 27, no. 6, pp. 3028–3040, Jun. 2012.

- [KIM03] H. Kim, M. C. Harke, and R. D. Lorenz, "Sensorless control of interior permanent-magnet machine drives with zero-phase lag position estimation", *IEEE Transactions on Industry Applications*, vol. 39, no. 6, pp. 1726–1733, Nov. 2003.
- [KIM04] H. Kim, K.-K. Huh, R. D. Lorenz, and T. M. Jahns, "A novel method for initial rotor position estimation for IPM synchronous machine drives," *IEEE Transactions on Industry Applications*, vol. 40, no. 5, pp. 1369–1378, Sep. 2004.
- [KIM11] H. Kim, J. Son, and J. Lee, "A high-speed sliding-mode observer for the sensorless speed control of a PMSM," *IEEE Transactions on Industrial Electronics*, vol. 58, no. 9, pp. 4069–4077, Sep. 2011.
- [KIM12] S. Kim, J. I. Ha, and S. K. Sul, "PWM switching frequency signal injection sensorless method in IPMSM," *IEEE Transactions on Industry Applications*, vol. 48, no.5, pp. 1576–1587, Sep./Oct. 2012.
- [KIM16] D. Kim, Y.-C. Kwon, S.-K. Sul, J.-H. Kim, and R.-S. Yu, "Suppression of injection voltage disturbance for high-frequency square-wave injection sensorless drive with regulation of induced high-frequency current ripple," *IEEE Transactions on Industry Applications*, vol. 52, no. 1, pp. 302–312, Jan. 2016.
- [KIM97] J.-S. Kim and S.-K. Sul, "New approach for high-performance PMSM drives without rotational position sensors," *IEEE Transactions on Power Electronics*, vol. 12, no. 5, pp. 904–911, Sep. 1997.
- [KRA04] C. Kral, T. G. Habetler, and R. G. Harley, "Detection of mechanical imbalances of induction machines without spectral analysis of time-domain signals," *IEEE Transactions on Industry Applications*, vol. 40, no. 4, pp. 1101–1106, Jul. 2004.
- [KWO15] Y.-C. Kwon, S.-K. Sul, N. A. Baloch, S. Morimoto, and M. Ohto, "Design of IPMSM with eccentric rotor and search coils for absolute position sensorless drive," in *2015 9th International Conference on Power Electronics and ECCE Asia (ICPE-ECCE Asia)*, Jun. 2015, pp. 1135–1142.

- [KWO16] Y.-C. Kwon, S.-K. Sul, N. A. Baloch, S. Morimoto, and M. Ohto, “Design, modeling, and control of an IPMSM with an asymmetric rotor and search coils for absolute position sensorless drive,” *IEEE Transactions on Industry Applications*, vol. 52, no. 5, pp. 3839–3850, Sep. 2016.
- [LAI03] Y.-S. Lai, F.-S. Shyu, and S. S. Tseng, “New initial position detection technique for three-phase brushless DC motor without position and current sensors,” *IEEE Transactions on Industry Applications*, vol. 39, no. 2, pp. 485–491, Mar. 2003.
- [LEE06] W. J. Lee and S. K. Sul, “A new starting method of BLDC motors without position sensor,” *IEEE Transactions on Industry Applications*, vol. 42, no. 6, pp. 1532–1538, Nov. 2006.
- [LEE10] J. Lee, J. Hong, K. Nam, R. Ortega, L. Praly, and A. Astolfi, “Sensorless control of surface-mount permanent-magnet synchronous motors based on a nonlinear observer,” *IEEE Transactions on Power Electronics*, vol. 25, no. 2, pp. 290–297, Feb. 2010.
- [LEE14] W.-J. Lee and S.-K. Sul, “DC-Link voltage stabilization for reduced dc-link capacitor inverter,” *IEEE Transactions on Industry Applications*, vol. 50, no. 1, pp. 404–414, Jan. 2014.
- [LEE15] Y. Lee, Y. C. Kwon, and S. K. Sul, “Comparison of rotor position estimation performance in fundamental-model-based sensorless control of PMSM,” in *2015 IEEE Energy Conversion Congress and Exposition (ECCE)*, Sep. 2015, pp. 5624–5633.
- [LI07] Y. Li, Z. Q. Zhu, D. Howe, and C. M. Bingham, “Modeling of cross-coupling magnetic saturation in signal-injection-based sensorless control of permanent-magnet brushless AC motors,” *IEEE Transactions on Magnetics*, vol. 43, no. 6, pp. 2552–2554, Jun. 2007.
- [LI09] Y. Li, Z.Q. Zhu, D. Howe, C.M. Bingham, and D. Stone, “Improved rotor position estimation by signal injection in brushless AC motors, accounting

for cross-coupling magnetic saturation,” *IEEE Transactions on Industry Applications*, vol.45, no.5, pp.1843-1849, 2009.

- [LI15] Y. Li, Q. Lu, Z. Q. Zhu, L. J. Wu, G. J. Li, and D. Wu, “Analytical synthesis of air-gap field distribution in permanent magnet machines with rotor eccentricity by superposition method,” *IEEE Transactions on Magnetics*, vol. 51, no. 11, pp. 1–4, Nov. 2015.
- [LI17] H. Li, X. Zhang, S. Yang, F. Li, and M. Ma, “Improved initial rotor position estimation of IPMSM using amplitude demodulation method based on HF carrier signal injection,” in *Conf. IECON IEEE-IES Annual Meeting*, 2017, pp. 1996–2001.
- [LIN02] M. Linke, R. Kennel, and J. Holtz, “Sensorless position control of permanent magnet synchronous machines without limitation at zero speed,” *Industrial Electronics Society 28th Annual Conference (IECON 02)*, vol.1, pp. 674-679, 2002.
- [LIN03] M. Linke, R. Kennel, and J. Holtz, “Sensorless speed and position control of synchronous machines using alternating carrier injection,” *Electric Machines and Drives Conference*, vol.2, pp. 1211-1217, 2003.
- [LIU04] Y. Liu, Z. Q. Zhu, Y. F. Shi, and D. Howe, “Sensorless direct torque control of a permanent magnet brushless AC drive via an extended Kalman filter”, in *Second International Conference on Power Electronics, Machines and Drives (PEMD 2004)*., Mar. 2004, vol. 1, pp. 303-307.
- [LIU06] Y. Liu, Z. Q. Zhu, and D. Howe, “Instantaneous torque estimation in sensorless direct-torque-controlled brushless DC motors”, *IEEE Transactions on Industry Applications*, vol. 42, no. 5, pp. 1275–1283, Sep. 2006.
- [LIU13] J. M. Liu, “Novel sensorless control of permanent magnet synchronous machines,” PhD thesis, University of Sheffield, 2013.
- [LIU14] J. M. Liu and Z. Q. Zhu, “Novel sensorless control strategy with injection of high-frequency pulsating carrier signal into stationary reference frame,” *IEEE Transactions on Industry Applications*, vol. 50, no. 4, pp. 2574–2583, Jul. 2014.

- [LIU15] J. M. Liu and Z. Q. Zhu, "Rotor position estimation for dual-three-phase permanent magnet synchronous machine based on third harmonic back-EMF", in *2015 IEEE Symposium on Sensorless Control for Electrical Drives (SLED)*, Jun. 2015, pp. 1–8.
- [LIU17] Z. Liu, J. Huang, and B. Li, "Diagnosing and distinguishing rotor eccentricity from partial demagnetisation of interior PMSM based on fluctuation of high-frequency d-axis inductance and rotor flux," *IET Electric Power Applications*, vol. 11, no. 7, pp. 1265–1275, 2017.
- [LU13] K. Lu, X. Lei, and F. Blaabjerg, "Artificial inductance concept to compensate nonlinear inductance effects in the back EMF-based sensorless control method for PMSM," *IEEE Transactions on Energy Conversion*, vol. 28, no. 3, pp. 593–600, Sep. 2013.
- [LU18] Q. Lu, X. Zhu, L. Quan, Y. Zuo, and S. Du, "Rotor position estimation scheme with harmonic ripple attenuation for sensorless controlled permanent magnet synchronous motors", *IET Electric Power Applications*, vol. 12, no. 8, pp. 1200–1206, 2018.
- [MAT96] N. Matsui, "Sensorless PM brushless DC motor drives," *IEEE Transactions on Industrial Electronics*, vol. 43, no. 2, pp. 300–308, Apr. 1996.
- [MOR02] S. Morimoto, K. Kawamoto, M. Sanada, and Y. Takeda, "Sensorless control strategy for salient-pole PMSM based on extended EMF in rotating reference frame," *IEEE Transactions on Industry Applications*, vol. 38, no. 4, pp. 1054–1061, Jul. 2002.
- [NAK00] S. Nakashima, Y. Inagaki, and I. Miki, "Sensorless initial rotor position estimation of surface permanent-magnet synchronous motor," *IEEE Transactions on Industry Applications*, vol. 36, no. 6, pp. 1598–1603, Nov. 2000.
- [NOG98] T. Noguchi, K. Yamada, S. Kondo, and I. Takahashi, "Initial rotor position estimation method of sensorless PM synchronous motor with no sensitivity to

- armature resistance,” *IEEE Transactions on Industrial Electronics*, vol. 45, no. 1, pp. 118–125, Feb. 1998.
- [ORL10] T. Orłowska-Kowalska and M. Dybkowski, “Stator-current-based MRAS estimator for a wide range speed-sensorless induction-motor drive”, *IEEE Transactions on Industrial Electronics*, vol. 57, no. 4, pp. 1296–1308, Apr. 2010.
- [PAC05] M. Pacas, and J. Weber, "Predictive direct torque control for the pm synchronous machine," *IEEE Transactions on Industrial Electronics*, vol. 52, no. 5, pp. 1350-1356, 2005.
- [PAR12] Y. Park and S.-K. Sul, “A novel method utilizing trapezoidal voltage to compensate for inverter nonlinearity,” *IEEE Transactions on Power Electronics*, vol. 27, no. 12, pp. 4837–4846, Dec. 2012.
- [PEL10] G. Pellegrino, P. Guglielmi, E. Armando, and R. I. Bojoi, “Self-commissioning algorithm for inverter nonlinearity compensation in sensorless induction motor drives,” *IEEE Transactions on Industry Applications*, vol. 46, no. 4, pp. 1416–1424, Jul./Aug. 2010.
- [PII08] A. Piippo, M. Hinkkanen, and J. Luomi, “Analysis of an adaptive observer for sensorless control of interior permanent magnet synchronous motors,” *IEEE Transactions on Industrial Electronics*, vol. 55, no. 2, pp. 570–576, Feb. 2008.
- [QUA14] N. K. Quang, N. T. Hieu, and Q. P. Ha, “FPGA-based sensorless Pmsm speed control using reduced-order extended Kalman filters”, *IEEE Transactions on Industrial Electronics*, vol. 61, no. 12, pp. 6574–6582, Dec. 2014.
- [RAC08] D. Raca, M.C. Harke, and R.D. Lorenz, “Robust magnet polarity estimation for initialization of PM synchronous machines with near-zero saliency,” *IEEE Transactions on Industry Applications*, vol. 44, no. 4, pp. 1199-1209, 2008.
- [RAC10] D. Raca, P. Garcia, D.D. Reigosa, F. Briz, and R.D. Lorenz, “Carrier-signal selection for sensorless control of PM synchronous machines at zero and very

low speeds,” *IEEE Transactions on Industry Applications*, vol. 46, no. 1, pp. 167-178, 2010

- [RAH06] K. M. Rahman, N. R. Patel, T. G. Ward, J. M. Nagashima, F. Caricchi, and F. Crescimbeni, “Application of direct-drive wheel motor for fuel cell electric and hybrid electric vehicle propulsion system,” *IEEE Transactions on Industry Applications*, vol. 42, no. 5, pp. 1185-1192, Sep./Oct. 2006.
- [RAJ07] S. Rajagopalan, W. I Roux, T. G. Habetler, and R. G. Harley, “Dynamic eccentricity and demagnetized rotor magnet detection in trapezoidal flux (brushless DC) motors operating under different load conditions,” *IEEE Transactions on Power Electronics*, vol. 22, no. 5, pp. 2061–2069, Sep. 2007.
- [RAU07] R. Raute, C. Caruana, J. Cilia, C. S. Staines, and M. Summer, “A zero speed operation sensorless PMSM drive without additional test signal injection,” in *2007 European Conference on Power Electronics and Applications*, Sep. 2007, pp. 1–10.
- [RAU08] R. Raute, C. Caruana, C. S. Staines, J. Cilia, M. Sumner, and G. Asher, “Operation of a sensorless PMSM drive without additional test signal injection,” in *2008 4th IET Conference on Power Electronics, Machines and Drives*, Apr. 2008, pp. 616–620.
- [RAU10] R. Raute, C. Caruana, C. S. Staines, J. Cilia, M. Sumner, and G. M. Asher, “Analysis and compensation of inverter nonlinearity effect on a sensorless PMSM drive at very low and zero speed operation,” *IEEE Transactions on Industrial Electronics*, vol. 57, no. 12, pp. 4065–4074, Dec. 2010.
- [REI08] D. Reigosa, P. Garcia, D. Raca, F. Briz, and R.D. Lorenz, “Measurement and adaptive decoupling of cross-saturation effects and secondary saliencies in sensorless-controlled IPM synchronous machines,” *IEEE Transactions on Industry Applications*, vol. 44, no. 6, pp. 1758–1767, 2008.
- [REI10] D. Reigosa, P. Garcia, F. Briz, D. Raca, and R. D. Lorenz, “Modeling and adaptive decoupling of high-frequency resistance and temperature effects in carrier-based sensorless control of PM synchronous machines,” *IEEE*

*Transactions on Industry Applications*, vol. 46, no. 1, pp. 139–149, Jan./Feb. 2010.

- [RIV13] J.D. Rivera, A. Navarrete, M. Meza, A. Loukianov, and J. Canedo, “Digital sliding mode sensorless control for surface mounted PMSM,” *IEEE Transactions on Industrial Informatics*, vol. PP, no. 99, pp. 1, 2013.
- [ROU07] W. le Roux, R. G. Harley, and T. G. Habetler, “Detecting rotor faults in low power permanent magnet synchronous machines,” *IEEE Transactions on Power Electronics*, vol. 22, no. 1, pp. 322–328, Jan. 2007.
- [SAG15] A. Saghaforia, H. W. Ping, M. N. Uddin, and K. S. Gaeid, “Adaptive fuzzy sliding-mode control into chattering-free IM drive”, *IEEE Transactions on Industry Applications*, vol. 51, no. 1, pp. 692–701, Jan. 2015.
- [SCH18] M. Schubert and R. W. D. Doncker, “Instantaneous phase voltage sensing in PWM voltage source inverters,” *IEEE Transactions on Power Electronics*, vol. 33, no. 8, pp. 6926–6935, Aug. 2018.
- [SCH96] M. Schroedl, “Sensorless control of AC machines at low speed and Standstill based on the “INFORM” method,” *Conf. Rec. IEEE-IAS Annual Meeting*, 1996, pp. 270–277.
- [SCH97] P. B. Schmidt, M. L. Gasperi, G. Ray, and A. H. Wijenayake, “Initial rotor angle detection of a nonsalient pole permanent magnet synchronous machine,” in *Proc. IEEE-IAS Annual Meeting*, 1997, pp. 459–463.
- [SIL06] C. Silva, G. M. Asher, and M. Sumner, “Hybrid rotor position observer for wide speed-range sensorless PM motor drives including zero speed,” *IEEE Transactions on Industrial Electronics*, vol. 53, no. 2, pp. 373–378, Apr. 2006.
- [SON15] X. Song, J. Hu, H. Huang, and J. Zhang, “Eccentricity harmonics detection-based speed estimation approach in a sensorless induction motors,” in *2015 IEEE International Conference on Cyber Technology in Automation, Control, and Intelligent Systems (CYBER)*, Jun. 2015, pp. 1405–1410.
- [SON17] J. Y. Song, K. J. Kang, C. H. Kang, and G. H. Jang, “Cogging torque and unbalanced magnetic pull due to simultaneous existence of dynamic and static

eccentricities and uneven magnetization in permanent magnet motors,” *IEEE Transactions on Magnetics*, vol. 53, no. 3, pp. 1–9, Mar. 2017.

- [SUN16] W. Sun, J. Gao, X. Liu, Y. Yu, G. Wang, and D. Xu, “Inverter nonlinear error compensation using feedback gains and self-tuning estimated current error in adaptive full-order observer,” *IEEE Transactions on Industry Applications*, vol. 52, no. 1, pp. 472–482, Jan./Feb. 2016.
- [TAJ93] H. Tajima, and Y. Hori, “Speed sensorless field-orientation control of the induction machine,” *IEEE Transactions on Industry Applications*, Vol. 29, No. 1, pp. 175-180, 1993.
- [TAK86] I. Takahashi, and T. Noguchi, “A new quick-response and high efficiency control strategy of an induction-motor,” *IEEE Transactions on Industry Applications*, vol. 22, no. 5, pp. 820-827, 1986.
- [TAL15] H. Talhaoui, A. Menacer, and R. Kechida, “Mixed eccentricity fault diagnosis in the sensorless field oriented control induction motor using DWT technique,” in *2015 IEEE 10th International Symposium on Diagnostics for Electrical Machines, Power Electronics and Drives (SDEMPED)*, Sep. 2015, pp. 97–103.
- [TAN14] S. Taniguchi, K. Yasui, and K. Yuki, “Noise reduction method by injected frequency control for position sensorless control of permanent magnet synchronous motor,” in *2014 International Power Electronics Conference (IPEC-Hiroshima 2014 - ECCE ASIA)*, May 2014, pp. 2465–2469.
- [TAN20] Q. Tang, D. Chen, and X. He, “Integration of improved flux linkage observer and I-F starting method for wide-speed-range sensorless SPMSM drives,” *IEEE Transactions on Power Electronics*, vol. 35, no. 8, pp. 8374–8383, Aug. 2020.
- [TAU17] J. Tau, K. Wu, and Y. Tzou, “Sensorless PMSM drive with large dc-link voltage fluctuation,” in *IECON 2017 - 43rd Annual Conference of the IEEE Industrial Electronics Society*, 2017, pp. 2166–2171.
- [TER01] B. Terzic, and M. Jadric, “Design and implementation of the extended Kalman filter for the speed and rotor position estimation of brushless

- DC motor,” *IEEE Transactions on Industrial Electronics*, vol. 48, no. 6, pp. 1065–1073, 2001.
- [TES03] N. Teske, M. Asher, K. J. Bradley, and G. M. Sumner, “Analysis and suppression of high-frequency inverter modulation in sensorless position controlled induction machine drives,” *IEEE Transactions on Industry Applications*, vol. 39, no. 1, pp. 10–18, Jan./Feb. 2003.
- [TUR00] M. Tursini, R. Petrella, and F. Parasiliti, “Adaptive sliding-mode observer for speed-sensorless control of induction motors,” *IEEE Transactions on Industry Applications*, vol. 36, no. 5, pp. 1380–1387, Sep. 2000.
- [TUR03] M. Tursini, R. Petrella, and F. Parasiliti, “Initial rotor position estimation method for PM motors,” *IEEE Transactions on Industry Applications*, vol. 39, no. 6, pp. 1630–1640, Nov. 2003.
- [WAN10] Y. Wang, N. Guo, J. Zhu, N. Duan, S. Wang, Y. Guo, W. Xu, and Y. Li, “Initial rotor position and magnetic polarity identification of PM synchronous machine based on nonlinear machine model and finite element analysis,” *IEEE Transactions on Magnetics*, vol. 46, no. 6, pp. 2016–2019, Jun. 2010.
- [WAN12a] G. Wang, G. Zhang, R. Yang, and D. Xu, “Robust low-cost control scheme of direct-drive gearless traction machine for elevators without a weight transducer,” *IEEE Transactions on Industry Applications*, vol. 48, no. 3, pp. 996–1005, May 2012.
- [WAN12b] Z. Wang, K. Lu, and F. Blaabjerg, “A simple startup strategy based on current regulation for back-EMF-based sensorless control of PMSM,” *IEEE Transactions on Power Electronics*, vol. 27, no. 8, pp. 3817–3825, Aug. 2012.
- [WAN13] G. Wang, R. Yang, and D. Xu, “DSP-based control of sensorless IPMSM drives for wide-speed-range operation,” *IEEE Transactions on Industrial Electronics*, vol. 60, no. 2, pp. 720–727, Feb. 2013.
- [WAN14a] G. Wang, H. Zhan, G. Zhang, X. Gui, and D. Xu, “Adaptive compensation method of position estimation harmonic error for emf-based observer in sensorless IPMSM drives,” *IEEE Transactions on Power Electronics*, vol. 29, no. 6, pp. 3055–3064, Jun. 2014.

- [WAN14b] F. Wang, Z. Zhang, S. A. Davari, R. Fotouhi, D. A. Khaburi, J. Rodriguez and R. Kennel, “An encoderless predictive torque control for an induction machine with a revised prediction model and EFOSMO,” *IEEE Transactions on Industrial Electronics*, vol. 61, no. 12, pp. 6635–6644, Dec. 2014.
- [WAN16] G. Wang, L. Yang, B. Yuan, B. Wang, G. Zhang, and D. Xu, “Pseudo-random high-frequency square-wave voltage injection based sensorless control of IPMSM drives for audible noise reduction,” *IEEE Transactions on Industrial Electronics*, vol. 63, no. 12, pp. 7423–7433, Dec. 2016.
- [WAN17a] G. Wang, L. Yang, G. Zhang, X. Zhang, and D. Xu, “Comparative investigation of pseudorandom high-frequency signal injection schemes for sensorless IPMSM drives,” *IEEE Transactions on Power Electronics*, vol. 32, no. 3, pp. 2123–2132, Mar. 2017.
- [WAN17b] Y. Wang, Y. Xu, N. Niimura, B. D. Rudolph, and R. D. Lorenz, “Using volt-second sensing to directly improve torque accuracy and self-sensing at low speeds,” *IEEE Transactions on Industry Applications*, vol. 53, no. 5, pp. 4472–4482, Sep./Oct. 2017.
- [WAN18] Y. Wang, W. Xie, X. Wang, and D. Gerling, “A precise voltage distortion compensation strategy for voltage source inverters,” *IEEE Transactions on Industrial Electronics*, vol. 65, no. 1, pp. 59–66, Jan. 2018.
- [WAN19] G. Wang, D. Xiao, G. Zhang, C. Li, X. Zhang, and D. Xu, “Sensorless control scheme of IPMSMs using HF orthogonal square-wave voltage injection into a stationary reference frame,” *IEEE Transactions on Power Electronics*, vol. 34, no. 3, pp. 2573–2584, Mar. 2019.
- [WAN20a] G. Wang, M. Valla, and J. Solsona, “Position sensorless permanent magnet synchronous machine drives—a review,” *IEEE Transactions on Industrial Electronics*, vol. 67, no. 7, pp. 5830–5842, Jul. 2020.
- [WAN20b] H. Wang, K. Lu, D. Wang, and F. Blaabjerg, “Simple and effective online position error compensation method for sensorless SPMSM drives,” *IEEE Transactions on Industry Applications*, vol. 56, no. 2, pp. 1475–1484, Mar. 2020.

- [WEH86] H. Weh and H. May, “Achievable force densities for permanent magnet excited machines in new configurations,” in *Proc. Int. Conf. Elect. Mach.*, Munchen, 1986, pp. 1107-1111.
- [WIP09] P. Wipasuramontorn, Z. Q. Zhu, and D. Howe, “Sensorless vector control of non-salient BLAC machines based on a modified rotor flux-linkage observer”, in *2009 International Conference on Power Electronics and Drive Systems (PEDS)*, Nov. 2009, pp. 1056–1061.
- [WU10] L. J. Wu, Z. Q. Zhu, J. T. Chen, and Z. P. Xia, “An analytical model of unbalanced magnetic force in fractional-slot surface-mounted permanent magnet machines,” *IEEE Transactions on Magnetics*, vol. 46, no. 7, pp. 2686–2700, Jul. 2010.
- [WU20] C. Wu, Y. Zhao, and M. Sun, “Enhancing low-speed sensorless control of PMSM using phase voltage measurements and online multiple parameter identification,” *IEEE Transactions on Power Electronics*, pp. 1–1, 2020.
- [WU91] R. Wu and G. R. Slemon, “A permanent magnet motor drive without a shaft sensor,” *IEEE Transactions on Industry Applications*, vol. 27, no. 5, pp. 1005–1011, Sep./Oct. 1991.
- [XIN20] J. Xing, Z. Qin, C. Lin, and X. Jiang, “Research on startup process for sensorless control of PMSMS based on I-F method combined with an adaptive compensator,” *IEEE Access*, vol. 8, pp. 70812–70821, 2020.
- [XU15] P. L. Xu and Z. Q. Zhu, “Comparison of carrier signal injection methods for sensorless control of PMSM drives,” in *2015 IEEE Energy Conversion Congress and Exposition (ECCE)*, Sep. 2015, pp. 5616–5623.
- [XU16a] P. L. Xu and Z. Q. Zhu, “Novel carrier signal injection method using zero-sequence voltage for sensorless control of PMSM drives,” *IEEE Transactions on Industrial Electronics*, vol. 63, no. 4, pp. 2053–2061, Apr. 2016.
- [XU16b] P. L. Xu, Zhu, Z.Q., Wu, D.: “Carrier signal injection-based sensorless control of permanent magnet synchronous machines without the need of magnetic

- polarity Identification”, *IEEE Transactions on Industry Applications*, vol. 52, no. 5, pp. 3916–3926, 2016.
- [XU16c] P. L. Xu and Z. Q. Zhu, “Carrier signal injection-based sensorless control for permanent-magnet synchronous machine drives considering machine parameter asymmetry,” *IEEE Transactions on Industrial Electronics*, vol. 63, no. 5, pp. 2813–2824, May 2016.
- [XU19] W. Xu, Y. Jiang, C. Mu, and F. Blaabjerg, “Improved nonlinear flux observer-based second-order SOIFO for PMSM sensorless control,” *IEEE Transactions on Power Electronics*, vol. 34, no. 1, pp. 565–579, Jan. 2019.
- [YAG14] S. Yaghubi, M. R. Tavakoli, F. Faradjizadeh, and E. Afjei, “Evaluation of eccentricities faults effects on sensorless operation of Switched Reluctance motors,” in *2014 5th Conference on Thermal Power Plants (CTPP)*, Jun. 2014, pp. 173–176.
- [YAN08] Yan, Y., Zhu, J.G., Guo, Y.G.: “Initial rotor position estimation and sensorless direct torque control of surface-mounted permanent magnet synchronous motors considering saturation saliency”, *IET Electric Power Applications*, 2008, 2, (1), pp. 42–48
- [YAN11a] S.C. Yang, T. Suzuki, R.D. Lorenz, and T.M. Jahns, “Surface permanent magnet synchronous machine design for saliency tracking self-sensing position estimation at zero and low speeds,” *IEEE Transactions on Industry Applications*, vol. 47, no. 5, pp. 2103–2116, 2011.
- [YAN12] S.-C. Yang and R. D. Lorenz, “Surface permanent magnet synchronous machine position estimation at low speed using eddy-current-reflected asymmetric resistance,” *IEEE Transactions on Power Electronics*, vol. 27, no. 5, pp. 2595–2604, May 2012.
- [YAN19] H. Yang, R. Yang, W. Hu, and Z. Huang, “FPGA-based sensorless speed control of PMSM using enhanced performance controller based on the reduced-order EKF,” *IEEE J. Emerg. Sel. Topics Power Electron.*, pp. 1–1, 2019.
- [YAO20] Y. Yao, Y. Huang, F. Peng, and J. Dong, “Position sensorless drive and online parameter estimation for surface-mounted PMSMs based on adaptive full-state

- feedback control,” *IEEE Transactions on Power Electronics*, vol. 35, no. 7, pp. 7341–7355, Jul. 2020.
- [YIN19] Z. Yin, F. Gao, Y. Zhang, C. Du, G. Li, and X. Sun, “A review of nonlinear Kalman filter applying to sensorless control for AC motor drives”, *CES Transactions on Electrical Machines and Systems*, vol. 3, no. 4, pp. 351–362, Dec. 2019.
- [YOO09a] A. Yoo and S. K. Sul, “Design of flux observer robust to interior permanent-magnet synchronous motor flux variation,” *IEEE Transactions on Industry Applications*, vol. 45, no. 5, pp. 1670–1677, Sep. 2009.
- [YOO09b] Y.D. Yoon, S.K. Sul, S. Morimoto and K. Ide, “High bandwidth sensorless algorithm for AC machines based on square-wave type voltage injection,” *Conf. Rec. IEEE ECCE*, 20-24 Sep. 2009, pp.2123-2130.
- [YOO11] Y.-D. Yoon, S.-K. Sul, S. Morimoto, and K. Ide, “High-bandwidth sensorless algorithm for AC machines based on square-wave-type voltage injection,” *IEEE Transactions on Industry Applications*, vol. 47, no. 3, pp. 1361–1370, May 2011.
- [YUA20] Q. Yuan, Y. Yang, H. Wu, and H. Wu, “Low speed sensorless control based on an improved sliding mode observation and the inverter nonlinearity compensation for SPMSM,” *IEEE Access*, vol. 8, pp. 61299–61310, 2020.
- [ZHA02] Zhang Yan and V. Utkin, “Sliding mode observers for electric machines-an overview”, in *IEEE 2002 28th Annual Conference of the Industrial Electronics Society. IECON 02*, Sevilla, Spain, 2002, vol. 3, pp. 1842–1847.
- [ZHA05] Y. Zhao and J. Chai, “Power factor analysis of transverse flux permanent machines,” in *Int. Conf. Elect. Mach. Syst.*, Nanjing, China, 2005, pp. 450-459.
- [ZHA11] Y.C. Zhang, J.G. Zhu, W. Xu, and Y.G. Guo, “A simple method to reduce torque ripple in direct torque-controlled permanent-magnet synchronous motor by using vectors with variable amplitude and angle,” *IEEE Transactions on Industrial Electronics*, vol. 58, no. 7, pp. 2848-2859, 2011.

- [ZHA13a] X. Zhang, “Sensorless induction motor drive using indirect vector controller and sliding-mode observer for electric vehicles”, *IEEE Transactions on Vehicular Technology*, vol. 62, no. 7, pp. 3010–3018, Sep. 2013.
- [ZHA13b] Y. Zhao, C. Wei, Z. Zhang, and W. Qiao, “A review on position/speed sensorless control for permanent-magnet synchronous machine-based wind energy conversion systems”, *IEEE Journal of Emerging and Selected Topics in Power Electronics*, vol. 1, no. 4, pp. 203–216, Dec. 2013.
- [ZHA14a] Y. Zhao, W. Qiao, and L. Wu, “Improved rotor position and speed estimators for sensorless control of interior permanent-magnet synchronous machines”, *IEEE Journal of Emerging and Selected Topics in Power Electronics*, vol. 2, no. 3, pp. 627–639, Sep. 2014.
- [ZHA14b] H. Zhaobin, Y. Linru, and W. Zhaodong, “Sensorless initial rotor position identification for non-salient permanent magnet synchronous motors based on dynamic reluctance difference,” *IET Power Electron.*, vol. 7, no. 9, pp. 2336–2346, Sep. 2014.
- [ZHA15] Y. Zhao, Z. Zhang, W. Qiao, and L. Wu, “An extended flux model-based rotor position estimator for sensorless control of salient-pole permanent-magnet synchronous machines,” *IEEE Transactions on Power Electronics*, vol. 30, no. 8, pp. 4412–4422, Aug. 2015.
- [ZHA17] N. Zhao, N. Schofield, R. Yang, and R. Gu, “Investigation of DC-link voltage and temperature variations on EV traction system design,” *IEEE Transactions on Industry Applications*, vol. 53, no. 4, pp. 3707–3718, Jul. 2017.
- [ZHA18] S. Zhao, X. Huang, Y. Fang, and J. Zhang, “Compensation of DC-Link voltage fluctuation for railway traction PMSM in multiple low-switching-frequency synchronous space vector modulation modes,” *IEEE Transactions on Vehicular Technology*, vol. 67, no. 1, pp. 235–250, Jan. 2018.
- [ZHA20] W. Zhang, Z. Yang, L. Zhai, and J. Wang, “Speed sensorless control of hybrid excitation axial field flux-switching permanent-magnet machine based on

model reference adaptive system”, *IEEE Access*, vol. 8, pp. 22013–22024, 2020.

[ZHO97] L. Zhong, M.F. Rahman, W.Y. Hu, and K.W. Lim, “Analysis of direct torque control in permanent magnet synchronous motor drives,” *IEEE Transactions on Power Electronics*, vol. 12, no. 3, pp. 528-536, 1997.

[ZHU13] Z. Q. Zhu, L. J. Wu, and M. L. M. Jamil, “Distortion of back-EMF and torque of PM brushless machines due to eccentricity,” *IEEE Transactions on Magnetics*, vol. 49, no. 8, pp. 4927–4936, Aug. 2013.

# APPENDIX A DESCRIPTION OF EXPERIMENTAL PLATFORMS

In the thesis, two test rigs are used, namely Test Rig I and Test Rig II. For both test rigs, the experiment platforms are based on the dSPACE1006 control system. The schematic setup of the overall experimental system is shown in Fig. A.1. It can be seen that the overall experimental platform generally consists of the DC power supply, the 2-level voltage source inverter, dSPACE control system, the test motor and load motor. For the test motor, three-phase stator currents and the DC-link voltage are measured by hall effect sensors. The rotor position and speed of the test motor are measured by an incremental encoder mounted on the shaft. Optionally, the output torque of the test motor can be measured by a torque transducer on the shaft.

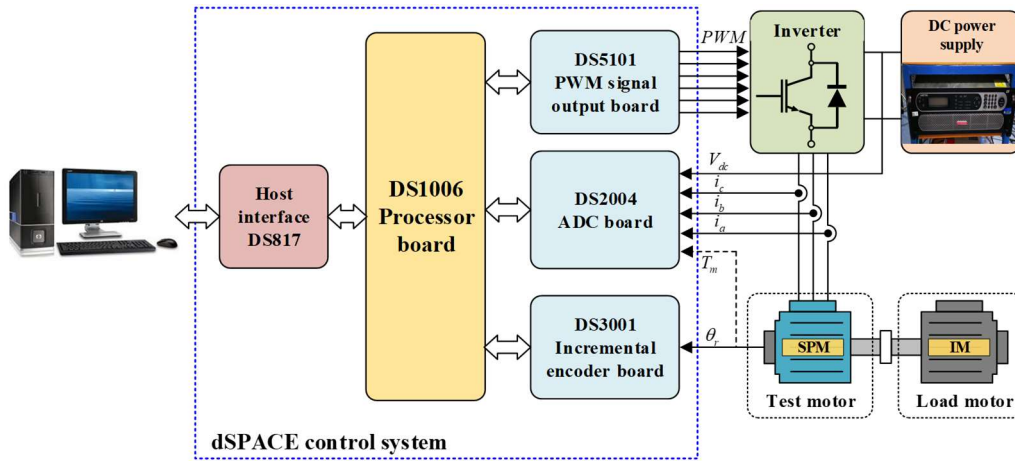


Fig. A.1. Schematic experimental platform setup.

For the dSPACE control system, the DS1006 processor board is based on a 2.4GHz multi-core AMD Opteron CPU, which is the heart of the real-time control system. The analog outputs of current and voltage sensors are converted to digital signals by DS2004 ADC board, and then transferred to the DS1006 processor board. The output of the incremental encoder is sent to DS3001 incremental encoder board and then transferred to DS1006 processor board. After receiving the PWM duty cycle information from DS1006 processor board, DS5101 board will output 6 channel PWM signals to the inverter module. At last, with the host interface board DS817, the real-time data from the platform can be transmitted to the PC interface software, the real-time data can be captured and monitored during the operation.

For Test Rig I, the overall experiment platform is shown in Fig. A.2. As shown in Fig. A.2, a load motor is connected to the test motor. The load motor is an induction motor driven by the Siemens servo drive S120, which can be controlled in a constant torque mode so that a desired load can be given. Moreover, the output torque of the test motor can be measured by a torque transducer mounted on the shaft of test motor.

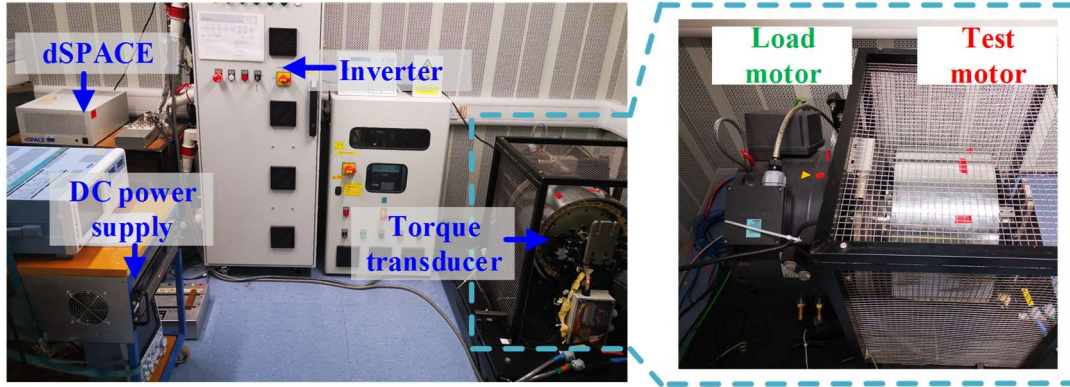


Fig. A.2. Overall experimental platform of Test Rig I.

The test motor is a modular dual three-phase surface-mounted PMSM with 42 slots/32 poles, which is shown in Fig. A.2. The parameters of the test motor are given in TABLE A.1. Since the main topic is focus on the single three-phase SPMSM, only one channel of the test motor is used.

TABLE A.1  
PARAMETERS OF THE TEST MOTOR I

Parameters	Value
Pole pairs	16
Resistance ( $\Omega$ )	4.1
Rated RMS current (A)	2.83
Rated speed (rpm)	170
Rated torque (Nm)	171
No-load PM flux linkage (Wb)	0.98
Rated power (kW)	3
Synchronous Inductance (mH)	17.21

For Test Rig II, the overall experiment platform is shown in Fig. A.3. As shown in Fig. A.3, a load motor is connected to the test motor. The load motor is a brush DC motor. A DC voltage is applied to the load motor to provide a load torque.

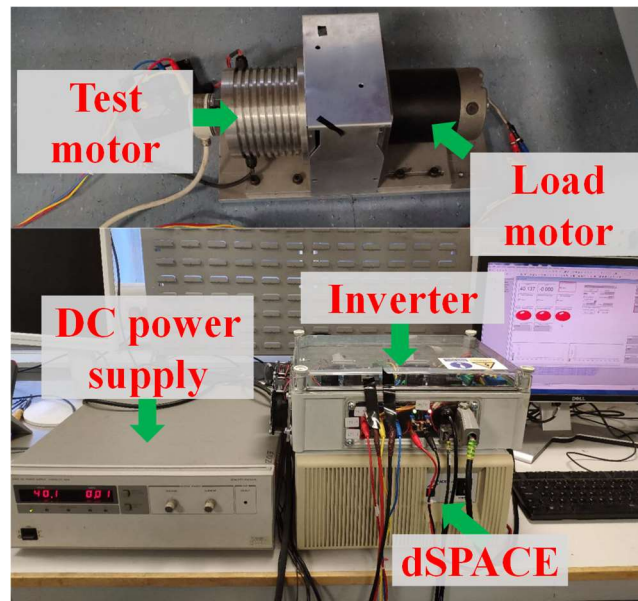


Fig. A.3. Overall experimental platform of Test Rig II.

The test motor is a dual three-phase surface-mounted PMSM with 12 slots/10 poles, which is shown in Fig. A.3. The parameters of the test motor are given in TABLE A.2. Since the main topic is focus on the single three-phase SPMSM, only one channel of the test motor is used.

TABLE A.2  
PARAMETERS OF THE TEST MOTOR II

Parameters	Value
Pole pairs	5
Resistance ( $\Omega$ )	1.096
Rated RMS current (A)	4
Rated speed (rpm)	400
Rated torque (Nm)	5
No-load PM flux linkage (Wb)	0.0734
Rated power (kW)	0.24
Synchronous Inductance (mH)	2.142

## APPENDIX B PUBLICATIONS

### Journal Papers:

- 1     **X. M. Wu**, Z. Q. Zhu, Z. Y. Wu, T. Y. Liu and Y. X. Li “Analysis and suppression of rotor eccentricity effects on fundamental model based sensorless control of permanent magnet synchronous machine,” *IEEE Transactions on Industry Applications*. In press.
- 2     **X. M. Wu**, Z. Q. Zhu and Z. Y. Wu, “A new simplified fundamental model based sensorless control method,” *IET Electric Power Applications*. Under revision.
- 3     **X. M. Wu** and Z. Q. Zhu, “A novel rotor initial position detection method for surface-mounted permanent magnet synchronous machine,” *IEEE Transactions on Energy Conversion*. Under revision.
- 4     **X. M. Wu** and Z. Q. Zhu, “A novel rotor initial position detection method utilizing DC-link voltage sensor,” *IEEE Transactions on Industry Applications*. Under revision.
- 5     Y. X. Li, Z. Q. Zhu, **X. M. Wu**, A. S. Thomas and Z. Wu, “Comparative Study of Modular Dual 3-Phase Permanent Magnet Machines With Overlapping/Non-overlapping Windings,” in *IEEE Transactions on Industry Applications*, vol. 55, no. 4, pp. 3566-3576, July-Aug. 2019.
- 6     Y. X. Li, Z. Q. Zhu, A. S. Thomas, Z. Y. Wu and **X. M. Wu**, “Novel Modular Fractional Slot Permanent Magnet Machines With Redundant Teeth,” in *IEEE Transactions on Magnetics*, vol. 55, no. 9, pp. 1-10, Sept. 2019, Art no. 8204810.

### Conference papers:

- 1     **X. M. Wu** and Z. Q. Zhu, “Simple Mechanical Rotor Position Estimation Method Based on Rotor Eccentricity,” *2019 IEEE International Electric Machines & Drives Conference (IEMDC)*, San Diego, CA, USA, 2019, pp. 412-418.
- 2     **X. M. Wu** and Z. Q. Zhu, “A Novel Rotor Initial Position Detection Method Utilizing DC-link Voltage Sensor,” *2019 IEEE International Electric Machines & Drives Conference (IEMDC)*, San Diego, CA, USA, 2019, pp. 1093-1098.
- 3     **X. M. Wu**, and Z. Q. Zhu, “A simple voltage pulse selection strategy for rotor initial position estimation,” *IET int. conf. on Power Electronics, Machines and Drives, PEMD, 2020*, Accepted.
- 4     **X. M. Wu**, and Z. Q. Zhu, “Comparative study of rotor initial position estimation,” *IET int. conf. on Power Electronics, Machines and Drives, PEMD, 2020*, Accepted.

- 5 Y. X. Li, Z. Q. Zhu, **X. M. Wu**, A. S. Thomas and Z. Y. Wu, “Comparison of Modular Dual 3-phase PM Machines with Overlapping/Non-overlapping Windings,” *2018 IEEE Energy Conversion Congress and Exposition (ECCE)*, Portland, OR, 2018, pp. 2335-2342.

**Patents:**

- 1 **X. M. Wu**, Z. Q. Zhu, Z. Y. Wu, J. M. Liu, “A sensorless control method for surface-mounted permanent magnet synchronous machine starting”, Siemens plc. 29 August 2018. (Siemens Ref: 2018E19708 GB PTT/REI).
- 2 **X. M. Wu**, Z. Y. Wu, Z. Q. Zhu, “A novel rotor initial position detection method for surface-mounted permanent magnet synchronous machine”, Siemens plc. 18 Oct. 2018. (Siemens Ref: 2018E22465 GB PTT/REI).
- 3 **X. M. Wu**, Z. Y. Wu, Z. Q. Zhu, “Method for determining the rotational position of a rotor in a permanent magnet synchronous machine”, Siemens Gamesa Renewable Energy, EU patent filing date: 12 December 2018, EU Patent Application Number 18211866.1-1202, Application date 27 Feb. 2019.